DAMAGE IDENTIFICATION IN LAYERED COMPOSITE PLATES USING KINEMATIC FULL-FIELD MEASUREMENTS

Cédric Devivier

▶ **To cite this version:**

Cédric Devivier. DAMAGE IDENTIFICATION IN LAYERED COMPOSITE PLATES USING KINEMATIC FULL-FIELD MEASUREMENTS. Solid mechanics [physics.class-ph]. Université de Technologie de Troyes, 2012. English. NNT : . tel-00817143

HAL Id: tel-00817143

https://theses.hal.science/tel-00817143

Submitted on 23 Apr 2013

HAL is a multi-disciplinary open access archive for the deposit and dissemination of scientific research documents, whether they are published or not. The documents may come from teaching and research institutions in France or abroad, or from public or private research centers.

L'archive ouverte pluridisciplinaire **HAL**, est destinée au dépôt et à la diffusion de documents scientifiques de niveau recherche, publiés ou non, émanant des établissements d'enseignement et de recherche français ou étrangers, des laboratoires publics ou privés.

IDENTIFICATION D'ENDOMMAGEMENTS AU SEIN DE PLAQUES COMPOSITES STRATIFIÉES À L'AIDE DE MESURES DE CHAMPS CINÉMATIQUES

DAMAGE IDENTIFICATION IN LAYERED COMPOSITE PLATES USING KINEMATIC FULL-FIELD MEASUREMENTS

19 Juillet 2012 – July, the 19th 2012

Thèse de doctorat – PhD Thesis

pour l'obtention du grade de – to obtain the grade of

Docteur – Doctor

de – from

Université de Technologie de Troyes

par – by

Cédric DEVIVIER

Directeur – Advisor

Fabrice PIERRON

Rapporteurs – Referees

M. Peter DAVIES	Ingénieur-chercheur HDR, SMS, IFREMER
M. Jerôme MOLIMARD	Professeur, B2M, École des Mines de Saint-Étienne

Éxaminateurs – Examiner

M. Michel GRÉDIAC	Professeur, Institut Pascal, Université Blaise Pascal
M. Guillaume MONTAY	Maître de conférence, LASMIS, Université de Technologie de Troyes
M. Fabrice PIERRON	Professeur, LMPF, Arts et Métiers ParisTech
M. Michael R. WISNOM	Professeur, ACCIS, University of Bristol UK

Toute ma vie, j'ai couru derrière un idéal qui était de comprendre et de connaıtre la science et je me suis bien amusé.

Hubert Reeves

ACKNOWLEDGEMENTS

First, I am grateful to Professor Fabrice Pierron and Professor Michael R. Wisnom for giving me the opportunity to undertake this PhD, and also for their support, advice, teaching, and trust along these four years. I would also like to express my sincere thanks to Dr. Alain Giraudeau for introducing me to the world of research during my final year at Arts et Métiers Paristech.

I would also like to thank all of my colleagues from Arts et métiers Paristech and from the University of Bristol for their great help and support throughout these years, and for all the interesting discussions.

I wish to thank the Champagne-Ardenne Regional Council and the ACCIS department from the University of Bristol for funding this PhD thesis and the Advanced Computing Research Centre from the University of Bristol, for providing the computational facilities (more info at http://www.bris.ac.uk/acrc/).

Finally, I would like to give my special thanks to my family and friends. They have always supported and encouraged me to do my best.

RÉSUMÉ EN FRANÇAIS

Les matériaux composites offrent de nombreux avantages par rapport aux matériaux traditionnels que sont les métaux par exemple : meilleures propriétés pour un poids plus faible. Les plastiques à renfort fibreux peuvent être fabriqués par l'empilement de couches de matériaux soit tissés soit unidirectionnels. Dans le cas de plis unidirectionnels, la direction des fibres possède de meilleurs propriétés par rapport aux directions transverses ce qui permet d'optimiser l'empilement pour l'adapter aux conditions de chargement. De part la structure stratifiée des composites fibreux et des caractéristiques fragiles de leurs composants, les mécanismes d'endommagements sont très différents de ceux des matériaux ductiles. Ces derniers absorbent de l'énergie par déformation plastique tandis que les stratifiés dissipent l'énergie par différents modes qui sont soit intralaminaire soit interlaminaire. Les phénomènes intralaminaires sont la rupture de la matrice, la rupture des fibres, le flambement des fibres et la décohésion fibre/matrice. La décohésion des couches est le seul phénomène interlaminaire. Cette décohésion, principalement appelée délaminage, provoque une redistribution du champ

des contraintes puisque les contraintes de cisaillement interlaminaires ne sont plus transférées par les nouvelles surfaces libres.

Les délaminages sont créés par de fortes contraintes interlaminaires dues à des impacts (collision avec des oiseaux, chute d'outils, grêle, ...), des problèmes lors de la fabrication, des effets de bords libres ou par des variations d'épaisseur. Si un composant contenant un délaminage est soumis à un chargement, sa capacité à y résister peut avoir été altérée par ce délaminage. Par exemple, dans le cas de la traction, les propriétés de ce composant ne sont que très faiblement modifiées par rapport à un composant sain. Tandis que dans le cas de la compression, il pourra y avoir flambement des sous-stratifiés ce qui réduirait dramatiquement la résistance de la pièce. De plus, caractériser cet endommagement peut permettre d'améliorer la sécurité en évaluant plus finement la durée de vie restante du composant. Cette évaluation peut être réalisée numériquement en créant des modèles de la structure et en la soumettant à différentes configurations de chargement. Ces résultats peuvent alors servir de base pour décider si la structure doit être réparée ou non. Ceci est d'autant plus crucial pour les endommagements invisibles par inspection visuelle. Le présent travail propose une méthode expérimentale pouvant aider à la définition des paramètres clefs du comportement après-impact à faibles chargements.

Ce mémoire est organisé en quatre chapitres. Le premier chapitre qui est une revue bibliographique se concentre sur les endommagements et leur évaluation dans les structures composites. Différentes techniques de mesures de champs y sont présentées ainsi que leurs applications à

la détection ou caractérisation des endommagements. Le second chapitre présente la méthode expérimentale utilisée d'un point de vue aussi bien analytique que pratique. Dans le troisième chapitre, la méthode expérimentale est appliquée à des échantillons de type poutres et les résultats comparés à des données issus de modèles numériques et à des tomodensitographies. Le dernier chapitre présente l'application de la méthode utilisée au chapitre précédent à des échantillons de types plaques minces impactées puis un indicateur d'endommagement basé sur la méthode des champs virtuels est développé et appliqué à ces plaques.

Chapitre 1

Les endommagements peuvent se décomposer en plusieurs phénomènes : rupture de la matrice, rupture des fibres, flambement des fibres, décohésion fibre/matrice et délaminage. Chacun de ces phénomènes influence différemment les propriétés mécaniques après impact. Comme le délaminage est spécifique aux structures stratifiées, il a été détaillé plus particulièrement. Il en existe deux types : profond ou proche d'une surface. Il est important de séparer ces deux cas comme ils ne se comportent mécaniquement pas de la même manière. Le délaminage profond se rapproche du cas d'une fissure à l'intérieur d'une pièce en métal tandis que le délaminage proche de la surface aura tendance à faire flamber le plus petit sous-stratifié augmentant les contraintes de l'autre sous-stratifié.

Les délaminages sont initiés par de grandes concentrations de contraintes à une interface entre deux plis. Ces concentrations peuvent apparaître sur le pourtour de défauts comme des régions riches en résine et donc

de plus faible résistance. Les dilatations induites par les réactions chimiques de la polymérisation ou par des différences de coefficients de dilatation thermique peuvent amener le matériau au delà de sa limite élastique créant par la même un voire des délaminages. L'effet de bords libres est une conséquence d'une différence des propriétés mécaniques de deux plis adjacents dont les orientations sont différentes. Les variations d'épaisseurs créent une zone riche en résine qui ne transfère pas les contraintes de cisaillement pouvant amener à la rupture locale de la matrice créant un délaminage. L'amorce de délaminage est généralement étudiée par une comparaison des contraintes interlaminaires avec leurs valeurs limites.

Les délaminages peuvent se propager de manière stable ou instable et cette stabilité est contrôlée par le niveau de déformation et la taille des délaminages. Trois modes de propagation existent : ouverture (mode I), glissement (mode II) et cisaillement (mode III). Dans le cas général, il n'est pas possible de séparer leurs effets mais certains cas de chargement favoriseront un mode plus que les autres. Deux méthodes existent pour étudier la propagation de délaminages, l'un est basé sur une étude des contraintes par le critère de Tresca et l'autre sur l'étude de l'énergie dissipée par unité de surface créée. Actuellement, la formulation appelée "Virtual Crack Closure Technique" de l'approche énergétique est la plus employée.

Comme décrit précédemment, l'endommagement par impacts est critique pour les structures stratifiées à cause du manque de renforcement à travers l'épaisseur. Il modifie l'intégrité de la structure en y intro-

duisant les différents modes d'endommagement. La répartition entre les différents modes varie en fonction de l'impact : conditions limites de l'échantillon (supporté, encastré, ...), forme de l'impacteur, énergie cinétique et vitesse de l'impacteur. Pour une haute vitesse d'impact, l'échantillon n'a que peu le temps de se déformer et ce sont principalement les ondes de contraintes dues au choc qui se propagent et endommagent la structure. Pour un impact à faible vitesse, l'inverse a lieu, les ondes généralement de faibles intensités se propagent mais ne créent pas d'endommagement et le champ des contraintes dus à la déformation de la structure induira des délaminages et autres modes d'endommagement. L'énergie peut servir de critère pour classer les impacts mais aussi la vitesse ou l'endommagement induit. Pour le moment, aucune norme n'a été définie pour les classer. Néanmoins, le cas le plus intéressant concerne les endommagements par impact très peu visibles. Ils réduisent significativement les propriétés mécaniques mais sont très difficilement voire impossible à détecter à l'œil nu. Ils nécessitent l'utilisation de techniques de détection appropriées.

La mécanique pilotant la formation de ces impacts est divisée en deux parties. D'abord, deux fissures de la matrice d'un pli apparaissent de part et d'autre de l'impacteur. Le plan de fissure dépend du rapport entre contraintes normales et de cisaillement d'une part et de l'orientation des fibres d'autre part. Si l'échantillon est impacté par le dessus, à l'interface supérieure du pli contenant la rupture de matrice se crée un délaminage à cause de la concentration de contraintes du front de fissure. La propagation du délaminage est guidée par les deux ruptures de matrice et empêchée sous la zone impactée par la contrainte de compression due à l'impact. Ceci cause une redistribution des contraintes

dans le reste de la pièce pouvant causer la formation d'autres fissures et délaminages associés.

L'endommagement par impact a un effet variable sur les différentes propriétés mécaniques. La traction, par exemple, est très affectée par la rupture des fibres mais relativement peu par les délaminages ou les ruptures de matrice. En compression, les délaminages ont un rôle prépondérant dans la diminution des propriétés en facilitant le flambement global par le flambement local des sous-stratifiés tout comme pour la torsion. En flexion, tous les modes d'endommagements ont un rôle dans la diminution des propriétés et la rupture des fibres dans une plus large mesure.

De nombreuses techniques permettent de détecter, localiser ou caractériser un endommagement dans un échantillon. La simple détection peut être réalisée par des indicateurs tels les fréquences propres ou les courbes force/déplacements. Utiliser un réseau de capteur puis trianguler permet de déterminer la localisation de l'endommagement. L'extension du concept de réseaux de capteur à un nombre très élevé de points de mesures correspond aux mesures de champs. Ces mesures permettent d'obtenir une "photographie" du comportement mécanique de l'échantillon. Parmi toutes les techniques de mesures de champs, certaines ont été spécialement appliquées à la détection/localisation ou à la quantification de l'endommagement. Parmi les techniques permettant de détecter/visualiser se trouvent les ultrasons, les rayons X, et la thermographie infrarouge. Il existe une version tridimensionnelle des ultrasons et des rayons X ce qui permet de connaître finement la profondeur des délaminages, spécialement pour les rayons X 3D (aussi appelé CT-scan). La

quantification de la sévérité de l'endommagement est basée en général sur des mesures de grandeurs cinématiques qui permettent de capturer les pertes locales de rigidités. Ces mesures peuvent être obtenues par des méthodes interférométriques telles l'holographie ou la shearographie, des méthodes thermiques telles la thermo-élasticité, ou en lumière blanche telles la corrélation d'image ou les méthodes de grilles. Ces méthodes sont généralement appliquées à la localisation des délaminages/fissures. La corrélation d'images a été largement utilisée pour l'étude du comportement de rupture après impact à cause du niveau important de déformations requis par cette méthode. La méthode de grille en déflectométrie, quant à elle, a déjà été utilisée pour caractériser des endommagements et identifier des cartes de pertes de rigidités. Cependant, il n'existe pas à notre connaissance de techniques expérimentales de validation du comportement mécanique après-impact sans propagation des endommagements.

Ce travail met en place une méthode de validation de modèles numériques du comportement de la structure après impact de manière non-destructive. Cette validation expérimentale à très faibles niveaux de chargement est rendue possible par l'utilisation de la déflectométrie qui donne accès à des cartes de déformation d'une finesse et d'une richesse inégalées. Les modèles numériques sont construits à partir d'observations de CT-scan des échantillons impactés. Un nouvel indicateur d'endommagement basé sur la méthode des champs virtuels est aussi proposé. Ces modèles une fois validés peuvent être utilisés pour simuler un essai de compression après impact.

Chapitre 2

La méthode de mesure utilisée, la déflectométrie, est une technique de mesures de champs en lumière blanche et est basée sur la réflexion spéculaire. Cette technique a été utilisée dans la configuration avec la caméra à coté de la grille. Une nouvelle expression du lien entre les déplacements de la grille et les pentes locales a été proposée ici. Une première expression avait été proposée auparavant qui prenait en compte la variation spatiale de la sensibilité mais elle était incorrecte car elle oubliait l'influence des déplacements selon une direction sur les déplacements selon l'autre direction. Pour une grande distance séparant l'échantillon de la grille, une simple formule de proportionnalité peut être obtenue. L'influence de la non-linéarité de l'expression a été étudiée et trouvée très faible pour les configurations utilisées dans ce travail. L'effet d'un déplacement rigide hors-plan sur les cartes de déformation a également été étudié et il s'avère qu'il est très faible comparé au niveau de déformations expérimentalement mesurées. Les déformations sont obtenues après analyse des images de grilles. D'abord, une image est prise au repos et une autre quand le chargement est établi. En utilisant un algorithme basé sur une transformée de Fourier discrète fenêtrée, les phases sont extraites horizontalement et verticalement pour les deux images. Les phases au repos sont soustraites aux phases sous chargement ce qui donne deux cartes de phases : selon la direction horizontale et la direction verticale. Ces cartes de phases sont déroulées puis converties en pentes grâce à la multiplication par la sensibilité. Ces deux cartes sont ensuite dérivées numériquement par la méthode des différences finies centrées et les courbures sont converties en déformations par la multiplication par la demi-hauteur de l'échantillon conformément à la théorie

de Love-Kirchhoff.

Comme les échantillons ne sont pas suffisamment réfléchissant spéculairement, ils sont recouverts par une résine rendue opaque par l'ajout de poudre de carbone. Ce revêtement n'a pas une rigidité nulle mais il est montré que son influence sur les rigidités globale est très faible. La résolution de la méthode a été évalué à deux microdéformations ce qui est extrêmement faible et montre la finesse de cette technique. La résolution spatiale, quant à elle, est environ égale au pas de la grille pour la méthode d'obtention des déformations utilisée ici.

Chapitre 3

Des échantillons de types poutres ont été testés par déflectométrie et les mesures confrontées aux résultats de modèles éléments finis qui permettent de représenter chaque couches du stratifié et donc les délaminages des échantillons impactés. Plusieurs types d'échantillons ont été testés : intacts, avec délaminages artificiels et impactés. Les modèles numériques correspondants ont été construits et la gestion des contacts au niveau des délaminages a été implémentée. La modélisation de la structure après impact a été réalisé d'après les observations faites sur des CT-scans et en utilisant des formes décrites dans la littérature.

Les résultats des échantillons intacts ont montrés une très bonne corrélation entre les expériences et les modèles numériques ce qui renforce la crédibilité des résultats présentés par la suite. Simuler des délaminages

expérimentalement est un problème connu et jusqu'à présent aucune norme n'existe à ce sujet. Cependant une pré-norme recommande de forcer l'ouverture du délaminage par l'insertion de lames à cette interface. Après les premiers essais, il a été remarqué que les délaminages artificiels modifiaient de manière beaucoup plus faible les cartes de déformation par rapport à ce que prédisaient les calculs numériques. Deux solutions ont donc été employées pour améliorer la corrélation et donc forcer le décollement du film de la résine : l'insertion d'une lame et l'essai de poutre courte en cisaillement. Les expériences ont montrées que la deuxième solution apportait de meilleurs résultats même si les raisons ne sont pas clairement identifiées, peut-être est-ce dû à une déformation des sous-stratifiés ou à une précontrainte de ceux-ci lors de l'insertion de la lame. Néanmoins, il y a des similarités entre les résultats ce qui indique que la méthode fonctionne mais que les modèles numériques ne représentent pas fidèlement la réalité.

Les résultats des échantillons impactés permettent de visualiser ce qui est décrit dans la littérature : deux lobes de part et d'autre du point impacté. Et l'influence du niveau d'énergie lors de l'impact est visible par une augmentation de l'intensité des variations locales de déformations engendrées par la présence de l'impact. Ceci montre la finesse de cette technique de mesure. Il est à noter également que la mesure ne reflète que le comportement mécanique du stratifié et la mesure est indépendante de l'indent créé lors l'impact. La comparaison avec les résultats des modèles éléments finis n'est pas concluante. Ceci s'explique par le manque de raffinement des modèles numériques, il faudrait des CT-scans d'une meilleure résolution pour modéliser plus finement les délaminages et intégrer les ruptures de matrices pour en étudier l'influence

par exemple.

Chapitre 4

La méthodologie précédente a été appliquée à des échantillons de type plaque mince. Ces échantillons avaient été impactés selon deux configurations et différents niveaux d'énergies. La première configuration est celle du chapitre précédent et la seconde consiste en un simple support sur le pourtour d'une ouverture rectangulaire. Comme dans le chapitre précédent, la non-linéarité géométrique a été étudiée ainsi que l'effet d'un déplacement rigide hors-plan. Tous deux ont été trouvés plus faibles que la résolution en déformation, ils sont donc tous deux négligés. Des CT-scans n'étant pas disponibles pour ces échantillons, seul un modèle éléments finis a été construit. Il correspond à l'échantillon impacté alors qu'il était maintenu entre deux plaques. Comme les conditions d'impacts sont similaires à celles du chapitre précédent, il peut être considéré que l'endommagement aura le même aspect entre la poutre et la plaque. Les délaminages ont été implémentés en utilisant la solution de la double ellipse.

L'indicateur basé sur la méthode des champs virtuels a été développé. Partant de l'expression générale du principe des travaux virtuels, il a été appliqué au cas d'une plaque mince en flexion utilisant des données expérimentales discrètes. Enfin la formulation des champs virtuels par éléments finis a été développée. L'équation finale permettant le calcul de l'écart à l'équilibre a ainsi été obtenue. Enfin, la combinaison des cas de chargement a aussi été présentée.

Les résultats obtenus par déflectométrie sont cohérents avec les résultats du chapitre précédent. Plus l'énergie d'impact est élevée plus les champs de déformations sont perturbés sur une large zone. Les deux lobes de la littérature ont également été retrouvés. Selon le point d'application de l'effort, l'endommagement est plus ou moins révélé. Ceci s'explique par le fait que si le cas de chargement ne sollicite que très peu la zone endommagée, la variation du champ des déformations due à l'endommagement sera très faible.

Les cartes d'écart à l'équilibre donnent des résultats variables suivant les cas de chargement. Pour que le calcul de l'équilibre se fasse bien, il faut que suffisamment d'information spatiale soit disponible. Ce point est crucial pour l'application aux données expérimentales car elles contiennent du bruit. Il a été montré que cet indicateur était sensible à des variations de rigidités et à la violation des hypothèses de plaques minces. Il en détecte les bords cependant.

Conclusions générales et perspectives

Ce travail a permis de proposer une méthodologie pour valider expérimentalement des modèles numériques simulant le comportement de structures stratifiées endommagées à faibles niveaux de chargement. Les données expérimentales sont obtenues par une méthode de mesures de champs cinématiques : la déflectométrie.

Conclusions générales

- Une nouvelle expression mathématique du lien entre les déplacements de grille et les changements de pente a été formulée. Elle prend désormais en compte la non-linéarité géométrique de ce problème bidimensionnel. Si la distance séparant l'échantillon de la grille est grande devant les dimensions de l'échantillon alors cette non-linéarité peut être négligée et l'expression simplifiée utilisée. L'influence d'un déplacement rigide hors-plan de l'échantillon sur les champs de déformations a été étudié et il a été montré qu'il est négligeable au vu du niveau de déformations que montrent les cartes présentées dans ce travail.

- La procédure nécessaire à la préparation des échantillons a été améliorée pour réduire les problèmes liés à la réflexion diffusive de la surface de l'échantillon. Cette amélioration a consisté en l'ajout d'une charge inerte ce qui a eu pour conséquence d'opacifier la résine. L'effet de la résine sur les rigidités de flexion a aussi été quantifié analytiquement et évaluée à moins de 2%.

- La déflectométrie a été appliquée à des échantillons de types "poutres" contenant des délaminages artificiels et de vrais impacts. Cette technique de mesure était suffisamment sensible pour capturer les effets de faibles endommagements comme un délaminage artificiel de 30 mm ou un impact à 10 J. Ceci est rendu possible par les très hautes résolution spatiale et sensibilité de cette technique.

- Par l'observation de CT-scans d'échantillons impactés, des modèles éléments finis ont été construits simulant le comportement après impact. Différentes formes de délaminages ont été implémentées et les résultats comparés à ceux tirés des expériences. Des

"signatures" similaires sont visibles mais la corrélation n'est pas parfaite.

– Des délaminages artificiels ont été réalisés par l'insertion de film de PTFE entre deux plis mais les résultats expérimentaux n'ont montrés aucuns effets de ces films. Pour forcer le décollement du film et obtenir ainsi un délaminage plus réaliste, deux solutions ont été envisagées : l'insertion d'une fine lame en métal et le chargement d'échantillons selon un test de cisaillement en poutre courte (CPC). Les résultats de déflectométrie après forçage montrent une nette amélioration surtout ceux après CPC. Cette technique est donc recommandée pour déclencher le décollement du film de PTFE.

– Des plaques impactées avec différentes conditions d'impact ont été testées par déflectométrie. Le lieu et l'étendue des endommagements ont été révélés pour la plupart des cas de chargement par l'observation directe des cartes de déformation. Cependant, certains cas de chargement n'ont rien révélé ou très peu. Ceci montre la nécessité d'un cas de chargement qui active les différentes rigidités dans la zone endommagée. Bien que cette détection d'endommagement ne soit que visuelle, les cartes de déformation permettent d'aider le développement et la validation de modèles numériques précis et détaillés simulant l'endommagement par impact.

– Un nouvel indicateur basé sur la méthode des champs virtuels a été développé et appliqué aux résultats obtenus avec les plaques pour tenter d'extraire le lieu et l'étendue des endommagements sans connaissance *a priori* de l'endommagement. Cet indicateur

a permis d'en identifier les contours pour la plupart des cas de chargement quand suffisamment d'information spatiale était disponible. Combiner les cas de chargement permet d'améliorer la détection en augmentant la quantité d'information spatiale provenant des différents cas de chargement. Un des avantages de cet indicateur est sa capacité à tirer profit de l'information disponible dans les trois cartes de déformation et à produire une seule et unique carte représentant l'information dans un format binaire.

Perspectives

– Dans l'expression du lien entre déplacements de grille et pentes locales, le mouvement hors-plan a été étudié séparément de la déformation de l'échantillon. Il pourrait être intéressant d'exprimer cette relation en considérant les deux effets simultanément. À cause du lien entre déplacements hors-plans et pentes locales, un jeu d'équations différentielles non-linéaires devrait être obtenu. Cette équation pourrait être utilisée pour simuler numériquement un essai de déflectométrie. Cependant, il n'est pas envisagé que cette nouvelle expression changera les conclusions de ce travail.

– À cause de la faible résolution des CT-scans, la forme des délaminages a été arbitrairement choisie et les fissures de matrice n'ont pas été implémentées dans les modèles. Des CT-scans plus détaillés permettraient de construire des modèles numériques plus représentatifs de la réalité. Ces modèles pourraient être ensuite validés expérimentalement par la technique de déflectométrie comme présenté ici. Surtout, les effets de frottement ou de pontage de fibres pourraient être explorés plus en profondeur. Des modèles

numériques fins sont d'une importance cruciale pour la prédiction du comportement en compression après impact par exemple. La poursuite de ce travail peut très certainement amener à la création d'un outil très performant pour aider à la conception de pièces en composites.

– Une étude pourrait être conduite sur la recherche d'un matériau qui permettrait de réaliser des délaminages ne nécessitant pas de forçage ou tout du moins qui minimiserait l'adhérence résine/film. Cette réduction permettrait de forcer les délaminages par un test de poutre courte en cisaillement à faible niveau de chargement, réduisant donc le risque de rupture de fibres aux points de chargement.

– Les résultats obtenus par l'indicateur d'écart à l'équilibre peuvent être améliorés grâce à l'augmentation de la résolution spatiale des résultats expérimentaux. Le principal facteur corrompant l'équilibre étant le niveau de bruit des mesures, un nombre minimum de points de mesure est nécessaire pour le cas de l'équilibre. Si plus de points de mesures étaient disponibles, alors plus d'écarts à l'équilibre pourraient être calculés et la zone endommagée serait plus précisément définie.

– Jusqu'à présent, la déflectométrie a été limitée aux surfaces planes. Il serait extrêmement intéressant d'étendre son utilisation aux surfaces courbes. Si cela était possible, cette méthode pourrait être appliquée à des aubes de moteurs d'avion et aider à la compréhension de leur endommagement. Une autre limite actuelle est la nécessité du rendu miroir de la surface à étudier. Étendre cette procédure aux surfaces courbes serait de première importance pour l'extension de cette méthode de mesure à ces surfaces.

CONTENTS

LIST OF FIGURES

List of Tables

INTRODUCTION

Composite materials offer many advantages compared to traditional materials like metals, such as higher specific stiffness. Fibre reinforced plastics (FRP) can be manufactured by stacking layers of materials, either woven or unidirectional. As the plies have an orientation along which the properties are maximum, the stacking sequence can be optimized to better withstand the loading conditions. Because of its layered structure and the brittle characteristics of fibres and resin, the failure mechanisms of FRP are very different from those of traditional materials. Ductile materials absorb energy via plasticity during yielding whereas brittle laminates can only dissipate energy via various damage modes either intralaminar or interlaminar [1–4]. The intralaminar damage process is a combination of several phenomena: matrix cracking, fibre failure, fibre microbuckling, and fibre-matrix debonding. On the contrary, the interlaminar damage process is dominated by the debonding of adjacent plies [5]. This debonding, also called delamination, causes a stress redistribution as interlaminar shear stresses are not transferred by this interface.

Delaminations are created by high interlaminar stresses caused by impacts (bird strike, tool drop, hailstorms, ... [6]), faulty manufacturing, free-edge effects, or ply drops. If a component containing a delamination is loaded, the delamination may reduce the load carrying capability depending on the loading conditions. For example, if this component is tested in tension there will be very little difference from the undamaged case. On the contrary, if the damaged component is tested in compression, the sublaminates can buckle and the buckling force will be much lower than the one for the undamaged panel. In the case of bending, the presence of delaminations will have a slight effect on the mechanical properties for small loads and may lead to catastrophic sublaminates buckling for higher loads. This will be discussed in more detail in the

first chapter. Moreover, characterizing this damage can help to improve the safety of the component by evaluating its remaining service life. This evaluation can be performed numerically by creating a model of the structure and submitting it to different loading configurations. These results can serve as a reference to decide whether the structure should be repaired or not. It is even more crucial for invisible damage as visual inspection does not provide information. This work addresses this issue by the development of an experimental technique which can help to define the key parameters for post-impact behaviour.

The present thesis is organized in four chapters. The first one is a literature review that focuses on damage and its assessment in composite structures. Delaminations are detailed in terms of initiation and propagation. The effect of impact damage on mechanical properties is also reviewed. Based on this study, the methods to assess damage in composites using full-field measurement techniques are reviewed and their application to detection or characterization of damage is highlighted. These full-field techniques have been divided in two groups: non-mechanical techniques and kinematic measurement techniques.

The second chapter focuses on the measurement technique: deflectometry. First, its principle is detailed and new formulæ are derived to link the grid shifts to the local slope variations of the specimen due to deformation. The effect of an out-of-plane rigid body translation is also studied. Then the data processing to extract strain fields from grid images is detailed along with the chosen algorithms for the phase extraction, unwrapping and differentiation steps. The specimen preparation is presented and the improvements brought by the use of an opaque coating studied. Finally, guidelines for printing the grids are given and a sensitivity study is performed.

The third chapter applies the deflectometry technique to beam samples in cantilever loading. The samples have different types of damage: undamaged, artificial delaminations and real impacts. Their experimental results are confronted to numerical models based on the observation of CT-scans of these samples.

In the last chapter, results of plate samples tested in bending are presented and analysed following the same approach. A new damage indicator based on the application of the Virtual Fields Method to plates in bending is developed and applied to the numerical and experimental plate results presented in the same chapter. Further improvements for this indicator are proposed: smoothing and load case combination.

CHAPTER 1

DAMAGE IN COMPOSITE STRUCTURES AND THEIR ASSESSMENT

Remaining life prognosis and mechanical property identification of damaged components have always been a great concern in composite structures because of the complex failure mechanisms. In this chapter, the damage process will be detailed in terms of delamination, impact damage and its effect on mechanical properties. Finally, damage assessment using full-field measurements will be reviewed by the use of non-mechanical and kinematic measurement techniques.

1.1 Damage process

This section first focuses on delamination and the phenomena driving its initiation and propagation. Then, it continues with the subject of impact damage, giving a broad view of the different types and focusing on the damage mechanisms for barely visible damage. This section ends with the effects of impact damage on strength and stiffness under different loading conditions.

1.1.1 Delamination

This type of damage is located at the interface between two plies. This resin rich region does not have any reinforcement in the stacking direction. Some work has been done to compensate for that by introducing fibres along that direction. This procedure is known as stitching or 3D weaving [7]. Because of the laminate principal axis, the stacking sequence can be optimized to carry the load more efficiently. Delaminations can only exist at the interface between two adjacent plies with different directions and their shape depends on the ply orientations [8]. Plies with larger differences in fibre angles are more prone to delaminations [8].

The stress redistribution caused by a delamination increases the stress magnitude at another location in the component and it may be large enough to initiate or propagate one or multiple delaminations. Once the delamination reaches a critical size, buckling can appear and cause failure. Therefore, the onset and growth of delaminations are two important phenomena to understand in the objective of remaining life prediction. Even though both events are caused by interlaminar normal and shear stresses, it is important to study them separately because of their difference in fracture behaviour [9].

1.1.1.1 Types of delamination

Depending on their location through the thickness within the laminate, two types of delamination can be defined: subsurface delaminations and internal delaminations as illustrated in Fig. 1.1 [10]. In the subsurface case Fig. 1.1a, as bending stiffnesses are proportional to the third power of thickness, buckling of the thinner sublaminate will appear prematurely. This results in the stress transfer to the thicker sublaminate which has a lower stiffness because of the reduction in section. The internal case Fig. 1.1b behaves the same way as a crack does in metals.

(a) Subsurface delamination (b) Internal delamination

Figure 1.1: Two types of delaminations: (a) subsurface delamination and (b) internal delamination [10].

1.1.1.2 Initiation

Large interlaminar stresses are the main cause of delaminations. These stresses can appear because of: manufacturing process, free edge-effect [11], ply drops [12], and low-energy impacts. The first cause is related to defects between layers and/or shrinkage [10]. Defects create a stress concentration at their boundary that are resin rich regions. The stress state can reach a critical value and initiate a delamination. Shrinkage can come from either chemical reactions (curing) or thermally induced deformations. Because of this shrinkage, the material strength may be reached during manufacturing or in-use. The free-edge effect is a result of the mismatch in mechanical properties of plies with different orientations [11]. Ply drops create a resin rich region where stresses are transferred from the dropped plies to the continuous plies via interlaminar shear stresses [12]. Two theories have been proposed to explain these large stresses during impact depending on the boundary conditions: transverse ply cracks due to bending stresses or interlaminar shear stresses [4]. If the span to thickness ratio is high, the bending stresses will be predominant and if this ratio is low, shear stresses will be predominant.

The initiation is generally predicted using strength analysis, which is the comparison between interlaminar stresses and strength. Several criteria have been proposed depending on the loading conditions [9]. For example under in-plane tensile and compressive loading, an average stress failure criterion was used to predict the delamination onset in [13, 14]. When interlaminar shear stresses must be considered, the quadratic interaction of the interlaminar stresses in conjunction with a characteristic distance have been successfully used in composite bolted joints [15] and in post-buckled dropped-ply laminates [16]. The characteristic distance is function of geometry and material properties, it is generally obtained by extensive testing. Because of the very important stress gradient at the delamination front, the influence of stress singularities is reduced by using an average stress criterion in numerical simulations [17].

1.1.1.3 Propagation

Two types of propagation exist: stable and unstable. The stable case is defined by the propagation evolving with loading. On the other hand the unstable growth is the propagation at constant load. The growth stability is a function of applied strains and delamination lengths [18, 19]. Even though both types are very different, the mechanics driving the propagation are the same, there is therefore no need to study them separately.

Three types of propagation mode exist: opening mode I (interlaminar tension), sliding shear

mode II (in-plane shear stress) and scissoring shear mode III (out-of-plane shear stress). They are illustrated in Fig. 1.2. Generally, it is not possible to distinguish the effect of each mode as they are mixed in most cases. However, some loading cases allow the predominance of one mode over the others and several authors have reviewed the different tests [20,21]. For instance, a standard test for mode I is the double cantilever beam (DCB) where an initially cracked specimen is subjected to interlaminar tension in the pre-cracked zone as shown in Fig. 1.3a. For mode II, several tests exist and among them is the end notched flexure (ENF) specimen as shown in Fig. 1.3b. For mode III, the edge crack torsion (ECT) specimen was demonstrated to be a promising mode III interlaminar fracture toughness test method and it is illustrated in Fig. 1.3c.

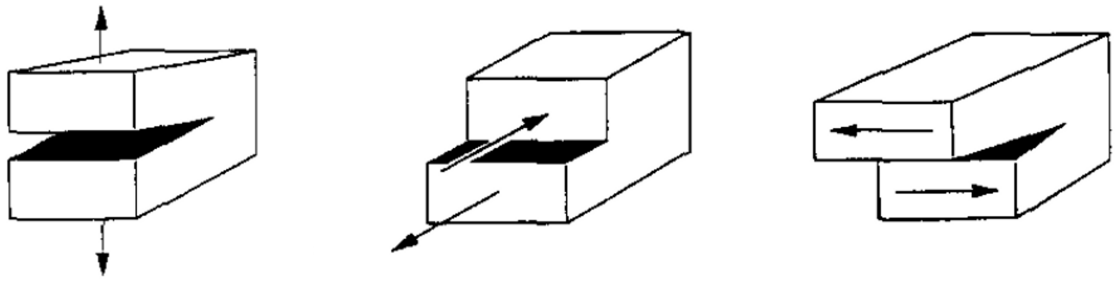

(a) Mode I (b) Mode II (c) Mode III

Figure 1.2: Three basic modes of crack tip propagation: (a) mode I (opening), (b) mode II (sliding) and (c) mode III (tearing) [20].

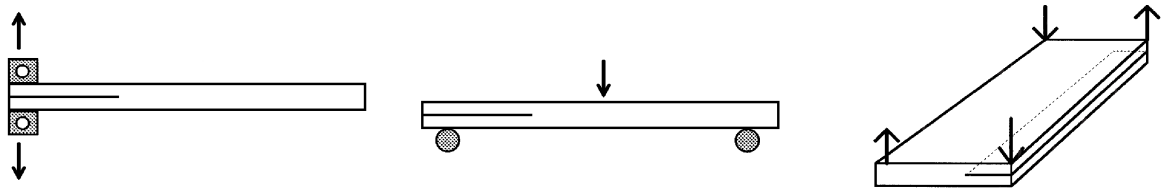

(a) Mode I (b) Mode II (c) Mode III

Figure 1.3: Three interlaminar fracture toughness tests: (a) DCB for mode I, (b) ENF for mode II and (c) ECT for mode III [21].

When studying propagation, the delamination location is known and an initial crack-like flaw exists. For example, in the case of a tapered laminate, the delamination will start in the resin rich region located at the ply-drop [22]. As said previously, when the delamination is located near the midplane, the tools of fracture mechanics developed for cracks can be used during the propagation stage. There are two approaches in fracture mechanics being used to characterize propagation: stress based and energy based.

The first approach, stress based, consists in evaluating stresses at the crack tip, for example, the stress intensity factor denoted K [10, 23]. In the case of non-isotropic materials, the function becomes mathematically very complicated giving a difficult evaluation of the stress state. The second one, energy based, is related to the strain energy release rate (SERR) denoted G. Analytical [24] and finite element approaches exist. Three formulations exist for this approach via finite element analysis [25], J-integral [26, 27], virtual crack extension [28, 29], and virtual crack closure technique (VCCT) [30]. They have been shown to produce similar numerical predictions in [10]. SERR characterizes the fracture and is defined as [31]:

$$G = \frac{dW}{dA} - \frac{dU}{dA} \tag{1.1}$$

where dW is the change in external work done, dU the change in total strain energy, and dA the change in crack area. The crack grows when the energy release rate G reaches a critical value G_C, also called material toughness. It corresponds to the energy dissipated per unit of created surface area during fracture. Nowadays, the most common formulation is VCCT and a review containing a more detailed explanation is available in [32].

1.1.2 Impact damage

As stated earlier, composite structures are very sensitive to transverse impacts because of the lack of through-thickness reinforcement. Because of the brittle behaviour of their components, composite materials absorb energy via different damage mechanisms such as matrix cracking with subsequent fibre/matrix debonding, delamination, and fibre failure [8]. The combination of damage mechanisms varies with the impact velocity, impactor shape, impact energy, laminate properties, etc. Several authors [3, 33–39] have proposed a categorization of impacts based on different parameters such as the velocity, the energy or the resulting damage but no standard has been adopted yet [40].

Regardless of the definition, in a high velocity impact the resulting damage is very local because the stress waves induced by the impact are travelling through the material before the global structure responds to the loading [41]. Fig. 1.4 illustrates the structural behaviour of low-velocity and high-velocity impact. High velocity impacts are not part of this work because the damage is generally visible with the naked eye. In the case of low velocity impact, the stress waves are usually very low in amplitude compared to static stresses and the global structure responds to the loading via bending moments and shear stresses. If the impact energy is high, the resulting damage will be visible on the surface, for example perforation or fibre failure. Whereas in the case of low velocity and low energy impacts, the resulting damage is larger in

size but generally not visible by eye as it is located within the laminate. This type of impact damage is referred to as barely visible impact damage (BVID). This type of damage is critical and it requires some specific technique to detect its location and characterize its severity. This work focuses on this issue.

(a) Low velocity (b) High velocity

Figure 1.4: Schematic representation of the response to impact under (a) low velocity and (b) high velocity conditions [42].

1.1.2.1 Damage mechanisms for BVID

On Fig. 1.5a, the impactor is coming from the top and going towards the bottom. Matrix cracks, which are intralaminar damage, appear on each side of the impactor when the stresses reach a critical value as shown by the black lines inside the 0° ply in Fig. 1.5a [43]. Their orientation depends on the ply orientation in the (x,y) plane and on the ratio between normal and shear stresses in the (y,z) plane. The matrix cracks of the ply underneath guide the delamination propagation at the ply interface producing the well known peanut shape as in Fig. 1.5b. Therefore if two adjacent plies have the same orientation, delaminations can not exist at that interface [8].

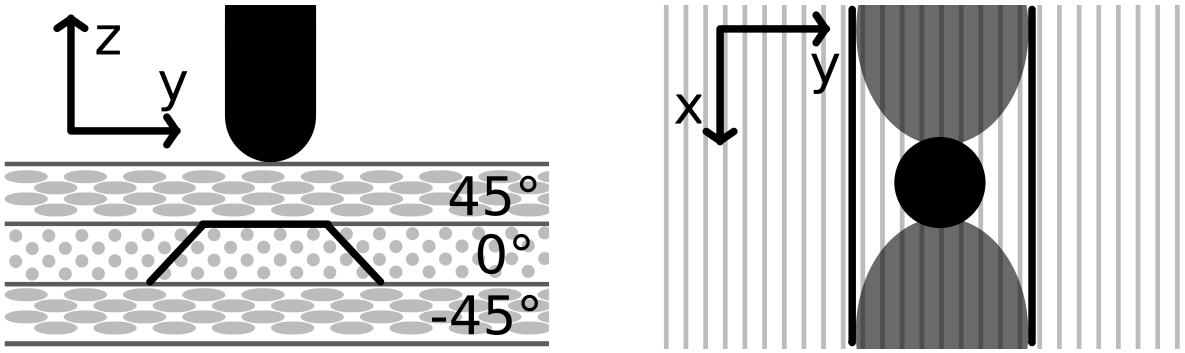

(a) Cross section (b) Top view interface between the 0° and +45° plies

Figure 1.5: Impacted laminates with a [-45 0 +45] lay-up. (a): cross section perpendicular to the 0° ply. Two matrix cracks are visible in the 0° ply and a delamination at the interface between the 0° and +45° plies. (b): top view of the interface between the 0° and +45° plies, matrix cracks are present on each side of the impactor (vertical black lines) and delaminations each side of the impactor (grey areas).

At the interface between two adjacent plies with different orientations, because of the shear stress concentrations (mode II/III fracture) at the matrix crack tip, a delamination appears [44, 45]. Its growth is constrained to occur between the two matrix cracks located on the ply below. Underneath the impactor, the delamination can not propagate because of the through-thickness compression stress but from a certain distance away from the impactor, the through-thickness compression stress is too low to prevent the propagation. This delamination generates a stress redistribution in other plies leading to the initiation of other cracks and subsequent delaminations if critical values are reached [42].

When shear stresses are predominant over bending stresses, typically during a short beam shear test, the first crack appears at an interface close to the impacted side. Whereas when bending stresses are predominant over shear stresses, the first crack appears near the rear surface. The starting point for cracks will give the final impact damage pattern, pine tree or reversed pine tree as shown in Fig. 1.6.

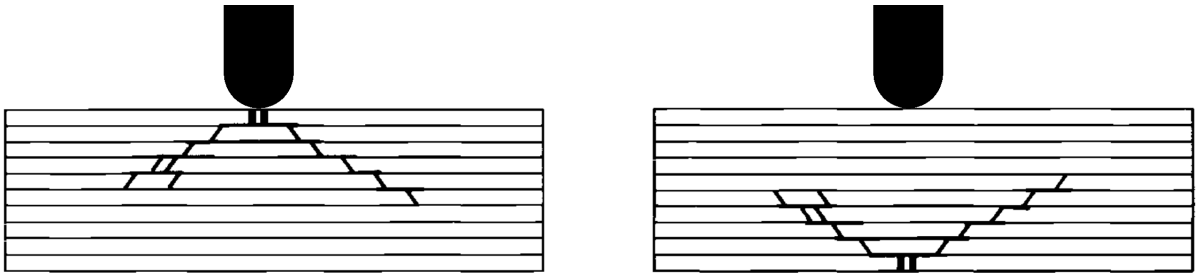

(a) Pine tree (b) Reversed pine tree

Figure 1.6: (a) pine tree and (b) reversed pine tree damage patterns result for an impact coming from the top [8].

Fibre breakage can appear during a low velocity impact because of two reasons. The first is the local stress concentration at the contact zone between the impactor and the structure. It is usually accompanied by a dent. The second is when stresses due to bending exceed the fibre strength and it is generally located on the rear side. As fibre failure is generally on the component surface, it is quite easy to detect. Reducing the impact energy, the bending moments, or changing the impactor shape helps to reduce this type of damage but damage such as delaminations and matrix cracks will still be induced in the structure.

1.1.3 Effects of impact damage on mechanical properties

Inside a ply, fibres carry longitudinal normal stresses whereas the matrix carries transverse normal stresses and shear stresses [46]. Depending on the loading conditions (tension, compression, torsion, or bending) and the damage modes (matrix crack, delamination, or fibre failure), the impact will have a varying effect on the residual properties, such as strength and stiffness. Strength is the critical value above which the structure will fail. The stiffness characterizes the deformation to a certain load.

1.1.3.1 Tension

In the case of tensile loading, fibre failure is the critical damage mode as fibres carry most of the load. Therefore as soon as the impact energy is sufficient to break fibres, the strength and stiffness drop [40, 42, 47–49]. Fig. 1.7 presents the residual tensile stiffness of slices from a 16-ply and a 48-ply laminates at different regions away from the impactor. Region I corresponds to the undamaged material, region II contains mainly delaminations and region III is the most damaged region, with matrix cracks, delaminations and fibre breakage. For the 16-ply sample in Fig. 1.7, region II has a stiffness reduced by a small percentage (10 %). Whereas the region with all damage modes (region III) has a large stiffness reduction (80 %) because fibres carrying the load in tension. The smaller stiffness reduction for the 48-ply sample is explained by the lower proportion of broken fibres in this case.

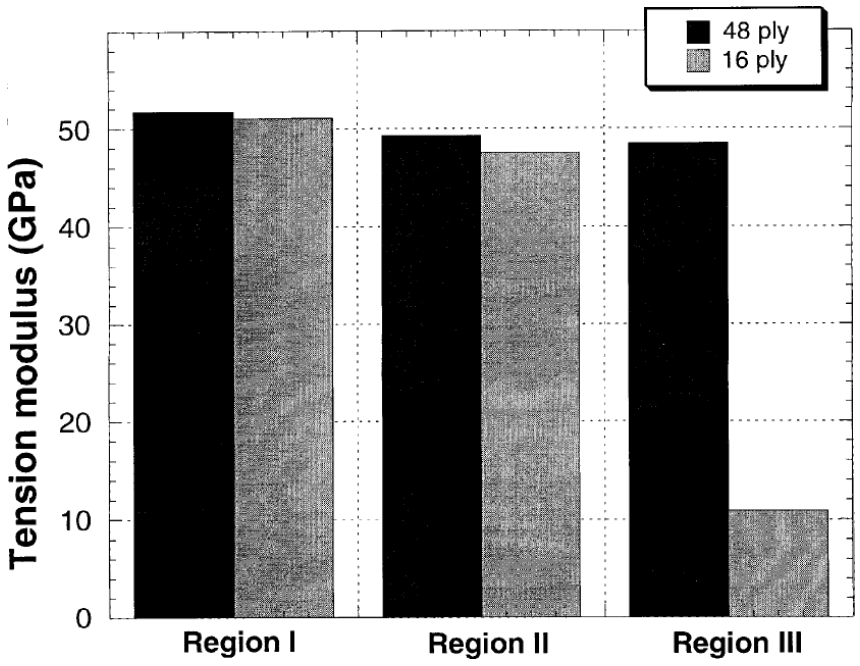

Figure 1.7: Residual tensile stiffness [50].

1.1.3.2 Compression

A large amount of work [51–71] has been published for the case of compressive loading after impact [72]. The behaviour is affected by the presence of all damage types but also by the local dent at the impact point causing some misalignments [73]. The damage mode most influencing the compressive behaviour is delamination [74]. Delaminations allow the sublaminates to buckle as their bending stiffnesses are lower than the undamaged one, lowering at the same time the buckling strength [75]. Because the delamination lengths influence the buckling mode (local buckling, global buckling or a combination), this test requires a guide to prevent global buckling but not the local one [33,76]. A standard has been developed to help with this issue [77]. Matrix cracks affect the compressive strength because they cause a stress redistribution [78]. It must be noted also that the ply stacking sequence and the fibre diametre have an important role on the compressive strength [5]. Several studies demonstrated that the stiffness reduction within the damaged region must be taken into account [79–81].

From [50], previously mentioned in 1.1.3.1, the stiffness was studied not only in tension but also in compression. As shown in Fig. 1.8, a small stiffness reduction is visible in region II for the 16-ply sample and a larger reduction for the most damaged zone. This is explained by the presence of matrix cracks and fibre failure in the most damaged region. The residual stiffness of zone III is more than twice higher in compression than in tension. This is explained by the broken fibres still carrying the load in compression. The 48-ply sample is only marginally affected by the impact because the impact energy is too low compared to the specimen thickness.

1.1.3.3 Torsion

Very little work has been done on torsional residual strength after impact [82, 83] and to the author's knowledge, the residual stiffness after impact has never been studied. [83] showed that impacting laminated tubes divides the torsional strength at least by two depending on the lay-up. No fibre-breakage was observed post-impact but delaminations and matrix cracks were present. From the results and the correlation with a finite element model, the strength reduction is governed by the local buckling of sublaminates at the delaminated interfaces [83].

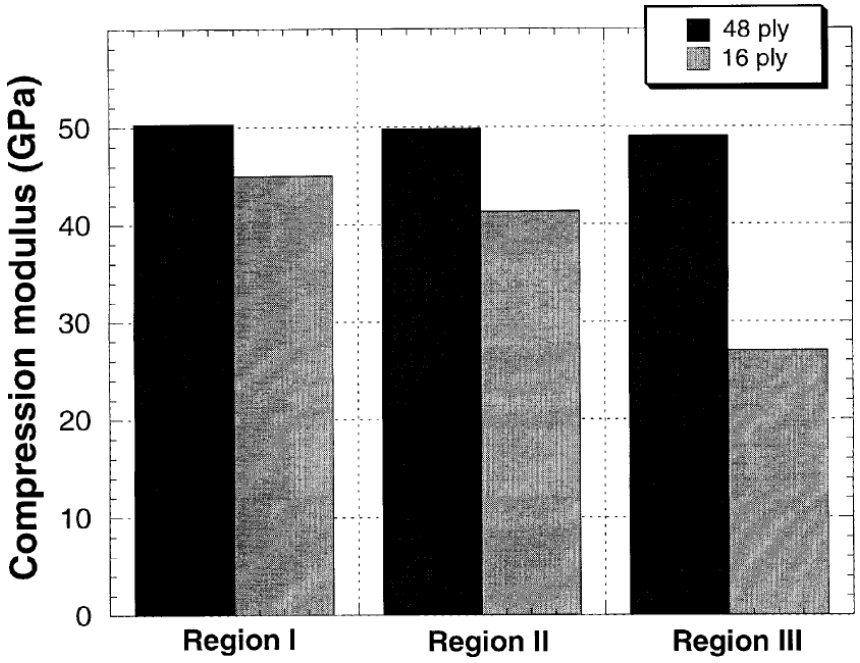

Figure 1.8: Residual compressive stiffness [50].

1.1.3.4 Bending

Some work has been done on flexural strength and/or stiffness after impact [8, 40, 43, 84–90]. The stress fields resulting from a bending load case are complex [40]. Three point bending test (span to thickness ratio of 20:1) after impact conducted on glass fibre composites showed that residual strength decreases with the increase in absorbed impact energy as shown in Fig. 1.9 [89]. The large number of superimposed data points in Fig. 1.9b is explained by the non linearity of absorbed impact energy with impact energy Fig. 1.9a. This non-linearity is explained by the damage development with impact energy: first a matrix crack appears, then it propagates and finally fibre failure leading to catastrophic failure. Therefore, the major damage mode is fibre failure. In the case of short beam shear test, the shear strength is not sensitive to fibre failure [85]. This has been confirmed by [91, 92], as the shear strength depends primarily on the matrix properties and the fibre/matrix interfacial shear strength.

The bending stiffness is very sensitive to fibre failure [67]. Away from the impact point, the main damage mode is delamination and there is a 25 % reduction in flexural stiffness as shown in Fig. 1.10. Closer to the impact point, more matrix cracks and fibre failure are present giving a stronger reduction in residual modulus and at the impacted point, the reduction is drastic [2]. These results have been confirmed by other studies [88, 89].

As the damage process has been explained and the effect of impact damage on mechanical prop-

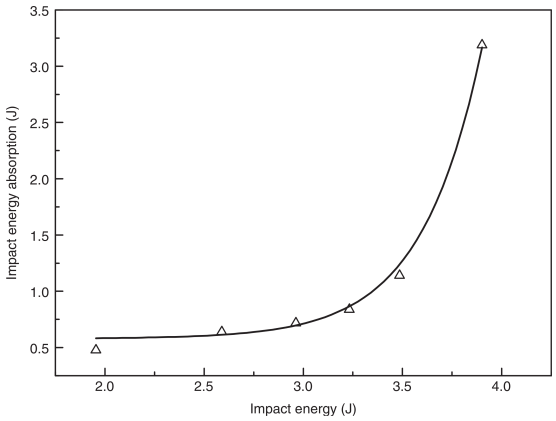

(a) Absorbed impact energy

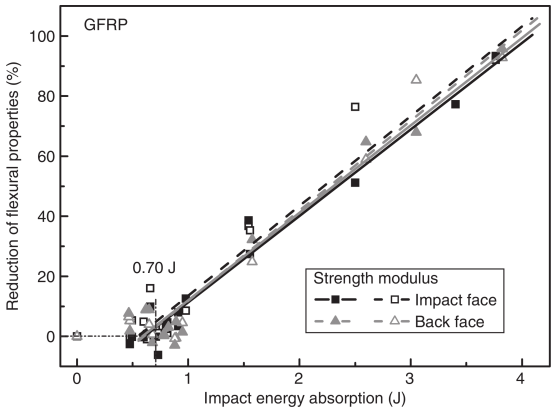

(b) Residual properties

Figure 1.9: (a) Absorbed impact energy as a function of impact energy and (b) residual flexural properties as a function of absorbed impact energy [89].

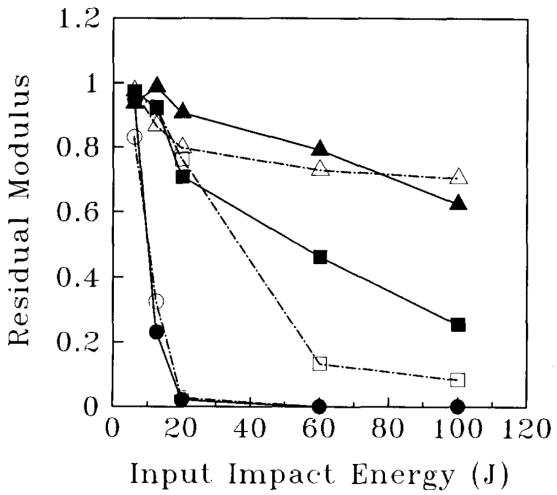

Figure 1.10: Normalized residual flexural stiffness as function of impact energy [2]. Triangles are samples taken 48 mm far from impact point, squares 24 mm and circles at impact point. Empty symbols are composite with non modified resin and filled symbols with rubber-modified resin.

erties reviewed, the next section will focus on damage detection using full-field measurements.

1.2 Full-field damage assessment

Damage assessment is of high importance for the understanding of the mechanisms driving the post-impact behaviour but is also a crucial issue for safety reasons. It has been extensively studied using different indicators. Among the studied damage indicators, one can find some local measurements reflecting global behaviour like deflections. They can be a marker of the onset of the different damage modes during an impact as in [93, 94]. Delaminations and cracks will be revealed by sudden drops in force/displacement curves as shown in Fig. 1.11. The point denoted *a* is the onset of the first delamination and the oscillations after point *b* are fibre failure, delamination initiation and propagation.

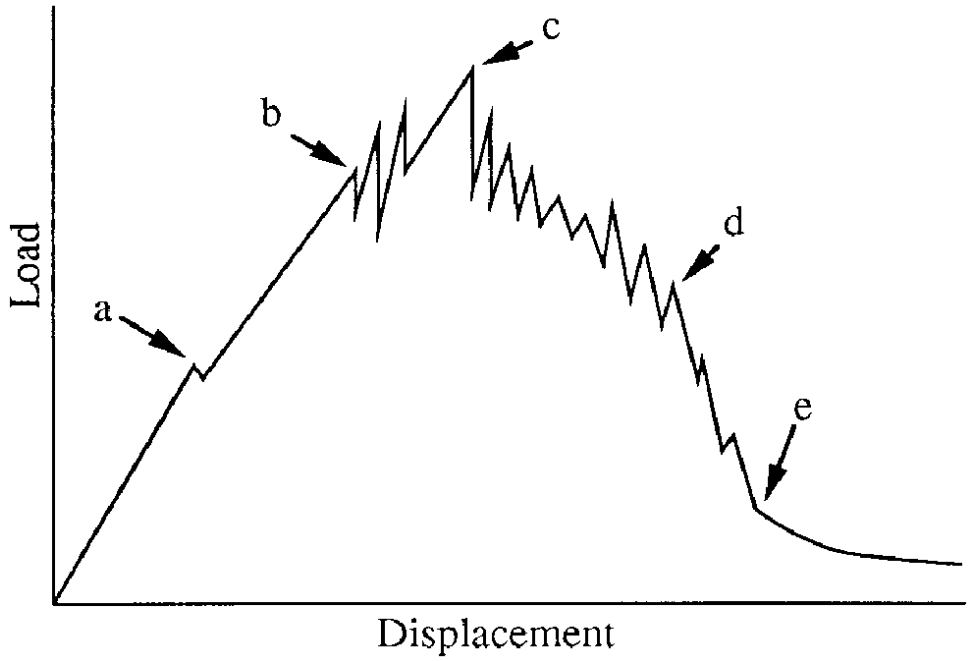

Figure 1.11: Schematic of a load/displacement curve during impact [93].

Another used indicator is modal frequencies [95, 96] and a review can be found in [97]. As modal frequencies are affected by the global stiffness of the component, a slight change in their values means that the structure has been altered. Even though these local indicators are easily accessible as they come from a single point, it is usually not possible to precisely locate a damage. The temporal analysis of signals coming from an array of sensors combined with triangulation can make it possible to locate the damage as performed with piezoelectric sensors in [98, 99]. Another method consists in looking at mode shapes, either in displacements, slopes

or curvatures as summarised in [97]. It works quite well as mode shapes depend directly on the local bending stiffnesses which are affected by the presence of damage. One of the issues with vibration based methods is the possibility of extending the damage as a cyclic load is required and also their sensitivity can be too low to detect small damage in large structures. Therefore static loading should be preferred. The extension of multiple single-point measurements, as undertaken with a vibrometer to extract the mode shapes, are full-field measurements.

A full-field technique provides data over an area with a high density of information, typically over 10,000 data points. Because of this characteristic, these techniques are well suited for damage detection. They can be classified in two categories based on the type of their measured quantities: non-mechanical techniques, giving only a spatial information (location and extent) and kinematic measurement techniques, giving mechanically related information.

1.2.1 Non-mechanical techniques

The most widespread non-mechanical techniques comprising visual inspection, ultrasound, X-ray, and thermography, will be reviewed in this section.

1.2.1.1 Visual inspection

Visual inspection is very well suited for impacts where visible surfaces are affected by the damage. Fig. 1.12 presents photographs of an impacted woven composite sample. Fibre breakage is visible on both surfaces. It is fast, inexpensive and gives an appreciation of damage severity but it cannot detect internal damage. Another drawback is that sometimes back surfaces are not accessible, wing panels for example. A last drawback is that it is operator dependent [100].

1.2.1.2 Ultrasound

Ultrasound techniques are based on the fact that these waves are reflected at interfaces between materials of different properties. An ultrasonic wave is induced in the material, and the reflected waves are recorded in time. If the amplitude of the reflected waves as a function of time is available, the A-scan representation can be used, amplitude versus time. If the location of the probe along a line and the amplitude of the reflected waves are available, the B-scan representation, amplitude versus location, can be used. The 2D extension of B-scan is C-scan. It allows the

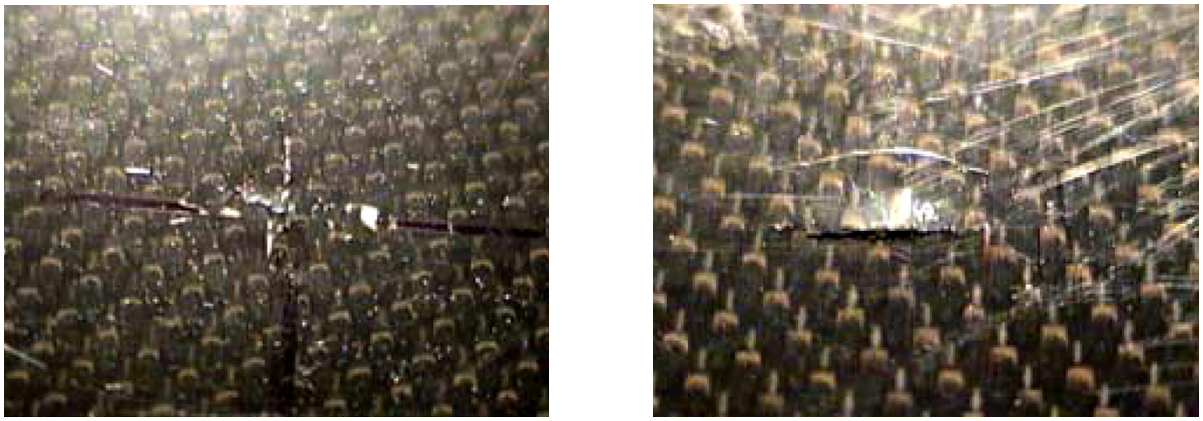

(a) Front view (b) Back view

Figure 1.12: 5 J impacted sample of woven composite: (a) front view and (b) back view [101].

localisation of the damage in 2D but does not give any indication along the third dimension as shown in Fig. 1.13a. If the signal's time-of-flight is analysed, it is possible to locate within the thickness the defect as shown in Fig. 1.13b. As most of the waves are reflected at an interface, it is not possible to determine the exact shape of a delaminated area if it is covered by another one. It is not too expensive, portable equipment exists for A-scans, and C-scans are widely used as a base for damage detection as in [6, 102–110]. Another drawback is the difficulty to perform *in-situ* C-scan inspection on a mounted component. Ultrasound techniques can help to determine the largest extent of delaminations for a given impact which is perfect for industrial delamination detection.

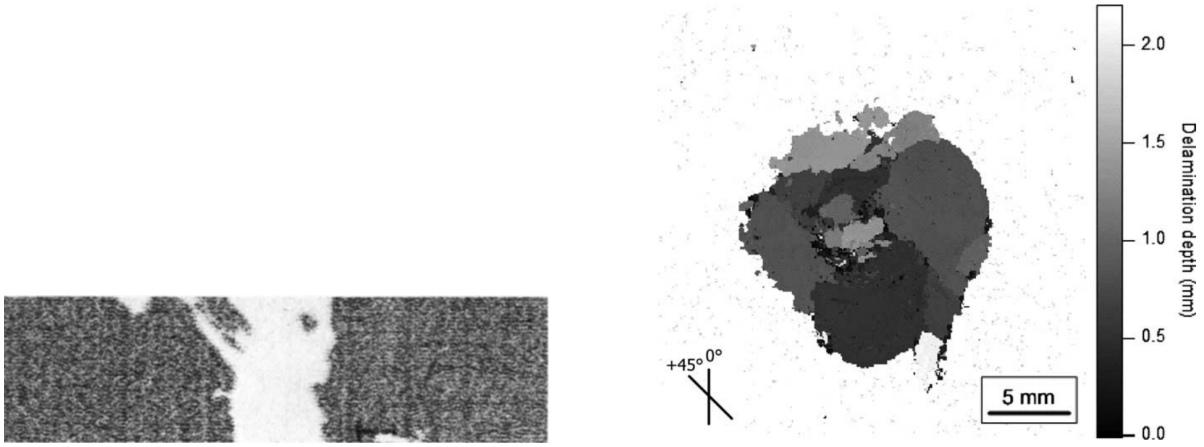

(a) C-scan result of an 8-ply +/-45°composite impacted at 4 J [111]

(b) Time-of-flight C-scan result for 16 ply quasi-isotropic sample impacted at 1.9 J [103]

Figure 1.13: Examples of (a) conventional and (b) time-of-flight C-scan results.

1.2.1.3 X-rays

Radiography is based on the projection of X-rays through the sample onto an X-ray sensitive film/sensor. Internal voids attenuate the transmitted signal and are visible on the final image as darker zones as shown in Fig. 1.14a [111–113]. This technique is fast but it does not give any indication on the defect depth. It is therefore perfect for fast damage detection. A version of radiography that contains depth information is called computed tomography (CT). The CT scan technique allows to reconstruct a volume from several X-ray pictures of the component rotated by a controlled angle. It is the finest method, it allows to navigate through the whole volume looking for signs of damage/defects as shown in Fig. 1.14b [113–117]. The first drawback is the time required to acquire the data, as the final resolution depends on the number of X-ray pictures. Another drawback is the cost of the machine. The last one is the time required to inspect the reconstructed volume to look for damage as the operator can spend one minute or so per slice and the dataset can contain several hundreds of slices. These volumes can also be used to construct refined FE models at the micro scale as in [118–120]. In this thesis, FE models were built on the observations made on CT-scans of impacted samples.

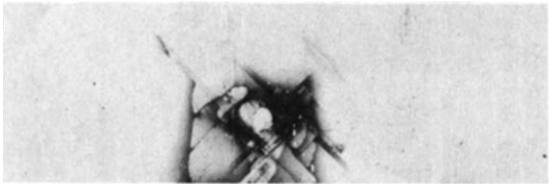

(a) X-ray result of an 8-ply +/-45°composite impacted at 4 J [111] (same sample as Fig. 1.13a)

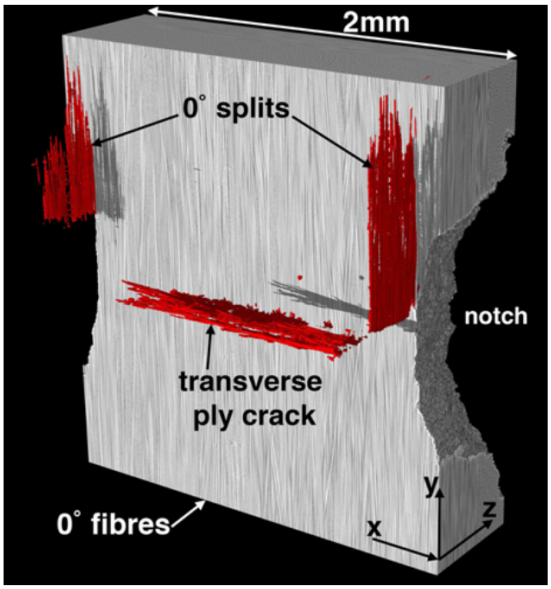

(b) Tomographic image of intralaminar damage in a notched 4-ply cross-ply laminated composite [115]

Figure 1.14: Examples of (a) radiography and (b) computed tomography results.

1.2.1.4 Thermography

This technique relies on the fact that a delamination reduces the heat diffusion through the thickness because thin layers of air at delaminations act as thermal insulators. The thermal gradient can be introduced using a hair drier or a halogen lamp, and the temperature map is observed with a thermal camera [102, 121–123]. The delaminated spot appears in a hotter colour as shown in Fig. 1.15. This is a very fast inspection technique, and inexpensive as low cost thermal cameras are now available. This technique is well suited for delamination detection. However, it is limited to thin components or shallow delaminations on thicker components.

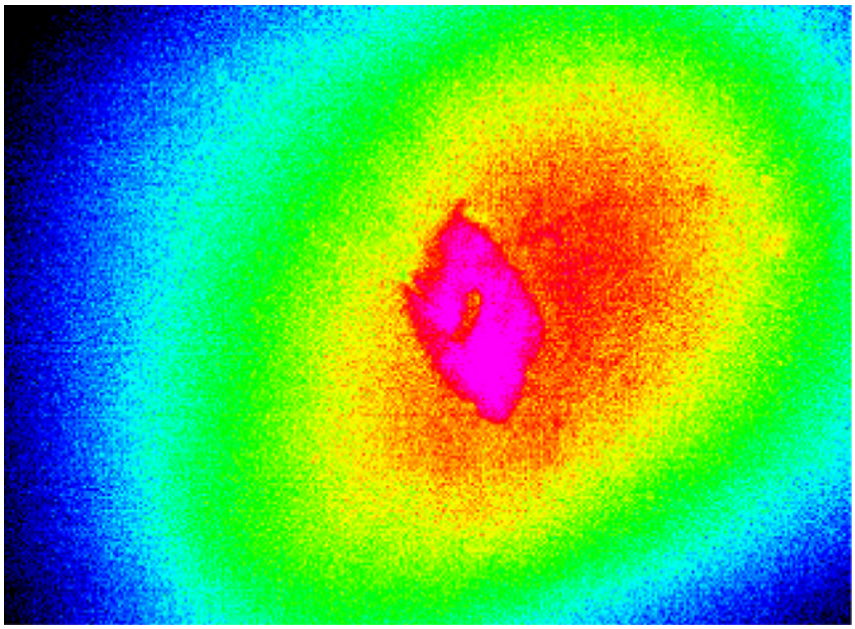

Figure 1.15: Infrared thermography map of an impacted carbon epoxy specimen [102].

These non-mechanical techniques are very well suited to detect damage and/or provide a spatial description of the damage. Because they are not related to mechanical phenomena they can not be used alone to determine the remaining service life. They should be coupled to kinematic measurement techniques to provide a tool helping to evaluate the post-impact mechanical behaviour of composite structures.

1.2.2 Kinematic measurement techniques

These methods give access to quantitative maps of mechanical quantities such as displacements, slopes, strains, or stresses. This group of methods includes holography, shearography, image correlation, thermoelasticity, the grid method, and deflectometry. This section briefly reviews

them and their application to damage detection/characterization.

1.2.2.1 Holography

Holography or Electronic/Digital Speckle Pattern Interferometry is based on an interferometric phenomenon and generally allows to obtain deflection fields. It is very sensitive and the spatial resolution is the resolution of the camera. It can be associated with thermal loading for delamination detection as in [103, 124] and an example is shown in Fig. 1.16. It can also be used in dynamic testing to extract mode shapes for instance as in [106, 125, 126]. As the local bending stiffnesses were modified by damage, the local mode shapes will be modified revealing the damage location at the same time. It is also possible to use it with a vacuum loading and to use the results to update finite element models to infer damage as in [127]. The downsides of this technique are a strong sensitivity to vibrations and the cost of the equipment capable of measuring displacements at the µm scale.

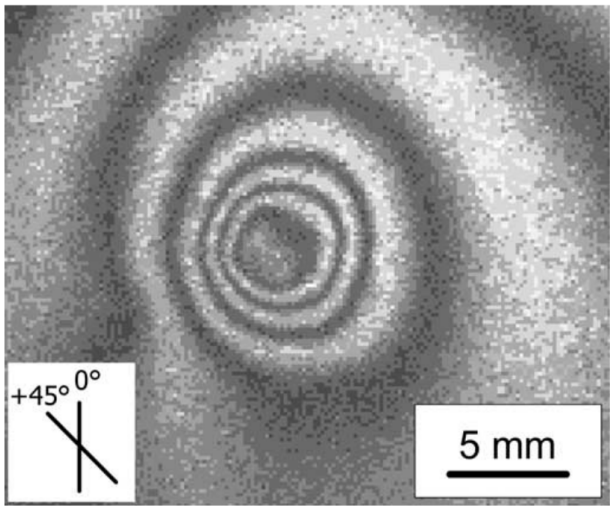

Figure 1.16: Holography results of a 16 ply quasi-isotropic sample impacted at 1.9 J [103] (same sample as Fig. 1.13b).

1.2.2.2 Shearography

Shearography is a differential interferometric technique that is sensitive to local slopes. A system is commercially available for the purpose of delamination detection and a review on its detection capability can be found in [128]. It is usually associated with thermal loading as in [102, 123, 129, 130] but can also be used in dynamic testing as in [131]. A typical result is

shown in Fig. 1.17. It is very sensitive as it is based on interferometry. An advantage for this technique is that even though it is based on interferometry, it is reasonably insensitive to vibrations as opposed to holography because it uses the same laser path. Drawbacks are the cost of the shearographic device and the fact that it gives only qualitative information. Another drawback is with shallow delaminations in thick composite structures: the resulting local change of slopes may be too small.

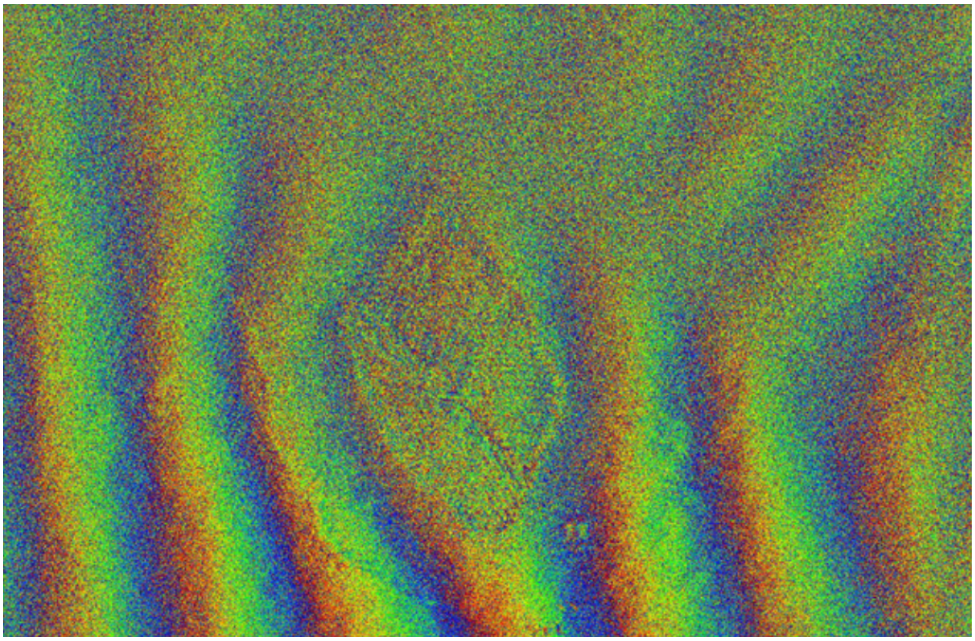

Figure 1.17: Shearography map of an impacted carbon epoxy specimen [102] (same sample as Fig. 1.15).

1.2.2.3 Thermoelasticity

Thermoelasticity requires cyclic loading to extract the temperature modulation from the temporally averaged temperatures. It is based on the principle of thermoelastic coupling which is sensitive to stiffness. It has been already used as a damage detection technique [132–135]. An example of damage tracking on a $[(0\ 90)_3\ 0\ (90\ 0)_3]$ open hole sample submitted to fatigue using thermoelasticity is shown in Fig. 1.18. For this technique, the cameras used for simple thermography are usually not precise enough and better infrared cameras are required which are expensive. From a non-destructive detection point-of-view, another drawback is the need for cyclic loading as it can propagate damage.

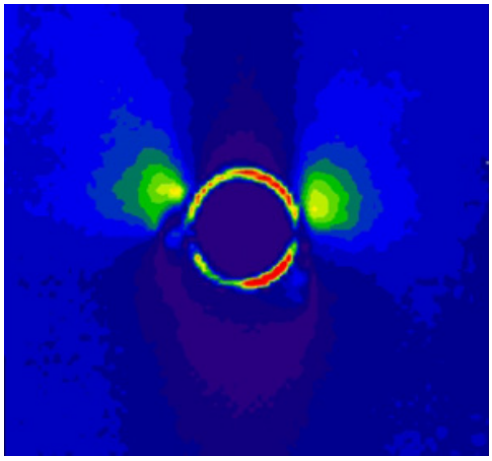

Figure 1.18: Strain sum results from thermoelasticity of a cross-ply sample fatigued in tension [134].

1.2.2.4 Image correlation

Digital image correlation (DIC) is more and more widely used because of its low cost and ease of use [136]. It is based on tracking the deformations of sets of random patterns. As it only provides displacements, it is more suitable for in-plane applications as only one differentiation is required to obtain strains. For the out-of-plane configuration, strains are proportional to curvatures which are double derivatives of out-of-plane displacements in thin plate theory (Love-Kirchhoff). These two differentiations decrease the signal to noise ratio leading to the necessity of smoothing. Therefore, DIC will present a poor resolution to spatial resolution compromise. It has been used by several groups to detect delaminations or track cracks as in [137–142] using in-plane loading configurations. An example of obtained results is visible in Fig. 1.19. A sandwich composite panel was subjected to a 11.5 J impact and then tested in uniaxial tension. The 0.72 % strain horizontal band is the effect on the strain field of a crack situated on the back surface. As the method is not very sensitive, higher levels of deformations are necessary, the opposite of shearography for example. It is worth noticing that with the progress in volume inspection techniques, some work has been done to implement a 3D version of DIC, called Digital Volume Correlation (DVC), [143] and applications to composites can be found in [115, 116, 118–120, 144]. An application consists of studying the crack opening for a notched specimen by comparing numerical results of models with built-in cracks and experimental data obtained from DVC on in-situ computed tomography [120]. Because of the higher level of deformations required with image correlation, this technique is therefore recommended for studying damage propagation and not to validate numerical models of post-impact mechanical behaviour at low load.

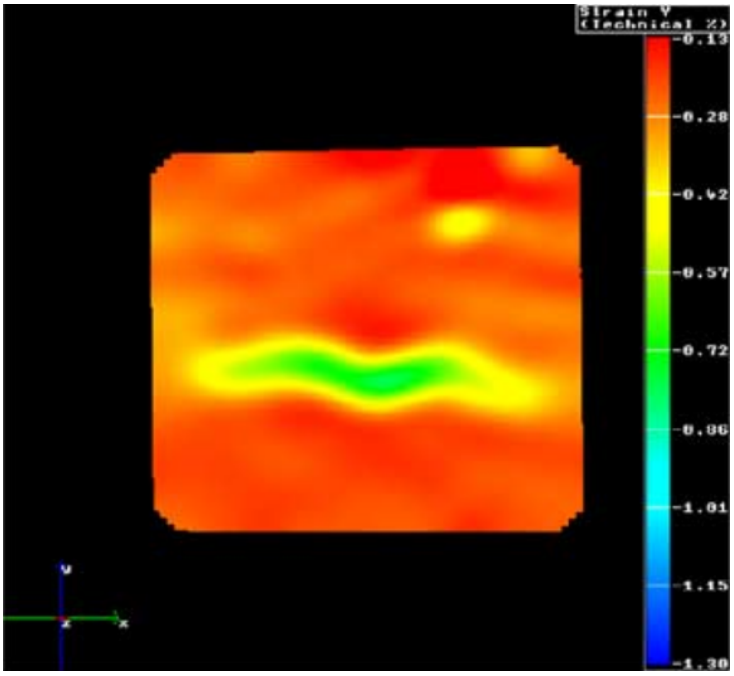

Figure 1.19: Y strain field of a sandwich composite impacted at 11.5 J obtained by DIC (in %) [142].

1.2.2.5 Grid method

The grid method tracks the movements of grid pitches and it has already been used to assess damage development in [145–147]. An example of results is shown in Fig. 1.20. It requires the use of a grid bonded onto the surface and provides 2D in-plane displacement fields with a cross-hatch grid. The major problem with this method is to have a grid with a constant pitch in both directions. To measure out-of-plane information, the grid method can be used in specular reflection, which is known as deflectometry. The measured quantities are not displacements but surface slopes and with a differentiation the surface curvatures, which are proportional to strains in thin plate theory, are obtained. The complete procedure is detailed later in this work. This technique is not onerous but is currently limited to plane surfaces and requires a reflective coating if the sample does not exhibit sufficient specular reflection (mirror-like). It is a very sensitive method and the resolution is tunable independently from its spatial resolution. It has already been used for damage characterisation using the virtual fields methods in [148, 149] with samples containing an area with reduced stiffnesses as illustrated in Fig. 1.21 and with an impacted sample.

The techniques mentioned previously can be organised differently depending on their use: *in-situ* damage detection (visual inspection, ultrasounds, thermography, and shearography) or basic understanding of damage mechanisms and validation of design procedures (holography,

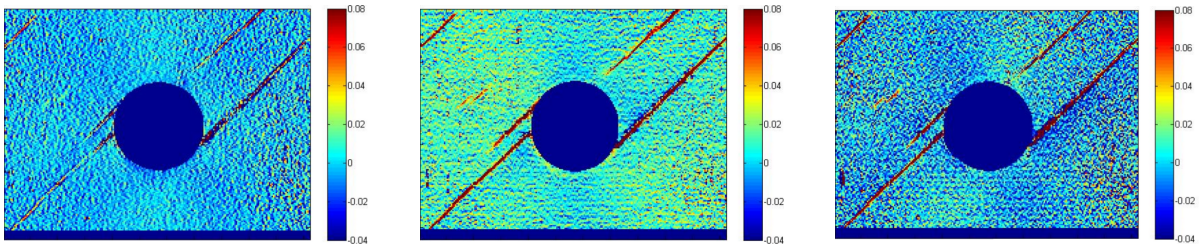

(a) ϵ_{xx} (b) ϵ_{yy} (c) γ_{xy}

Figure 1.20: Strain fields from in-plane grid method for a $[\text{-}45_4\ 90_4\ 45_4\ 0_4.]_s$ glass-fibre open hole specimen [145].

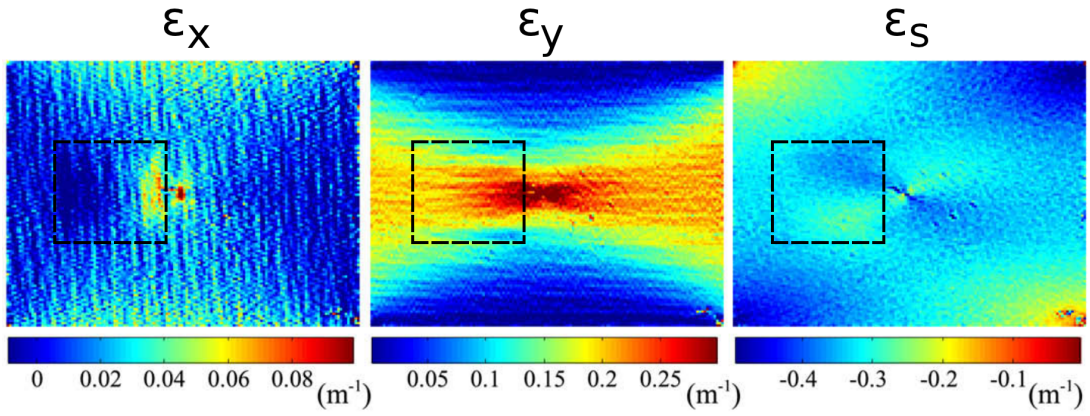

Figure 1.21: Strain fields from deflectometry of a cross-ply sample with a cut-out (dashed square) [149].

radiography, computed tomography, DIC, thermoelasticity, grid method, and deflectometry).

1.3 Conclusion

The detection of barely visible impact damage has been studied for decades using non-destructive techniques and commercial equipment is nowadays available for this particular purpose. Several groups have worked on the understanding of the impact damage process using different techniques (thermoelasticity, DIC, ...) and there is now a fine description of this process. On the other hand, post-impact behaviour of composites has not yet been precisely modelled, for instance compression after impact (CAI). This test is a reference for residual strength evaluation of composites [77] and is widely used in industry as compression strength is the key parameter for the design of composite structures [150]. During a CAI test, the failure of the structure is catastrophic because it is governed by local buckling of sublaminates at the impacted zone. This chaotic behaviour makes accurate CAI strength predictions quite difficult. To improve the prediction, fine CT-scans can be used to implement delaminations and cracks in numerical models. Nevertheless, these models have to be experimentally validated in a non-destructive way to make sure that the initial structure simulates accurately the post-impact behaviour.

By taking advantage of the fine description of the internal structure of impacted samples provided by CT-scans and of the high sensitivity of the deflectometry method, this work focuses on the validation of finite element models simulating post-impact behaviour of laminated structures. The finite element models were built based on the observations of CT-scans and their results were compared to rich and detailed experimental data obtained by deflectometry. This methodology is thought to lead to the definition of the key parameters for numerically simulating impact damage as validated with refined experimental assessment. First, the technique has been applied to beam samples containing simulated delaminations and real impacts. It has been applied to plates with real impacts in a second step and the experimental data from the plates have been processed with the virtual fields method (VFM).

CHAPTER 2

DEFLECTOMETRY

Deflectometry is a white light full-field measurement technique. Even though it is not an interferometric method, this technique is very sensitive [151, 152]. Its principle is explained in a first step, followed by the numerical procedure to obtain strain fields from the grid pictures. It continues with the procedure to prepare the sample. The grid quality is reviewed, and finally the resolution and spatial resolution are evaluated and reported.

2.1 Principle

Deflectometry is based on specular reflection of light as expressed in the Snell-Descartes law. First, it was developed with the camera behind the grid as shown in Fig. 2.1a and then modified to place the camera beside the grid as shown in Fig. 2.1b [153]. The drawback of the first configuration (camera behind the grid) is the missing data from the reflected image of the hole. Spatial smoothing or interpolation can be used to reconstruct these data. Nonetheless, if the damage is located near the hole region, it may be missed. For this reason, the configuration with the camera beside the grid has been used in this work. An example of the set-up with the camera beside the grid is shown in Fig. 2.2. Even though the local slopes depend on both grid shifts for both configurations, this dependency is more critical for the second configuration because of the offset of the camera.

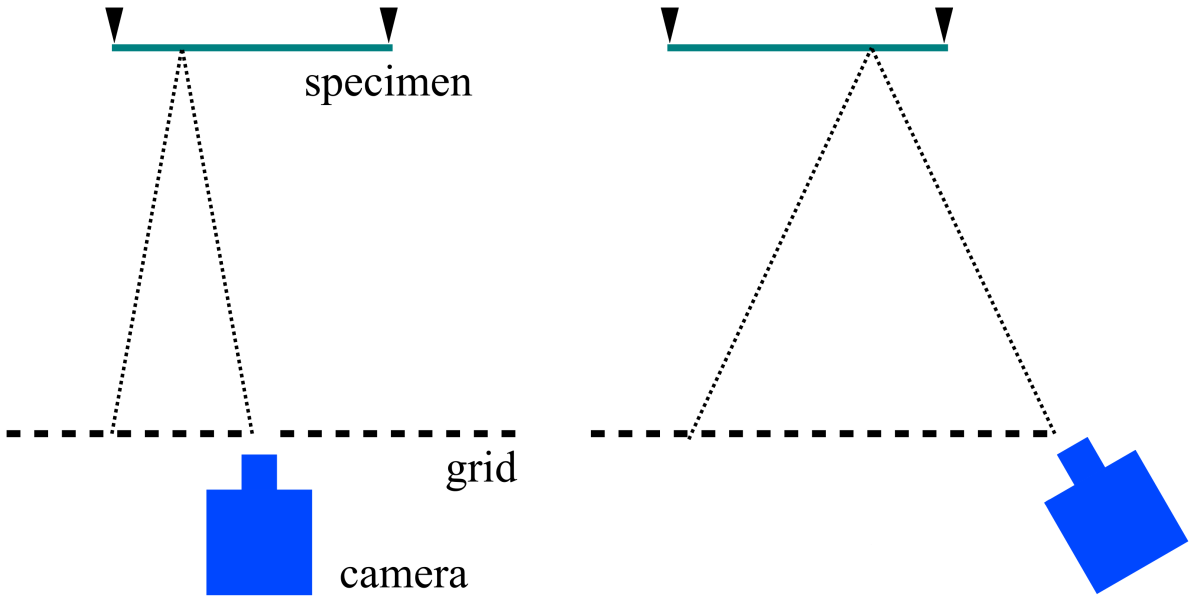

(a) Camera behind the grid (b) Camera beside the grid

Figure 2.1: Two configurations of deflectometry: camera (a) behind the grid and (b) beside the grid [153].

2.1.1 From grid shifts to slopes

This technique looks at the movement of the reflected image of a cross hatched grid due to the loading. A schematic view of its principle is shown in Fig. 2.3 to obtain 2D slope fields from a cross hatched grid. The camera, point *C*, is offset by e with respect to the axis *(O,y)* defined at the closest edge of the specimen. The coordinates of point *M* (x, y) belong to the interval $[0, L] \times [-H/2, H/2]$ with L being the length and H the width. At rest, the camera (point *C*) looks at the reflection of point *P* on point *M*. When the plate is loaded in bending, the local slope at point *M* is modified by $d\alpha_r$ and $d\alpha_t$ and the camera now sees the reflection of point *Q* on point *M* on the specularly reflective flat specimen. Therefore, a local change of slope on the specimen leads to a shift of the reference grid image as viewed by the camera. This grid shift can be evaluated by different techniques reviewed later. A consequence of the reflections is that point *Q* does not necessarily belong to the plane defined by points *C*, *M*, and *P*. Using Fig. 2.3, the following equations derive the link between the local changes of slope $d\alpha_x$ and $d\alpha_y$ and the spatial grid shifts u_x and u_y.

In Fig. 2.3a, the rotated Cartesian coordinate system (C,$\vec{u}_r$,$\vec{u}_t$) is linked to the global Cartesian

(a) General view

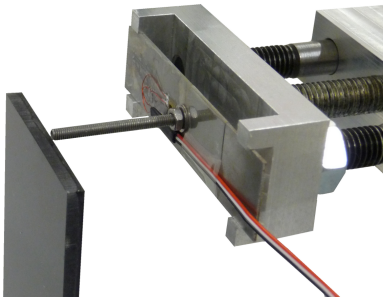

(b) Point load

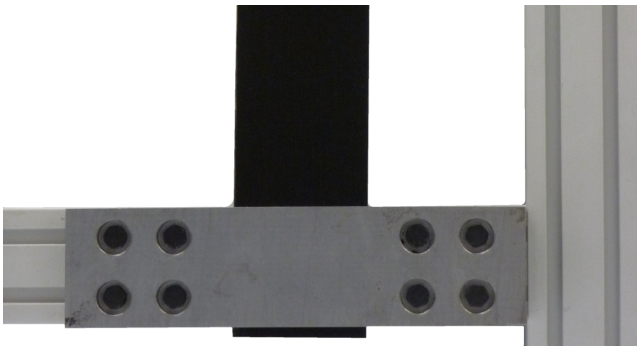

(c) Clamp

Figure 2.2: (a) General and close-up views of the set-up. The grid and the camera are on the left and the rig with the sample on the right. (b) Close-up view of the point load. (c) Close-up view of the clamp.

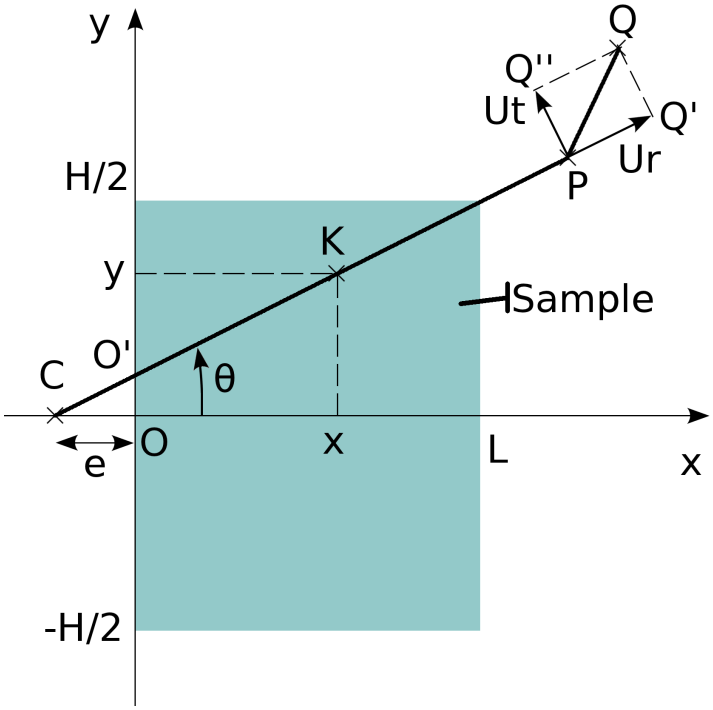

(a) View in the *(x,y)* plane

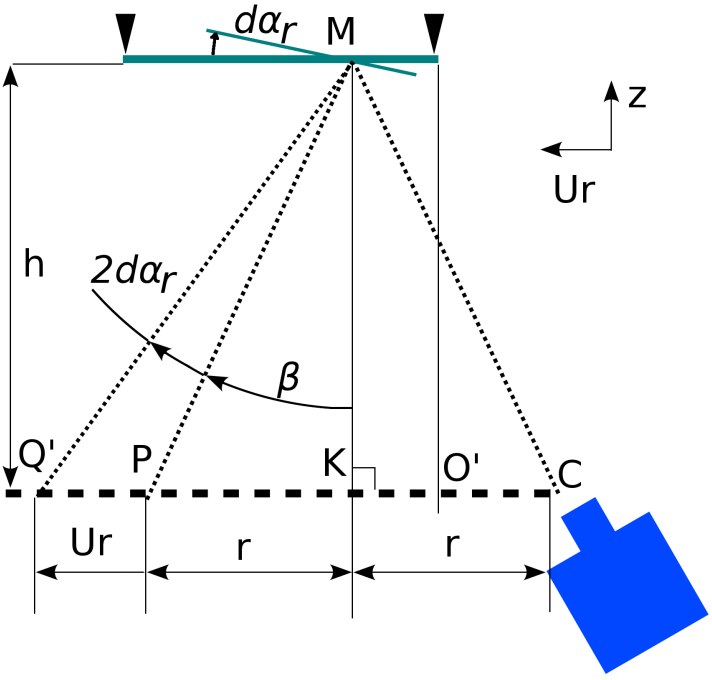

(b) View in the *(z,ur)* plane

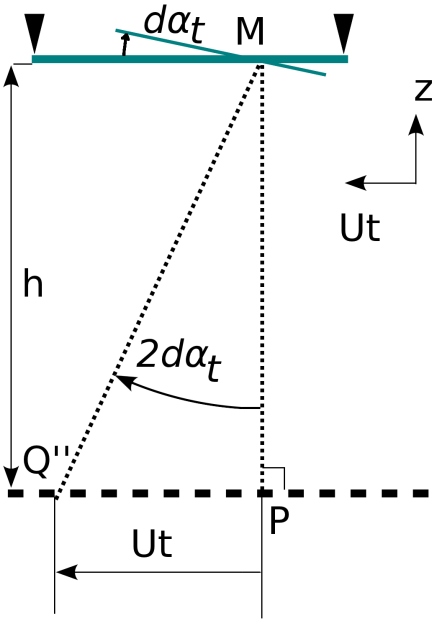

(c) View in the *(z,ut)* plane

Figure 2.3: Principle of deflectometry.

coordinate system (O,$\vec{x}$,$\vec{y}$) by the following equations:

$$\begin{cases} x_r = x\cos\theta + y\sin\theta \\ x_t = -x\sin\theta + y\cos\theta \end{cases} \tag{2.1}$$

The derivatives are expressed as:

$$\frac{\partial x_r}{\partial x} = \cos\theta \qquad \frac{\partial x_r}{\partial y} = \sin\theta \qquad \frac{\partial x_t}{\partial x} = -\sin\theta \qquad \frac{\partial x_t}{\partial y} = \cos\theta \tag{2.2}$$

From Fig. 2.3a, θ is expressed as:

$$\theta = \arctan\frac{y}{x+e} \qquad (x,y) \in [0,L]\times[-H/2,H/2] \tag{2.3}$$

Using (2.3), one can express the following:

$$\begin{cases} \cos\theta = \dfrac{x+e}{\sqrt{(x+e)^2+y^2}} \\ \sin\theta = \dfrac{y}{\sqrt{(x+e)^2+y^2}} \end{cases} \tag{2.4}$$

Combining (2.4) in (2.1) leads to:

$$\begin{cases} x_r = \sqrt{(x+e)^2+y^2} = r \\ x_t = 0 \end{cases} \tag{2.5}$$

Combining (2.4) in (2.2) leads to:

$$\begin{cases} \dfrac{\partial x_r}{\partial x} = \dfrac{x+e}{\sqrt{(x+e)^2+y^2}} & \dfrac{\partial x_r}{\partial y} = \dfrac{y}{\sqrt{(x+e)^2+y^2}} \\ \dfrac{\partial x_t}{\partial x} = -\dfrac{y}{\sqrt{(x+e)^2+y^2}} & \dfrac{\partial x_t}{\partial y} = \dfrac{x+e}{\sqrt{(x+e)^2+y^2}} \end{cases} \tag{2.6}$$

One can also express the spatial grid shifts in the rotated coordinate system, u_r being radial and u_t ortho-radial, with the following expressions:

$$\begin{cases} u_r = u_x\cos\theta + u_y\sin\theta \\ u_t = -u_x\sin\theta + u_y\cos\theta \end{cases} \tag{2.7}$$

From Fig. 2.3b, one has:

$$\tan\beta = \frac{r}{h} \tag{2.8}$$

$$\tan(\beta + 2d\alpha_r) = \frac{r+u_r}{h} \tag{2.9}$$

Subtracting (2.9) from (2.8) gives:

$$\tan(\beta + 2d\alpha_r) - \tan\beta = \frac{r + u_r}{h} - \frac{r}{h} = \frac{u_r}{h} \tag{2.10}$$

With the help of trigonometric formulæ, (2.10) can be simplified as:

$$\frac{u_r}{h} = \frac{\tan\beta + \tan 2d\alpha_r}{1 - \tan\beta\tan 2d\alpha_r} - \tan\beta = \frac{\tan 2d\alpha_r(1 + \tan^2\beta)}{1 - \tan\beta\tan 2d\alpha_r} \tag{2.11}$$

As one is interested in expressing the change of slope as a function of the spatial grid shift, one has:

$$d\alpha_r = \frac{1}{2}\arctan\left(\frac{\frac{u_r}{h}}{1 + \frac{u_r}{h}\tan\beta + \tan^2\beta}\right) \tag{2.12}$$

From Fig. 2.3c, one has:

$$d\alpha_t = \frac{1}{2}\arctan\frac{u_t}{h} \tag{2.13}$$

With u_z the out-of-plane bending displacement of the tested specimen, one can write:

$$\begin{cases} d\alpha_x &= \dfrac{\partial u_z}{\partial x} &= \dfrac{\partial u_z}{\partial x_r}\dfrac{\partial x_r}{\partial x} + \dfrac{\partial u_z}{\partial x_t}\dfrac{\partial x_t}{\partial x} \\ d\alpha_y &= \dfrac{\partial u_z}{\partial y} &= \dfrac{\partial u_z}{\partial x_r}\dfrac{\partial x_r}{\partial y} + \dfrac{\partial u_z}{\partial x_t}\dfrac{\partial x_t}{\partial y} \end{cases} \tag{2.14}$$

Since $\frac{\partial u_z}{\partial x_r} = d\alpha_r$ and $\frac{\partial u_z}{\partial x_t} = d\alpha_t$, (2.14) can be written as:

$$\begin{cases} d\alpha_x = \dfrac{\partial x_r}{\partial x}d\alpha_r + \dfrac{\partial x_t}{\partial x}d\alpha_t \\ d\alpha_y = \dfrac{\partial x_r}{\partial y}d\alpha_r + \dfrac{\partial x_t}{\partial y}d\alpha_t \end{cases} \tag{2.15}$$

Combining (2.4, 2.6, 2.7, 2.12, 2.13, and 2.15) gives the final expression:

$$\begin{cases} d\alpha_x = \dfrac{1}{2}\dfrac{x+e}{\sqrt{(x+e)^2+y^2}}\arctan\left(\dfrac{\dfrac{u_x}{h}\dfrac{x+e}{\sqrt{(x+e)^2+y^2}} + \dfrac{u_y}{h}\dfrac{y}{\sqrt{(x+e)^2+y^2}}}{1 + \dfrac{u_x}{h}\dfrac{x+e}{h} + \dfrac{u_y}{h}\dfrac{y}{h} + \dfrac{(x+e)^2+y^2}{h^2}}\right) \\ \qquad - \dfrac{1}{2}\dfrac{y}{\sqrt{(x+e)^2+y^2}}\arctan\left(-\dfrac{u_x}{h}\dfrac{y}{\sqrt{(x+e)^2+y^2}} + \dfrac{u_y}{h}\dfrac{x+e}{\sqrt{(x+e)^2+y^2}}\right) \\ d\alpha_y = \dfrac{1}{2}\dfrac{y}{\sqrt{(x+e)^2+y^2}}\arctan\left(\dfrac{\dfrac{u_x}{h}\dfrac{x+e}{\sqrt{(x+e)^2+y^2}} + \dfrac{u_y}{h}\dfrac{y}{\sqrt{(x+e)^2+y^2}}}{1 + \dfrac{u_x}{h}\dfrac{x+e}{h} + \dfrac{u_y}{h}\dfrac{y}{h} + \dfrac{(x+e)^2+y^2}{h^2}}\right) \\ \qquad + \dfrac{1}{2}\dfrac{x+e}{\sqrt{(x+e)^2+y^2}}\arctan\left(-\dfrac{u_x}{h}\dfrac{y}{\sqrt{(x+e)^2+y^2}} + \dfrac{u_y}{h}\dfrac{x+e}{\sqrt{(x+e)^2+y^2}}\right) \end{cases} \tag{2.16}$$

Since the specimen dimensions (L, H), u_x, and u_y are small compared to h, $d\alpha_x$ can be simplified as:

$$\begin{cases} d\alpha_x \simeq \dfrac{1}{2}\dfrac{x+e}{\sqrt{(x+e)^2+y^2}}\arctan\left(\dfrac{u_x}{h}\dfrac{x+e}{\sqrt{(x+e)^2+y^2}}+\dfrac{u_y}{h}\dfrac{y}{\sqrt{(x+e)^2+y^2}}\right) \\ \qquad -\dfrac{1}{2}\dfrac{y}{\sqrt{(x+e)^2+y^2}}\arctan\left(-\dfrac{u_x}{h}\dfrac{y}{\sqrt{(x+e)^2+y^2}}+\dfrac{u_y}{h}\dfrac{x+e}{\sqrt{(x+e)^2+y^2}}\right) \end{cases} \tag{2.17}$$

As $\arctan x \simeq x$ when $x \ll 1$, (2.17) can be simplified as:

$$\begin{cases} d\alpha_x \simeq \dfrac{1}{2}\dfrac{x+e}{\sqrt{(x+e)^2+y^2}}\left(\dfrac{u_x}{h}\dfrac{x+e}{\sqrt{(x+e)^2+y^2}}+\dfrac{u_y}{h}\dfrac{y}{\sqrt{(x+e)^2+y^2}}\right) \\ \qquad -\dfrac{1}{2}\dfrac{y}{\sqrt{(x+e)^2+y^2}}\left(-\dfrac{u_x}{h}\dfrac{y}{\sqrt{(x+e)^2+y^2}}+\dfrac{u_y}{h}\dfrac{x+e}{\sqrt{(x+e)^2+y^2}}\right) \end{cases} \tag{2.18}$$

Expanding (2.18) will simplify its expression and using the same way $d\alpha_y$ can be simplified to finally obtain:

$$\begin{cases} d\alpha_x \simeq \dfrac{1}{2h}u_x \\ d\alpha_y \simeq \dfrac{1}{2h}u_y \end{cases} \tag{2.19}$$

This expression corresponds to the one expressed in [152].

Fig. 2.4 presents the experimental strain fields for an undamaged sample obtained using (2.16) or (2.19) and their relative difference in percentage. The experimental parameters to obtain the grid shifts are summarized in Tab. 2.1. As the maximum difference between the two approaches is less than 1 µm/m, the correction is not necessary. Nonetheless, the correction proposed in [149] is incorrect because it was assumed that the slope in one direction did not influence the slope in the other direction.

Camera		Dantec Q-400
Technology		CCD
Resolution		2448×2050 pix^2
Pixel size		3.45 µm
Dynamic range		12 bits
Exposure		1 s
Lens		Nikon 28-200 mm AF-D
Focal length		200 mm
Aperture		f/11
Others		
Grid-sample	h	1.66 m
Grid pitch	p	1.524 mm
Camera offset	e	15 mm
Sampling	N	7 pix
Resolution in phase	σ_φ	10.70 mrad
Resolution in slope	σ_θ	0.78 mm/km
Resolution in curvature	σ_κ	1.45 1/km
Resolution in strain	σ_ε	2.9 µm/m
Spatial resolution		$\sim$14 pix

Table 2.1: Experimental parameters for deflectometry measurements on the beams.

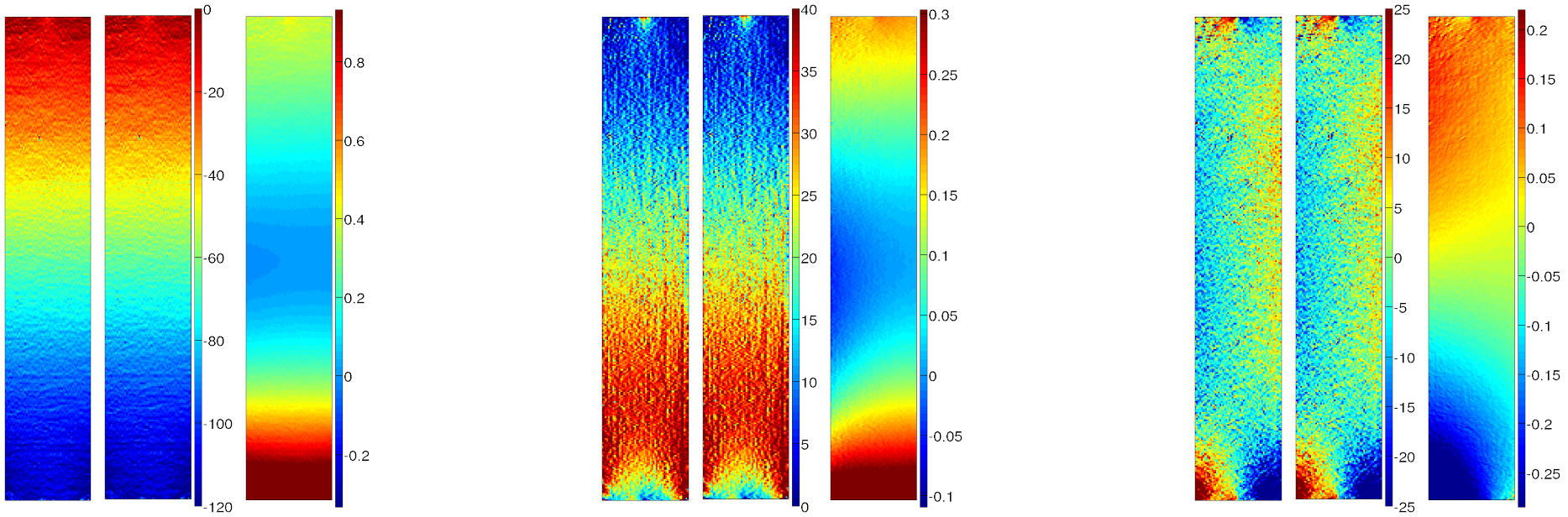

(a) (b) (c) (d) (e) (f) (g) (h) (i)

Figure 2.4: Effect of simplifications in (2.19) compared to (2.16) on measured strain fields (in µm/m). (a) longitudinal strain field using (2.16), (b) longitudinal strain field using (2.19), (c) difference between (a) and (b). (d) transverse strain field using (2.16), (e) transverse strain field using (2.19), (f) difference between (d) and (e). (g) shear strain field using (2.16), (h) shear strain field using (2.19), (i) difference between (g) and (h).

2.1.2 Effect of an out-of-plane displacement

In the analysis developed previously, the out-of-plane displacement of the tested sample has been neglected. Its influence can be studied with a rigid body movement as illustrated in Fig. 2.5. At rest the camera (point *C*) looks at the reflection of point *P* on point *M*. When the plate is moved by dh, the camera now sees the reflection of point *Q* on point *M* on the specularly reflective flat specimen. A consequence of the reflections is that point *Q* belongs to the plane defined by points *C*, *M*, and *P*. Using Fig. 2.5, the following equations derive the link between the rigid body displacement dh and the strain fields.

From geometrical considerations in Fig. 2.5b, one has:

$$\tan\beta = \frac{r}{h} = \frac{r - \frac{u_r}{2}}{h - dh} \tag{2.20}$$

From (2.20), one can extract the relation between the spatial grid shift u_r and the rigid body movement dh:

$$u_r = \frac{2r}{h} dh \tag{2.21}$$

Since $u_t = 0$, (2.7) can be written and simplified using (2.4) as:

$$\begin{cases} u_x = u_r \cos\theta - u_t \sin\theta & = \dfrac{2}{h}(x+e)dh \\ u_y = u_r \sin\theta + u_t \cos\theta & = \dfrac{2}{h} y dh \end{cases} \tag{2.22}$$

Using (2.18), the effect of an out-of-plane movement on the slope fields can be expressed as:

$$\begin{cases} d\alpha_x = \dfrac{x+e}{h^2} dh \\ d\alpha_y = \dfrac{y}{h^2} dh \end{cases} \tag{2.23}$$

Therefore, its effect on the strain fields can be expressed as:

$$\begin{cases} \varepsilon_x & = \dfrac{t}{2}\dfrac{\partial d\alpha_x}{\partial x} & = \dfrac{t}{2}\dfrac{dh}{h^2} \\ \varepsilon_y & = \dfrac{t}{2}\dfrac{\partial d\alpha_y}{\partial y} & = \dfrac{t}{2}\dfrac{dh}{h^2} \\ \varepsilon_s & = \dfrac{t}{2}\left(\dfrac{\partial d\alpha_x}{\partial y} + \dfrac{\partial d\alpha_y}{\partial x}\right) & = 0 \end{cases} \tag{2.24}$$

For the beams, the out-of-plane displacement was of the order of the thickness (4 mm). Therefore, ε_x is equal to 1.45 µm/m. The effect of the out-of-plane displacement is negligible in comparison with the level of strains in the maps Figs. 2.4a, 2.4d, and 2.4g.

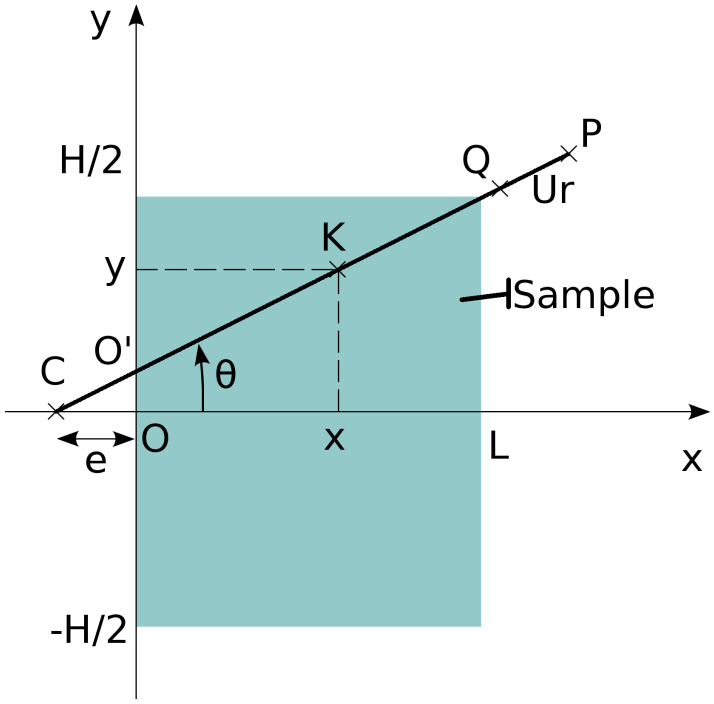

(a) View in the *(x,y)* plane

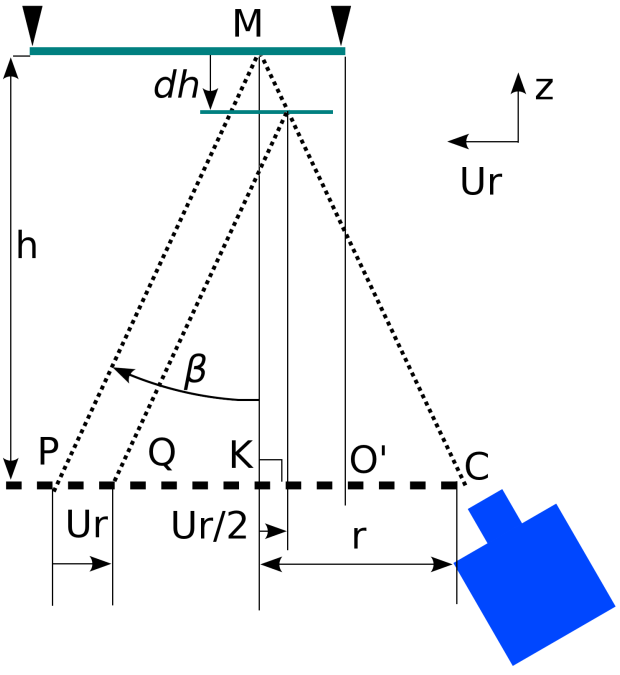

(b) View in the *(z,ur)* plane

Figure 2.5: Effect of out-of-plane movement on deflectometry.

2.2 Strain extraction

Several steps are required to obtain strain fields from pictures of the grid reflection. Fig. 2.6 presents the complete process. A first picture of the reflected grid is taken at rest and another one when the plate is loaded. Because a cross hatched grid is used, the phase fields can be extracted along the longitudinal and transverse directions for both pictures using a windowed discrete Fourier transform algorithm. The phase fields at rest are subtracted from the phase fields after loading giving longitudinal and transverse phase maps. As these phase maps are wrapped between $[-\pi, +\pi]$, an unwrapping process is required to remove the 2π-jumps present in the maps. The unwrapped phase maps are then converted into slopes using (2.16). Curvatures are obtained by the numerical differentiation of the slope fields. The curvatures are then converted to strains by multiplying by half the specimen thickness as expressed in the thin plate theory. It must be noted that in the presence of delaminations, the obtained values are not strains any more as assumptions of the thin plate theory are not satisfied (linear through-thickness evolution of strains). Therefore, in this work, the results will be referred to as "equivalent strains" and not simply strains.

The following sections detail the chosen algorithms.

2.2.1 Phase extraction

To extract phases from grid pictures, two approaches exist: global and local. The first one is based on the processing of the full image by a Fourier transform. Even though this method is widely used, it has several drawbacks, like accuracy and spatial resolution, compared to local approaches [154]. The local analysis can be done either temporally or spatially. With the first, the phase value for each pixel is computed using the same pixel data from several pictures separated by a known spatial shift. This method is mainly used with interferometric techniques. The spatial phase stepping method is based on a carrier with a known periodicity [155]. It is used only with the in-plane grid method and deflectometry. The spatial phase stepping method reduces the number of output points as not more than one independent value can be extracted from a period.

The grid shift in phase is 2π when the spatial grid shift is equal to the grid pitch, p. Therefore,

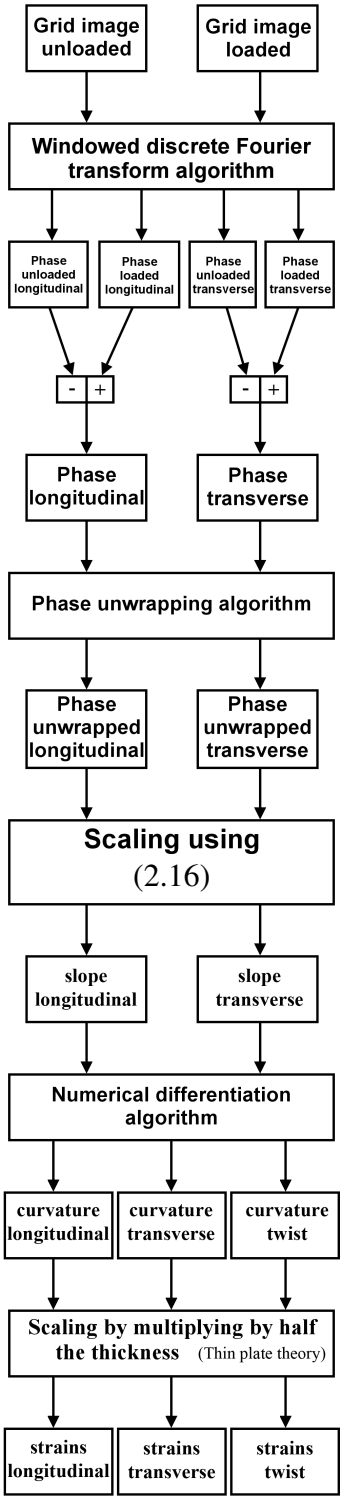

Figure 2.6: Grid processing for strain extraction from grid pictures.

the relation between the grid shift in phase $\Delta\varphi$ and the spatial grid shift u is:

$$\begin{cases} u_x(x,y) = -\dfrac{p}{2\pi}\Delta\varphi_x(x,y) \\ u_y(x,y) = -\dfrac{p}{2\pi}\Delta\varphi_y(x,y) \end{cases} \tag{2.25}$$

Considering a 1-dimensional problem, the grid reflection can be assimilated to a sinusoidal signal and can be described by the following equation [155, 156]:

$$I(x) = I_0(x)\left[1 + \gamma(x)\cos(\varphi(x))\right] \tag{2.26}$$

where I_0 and γ are, respectively, the average intensity and the contrast, which are slowly varying functions, and φ is the phase of the considered point. After the grid is deformed, the intensity distribution is changed slightly to I':

$$I'(x) = I_0(x)\left[1 + \gamma(x)\cos(\varphi(x) + \Delta\varphi(x))\right] \tag{2.27}$$

where $\Delta\varphi$ is the phase variation. φ is related to the position of the periodic signal and is written as:

$$\varphi(x) = \frac{2\pi x}{p} \tag{2.28}$$

with *x* being the position and *p* the grid pitch. From (2.25), the phase variation due to the deformation u_x is:

$$\Delta\varphi(x) = -\frac{2\pi u_x}{p} \tag{2.29}$$

If four pixels on the camera sample a period of the grid, then the intensity profile of each pixel can be formulated as:

$$\begin{cases} I_1 = I_0\left[1 + \gamma\cos(\varphi + 0)\right] & = I_0\left[1 + \gamma\cos(\varphi)\right] \\ I_2 = I_0\left[1 + \gamma\cos(\varphi + \dfrac{\pi}{2})\right] & = I_0\left[1 - \gamma\sin(\varphi)\right] \\ I_3 = I_0\left[1 + \gamma\cos(\varphi + \pi)\right] & = I_0\left[1 - \gamma\cos(\varphi)\right] \\ I_4 = I_0\left[1 + \gamma\cos(\varphi + \dfrac{3\pi}{2})\right] & = I_0\left[1 + \gamma\sin(\varphi)\right] \end{cases} \tag{2.30}$$

By solving this system, one can express the phase as a function of the intensities as:

$$\varphi = \arctan\left[\frac{I_4 - I_2}{I_1 - I_3}\right] \tag{2.31}$$

The same way, one can express $\varphi + \Delta\varphi$ as a function of the intensities from the deformed image and subtract (2.31) from it. The phase variation $\Delta\varphi$ will then be expressed as:

$$\Delta\varphi = \arctan\left[\frac{I'_4 - I'_2}{I'_1 - I'_3}\right] - \arctan\left[\frac{I_4 - I_2}{I_1 - I_3}\right] \tag{2.32}$$

It must be noted that this simple example is based on the assumption that the periodicity is not changed during deformation [156]. Also because the experimental intensity profile is not a perfect sinusoidal function, it is not possible to use the algorithm from (2.32). A last reason for not using this algorithm with experimental data is the fact that experimentally, it is very difficult if not impossible to have an exact integer number of pixels per period. The adjustment to an integer number of pixels per period is called "tuning requirement" and the defect is called miscalibration. Algorithms have been designed to overcome this problem and especially the windowed discrete Fourier transform (WDFT) one [155, 157–159]. Its formula is:

$$\varphi = \arctan\left[-\frac{\sum_{k=1}^{N-1} k\left(I_{k-1} - I_{2N-k-1}\right)\sin\left(\frac{2k\pi}{N}\right)}{NI_{N-1} + \sum_{k=1}^{N-1} k\left(I_{k-1} + I_{2N-k-1}\right)\cos\left(\frac{2k\pi}{N}\right)}\right] \tag{2.33}$$

where I_k is the light intensity profile of the kth pixel ($k = 0, \cdots, 2N-1$) and N the number of pixels per period. Because of its formulation, this algorithm is also insensitive to harmonics up to $N-2$ [155]. Also this algorithm uses $2N-1$ point and features a triangular weighting kernel. This weighting helps to reduce the sensitivity to miscalibration. Because of this triangular window, the spatial resolution is between N and $2N-1$. There is also another $2N-1$ triangular window in the perpendicular direction to extract the phases along a single direction as illustrated in Fig. 2.7.

To overcome the differentiation requirement, strains were directly obtained from grid pictures using the derivative of a Gaussian kernel [160]. The main advantage of this technique, in addition to obtain directly the phase derivative, is the relative insensitivity to the small variations of the grid pitch. It is computationally demanding as shown in Tab. 2.3. This is explained by the number of convolution products and the kernel sizes used for these convolution products. These products are used to extract the phases and phase derivatives from the grid images. The formulæ to determine the kernel size for both approaches are expressed in Tab. 2.2. 2 convolution products are necessary for the direct approach from Fig. 2.6 (one per direction) and 6 for the Gaussian (3 per direction).

Figs. 2.8 to 2.10 present the comparison between the direct and Gaussian approaches on strain extraction for a sample with a 50 mm long delamination across the whole width and located in the midplane, called FW50. Even though, no limits were specified for the span of the Gaussian formulation, it seems that a span lower than the number of pixels per period is not recommended as shown in Figs. 2.8b, 2.9b, and 2.10b. Unfortunately, this algorithm acts as a kind of smoothing and the larger the span, the smoother the maps. Because a very fine spatial resolution was

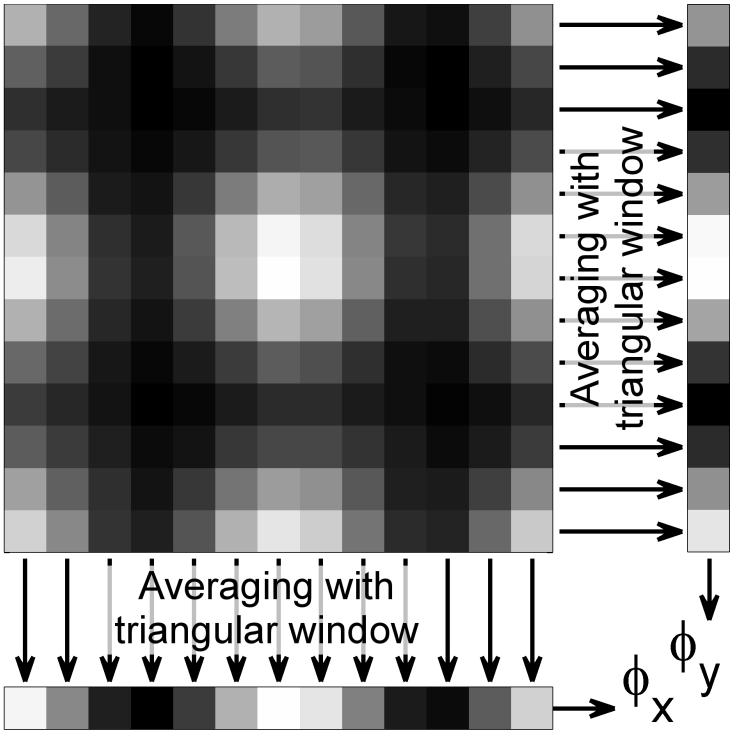

Figure 2.7: Illustration of removing the periodic horizontal or vertical information by period-wise averaging.

	Kernel size	Spatial resolution
Direct	$2N-1$	$2N-1$
Gaussian	$2\lfloor(3+4/5)\sigma\rceil-1$	$2\lfloor 3\sigma\rceil$

Table 2.2: Formulæ for the computation of the kernel sizes and spatial resolution for the direct approach from Fig. 2.6 and the Gaussian approach [160]. σ is the span of the Gaussian approach, N the number of pixels per period, here 7, and $\lfloor\rceil$ rounds to the nearest integer.

Method	Direct	Gaussian	Gaussian	Gaussian
Span σ (pixels)	-	4	7	14
Kernel size (pixels)	13	31	55	107
Spatial resolution (pixels)	13	24	42	84
CPU time (s)	0.83	15.38	33.29	115.27

Table 2.3: Comparison between the direct approach from Fig. 2.6 and the Gaussian [160] approaches. Tests were performed on a computer with an Intel core 2 duo 2.10 GHz processor and 3 Gb of RAM.

sought here and the printed grids were of good quality, the Gaussian algorithm has not been used.

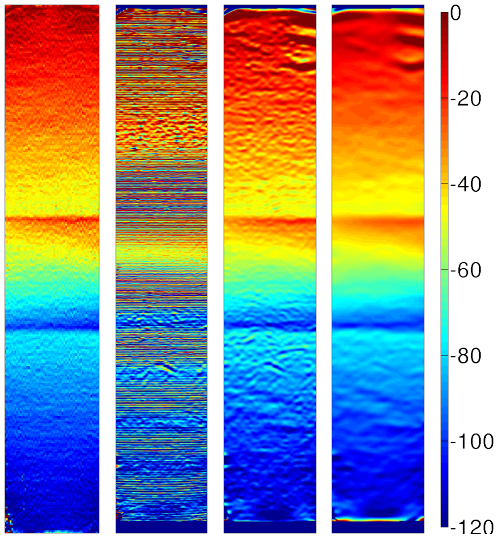

Figure 2.8: Equivalent longitudinal strain maps obtained by: (a) the direct method, the Gaussian method with a span of (b) 4 pixels, (c) 7 pixels, and (d) 14 pixels for the FW50 specimen (in μm/m).

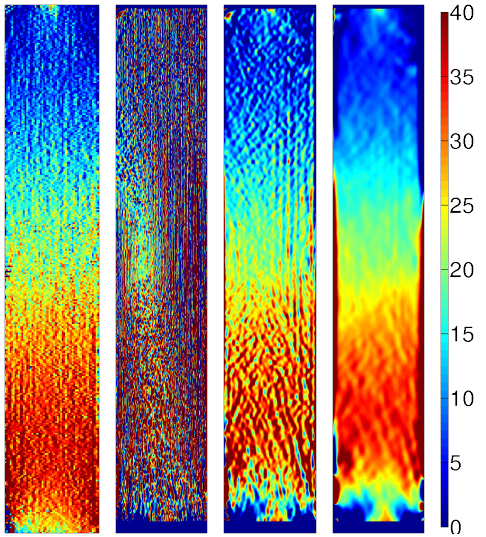

Figure 2.9: Equivalent transverse strain maps obtained by: (a) the direct method, the Gaussian method with a span of (b) 4 pixels, (c) 7 pixels, and (d) 14 pixels for the FW50 specimen (in μm/m).

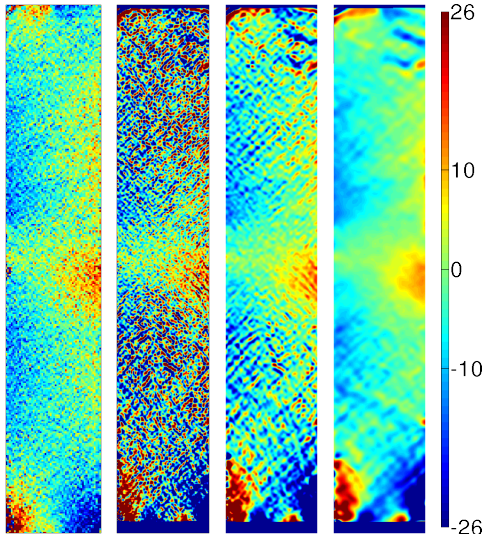

Figure 2.10: Equivalent shear strain maps obtained by: (a) the direct method, the Gaussian method with a span of (b) 4 pixels, (c) 7 pixels, and (d) 14 pixels for the FW50 specimen (in μm/m).

2.2.2 Unwrapping

Because the phase maps are wrapped between $[-\pi, +\pi]$, the 2π jumps need to be removed as shown in Fig. 2.11. For a two dimensional phase field, the unwrapped phase φ is equal to the wrapped phase ψ modulo 2π [161]:

$$\varphi(x, y) = \psi(x, y) + 2k\pi, \quad k \in \mathbb{Z} \tag{2.34}$$

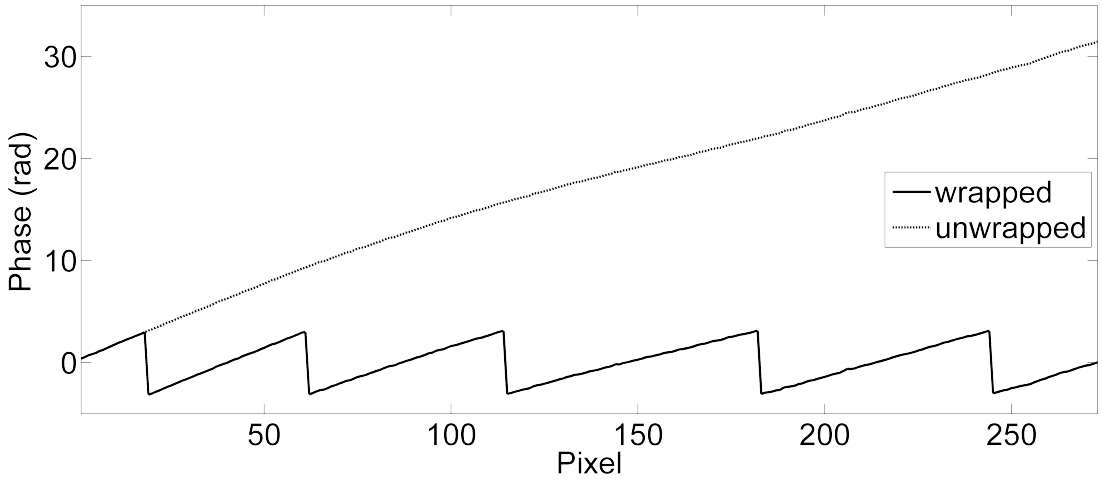

Figure 2.11: Unwrapping procedure for a one dimensional example.

This problem has been extensively studied because of the wide variety of phase-based techniques (sonar, MRI, ...) [162–166]. For this work, there were several requirements for the algorithm selection:

– Fast: a few seconds on a normal computer,
– Memory efficient: less than 2 Gb RAM for 100k data points,
– Robust to noise,
– Robust to corrupted data.

The algorithm presented in [167] respects the requirements. It is based on energy minimization using graph-cuts to solve a max-flow/min-cut graph. Another algorithm which respects the requirements is presented in [168]. This method is based on unwrapping points with high reliability values first by not following a continuous path. Both these algorithms work well with the data from this work but only the first one has been used here.

2.2.3 Filtering and numerical differentiation

Depending on the noise level present in the experimental measurements, numerical differentiation may require smoothing. Many algorithms have been developed to smooth and numerically

differentiate based on different techniques such as: global polynomial fitting [149], finite elements [169], and local polynomial fitting (diffuse approximation [169, 170] or Savitzky-Golay smoothing differentiation [171–174]). If one needs to keep high spatial frequency evolution in the strain fields, smoothing is not recommended. Nonetheless, among the local polynomial fitting algorithms, Savitzky-Golay is the fastest. For small smoothing radii, the difference from the diffuse appoximation is small.

In this work, a simple centred finite difference algorithm has been used. It computes the derivative of a 1-dimensional second order polynomial fit using three points. The formula is given in (2.35). It is possible to use this simple algorithm with experimental data here because deflectometry has a very good signal-to-noise ratio as explained later, eliminating the need for smoothing.

$$\frac{\partial}{\partial x} f(n,m) \simeq \frac{f(n+1,m) - f(n-1,m)}{x(n+1,m) - x(n-1,m)} \tag{2.35}$$

where n represents the data points along x and m along y.

2.3 Specimen preparation

As the useful reflection from the sample is the specular one, it is necessary to prepare the sample which is naturally both diffusive and specular. To obtain this mirror like surface (flat and specularly reflective), a gel-coat is applied as described in [175]. The sample prepation is detailed in the following subsections. As some of the chemical products used in this process are irritant or corrosive, glasses, gloves and a labcoat must be worn during the process. Also the gloves help to keep the glass panel and samples clean from any fingerprints. The required equipment is nitrile gloves, safety glasses, lab coat, standing knife, a glass panel, acetone, a plastic cup, a mixing stick, *SD SurfClear* resin, *SR SurfClear* hardener, and *Poudre de graphite* graphite powder, all last three marketed by Sicomin.

2.3.1 Preparation

Clean any resin from the glass panel with a blade from a standing knife. Then use some acetone to make sure the glass is clean and free of greasy marks. Wipe also the surface of the specimen on which the resin will be applied with some acetone. To improve the adhesion of the resin on the composite, the samples can be subjected to mild abrasive sand blasting.

2.3.2 Release agent

The *Hi temp paste wax* (from Finish care) was used as a release agent to help in debonding the cured resin from the glass panel. Use a soft cloth to take a small amount of the release agent and spread it over the whole plate. With the cloth, wipe it to have a smooth surface. Repeat these steps several times. It must be noted that any stains present on the glass will be transferred onto the reflective coating, therefore corrupting the measurements.

2.3.3 Mixing epoxy resin, hardener and graphite powder

The *SurfClear* resin is a mix between the *SD SurfClear* resin and the *SR SurfClear* hardener. This resin is normally transparent but can be opacified by adding mineral inert charges like graphite powder. The proportions for the resin and hardener are 100:38 in mass. The powder manufacturer recommends a concentration between 20 and 70 grams for 100 g of mixed resin. It has been found that the best concentration for the graphite powder is around 30 g to keep a good fluidity and provide enough opacity. To cover a 300 mm by 400 mm plate, 75 g of resin, 28.5 g of hardener and 31 g of graphite powder are necessary.

Mix everything in the plastic cup using a flat stick until a smooth paste is obtained. Then leave the mix for 5 to 10 minutes to eliminate trapped air bubbles. It is important to respect some working conditions, the temperature must be between 20 °C and 35 °C and remain constant during the whole process. The humidity must be lower than 70%.

2.3.4 Applying the resin

Pour the resin onto the sample and spread it over to cover the whole specimen by tilting the sample.

2.3.5 Applying the sample

First, apply one of the longest edges onto the resin and then push the plate by pressing down from the first edge towards the opposite side. Gather the resin near the corners in order to make sure they are also coated. Squeeze the air bubbles out by pressing from the centre toward the edges. Lift the glass panel, look under it for bubbles. Squeeze the spotted bubbles out.

2.3.6 Curing

The resin manufacturer recommends the following curing cycle:

1. time before curing: 24 hours at room temperature
2. curing: minimum 12 hours @ 40°C, optimum 8 h @ 60°C

Unfortunately, because of a mismatch in thermal coefficients of the resin and composite, a slight bend can be observed. Therefore, room temperature curing is preferred. It can take up to 4 days depending on the temperature and ambient humidity. After one month, acetone can be used on the resin without affecting its reflectivity.

2.3.7 Finishing

Release the specimen from the glass panel by sliding the standing knife between the cured resin and the glass. Trim the edges using a grinding wheel but leave 1 mm all around the sample. Because the camera is focused on the grid, the edges of the reflective coating are not in the sharpness zone, they are therefore blurred in the image. Leaving an extra-edge of gel-coat around the sample allows to obtain good quality measurements to the very edges of the sample.

2.3.8 Cleaning

To clean tools covered by **uncured** resin, simply use some paper and acetone to wipe it off. For **cured** resin, use a knife.

2.3.9 Removing the coating

Ease of coating removal depends on the sample roughness. Start by the resin on the edges of the specimen using a Stanley knife and then just lift the film of resin from the surface. If some resin is still stuck on the surface, carefully pass the blade along the resin-composite interface.

2.3.10 Effect of the coating on the stiffnesses

Because the coating has a non-zero stiffness, it may have an effect on the mechanical properties of the structure. This effect can be studied using Classical Lamination Theory (CLT). It will allow to obtain the global homogeneous properties of the laminate, knowing the lay-up and the

plies' material properties. CLT is based on the Love-Kirchhoff theory but with additional assumptions [176]. It is assumed that there is a perfect bonding between layers and out-of-plane stresses are negligible with respect to in-plane components. Also the plate thickness is constant over the whole area and the plate is subjected to small displacements.

From the Love-Kirchhoff theory, the (u, v, w) displacement components of a point are calculated relative to the mid-plane displacement (u_0, v_0, w_0) components and through-thickness position z:

$$\begin{cases} u(x,y,z) = u_0(x,y) - z\dfrac{\partial w_0(x,y)}{\partial x} \\ v(x,y,z) = v_0(x,y) - z\dfrac{\partial w_0(x,y)}{\partial y} \\ w(x,y,z) = w_0(x,y) \end{cases} \tag{2.36}$$

The related strain tensor is:

$$\begin{cases} \varepsilon_x(x,y,z) = \dfrac{\partial u}{\partial x} & = \dfrac{\partial u_0}{\partial x} - z\dfrac{\partial^2 w_0}{\partial x^2} & \varepsilon_{xz}(x,y,z) = 0 \\ \varepsilon_y(x,y,z) = \dfrac{\partial v}{\partial y} & = \dfrac{\partial v_0}{\partial x} - z\dfrac{\partial^2 w_0}{\partial y^2} & \varepsilon_{yz}(x,y,z) = 0 \\ \varepsilon_s(x,y,z) = \dfrac{\partial u}{\partial y} + \dfrac{\partial v}{\partial x} & = \dfrac{\partial u_0}{\partial y} + \dfrac{\partial v_0}{\partial x} - 2z\dfrac{\partial^2 w_0}{\partial x \partial y} & \varepsilon_{zz}(x,y,z) = 0 \end{cases} \tag{2.37}$$

This formulation implies the following consequences:

– Straight lines normal to the mid-surface remain straight after deformation (displacement linear in z),
– Straight lines normal to the mid-surface remain normal to the mid-surface after deformation (no through-thickness shear components),
– The thickness of the plate does not change during deformation ($\varepsilon_{zz} = 0$).

By introducing vectors $\{\varepsilon_0\}$ and $\{\kappa\}$, respectively mid-plane strains and curvatures, (2.37) can be rewritten as:

$$\{\varepsilon\} = \{\varepsilon_0\} + z\{\kappa\} \tag{2.38}$$

with $\{\varepsilon_0\}$ and $\{\kappa\}$ being:

$$\{\varepsilon_0\} = \begin{pmatrix} \varepsilon_x^0 \\ \varepsilon_y^0 \\ \varepsilon_s^0 \end{pmatrix} \qquad \{\kappa_0\} = \begin{pmatrix} \kappa_x \\ \kappa_y \\ \kappa_s \end{pmatrix} = \begin{pmatrix} -\dfrac{\partial w_0}{\partial x} \\ -\dfrac{\partial w_0}{\partial y} \\ -2\dfrac{\partial^2 w_0}{\partial x \partial y} \end{pmatrix}$$

The constitutive equation, also known as the generalized Hooke's law, is:

$$\{\sigma\} = [Q]\{\varepsilon\} \tag{2.39}$$

$[Q]$ is called the stiffness matrix.

Combining (2.39) and (2.38), one has:

$$\{\sigma\} = [Q]\{\varepsilon_0\} + z[Q]\{\kappa\} \tag{2.40}$$

The force, $\{N\}$, and moment, $\{M\}$, resultants are calculated by integrating the stresses over the thickness of the laminate. Combining with (2.40), one has:

$$\begin{cases} \{N\} = \int_{-\frac{h}{2}}^{\frac{h}{2}} \{\sigma\} dz & = \int_{-\frac{h}{2}}^{\frac{h}{2}} [Q]\{\varepsilon_0\} + z[Q]\{\kappa\} dz \\ \{M\} = \int_{-\frac{h}{2}}^{\frac{h}{2}} z\{\sigma\} dz & = \int_{-\frac{h}{2}}^{\frac{h}{2}} z[Q]\{\varepsilon_0\} + z^2[Q]\{\kappa\} dz \end{cases} \tag{2.41}$$

If all plies have the same angle, the laminate is considered homogeneous through the thickness and the stiffness matrix is constant within the whole laminate. (2.41) can be written as:

$$\begin{cases} \{N\} = h[Q_h]\{\varepsilon_0\} \\ \{M\} = \dfrac{h^3}{12}[Q_h]\{\kappa\} \end{cases} \tag{2.42}$$

where $[Q_h]$ is the stiffness matrix of the homogeneous laminate.

If the laminate consists of plies with different orientations, the stiffness matrix is constant within each ply. (2.41) can be written as:

$$\begin{cases} \{N\} = \sum_{k=1}^{N} [\overline{Q}_k] \int_{h_{k-1}}^{h_k} \{\varepsilon_0\} + z\{\kappa\} dz & = \sum_{k=1}^{N} [\overline{Q}_k] \left((h_k - h_{k-1})\{\varepsilon_0\} + \frac{1}{2}(h_k^2 - h_{k-1}^2)\{\kappa\} \right) \\ \{M\} = \sum_{k=1}^{N} [\overline{Q}_k] \int_{h_{k-1}}^{h_k} z\{\varepsilon_0\} + z^2\{\kappa\} dz & = \sum_{k=1}^{N} [\overline{Q}_k] \left(\frac{1}{2}(h_k^2 - h_{k-1}^2)\{\varepsilon_0\} + \frac{1}{3}(h_k^3 - h_{k-1}^3)\{\kappa\} \right) \end{cases} \tag{2.43}$$

with $[\overline{Q}_k]$ the ply stiffness matrix expressed in the global coordinate system, N the number of plies and h_k the distance of the k^{th} interface to the midplane as illustrated in Fig. 2.12.

To obtain $[\overline{Q}_k]$, a simple matrix rotation is necessary. It transforms the stiffness matrix expressed in the ply coordinate system $[\tilde{Q}_k]$ into its expression in the global coordinate system.

$$[\overline{Q}_k] = [T_\theta][\tilde{Q}_k][T_\theta]^t; \tag{2.44}$$

Figure 2.12: Illustration for the h_k distances in (2.43).

with θ the angle between the ply coordinate system and the global coordinate system as illustrated in Fig. 2.13 and $[T_\theta]$ the rotation matrix expressed as:

$$[T_\theta] = \begin{pmatrix} \cos^2\theta & \sin^2\theta & -2\cos\theta\sin\theta \\ \sin^2\theta & \cos^2\theta & 2\cos\theta\sin\theta \\ \cos\theta\sin\theta & -\cos\theta\sin\theta & \cos^2\theta - \sin^2\theta \end{pmatrix}$$

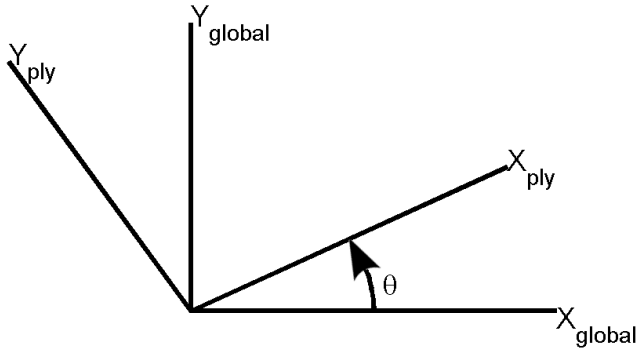

Figure 2.13: Illustration of the orientation of the θ angle.

$[\tilde{Q}_k]$ is the inverse of the compliance matrix $[\tilde{S}_k]$ which is written as:

$$[\tilde{S}_k] = \begin{pmatrix} \frac{1}{E_{11}} & -\frac{\nu_{12}}{E_{11}} & 0 \\ -\frac{\nu_{12}}{E_{11}} & \frac{1}{E_{22}} & 0 \\ 0 & 0 & \frac{1}{G_{12}} \end{pmatrix}$$

with E_{11} and E_{22}, respectively, the longitudinal and transverse Young's modulus, ν_{12} major Poisson's ratio, and G_{12} the shear modulus.

(2.43) can be written in matrix form:

$$\begin{pmatrix} \{N\} \\ \{M\} \end{pmatrix} = \begin{pmatrix} [A] & [B] \\ [B] & [D] \end{pmatrix} \begin{pmatrix} \{\varepsilon_0\} \\ \{\kappa\} \end{pmatrix} \tag{2.45}$$

where

$$\begin{cases} [A] = \sum_{k=1}^{N} [\overline{Q}_k] \left(h_k - h_{k-1}\right) \\ [B] = \frac{1}{2} \sum_{k=1}^{N} [\overline{Q}_k] \left(h_k^2 - h_{k-1}^2\right) \\ [D] = \frac{1}{3} \sum_{k=1}^{N} [\overline{Q}_k] \left(h_k^3 - h_{k-1}^3\right) \end{cases} \tag{2.46}$$

$[A]$, $[B]$, and $[D]$ are 3x3 matrices and are called, respectively, extension, extension-bending, and bending stiffness matrices. They are expressed in the global coordinate system. Unlike traditional materials, laminated structures present a unique mechanical behaviour: couplings can exist between extension, bending, and shearing modes. For a symmetrical laminate, the extension-bending stiffness matrix, $[B]$, vanishes. For a balanced laminate, the extension-shear coupling terms, A_{16} and A_{26}, are zero. A balanced laminate has an equal number of plies with $+\theta$ and $-\theta$ orientations. The bending-twist coupling terms, D_{16} and D_{26}, are zero for cross-ply or unidirectional laminates and can be neglected for laminates with "many" layers [177].

The *SurfClear* resin is an isotropic material and its properties are summarized in Tab. 2.4. Using the UD material properties from Tab. 2.5 and the lay-up used experimentally $[0/45/\text{-}45/90]_{4s}$, an analysis based on CLT has been performed for 4 cases: without coating, with a 0.1 mm, 0.2 mm, and 0.3 mm thick coating. The results are presented in Tab. 2.6.

Young's modulus	Poisson's ratio	Shear modulus
3.36 GPa	0.3	1.29 GPa

Table 2.4: *SurfClear* resin mechanical properties from the manufacturer's datasheet.

The effect of the coating is very small (less than 3%) even for the thicker resin layer case. The thickness of the coating used for the experiments was evaluated at 0.15 mm giving a modification of the stiffness components smaller than 1%. It can therefore be considered that the coating has a negligible effect on the global stiffnesses.

E_{xx}	E_{yy}	E_{zz}	G_{xy}	G_{xz}	G_{yz}	ν_{xy}	ν_{xz}	ν_{yz}
161 GPa	11.38 GPa	11.38 GPa	5.17 GPa	5.17 GPa	3.98 GPa	0.32	0.32	0.436

Table 2.5: Material properties of cured Hexcel IM7-8552 UD carbon-fibre pre-preg [178].

Coating thickness (mm)	Units	D_{xx}	D_{yy}	D_{xy}	D_{ss}	D_{xs}	D_{ys}
Without	(Nm)	423.61	310.57	115.51	123.52	9.42	9.42
0.1	(%)	0.51	0.70	0.57	0.61	0.00	0.00
0.2	(%)	1.35	1.84	1.53	1.59	0.00	0.00
0.3	(%)	2.51	3.42	2.86	2.96	0.00	0.00

Table 2.6: Influence of the coating thickness on the homogenized stiffnesses.

2.3.11 Opaque resin improvements

In [175] the resin was used without any additives so it was transparent. Here, it has been opacified to reduce the parasitic back-reflections, both specular and diffusive, from the resin-composite interface as shown in Fig. 2.14a. If a 100 % opaque resin is used, these back-reflections are suppressed as shown in Fig. 2.14b. It must be noted that for certain configurations, the parasitic back-reflections can totally blur the grid image.

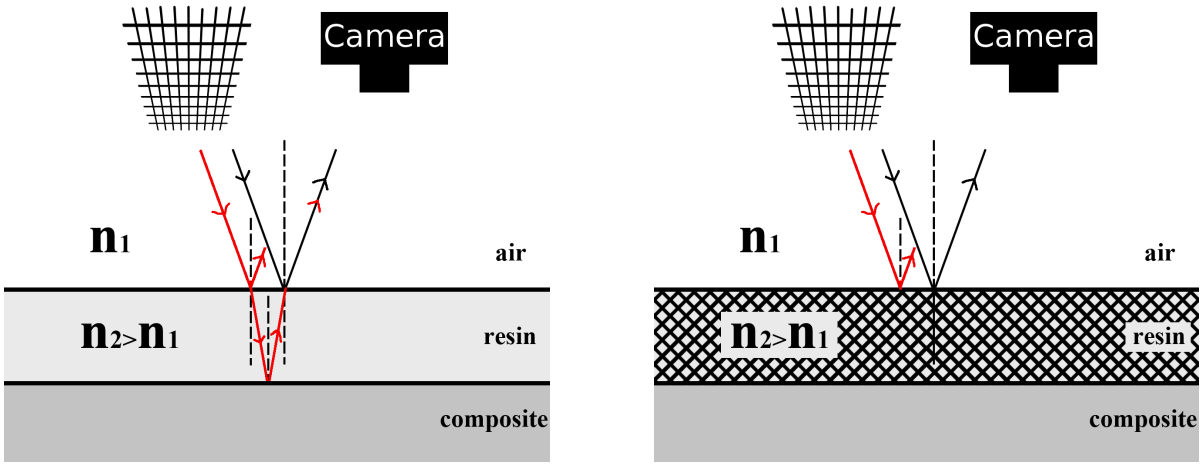

(a) Transparent resin

(b) Opaque resin

Figure 2.14: Improvements in terms of parasitic back-reflection suppression: (a) transparent resin and (b) opaque resin.

Here, the resin used is not 100 % opaque but it improved the results. Fig. 2.15 presents experimental evidence of the improvements brought by the opaque resin for the same sample being coated a first time with the transparent resin and then with the opaque resin for a sample with a single 30 mm long delamination across the whole width and located in the midplane, called FW30. In Figs. 2.15a, 2.15c, and 2.15e, a pattern is visible in the centre of the sample and not

any more with the opaque resin as shown in Figs. 2.15b, 2.15d, and 2.15f. This pattern comes from creases in the release film used during manufacturing that engraved lines in the sample. This shows that any imperfections on the composite surface will affect the final results much less with the opaque resin.

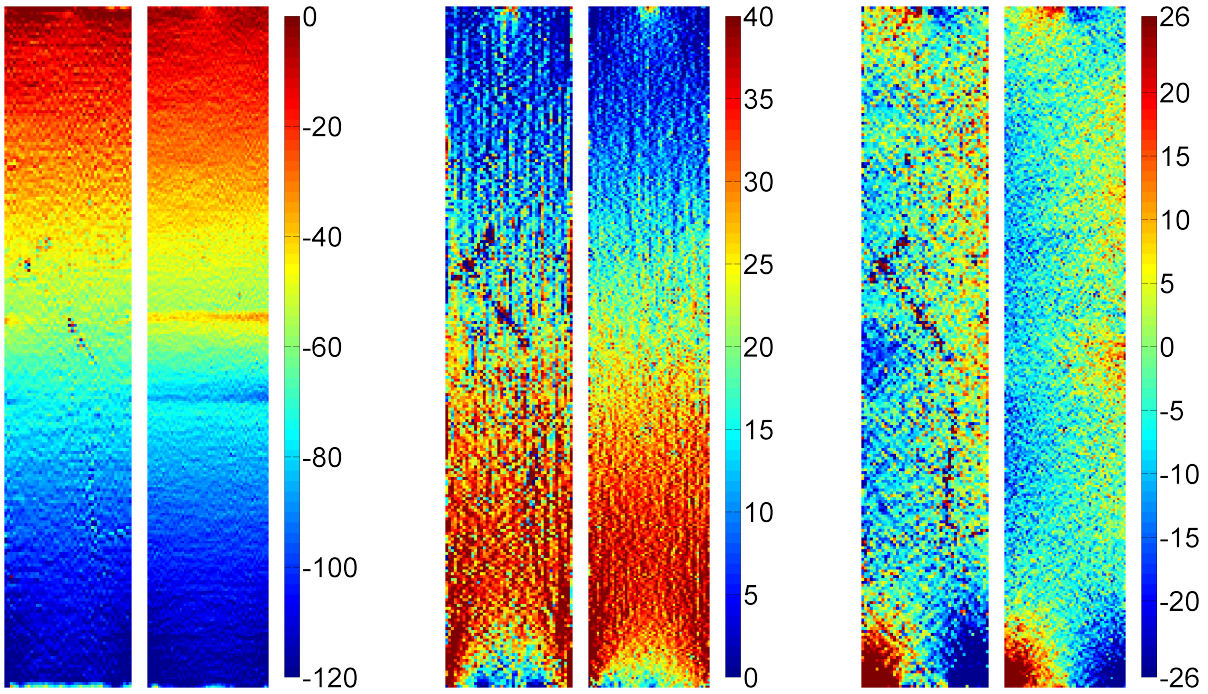

(a) Transp. (b) Opaq. (c) Transp. (d) Opaq. (e) Transp. (f) Opaq.

Figure 2.15: Strain maps for the FW30sample coated with the transparent resin (Transp.) or the opaque resin (Opaq.) in µm/m. (a) and (b) present the longitudinal strain maps, (c) and (d) the transverse strain maps, and (e) and (f) the shear strain maps.

2.4 Grid

The remarkable resolution of grid methods depends directly on the printing quality of the grid. There are several parameters to control in order to produce a grid which maximizes the quality of the measurements. First, during the grid generation, one must make sure that an integer number of printed dots will be used per half pitch or else an aliasing may be visible in the printed grid. For this purpose, the printing resolution must be known and the grid pitch adjusted accordingly.

The second issue concerns the paper, as it usually shrinks or stretches with changing ambient conditions. It is recommended to store and use the grids under a controlled environment in terms

of hygrometry and temperature. Even though some papers are certified to withstand weather conditions, they will change in size with changing ambient conditions. Also, a compromise on the quantity of ink during printing must be achieved to have a good contrast but not wet the paper. A last concern is the quality of the printing machine [179]. References of successfully used printers are available in [160, 180].

2.5 Resolution and spatial resolution

As defined in [181], the resolution is *the smallest change in the physical property that can be reliably measured*. For the current type of measurement, it is strongly affected by the level of noise arising from different sources. It must be noted that the noise is a space and time varying value. A first source is the CCD sensor: it converts photons into electron charges which are then amplified, sampled and digitized. A review on noise sources from CCD sensors is available in [182]. A second source is the lens: it focuses light from the object to the camera sensor. As the lens is not perfect (shape error and variation of glass index), the lens fails to perfectly focus the light blurring the image of the viewed object. A third source is the change of density of the air. It will cause a ray of light to be deflected from its normal path introducing a "virtual" displacement of the object. The previous sources are common for all optical measurement techniques, the following ones are more applicable to grid methods. A fourth source is the grid quality. A last source is the parasitic back-reflections from the sample.

There are several definitions for the spatial resolution: frequency or distance based. The distance approach considers that the spatial resolution is the smallest distance between two independent measurement points. The frequency approach defines the spatial resolution as *one-half of the period of the highest frequency component contained in the frequency band of the encoded data* [181]. To evaluate the spatial resolution, a 2D Dirac function can be used as input data for the whole data processing. The spatial resolution can be defined in practice as the largest dimension of the area where points are affected by more than a threshold. This approach has the advantage of being applicable to more complex post-processing as analytical expressions are generally not available [183]. Semantically, a high resolution corresponds to a low resolution value and vice-versa. This is also true for spatial resolution.

To evaluate the phase noise level, two images can be taken at rest. From them, the phase maps

are obtained as described earlier and their standard deviation is computed giving σ_{φ_x} and σ_{φ_y}.

$$\sigma_\varphi = \max\left(std(\Delta\varphi_x), std(\Delta\varphi_y)\right) \tag{2.47}$$

Averaging over a number of images helps to reduce the noise level as shown in Fig. 2.16. To generate this chart, 200 pictures were taken at rest and the standard deviation of the phase difference was computed for different numbers of image averaging. Using 20 pictures reduces the phase noise level by a factor of 3 (0.011 rad). The reason why the noise level in phase is not reduced when averaging over more than 20 frames is unknown. Averaging over 100 frames should divide the noise level in phase by $\sqrt{100} = 10$.

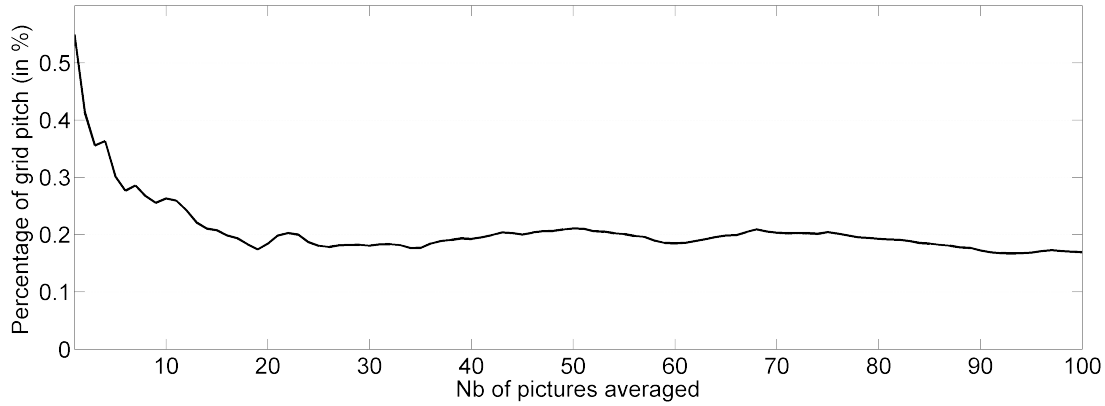

Figure 2.16: Influence of the number of pictures on the noise level in phase.

In deflectometry, the sensitivity, denoted *s*, is defined as [1]:

$$s = \frac{4\pi h}{p} \tag{2.48}$$

This parameter corresponds to the link between the phase difference and the local slope as expressed in (2.17). Using this sensitivity parameter, one can convert the phase noise level into slope:

$$\sigma_S = \frac{\sigma_\varphi}{s} \tag{2.49}$$

Slopes are linked to strains by their derivatives and the thickness of the specimen:

$$\varepsilon = \frac{t}{2}\frac{\partial S}{\partial x} \tag{2.50}$$

Because discrete data are used and because direct finite difference differentiation is used without any smoothing, the strain noise level is related to the slope noise level by the following

1. Simplified expression for $L, H \ll h$, see Section 2.1.1

expression:

$$\sigma_\varepsilon = \sqrt{2}\frac{t}{2}\frac{\sigma_S}{dx} \tag{2.51}$$

It must be noted that, in this case, dx is the spatial resolution. The final equation is:

$$\sigma_\varepsilon = \sqrt{2}\frac{t}{4h}\frac{p}{2\pi dx}\sigma_\varphi \tag{2.52}$$

with t being the specimen thickness, h the distance grid-sample, p the grid pitch, dx the data point dimension, and σ_φ the phase noise level. With the parameters from Tab. 2.1 (h = 1.66 m, t = 4 mm, p = 1.5 mm, and dx = 0.75 mm) and a phase noise level of 0.011 rad, the strain noise level is:

$$\sigma_\varepsilon = 2.8\ \mu m/m \tag{2.53}$$

This noise level is very low for such a large number of simultaneously acquired data points (close to 20000).

For the in-plane grid method [184,185], the grid is bonded onto the sample and directly observed by the camera. The phase modulation is 2π when the grid moves by one pitch, denoted p, leading to (2.54) linking the phase difference φ and the displacement u.

$$u = \frac{p}{2\pi}\varphi \tag{2.54}$$

From (2.54), the strain noise level can be expressed as:

$$\sigma_\varepsilon = \frac{du}{dx} = \sqrt{2}\frac{p}{2\pi dx}\sigma_\varphi = 2400\mu m/m \tag{2.55}$$

The difference in resolution between in-plane and bending grid method comes from the reflection. It introduces a term, $t/4h$, which allows the resolution to be modified independently from the spatial resolution in the case of deflectometry. Since t is usually much smaller than h, several orders of magnitude can be gained in strain resolution.

Another way to decrease the noise level would be to increase the number of pixels to sample a period. Unfortunately, this lowers the spatial resolution. Because the CCD sensor has a fixed number of pixels, increasing the sampling will decrease the number of independent data points. Because high spatial resolution was sought here, this has not been considered.

2.6 Conclusion

Deflectometry was used in the configuration where the camera is beside the grid to obtain bending strain fields, eliminating the need for reconstructing missing data. A formula was derived to obtain the slope fields from the phase grid shifts. It takes into account the spatial dependence of the sensitivity caused by the reflection. Its effect was evaluated in the case of small samples and found to be negligible. The strain fields were obtained after differentiation of the measured slope fields. No smoothing was used in data processing thanks to the high signal-to-noise ratio. The strain resolution was evaluated with the parameters used experimentally and found to be very low, 3 μm/m. The spatial resolution is also very small, 1 mm for a 50 by 250 mm beam. The specimen preparation was detailed and the improvements coming from the resin opacity were presented. Guidelines were given for printing the grids. This technique proved to be very sensitive. It is remarkably inexpensive compared to interferometric techniques and much easier to use. It is however restricted to flat mirror-like specimen surfaces.

CHAPTER 3

APPLICATION TO BEAMS

In this chapter, the experimental technique detailed in the previous chapter is applied to beam samples. First the lay-up and the material properties are summarized. Then the different types of tested samples are exposed as well as the experimental configuration followed by the finite element models. Finally the experimental results are reviewed.

3.1 Material

The samples were made from Hexcel IM7-8552 carbon-fibre/epoxy pre-preg cured in autoclave in a vacuum bag. The unidirectional material properties are summarised in Tab. 3.1 [178]. The properties of the material used here have been previously checked to correspond the ones found in [178]. The thickness was also measured and found to be 0.125 mm. It is the constituent of the 32-plies quasi isotropic lay-up $[0/45/\text{-}45/90]_{4s}$ panel used here.

E_{xx}	E_{yy}	E_{zz}	G_{xy}	G_{xz}	G_{yz}	ν_{xy}	ν_{xz}	ν_{yz}
161 GPa	11.38 GPa	11.38 GPa	5.17 GPa	5.17 GPa	3.98 GPa	0.32	0.32	0.436

Table 3.1: Material properties of cured Hexcel IM7-8552 UD carbon-fibre pre-preg [178].

3.2 Samples

Several types of samples were used for this study depending on the damage. The samples were cut from larger plates using a diamond saw and two samples have been manufactured for each damage case. Their dimensions are 250 mm in length, 50 mm in width and 4 mm in thickness.

3.2.1 Undamaged

The undamaged samples will be used as a reference.

3.2.2 Artificial delaminations

In order to test the sensitivity of the measurement technique and to validate the numerical model of delaminations, some artificial delaminations have been introduced: two simple cases with a single delamination and two more complex cases with several delaminations through the thickness.

3.2.2.1 Single delamination

Two cases with one artificial delamination have been studied: 50 mm and 30 mm-long delaminations located in the mid-plane and centred longitudinally. These delaminations have been created by inserting a single layer of 25 µm thick PTFE film between two adjacent plies. The samples will be denoted FW50 and FW30 (FW stands for "Full Width"). They are illustrated in Figs. 3.1 and 3.2.

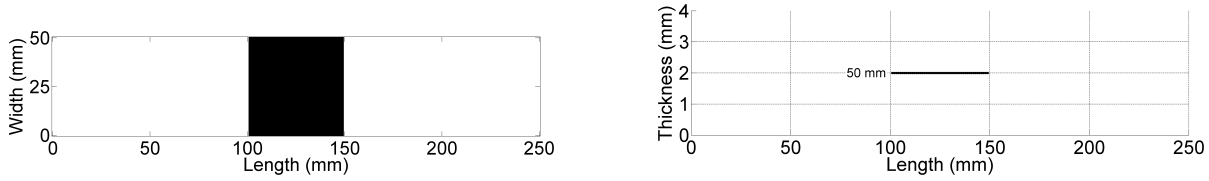

(a) Top view (b) Front view

Figure 3.1: Schematic views of the FW50 sample: (a) top view and (b) front view.

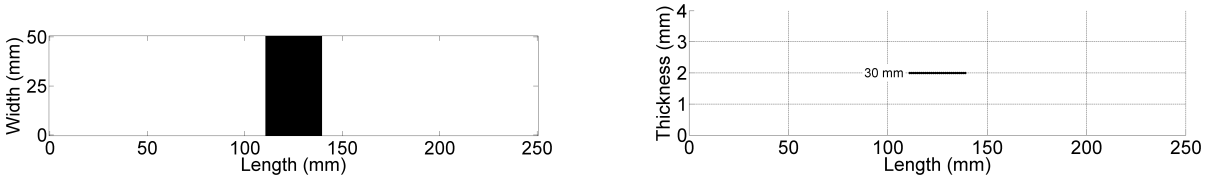

(a) Top view (b) Front view

Figure 3.2: Schematic views of the FW30 sample: (a) top view and (b) front view.

3.2.2.2 Multiple delaminations

The first case consists of 3 delaminations through the thickness, arranged in an A shape with increasing length, as shown in Fig. 3.3. The second case contains 7 delaminations as shown in Fig. 3.4. After the first tests with the single delamination specimen, it appeared that a single layer of PTFE film did not work well as a delamination if not forced to open up. Therefore two layers of film were used to simulate the delamination for these samples. To keep the insert the thinnest possible, a thinner film was used, an 8 µm-thick ETFE film but opening up the delaminated areas was still required. For these samples, the smallest delamination has been positioned the closest to the studied surface. The samples with three full-width delaminations in an A shape will be called FW3A and the ones with 7, FW7A.

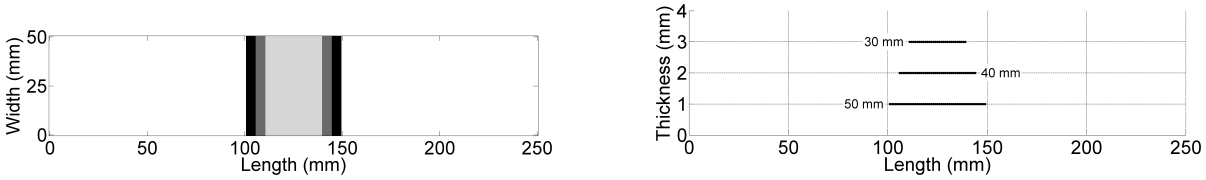

(a) Top view (b) Front view

Figure 3.3: Schematic views of the FW3A sample: (a) top view and (b) front view.

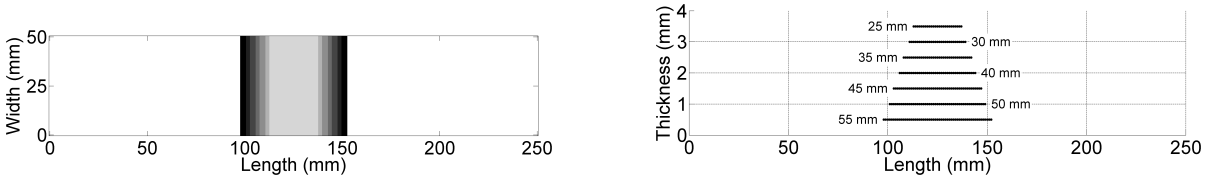

(a) Top view (b) Front view

Figure 3.4: Schematic views of the FW7A sample: (a) top view and (b) front view.

3.2.2.3 Experimentally manufactured delaminations

Experimentally simulating a delamination has been investigated for more than two decades as part of measuring the fracture toughness of composites [6, 20, 21, 186–191]. It is usually done using thin films of aluminium, PTFE, or Kapton combined with release agents. Depending on the opening mode, the inserts may or may not have an effect. For instance under mode I, any type of insert will reduce to nearly zero the load required to open up this delamination. For modes II and II, the shear strength of the resin-insert interface is too high compared to the applied shear stresses explaining why it is recommended to force the delamination to open [21]. Here, the delaminations have been opened manually by forcing a 0.1 mm shim into the specimen at the delamination interface. Figs. 3.5 to 3.7 present the results obtained from a finite element model compared to experimental results on the beams, before and after opening for the FW50 sample. The details of the FE model are given later in Section 3.4.

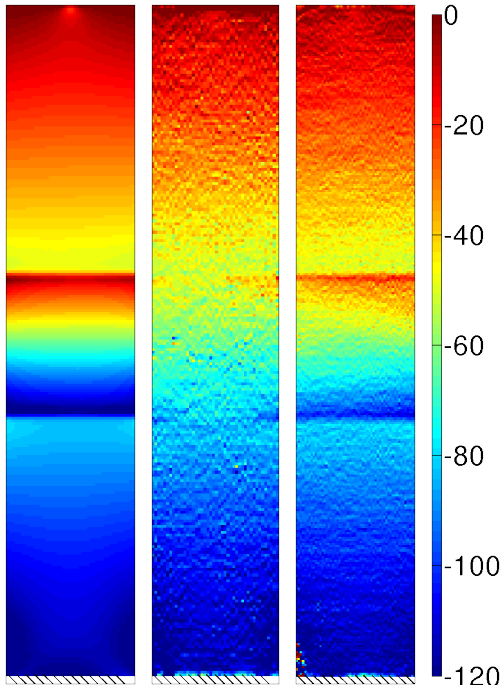

(a) FE (b) Before (c) After

Figure 3.5: Equivalent longitudinal strain maps for the FW50 sample in µm/m.

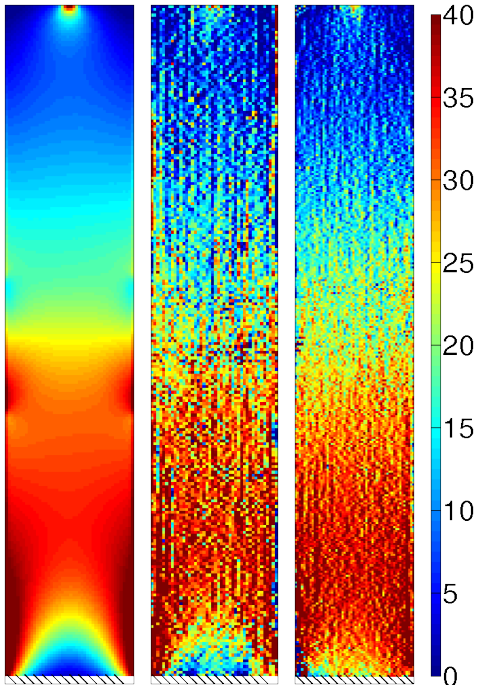

(a) FE (b) Before (c) After

Figure 3.6: Equivalent transverse strain maps for the FW50 sample in µm/m.

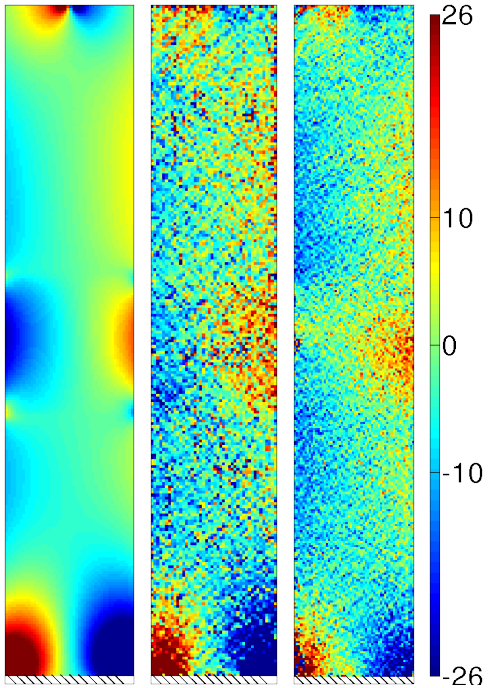

(a) FE (b) Before (c) After

Figure 3.7: Equivalent shear strain maps for the FW50 sample in µm/m.

Even though, the results after opening Fig. 3.5c are more similar to the FE predictions Fig. 3.5a, the correlation is not perfect Fig. 3.7. It can be explained by the fact that the experimental delamination is not acting as a perfect delamination even after the opening. Maybe the film is still sticking to the resin or there might be some friction between the plies and the film. This approach was followed in this work for all the specimens with artificial delaminations.

In order to help the delamination especially when it does not reach an edge, short beam shear tests could be performed as illustrated in Fig. 3.8. A test has been conducted on a sample containing a 30 mm square delamination located at the midplane as illustrated in Fig. 3.9. Initially, the delamination should have been centred but the film moved during lay-up and curing resulting in an asymmetric sample. This sample is called S30 as in Square 30 mm. Experimentally, this delamination has been simulated using two layers of 8 µm-thick ETFE film.

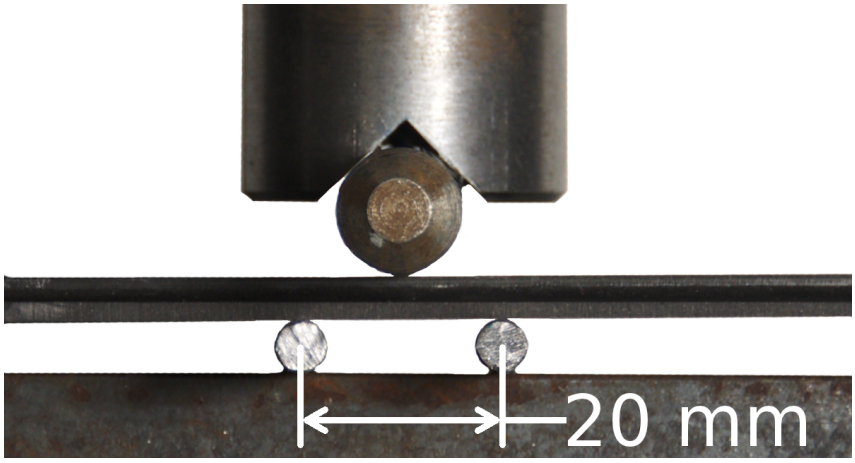

Figure 3.8: Photo of the set-up for the short beam shear test.

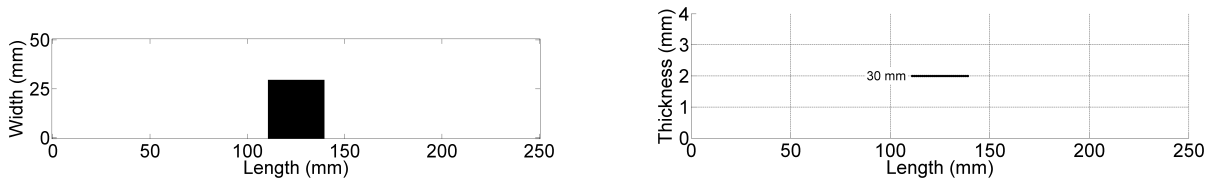

(a) Top view

(b) Front view

Figure 3.9: Schematic views of the S30 sample: (a) top view and (b) front view.

The span of the beam was 20 mm, its width 50 mm and its thickness 4 mm. Only the central part of the delamination was subjected to shear stresses as the delamination is 30 mm long and the span 20 mm. The test was stopped when a drop was visible on the load-displacement

curves accompagnied by the characteristic sound of delamination. Fig. 3.10 presents the load-displacement curve of the short beam shear test.

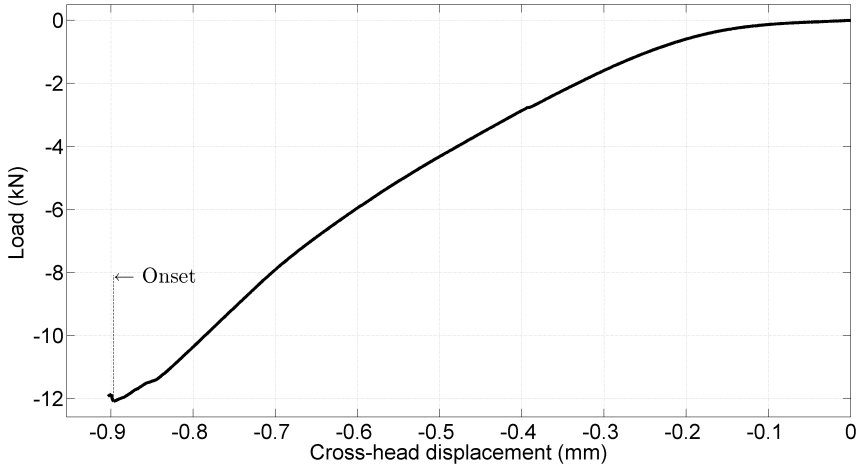

Figure 3.10: Load-displacement curve of the short beam shear test.

For the short beam shear test, the shear stress distribution is parabolic though the thickness. Its maximum at the midplane is related to the applied force F by:

$$\tau_{max} = \frac{3F}{4wh} \tag{3.1}$$

with w the width of the sample and h its thickness. From Fig. 3.10, the onset load is 12 kN and this gives an onset shear stress of 45 MPa. Even though it is lower than the value provided by the manufacturer, 137 MPa [192], it shows that the resin has a very good adherence to ETFE films. Reducing this adherence will allow to lower the onset load, lowering at the same time the local stress concentration at the supports.

Figs. 3.11 to 3.13 present the results from the FE models compared to the experimental results for the beam before and after the short beam shear test. The span of the beam for deflectometry was shorter for delamination assessment after shear testing. The reason is a difference in the experimental parameters (grid-sample distance, focal length and grid pitch) for the experiments before and after shear testing. The load for the shorter beam was increased to 6 N in order to present sufficient strain levels. It shows that loading artificially delaminated samples by short beam shear test helps to create a delamination without the risk of deforming the sample. Another advantage is the applicability to delaminations not accessible from the side.

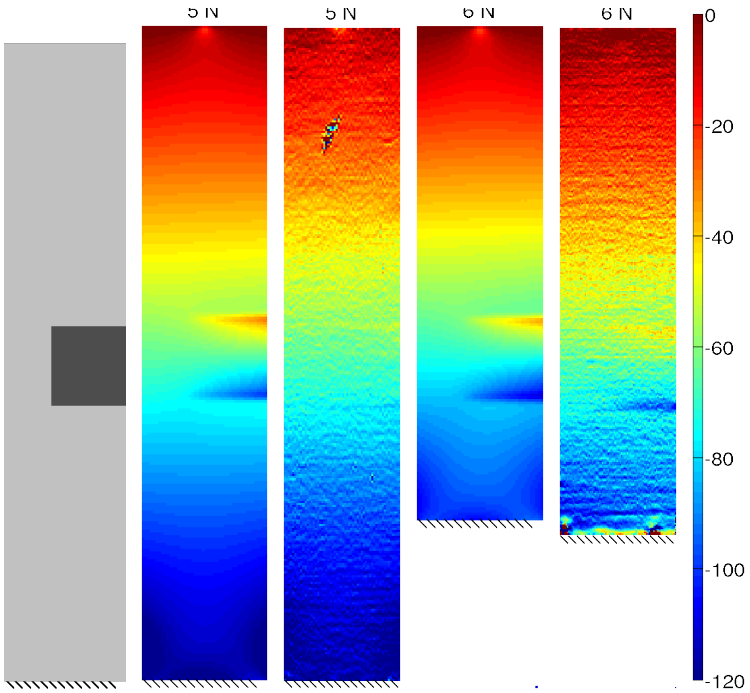

Figure 3.11: Equivalent longitudinal strain maps for the S30 sample in µm/m. Dark area in (a) corresponds to the delamination.

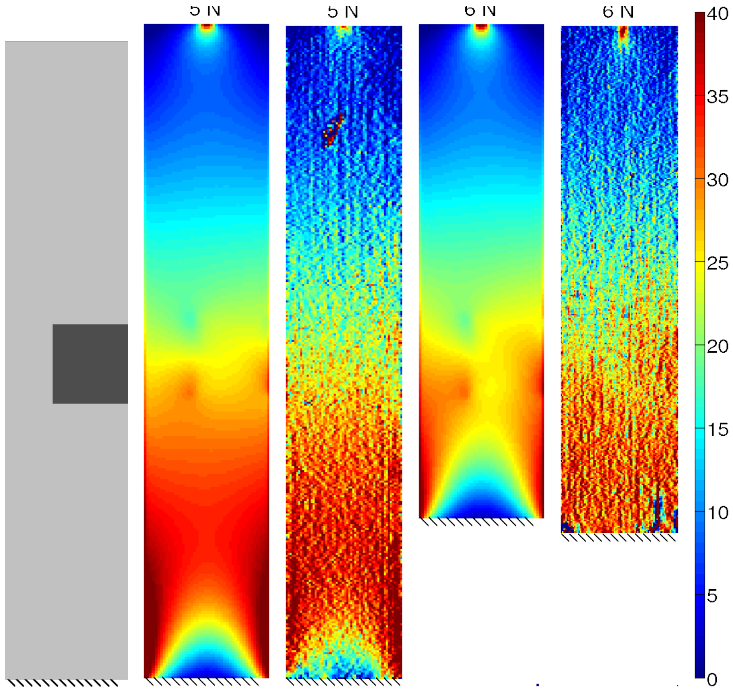

(a) Schem (b) FE (c) Before (d) FE (e) After

Figure 3.12: Equivalent transverse strain maps for the S30 sample in µm/m. Dark area in (a) corresponds to the delamination.

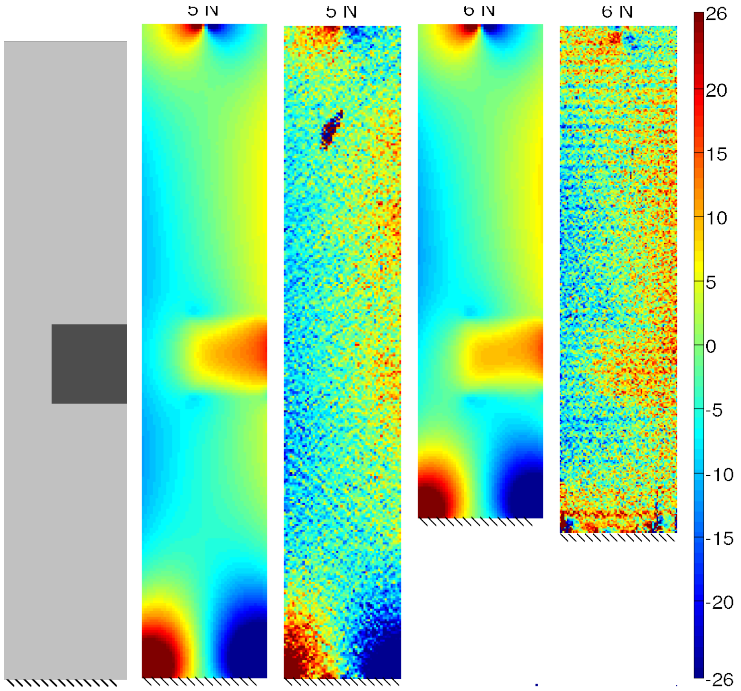

(a) Schem (b) FE (c) Before (d) FE (e) After

Figure 3.13: Equivalent shear strain maps for the S30 sample in µm/m. Dark area in (a) corresponds to the delamination.

3.2.3 Impacted

The beams were impacted while clamped between two steel plates, both containing a 40 mm-diameter cut-out, as detailed by the ASTM-D5628 standard in [193]. An illustration is presented in Fig. 3.14. It allowed the impactor to hit the sample and the sample to bend underneath. This led to a constraint of the delaminations inside the area of the cut-out and it explains why the delaminations did not spread further than 40 mm. For these samples, the studied surface is the impacted side where minimal visible damage can be seen. It was also selected because this is usually the only accessible side of an in-service component.

Figure 3.14: View of the top steel plate with the 40 mm diametre cut-out and the sample ready for impact.

3.2.3.1 Small impact tup, 15 mm radius hemi-sphere

One sample was impacted at 9.8 J (weight: 5.3 kg, impact velocity: 1.92 $m.s^{-1}$, drop height: 0.188 m) and another at 14.8 J (weight: 5.3 kg, impact velocity: 2.36 $m.s^{-1}$, drop height: 0.283 m). CT-scans from the sample impacted at 15 J have been obtained by reconstructing the volume with the software CT-PRO from 2356 pictures rotated by 0.15° and exposed for 250 ms. The tube current was 125 µA and the tube potential 200 kV. As the ply thickness is 0.125 mm and the voxel size 0.14 mm, one slice from the CT-scans is an average over more than one ply. Because of that, a voxel in Fig. 3.15b contains information from 3 plies, 0°, +45°, and -45° as presented in Fig. 3.15d. The three plies are visible with the 0° whiter band in the centre and the +45° and -45° sharp delimitations between dark and white areas. The black

zone in Fig. 3.15a reveals the location of the indent created by the impactor tup and between Figs. 3.15b and 3.15c, one can notice an increase of delaminated area. In Fig. 3.15c the delamination diameter is approximatively 40 mm showing that the boundary conditions limited the propagation of delaminations. The vertical lines visible in Fig. 3.15a are a numerical artefact from the CT-scans and do not indicate any change in fibre density. The samples impacted at 10 J will be called R15-10 and the one at 15 J, R15-15 (R15-15 as Radius 15 mm - 15 J).

Many authors have addressed the subject of delamination modelling, e.g. [104, 107, 194–196] and complete deplying has confirmed the type of damage obtained [6, 197]. Depending on the lay-up, the shape of the delaminated area varies but a global trend can be captured. Let us consider that the sample is impacted from the top as presented in Fig. 3.15. Because of the through-thickness compression under the point of impact, a dent is created (cf black disc in Fig. 3.15a). The sharp delimitations are matrix cracks within the plies following the fibre orientation and the dark areas are the delaminations as visible in Fig. 3.15b. This confirms the general understanding of the low-velocity impact process [8]. At a ply interface, two matrix cracks appear in the ply underneath parallel to the fibres on either side of the impact point. From these matrix cracks, a delamination initiates and the two matrix cracks delimit a zone at that ply interface where the delamination can grow. Its propagation is inhibited under the point of impact because of the through-thickness compression. It was stated previously that a voxel in Fig. 3.15c contains the -45° and +45° plies but 0° and 90° fibre cracks are also visible. This is explained by the fact that the specimen deformed with the impact as shown in Fig. 3.15e.

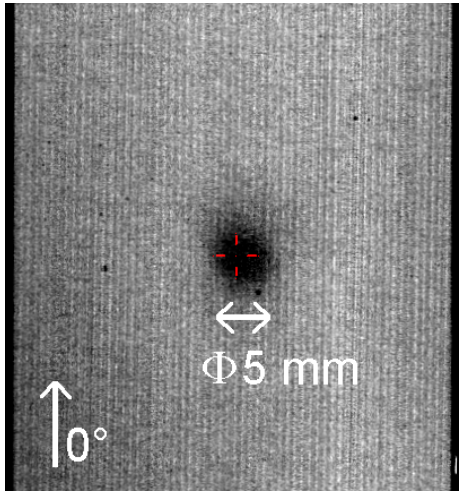

(a) Impact surface

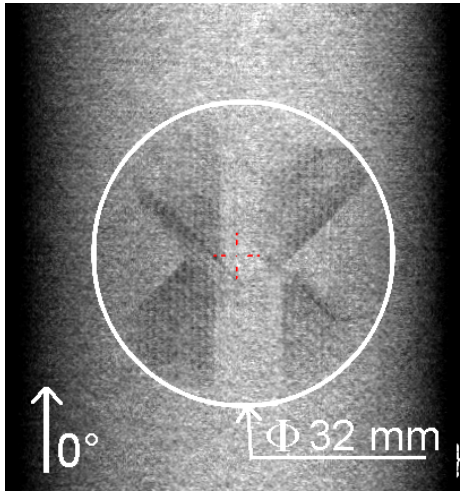

(b) 1.24 mm deep from impact surface

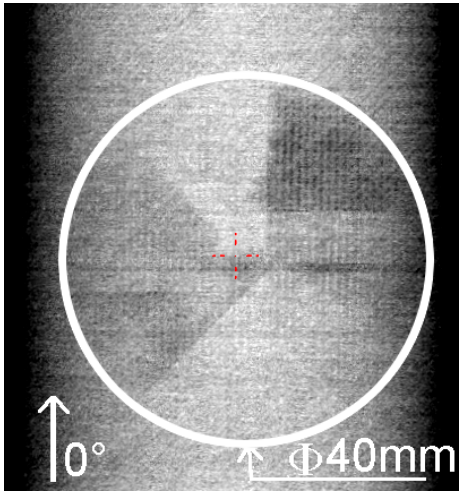

(c) 2.76 mm deep from impact surface

(d) Schematic view of the lay-up with locations of sections

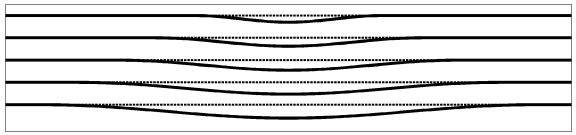

(e) Schematic view of the deformation from the impact

Figure 3.15: Through-thickness slices for the impacted sample named R15-15: (a) on the impact surface, (b) at 1.24 mm deep from the impact side, and (c) at 2.76 mm deep from the impact side. (d) presents a lay-up's schematic view illustrating the location of plane cuts. (e) local bend caused by the impact.

3.2.3.2 Larger impact tup, 50 mm radius hemi-sphere

Both samples have been impacted at 24.75 J (weight: 5.65 kg, impact velocity: 2.96 $m.s^{-1}$, drop height: 0.447 m). Some slices from the CT-scans are presented in Fig. 3.16 for sample 1. They have been obtained using the same parameters as for the R15-15 sample. In Fig. 3.16a, it is noticeable that the indent is less marked than in Fig. 3.15a. This is explained by a lower local stress concentration for the larger radius tup than for the smaller one. The same remark holds about the vertical lines in Fig. 3.16a as for Fig. 3.15a. Also by comparing Fig. 3.16b and Fig. 3.16c, one can notice that the diameter of the delaminated area is constant with the depth. This is explained by the fact that the 50 mm radius tup induces through-thickness shear strain concentrations are close to the edges of the cut-out from a smaller depth than with the 20 mm radius tup. These impacted samples will be called R50-25.

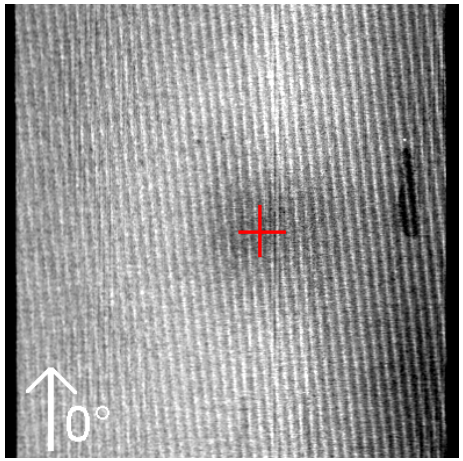

(a) Impact surface

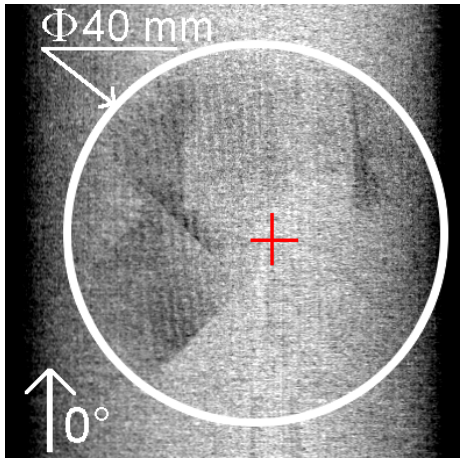

(b) 0.57 mm deep from impact surface

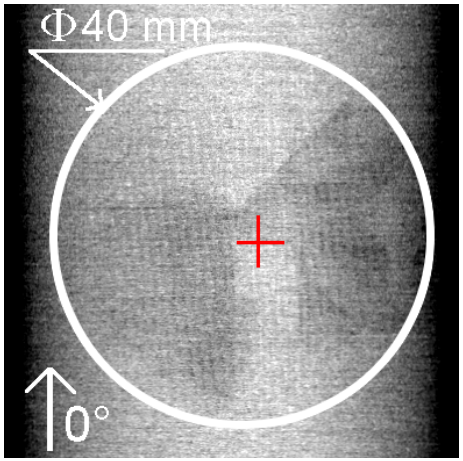

(c) 3.14 mm deep from impact surface

(d) Schematic view of the lay-up with locations of sections

Figure 3.16: Through-thickness slices for the impacted sample named R50-25 (sample 1): (a) on the impact surface, (b) at 0.57 mm deep from the impact side and (c) at 3.14 mm deep from the impact side and lay-up's schematic view presenting the location of plane cuts (d).

Tab. 3.2 summarizes the naming conventions for the different damage types and gives a brief description.

Name	Description
unda	Undamaged
FW30	Single midplane full-width 30 mm delamination
FW50	Single midplane full-width 50 mm delamination
FW3A	3 delaminations arranged in a A shape
FW7A	7 delaminations arranged in a A shape
R15-10	Impacted at 10 J with a 15 mm radius tup
R15-15	Impacted at 15 J with a 15 mm radius tup
R50-25	Impacted at 25 J with a 50 mm radius tup

Table 3.2: Naming conventions for the different damage types and brief descriptions.

3.3 Experimental set-up

Fig. 3.17 presents the experimental set-up used for these experiments. The grid and the camera are on the left-hand side and the sample clamped onto the rig on the right-hand side. The clamping was realized experimentally by bolting a piece of steel to the rig over the sample and maintaining it with a clamp. The quality of the clamping will be assessed in the results for the undamaged specimen but it is not a critical parameter for this work. The applied load was measured using an in-house built load cell with a resolution of 0.04 N. Tab. 3.3 presents the parameters used for the experiments of this chapter. The error arising from the simplified sensitivity formulation was computed in the previous chapter Section 2.1.1 and found to be smaller than 0.5 µm/m. The effect of an out-of-plane displacement was also computed in the previous chapter Section 2.1.2 and found to be 2.5 µm/m. The global uncertainty in strains can be evaluated as the sum of the resolution in strains, the error arising from the simplified expression, and the effect of an out-of-plane displacement which gives a value of 5.35 µm/m.

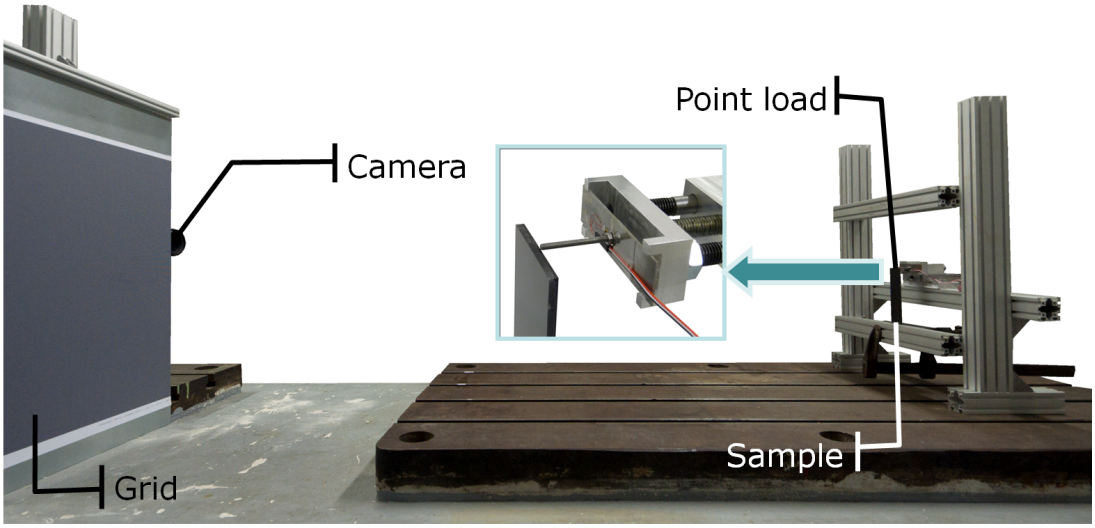

Figure 3.17: General view of the set-up. The grid and the camera are on the left and the rig with the sample on the right.

Camera		Dantec Q-400
Technology		CCD
Resolution		2448×2050 pix^2
Pixel size		3.45 µm
Dynamic range		12 bits
Exposure		1 s
Lens		Nikon 28-200 mm AF-D
Focal length		200 mm
Aperture		f/11
Others		
Grid-sample	h	1.66 m
Grid pitch	p	1.524 mm
Camera offset	e	15 mm
Sampling	N	7 pix
Resolution in phase	σ_φ	10.70 mrad
Resolution in slope	σ_θ	0.78 mm/km
Resolution in curvature	σ_κ	1.45 1/km
Resolution in strain	σ_ε	2.9 µm/m
Global uncertainty	σ_{global}	5.35 µm/m
Spatial resolution		∼14 pix

Table 3.3: Experimental parameters for deflectometry measurements on the beams.

3.4 Finite element models

In order to back-up the experimental observations, FE modelling was used to simulate the deformation of the beams. The models use an 8-noded 3D linear brick (C3D8 in Abaqus/standard) and the element dimensions are 1 mm long, 1 mm wide and 0.125 mm thick. In these models, each layer of elements through the thickness represents a single ply of composite, therefore they have the unidirectional material properties and an orientation. At the root, all the nodes have been clamped and a 5 N point load has been introduced at the centre of the free edge. The analysis assumes small displacements. The delaminations have been inserted by disconnecting the nodes in the delaminated area and using a frictionless surface contact interaction to prevent any inter-element penetration [198]. It must be noted that for the FW7A model, the surface contact interaction was removed because of convergence issues. The results from this model must be used with care as element interpenetration is present. Also it was checked that this element interpenetration had an effect on the curvature fields comparing the results from the FW3A sample with and without surface contact interaction. This comparison proved that the contact interaction has an effect on the results.

As the phases are extracted using a WDFT algorithm with a $2N-1$ pixel kernel, the information on the edges is corrupted. It is therefore necessary to remove 1 grid pitch all around the field of view. Also, a length of 5 mm at the bottom was discarded because of the shadow of the steel clamp. Fig. 3.18 represents a front view of the sample. The black zone on the bottom is the clamp and the cross at the top is the point load. The light grey area represents the final data set.

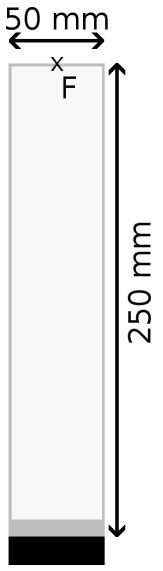

Figure 3.18: View of the area (light grey) kept from the FE results (dark grey), with the clamp (black bottom edge) and the loading point (cross).

3.4.1 Equivalent strains vs. FE strains

As the experimental final results are curvatures from measured slopes, it is better to process the numerical results in the same way to make a direct comparison. The out-of-plane displacements have been output for the nodes on the top surface (compressive side), they have then been differentiated twice to obtain the curvatures and multiplied by half the thickness to obtain the so-called "equivalent strains".

In Fig. 3.19, a comparison between the real strains and the equivalent strains for the FE model with a 30 mm long delamination, FW30, and an undamaged sample as reference is presented. Figs. 3.19b and 3.19c show that the "equivalent strains" are much more sensitive to the presence of a delamination than the actual surface strains. The shear strain maps from Figs. 3.19j and 3.19k present also a difference in favour of the equivalent strains. The transverse strain maps from Figs. 3.19e to 3.19g do not show much difference between the undamaged and the damaged states, which is due to the overall symmetry of the system and boundary conditions. This difference comes from the fact that a delamination produces more changes in curvatures than in element strains.

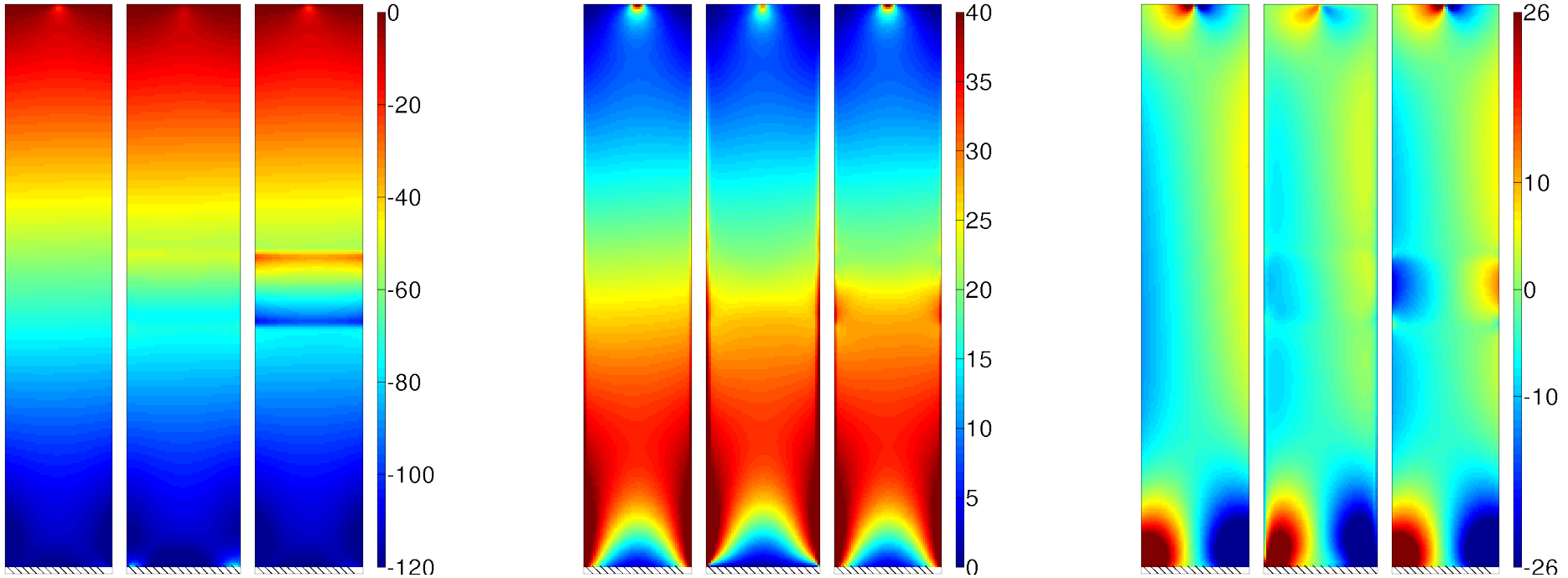

(a) unda. (b) real (c) equiv. (e) unda. (f) real (g) equiv. (i) unda. (j) real (k) equiv.

Figure 3.19: Strain maps output by the FE package for the undamaged sample ((a), (e), and (i)), the FW30 sample ((b), (f), and (j)), and equivalent longitudinal strain map ((c), (g), and (k)) for the FW30 sample.

3.4.2 Impact damage modelling

In the literature, several patterns have been proposed to numerically model delaminations induced by a low-velocity impact: annuli [33], twin-ellipse pattern [199], lemniscates (peanut shape) [200], split peanuts [201], and parts of annuli delimitated by the matrix cracks [202]. These models are illustrated in Fig. 3.20.

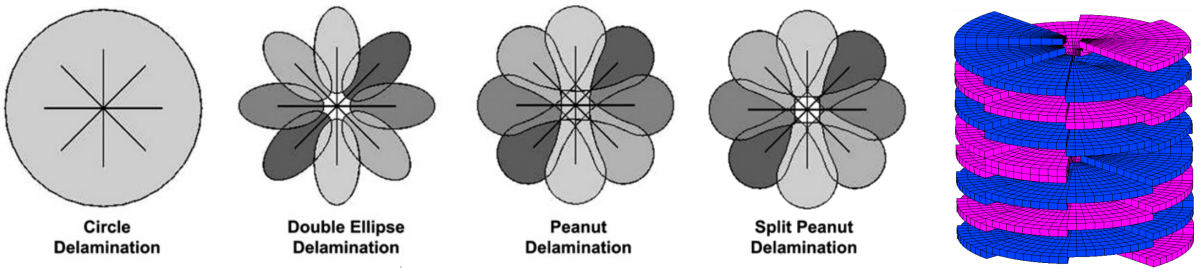

(a) [203] (b) [202]

Figure 3.20: Delamination modelling.

For the impacted samples, as a first approach, a delaminated region in the form of an annulus has been introduced at each interface where the CT-scans showed a delamination. The centre of the annulus corresponds to the point of impact, the inner radius corresponds to the non-delaminated region under the point of impact and the outer radius contains the delaminated region visible in the CT-scans Fig. 3.15. Schematic views of the simulated delaminations are given in Figs. 3.21 and 3.22 based on annuli. These FE models are a rough representation of the damage inside the composite as seen in the CT-scans. Nonetheless, they are consistent with the literature in the fact that no delaminations are present at interfaces between two plies with the same orientation and underneath the impactor. The model representing the impacted sample R15-15 will be called R15-ann as in 15 mm radius tup with annulus delaminations. It is illustrated in Fig. 3.21. The model representing the impacted sample R50-25 will be called R50-ann and it is illustrated in Fig. 3.22.

Additional refined models were created to represent more closely the resulting structure of the impact for the R15-15 sample. The first one is based on twin ellipses as in [199]. A schematic representation is shown in Fig. 3.23. Both ellipses are orientated along the same main axis and this axis is parallel to the orientation of the ply underneath. The dimensions of the ellipses were retrieved from the CT-scans and their aspect ratio is 1.5. This model is called R15-ell as in 15 mm radius tup with ellipsoidal delaminations. A second version of this model that accounted for friction at the delaminated interface was created. The friction coefficient is 0.43 and taken

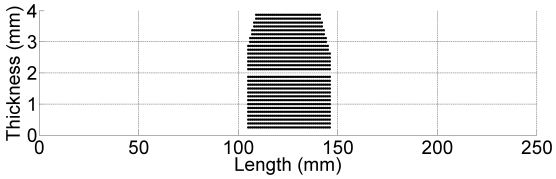

(a) Side view

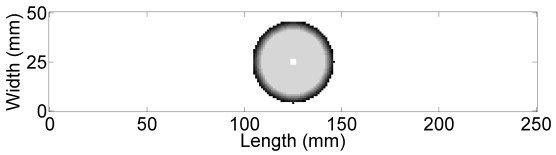

(b) Top view

Figure 3.21: Side view (a) and top view (b) of the FE-model for the specimen impacted at 15 J with a 15 mm radius tup called R15-15. This model is called R15-ann.

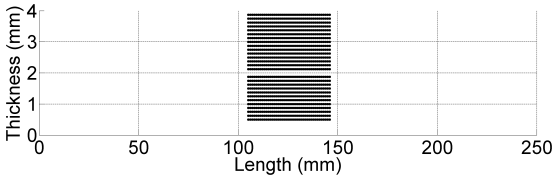

(a) Side view

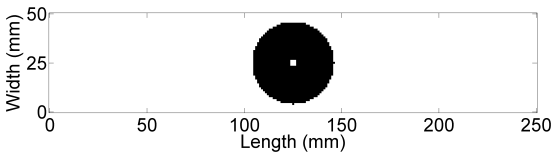

(b) Top view

Figure 3.22: Side view (a) and top view (b) of the FE-model for one of the specimens impacted at 25 J with a 50 mm radius tup called named R50-25. This model is called R50-ann.

from the literature [204]. It is called R15-fri as in 15 mm radius tup with friction.

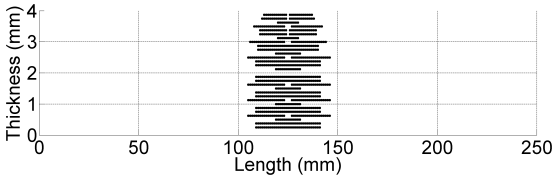

(a) Side view

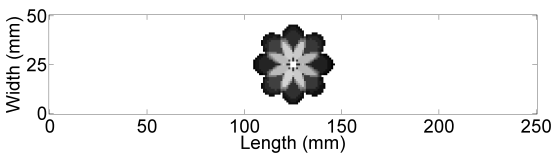

(b) Top view

Figure 3.23: Side view (a) and top view (b) of the FE-model for sample R15-15 with two ellipses delaminated area [199].

The second model is based on areas defined by angular sectors of annuli [202] and its schematic representation is shown in Fig. 3.24. The delaminated areas are limited to the angular sector defined by the ply orientations and the angular sector is always smaller than 180°. This model is called R15-as as in 15 mm radius tup with angular sector delaminations.

3.5 Results

In the following representations of the equivalent strain maps, the bottom edge is the clamped zone and the load is applied at the middle of the top edge as presented in Fig. 3.18. For ease of

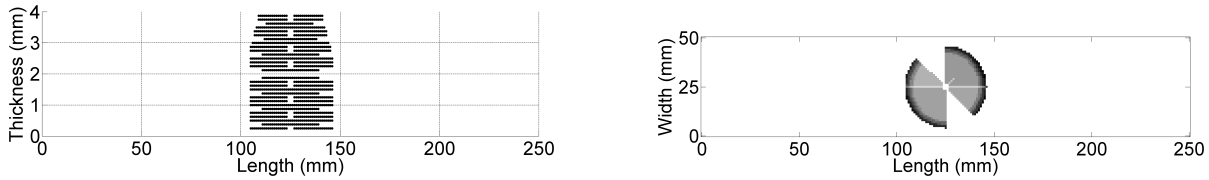

(a) Side view (b) Top view

Figure 3.24: Side view (a) and top view (b) of the FE-model for sample R15-15 with delaminated area defined by angular sectors of annuli [202].

comparison, the different sub-figures of a figure have been represented using the same colour scale but different figures may have different colour scales.

3.5.1 Undamaged specimens

The equivalent strain maps from the FE simulation and two samples of the undamaged specimens are presented in Figs. 3.25 to 3.27. These results show very good agreement between the FE analysis and the measurements. In Fig. 3.25c, the small dot in the centre is the result of the lack of data because of a bubble in the resin. The measurement resolution in the equivalent twist strains from Fig. 3.27 is remarkable, they are between only -25 µm/m and 25 µm/m over a 63 by 313 data point map, each of them corresponding to a 0.75 mm by 0.75 mm area. The slight asymmetry visible in Fig. 3.27a comes from the bending/twist coupling for this particular lay-up. One can notice in Fig. 3.26 the red dot at the middle of the top edge, causing a local bulge. This tensile strain comes from the point-load at the back. This shows also in Fig. 3.25 and is revealed in Fig. 3.27 as a local sign change in the shear strains. This illustrates the extraordinary resolution for uncompromised spatial resolution (no smoothing was used to obtain the data). It is comparable to interferometric measurements if not better.

The excellent correlation between the FE maps and the measurements indicates that the experimental loading conditions are very close to an actual point load. In the clamp region there is a slight mismatch as shown in Figs. 3.25 to 3.27. It is normal to have slightly lower experimental strains in this zone as some deformation certainly occurs at the clamp. Clamping is one of the most difficult boundary conditions to realise experimentally. The next section presents the results for the specimens containing artificial delaminations.

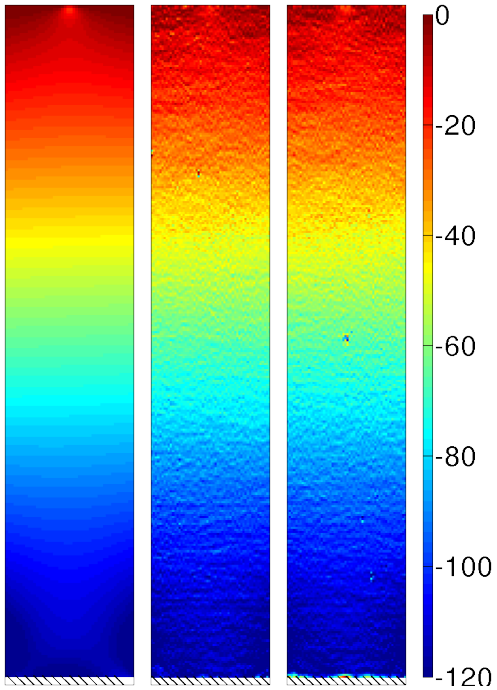

(a) FE (b) Exp. 1 (c) Exp. 2

Figure 3.25: Equivalent longitudinal strain maps for the undamaged case (in μm/m).

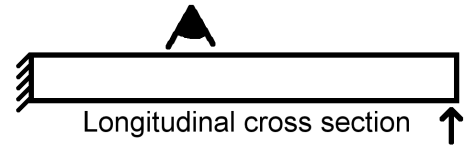

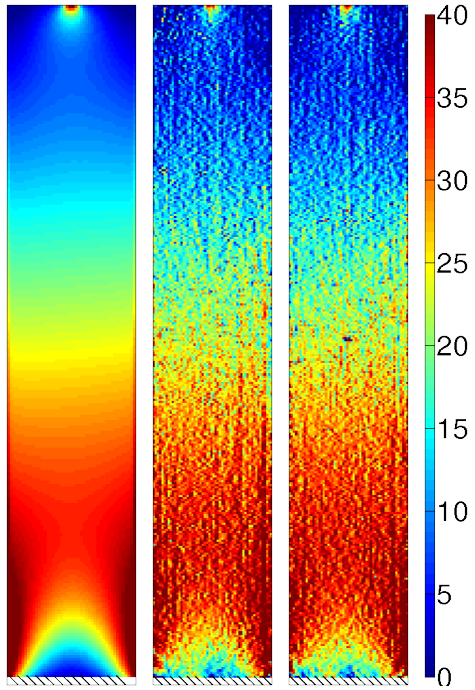

(a) FE (b) Exp. 1 (c) Exp. 2

Figure 3.26: Equivalent transverse strain maps for the undamaged case (in μm/m).

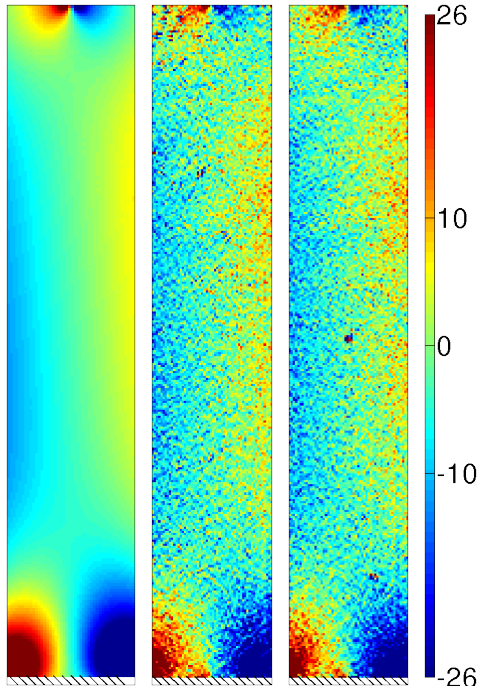

(a) FE (b) Exp. 1 (c) Exp. 2

Figure 3.27: Equivalent shear strain maps for the undamaged case (in μm/m).

3.5.2 Artificially delaminated specimens

3.5.2.1 Single delamination

3.5.2.1.1 FW50 specimens The equivalent strain maps from the FE simulation and two samples for the specimen with a single 50 mm-long delamination are presented in Figs. 3.28 to 3.30. The longitudinal equivalent strain maps Figs. 3.28b and 3.28c show good correlation with the FE data Fig. 3.28a. But in Fig. 3.28c, one can see a curved line at the lower third in the delaminated area. This is probably due to a crease in the release film used to produce the delamination as it may have been moved by the blade when opening up the delamination. The main differences between the delamination behaviour in Fig. 3.28 can be explained by the fact that the experimental delamination was not a perfect delamination. Maybe the film was still sticking to the resin or there might have been some friction between the plies and the film. As the predicted effect in the FE results for the transverse equivalent strain maps Fig. 3.29a is very small, it is not surprising to observe no significant modifications in the measurements Figs. 3.29b and 3.29c. In the equivalent shear maps Fig. 3.30, the predicted effect from the FE results in the delaminated region (negative values on the left and positive on the right) is not visible in the measurements. For sample 1, Fig. 3.30b, it looks like the pattern has been shifted by a constant value. Once again, the previous remark about the delamination not being perfect is valid here because significant differences in this respect were found between sample 1 and sample 2, and sample 1 was the closest to the FE prediction. This suggests that sample 1 was close to a perfect delamination but not sample 2. Some more modelling is required to investigate the possible effect of friction. Also it must be noted that because of the extremely small load and resulting deformations, there is no buckling. This is confirmed by the similarity of the FE results which do not incorporate any buckling. As a consequence, similar effects should also be seen on the tensile side as presented in the next chapter.

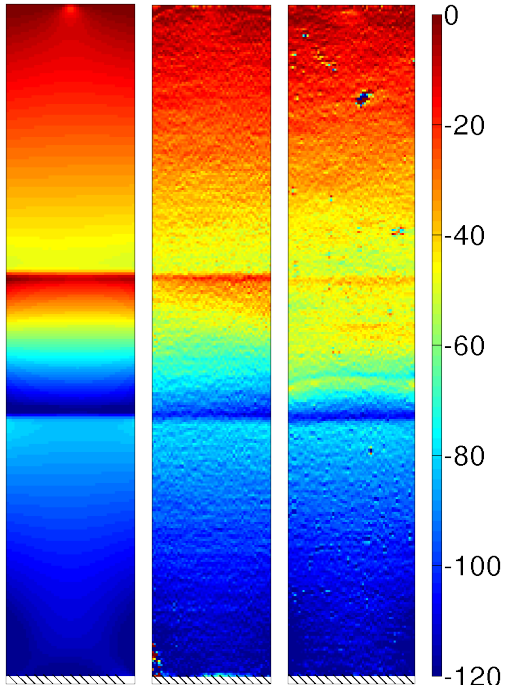

(a) FE (b) Exp. 1 (c) Exp. 2

Figure 3.28: Equivalent longitudinal strain maps for the FW50 case (in µm/m).

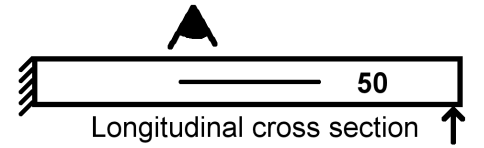

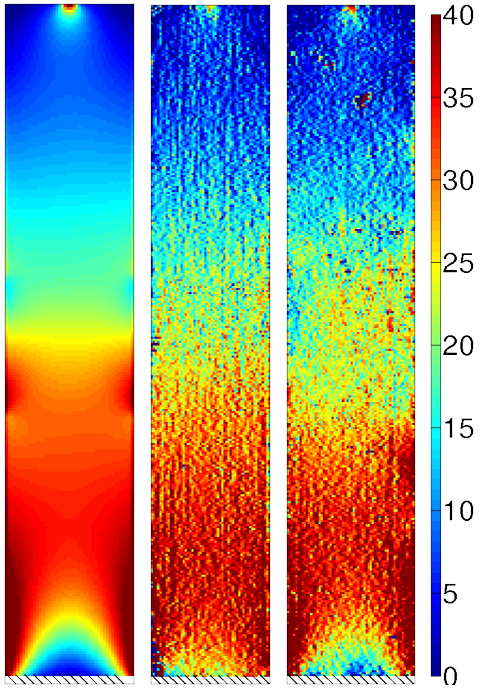

(a) FE (b) Exp. 1 (c) Exp. 2

Figure 3.29: Equivalent transverse strain maps for the FW50 case (in µm/m).

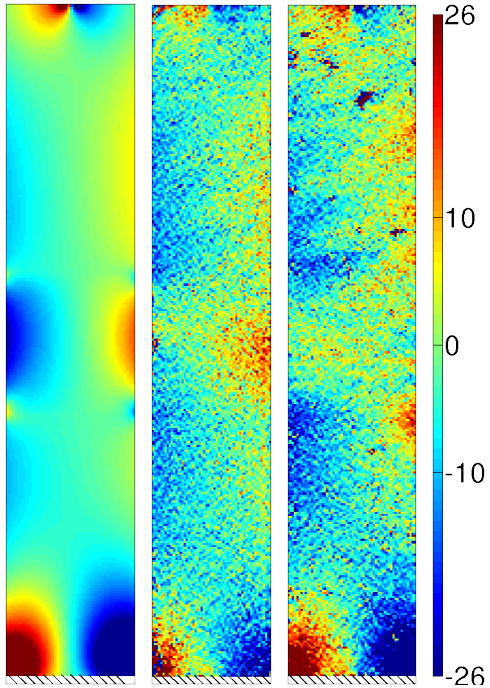

(a) FE (b) Exp. 1 (c) Exp. 2

Figure 3.30: Equivalent shear strain maps for the FW50 case (in µm/m).

3.5.2.1.2 FW30 specimens The equivalent strain maps from the FE simulation and two samples of the specimens with a single 30 mm-long delamination are presented in Figs. 3.31 to 3.33. One can see the effect of the delamination in the central area for the FE results Fig. 3.31a which is also visible in the experimental results Figs. 3.31b and 3.31c as seen for the FW50 specimen. As stated previously for the FW50 specimen, nothing is visible in the transverse maps Fig. 3.32. For the shear equivalent strain maps, the predicted effect from FE analysis described for the FW50 specimen is also visible in these FE results Fig. 3.33a but is only slightly visible in the experimental results Figs. 3.33b and 3.33c. This again is probably caused by some friction at the interface. As the delamination is only 30 mm long, it was difficult to slide the blade in the mid-plane and it may have not been completely opened up.

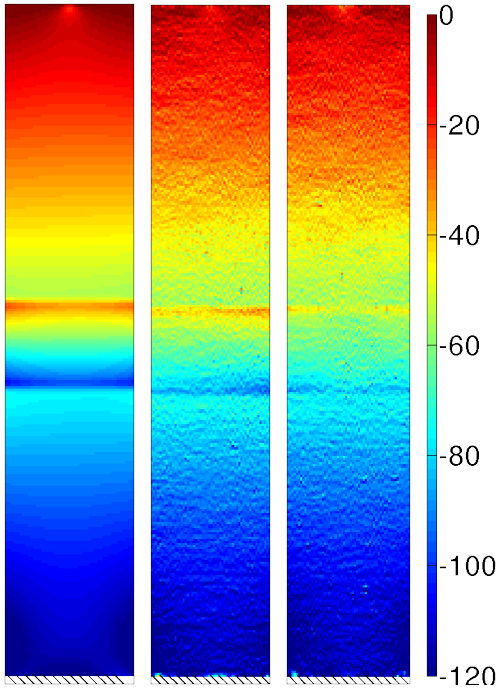

(a) FE (b) Exp. 1 (c) Exp. 2

Figure 3.31: Equivalent longitudinal strain maps for the FW30 case (in µm/m).

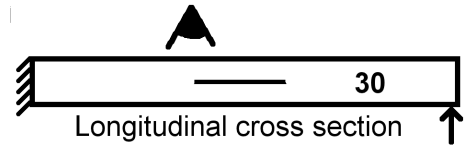

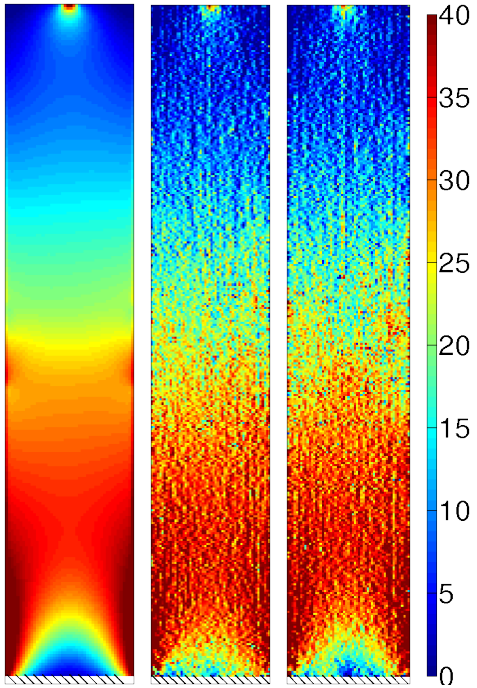

(a) FE (b) Exp. 1 (c) Exp. 2

Figure 3.32: Equivalent transverse strain maps for the FW30 case (in µm/m).

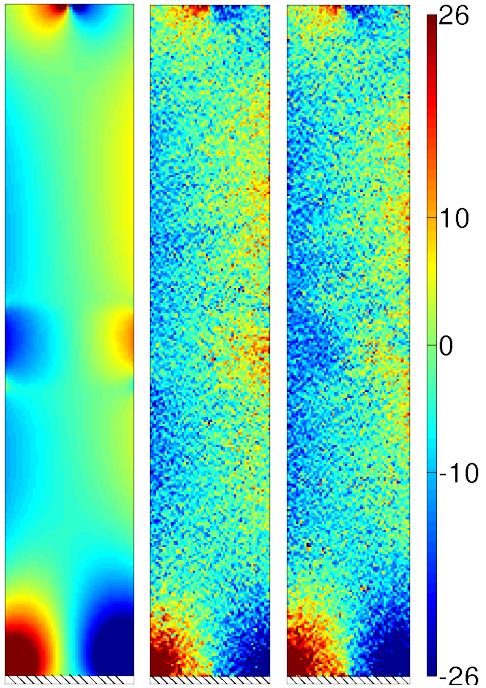

(a) FE (b) Exp. 1 (c) Exp. 2

Figure 3.33: Equivalent shear strain maps for the FW30 case (in µm/m).

3.5.2.2 Multiple delaminations

3.5.2.2.1 FW3A specimens The equivalent strain maps from the FE simulation and two samples of the specimen with three delaminations through the thickness are presented in Figs. 3.34 to 3.36. In the longitudinal equivalent strain maps Fig. 3.34, the FE simulation predicts a very significant modification of the strain gradient in the "damaged" area which is visible in sample 2 Fig. 3.34c but not as much in sample 1 Fig. 3.34b. Once again, there have been some issues when opening up the delaminations. For sample 1, it was very difficult to get the blade sliding between the plies especially for the small delaminations but it was easier for sample 2. The difference between experiments and simulation is probably mainly explained by the partial opening. The experimental maps of the equivalent shear strains Figs. 3.36b and 3.36c show a modification in comparison with the undamaged sample Fig. 3.27 but it is somewhat different from the FE prediction. This probably comes again from the pre-straining due to the delamination opening. Therefore, the solution that consists in submitting the samples to short beam shear loading before testing should improve the correlation.

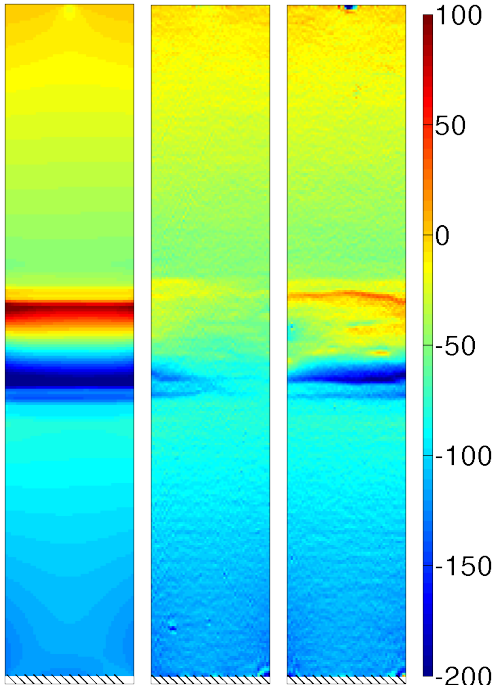

(a) FE (b) Exp. 1 (c) Exp. 2

Figure 3.34: Equivalent longitudinal strain maps for the FW3A case (in µm/m).

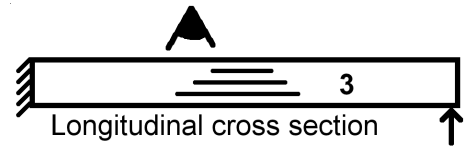

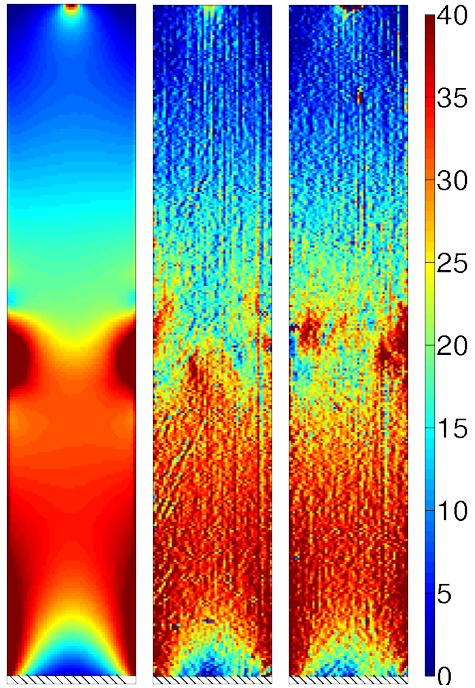

(a) FE (b) Exp. 1 (c) Exp. 2

Figure 3.35: Equivalent transverse strain maps for the FW3A case (in µm/m).

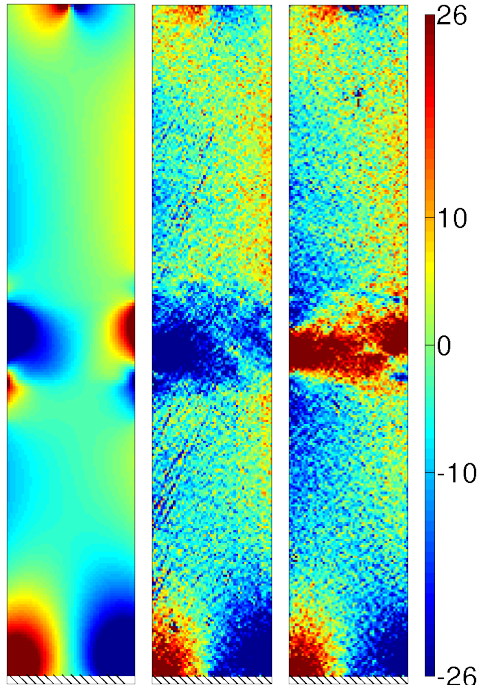

(a) FE (b) Exp. 1 (c) Exp. 2

Figure 3.36: Equivalent shear strain maps for the FW3A case (in µm/m).

3.5.2.2.2 FW7A specimens The results are presented in Figs. 3.37 to 3.39. The maps obtained by the numerical analysis are given for information purposes only as there is inter-element penetration. These maps show exactly the same issue as the ones from the FW3A specimens: a partial correlation in the longitudinal maps but nothing much in the other two. Even though no correlation can be made with the FE results, the effect of the number of delaminations is clearly visible, Fig. 3.37 compared to Fig. 3.34. In sample 2, in the centre on the left hand side of Fig. 3.37c, the area with smaller strains comes from a missing patch of coating.

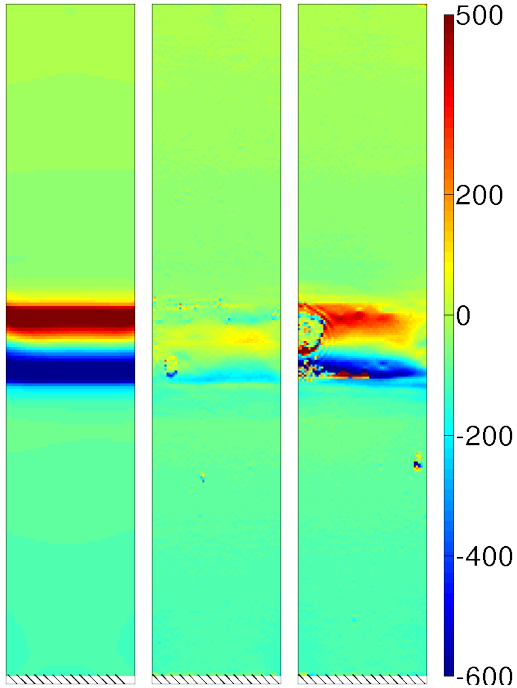

(a) FE (b) Exp. 1 (c) Exp. 2

Figure 3.37: Equivalent longitudinal strain maps for the FW7A case (in µm/m).

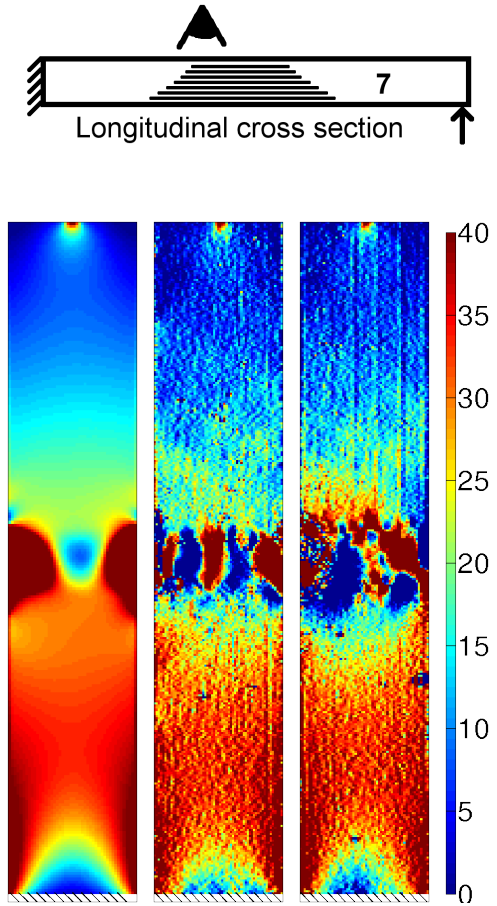

(a) FE (b) Exp. 1 (c) Exp. 2

Figure 3.38: Equivalent transverse strain maps for the FW7A case (in µm/m).

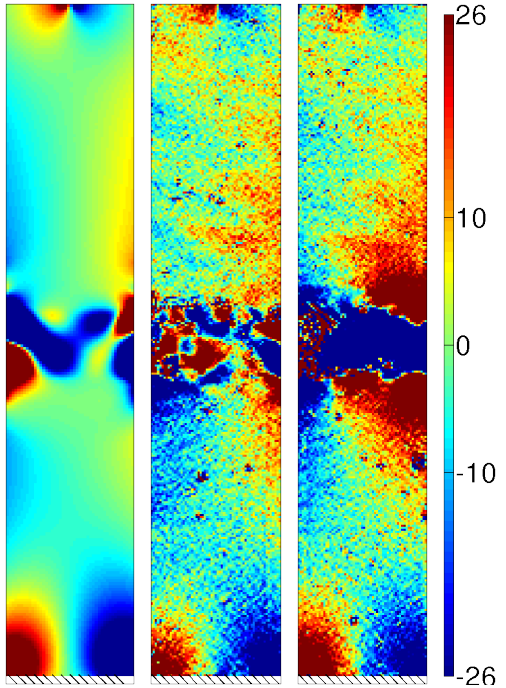

(a) FE (b) Exp. 1 (c) Exp. 2

Figure 3.39: Equivalent shear strain maps for the FW7A case (in µm/m).

3.5.3 Impacted specimens

3.5.3.1 Small impactor - R15-10 and R15-15 specimens

The equivalent strain maps for the impacted specimen with a 15 mm radius tup from the FE simulation and two samples (one impacted at 10 J and the other at 15 J) are presented in Figs. 3.40 to 3.42. It must be emphasised that because of the coating, its opacity and also because the measurement is differential, the measured information does not come from the dent but from the actual curvatures induced by the loading. Also, in Figs. 3.42b and 3.42c, 25 µm/m was added to the whole map to use the same colour scale. The twist maps Figs. 3.42b and 3.42c are significantly different from the FE prediction and this does not come from the loading. If the point load was not centred, for instance slightly offset to the right hand side, the effect on the shear strains would be to add a constant negative value over the map. Adding a constant value as done in Figs. 3.42b and 3.42c did not improve the correlation with the FE results, therefore there is a problem somewhere else.

As shown by the equivalent longitudinal strain maps from sample 1 Fig. 3.40b and 2 Fig. 3.40c, the increasing effect coming from the increasing impact energies (10 J and 15 J) is obvious. The larger the impact energy, the larger the effect on the maps. This shows that the measurement system is able to capture the effect of small impacts (10 J, 5 kg falling from 18 cm). In the transverse and twist maps, some vertical lines spaced by approximately 10 mm can be seen. They come from high frequency phase values due to the grid and not from any tow structure in the pre-preg as nothing is visible in the CT-scans in Fig. 3.15a. As stated before this kind of noise can be minimised by using a different type of grid, by improving the printing quality or by using another algorithm to extract the phases as in [160]. These vertical lines would appear in the noise evaluation if small rigid rotations were used instead of only images of the stationary specimens. But this was not performed here. The two lobes described in the literature [8] are visible in the measurements Fig. 3.40. Also in Figs. 3.41a and 3.42a, the FE analysis qualitatively predicts alternate lower/higher values around the impact point which is visible in the measurements.

Figs. 3.40d, 3.41d, and 3.42d present the results obtained by the model with the ellipsoidal delaminations, Figs. 3.40e, 3.41e, and 3.42e by the model with the friction and ellipsoidal delaminations, and Figs. 3.40f, 3.41f, and 3.42f by the model with the angular sectors of annuli. When comparing the results of the model with or without friction, the effect of friction appears to be negligible compared to the shape of delaminated areas. It is difficult to decide which ap-

proach is the best because depending on the map one or another seems closer. This shows the quality of the information provided by this measurement technique.

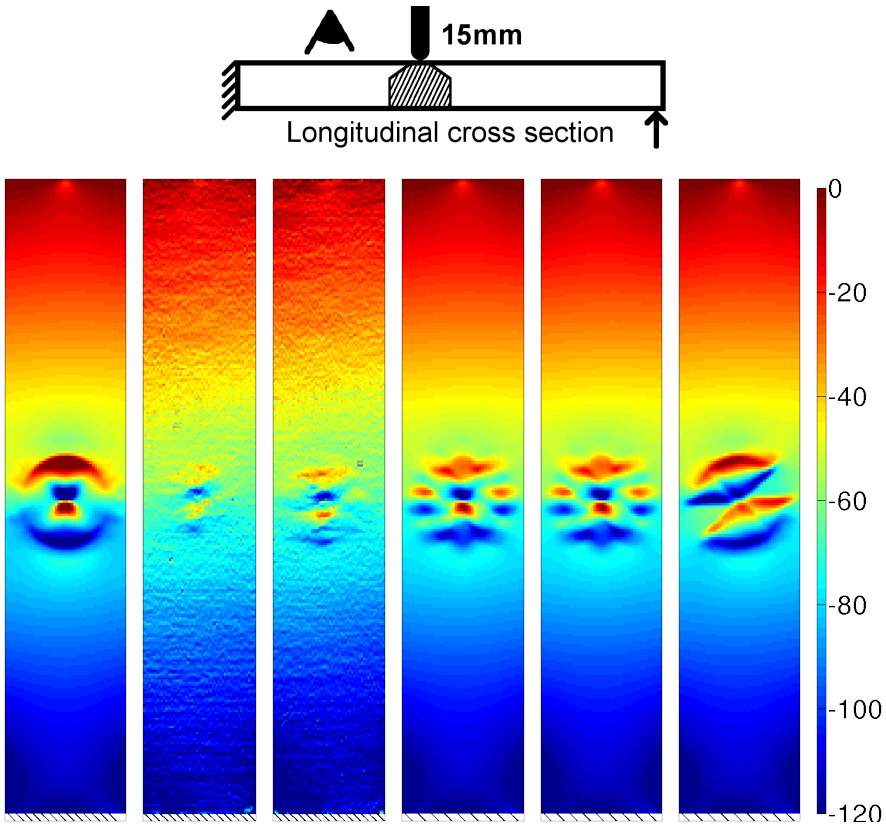

(a) R15-ann (b) 10 J (c) 15 J (d) R15-ell (e) R15-fri (f) R15-as

Figure 3.40: Equivalent longitudinal strain maps for the specimens impacted with the 15 mm radius tup (in µm/m).

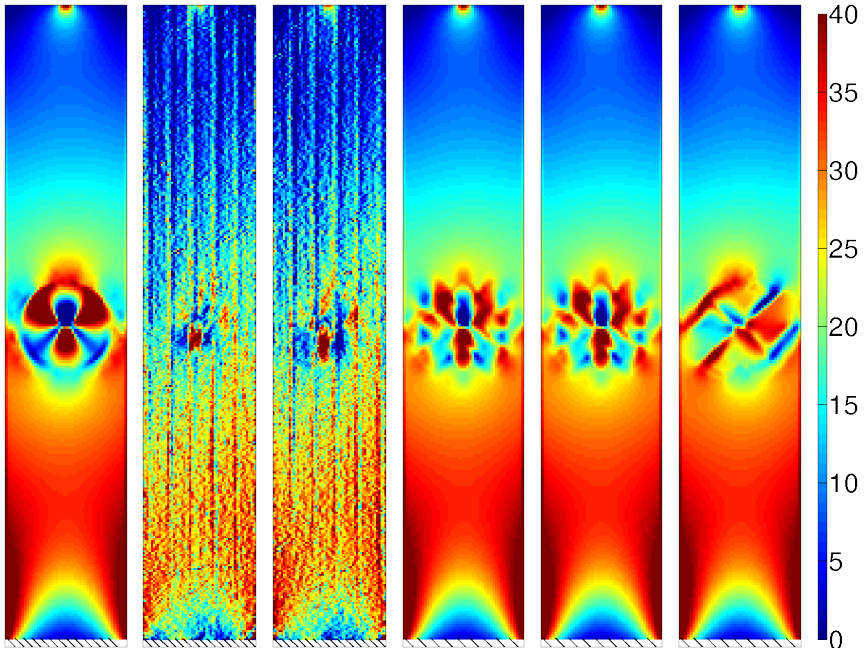

(a) R15-ann (b) 10 J (c) 15 J (d) R15-ell (e) R15-fri (f) R15-as

Figure 3.41: Equivalent transverse strain maps for the specimens impacted with the 15 mm radius tup (in µm/m).

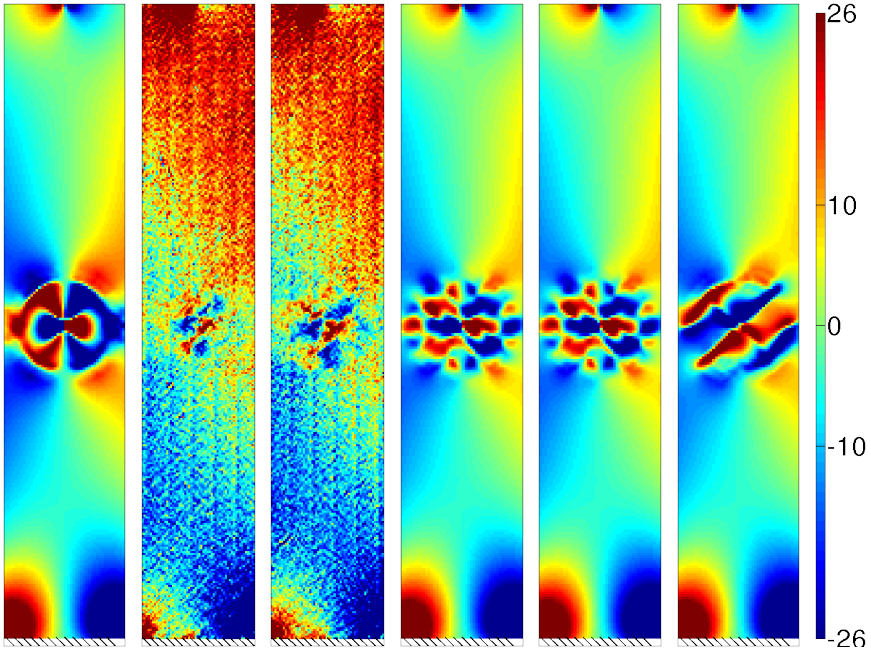

(a) R15-ann (b) 10 J (c) 15 J (d) R15-ell (e) R15-fri (f) R15-as

Figure 3.42: Equivalent shear strain maps for the specimens impacted with the 15 mm radius tup (in µm/m). $+25\mu m/m$ was added to Fig. 3.42b and Fig. 3.42c.

3.5.3.2 Larger impactor - R50-25 specimens

The equivalent strain maps from two nominally identical impacted specimens with a 50 mm radius tup at 25 J and from the FE simulation are presented in Figs. 3.43 to 3.45. In the results from sample 2 Fig. 3.43c, the inconsistent values come from a missing patch in the reflective coating. As said previously, the model overestimates the damage in the specimen which is normal if one looks at the CT-scans Fig. 3.16. In the three experimental equivalent strain maps Figs. 3.43 to 3.45, patterns similar to the ones in the R15 specimens Figs. 3.40 to 3.42 are visible. It is also possible to state that for sample 1 the impact was not right in the middle of the beam but slightly offset to the right and the top.

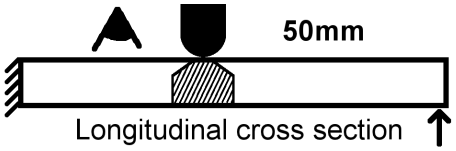

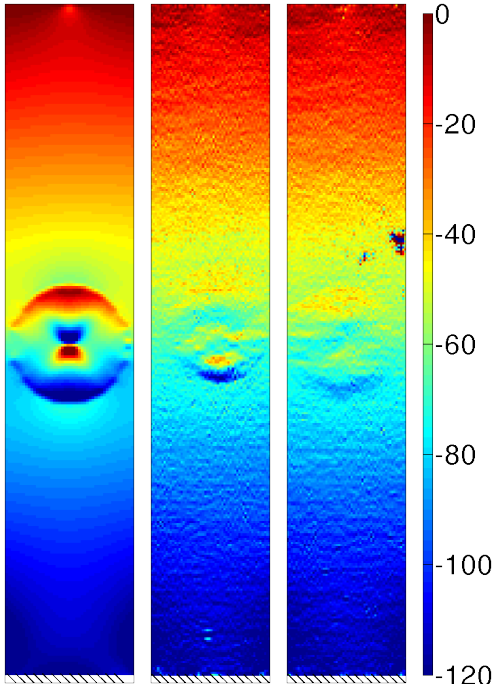

(a) R50-ann (b) Exp. 1 (c) Exp. 2

Figure 3.43: Equivalent longitudinal strain maps for the specimens impacted with the 50 mm radius tup (in µm/m).

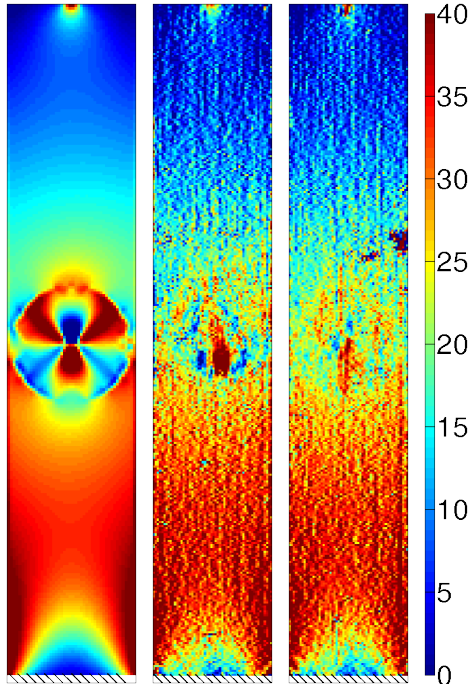

(a) R50-ann (b) Exp. 1 (c) Exp. 2

Figure 3.44: Equivalent transverse strain maps for the specimens impacted with the 50 mm radius tup (in µm/m).

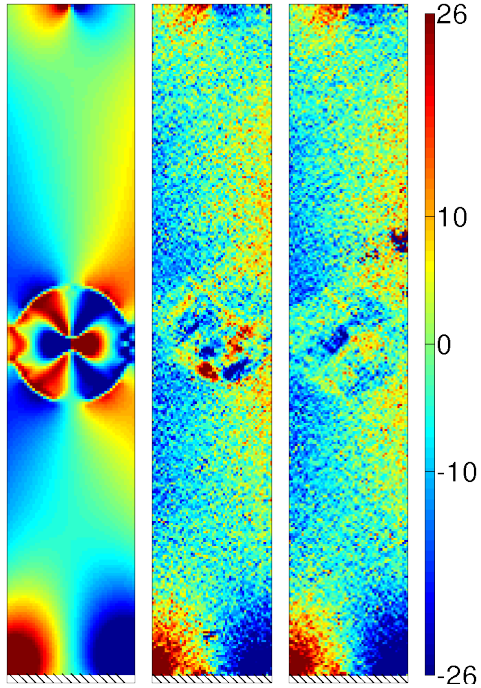

(a) R50-ann (b) Exp. 1 (c) Exp. 2

Figure 3.45: Equivalent shear strain maps for the specimens impacted with the 50 mm radius tup (in µm/m).

3.6 Conclusion

The experimental technique developed in the previous chapter has been applied to beam samples and it proved sufficiently sensitive to detect damage in composite specimens from surface slope measurements. It was able to reveal the location and extent of small damage, such as 30 mm long central delaminations or 10 J impacted samples. For the artificially delaminated samples, the measurement technique did not give the same results as the FE models mainly because of difficulties with the experimental simulation of delaminations. Creating an artificial delamination is a problem reported in several papers and a standard [21] was even proposed for it but so far it has not been possible to create a delamination without some after cure mechanical straining. Among the methods used to open up the delaminations, shim insertion and shear tests, the latter is thought to be the best as it does not lead to permanent deformation of the samples and can be applied to delaminations not accessible to insert a shim. The impacted samples illustrated very nicely what the literature describes about barely visible impact damage. Also these experimental results pointed out that the FE models need to be refined to obtain a better correlation and finer CT-scans are required. The technique proved to be very sensitive, a resolution of about 3 μm/m over a 63 by 313 data point map was achieved. This is a nice feature of this reflection technique. Although similar data processing would be possible with a random speckle pattern (reflection DIC), the spatial resolution would have been poorer. Another advantage of looking at strain maps instead of displacements is the existence of 3 maps for each measurement, each one representing a different behaviour affected by different components of the stiffness matrix. This is an excellent experimental technique to validate impact damage simulations for post-impact behaviour at low load.

CHAPTER 4

APPLICATION TO PLATES

In this chapter, the experimental technique detailed previously is applied to plate samples. First the lay-up, the material properties, and the different types of tested samples are described. Then the experimental configuration is presented as well as the finite element models, followed by the theoretical application of the virtual fields method to the present case. Finally the experimental results are reviewed and processed by the VFM.

4.1 Samples

The samples were made from Hexcel IM7-8552 carbon-fibre/epoxy pre-preg cured in an autoclave in a vacuum bag. The unidirectional material properties are summarised in Tab. 4.1 [178]. It has been used in a 24-plies quasi-isotropic lay-up $[0/45/\text{-}45/90]_{3s}$. The samples were cut from bigger plates using a diamond saw and one sample has been manufactured for each damage case. Several types of samples were used for this study depending on the damage.

E_{xx}	E_{yy}	E_{zz}	G_{xy}	G_{xz}	G_{yz}	ν_{xy}	ν_{xz}	ν_{yz}
161 GPa	11.38 GPa	11.38 GPa	5.17 GPa	5.17 GPa	3.98 GPa	0.32	0.32	0.436

Table 4.1: Material properties of cured Hexcel IM7-8552 UD carbon-fibre pre-preg [178].

4.1.1 Undamaged

The undamaged case has been studied only by finite element analysis. It will be used as a validation for the procedure.

4.1.2 Impacted

Two boundary conditions were considered for the impact. The first one is the same as in the previous chapter: clamped between two steel plates, both containing a 40 mm-diameter cut-out, as detailed by the ASTM-D5628 standard [193]. The second one follows the ASTM-D7136 standard [205] and an illustration is shown Fig. 4.1. All impacts were performed using a 50 mm radius steel tup. For the first configuration, the sample was impacted at 15 J. For the second configuration, three impact energies were used: 15 J, 20 J, and 25 J.

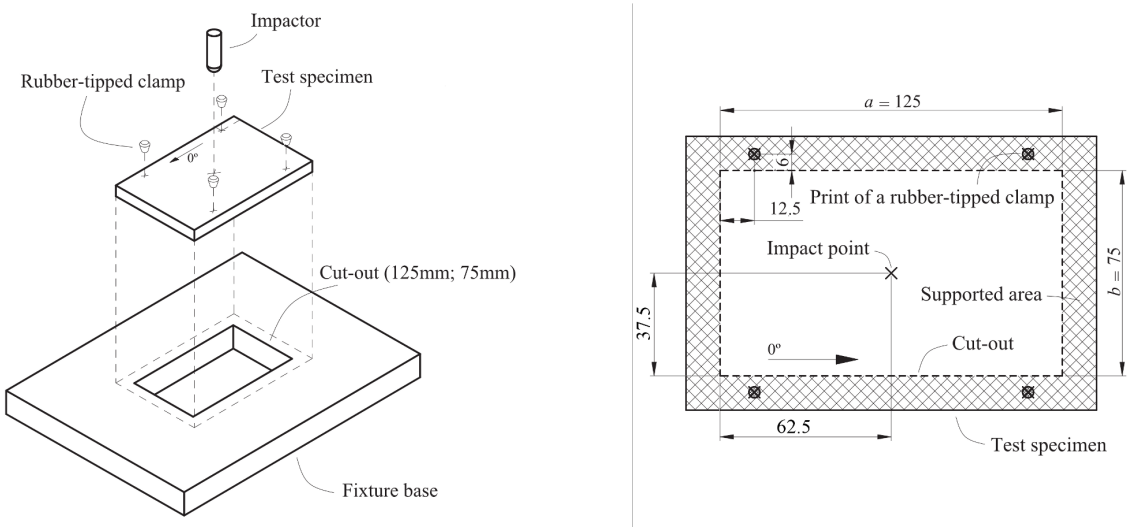

(a) (b)

Figure 4.1: (a) Impact support fixture and (b) detail of the support area and clamping points of the specimen [206] as detailed by the ASTM-D7136 standard [205].

Tab. 4.2 summarizes the naming convention, dimensions, and impact parameters for all samples.

Sample name	Length (mm)	Width (mm)	Thickness (mm)	ASTM standard	Energy (J)	Speed ($m.s^{-1}$)	Height (m)	Mass (kg)	Bending load (N)
unda	100	190	3	-	-	-	-	-	20
S1	100	190	3	D5628	15	2.31	0.27	5.64	20
S2	140	200	3	D7136	15	2.22	0.25	6.08	20
S3	140	200	3	D7136	25	2.87	0.42	6.08	20
S4	140	200	3	D7136	20	2.61	0.35	6.08	40

Table 4.2: Naming convention, dimensions, and impact parameters for all samples.

4.2 Experimental set-up

Fig. 4.2 presents views of the set-up for the plate specimens. In Fig. 4.2a, the light source, rig, and sample are on the right-hand side and the camera and grid on the left-hand side. Fig. 4.2b presents a closer view of the plate mounted on the rig. Fig. 4.2c presents a close-up view of the support for the simply supported condition. These supports are stiff enough to prevent any rigid-body rotation of the sample due to the loading.

As the strain fields from the plates are more complex than the ones from the beams, different loading points were used and they are illustrated in Fig. 4.3. The red crosses indicate the simple support points.

Similarly to what has been done previously with the beams, the influence of the variation of sensitivity on the strain fields was studied and the results are shown in Figs. 4.4 to 4.6. The data comes from a test on sample S1 loaded at point 1. The error arising from the simplified sensitivity formulation is smaller than 0.5 µm/m.

Also the effect of an out-of-plane displacement of the order of the plate thickness was evaluated using the previously obtained equation (2.24) and the numerical values from Tab. 4.3. It was found to be 2.5 µm/m.

The resolution was finally evaluated at 2.2 µm/m using the previously derived equation (2.52) and the values from Tab. 4.3. Fig. 4.7 presents the evolution of the noise level in phase with the number of averaged images. The value for 100 averaged images was used for the resolution computation.

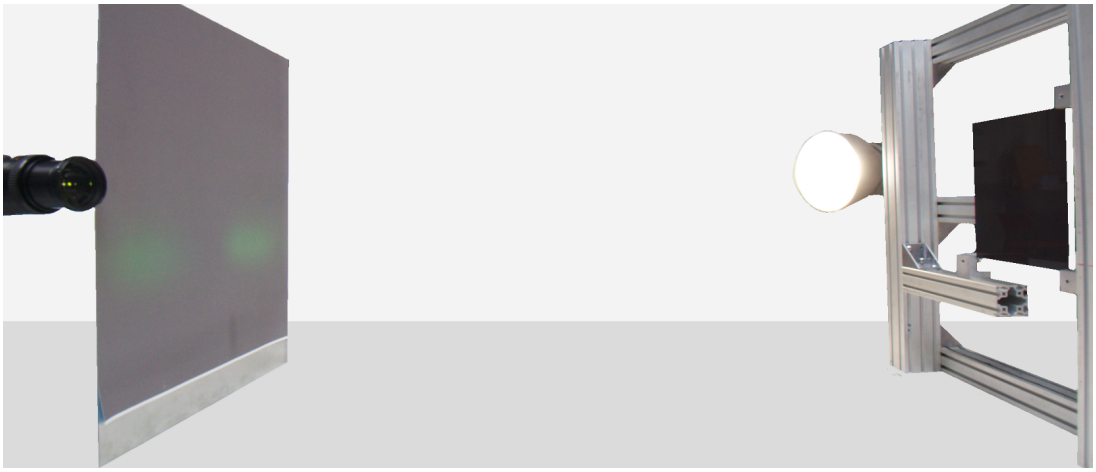

(a) General view

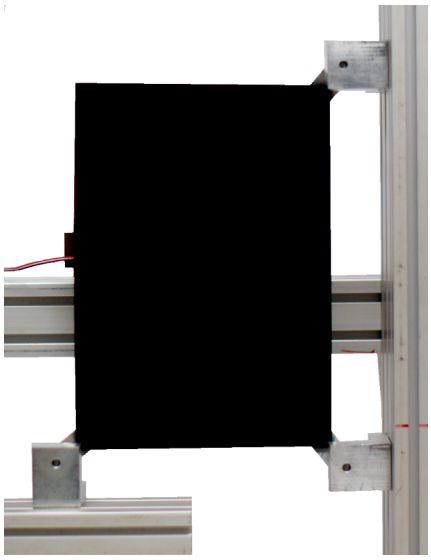

(b) Plate

(c) Support

Figure 4.2: (a) General view of the set-up, close-up view of (b) the sample and (c) the supports.

Camera		Jai TM-4200 CL
Technology		CCD
Resolution		2048×2048 pix^2
Pixel size		7.4 µm
Dynamic range		8 bits
Exposure		0.3 s
Lens		Nikon 28-105 mm AF-D
Focal length		105 mm
Aperture		f/11
Others		
Grid-sample	h	1.34 m
Grid pitch	p	1.016 mm
Camera offset	e	15 mm
Sampling	N	5 pix
Resolution in phase	σ_φ	8.80 mrad
Resolution in slope	σ_θ	0.53 mm/km
Resolution in curvature	σ_κ	1.48 1/km
Resolution in strain	σ_ε	2.2 µm/m
Global uncertainty	σ_{global}	5.2 µm/m
Spatial resolution		$\sim$10 pix

Table 4.3: Experimental parameters for deflectometry measurements on the plates.

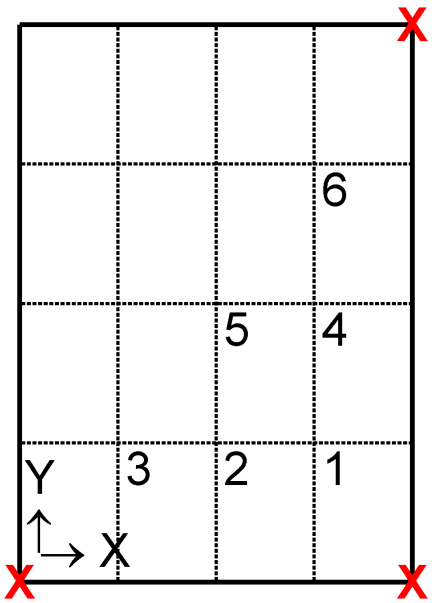

Figure 4.3: Simply supported points (red crosses) and point load positions (numbers).

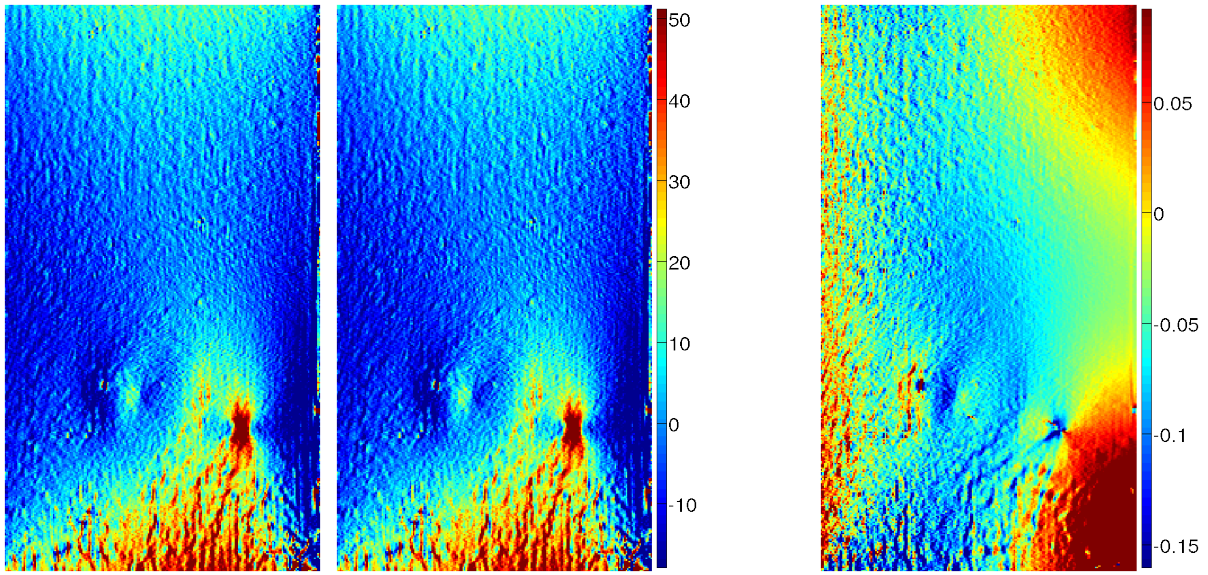

(a) With correction (b) Without correction (c) Difference

Figure 4.4: Effect of simplifications in (2.19) compared to (2.16) on measured ε_x strain fields (in µm/m).

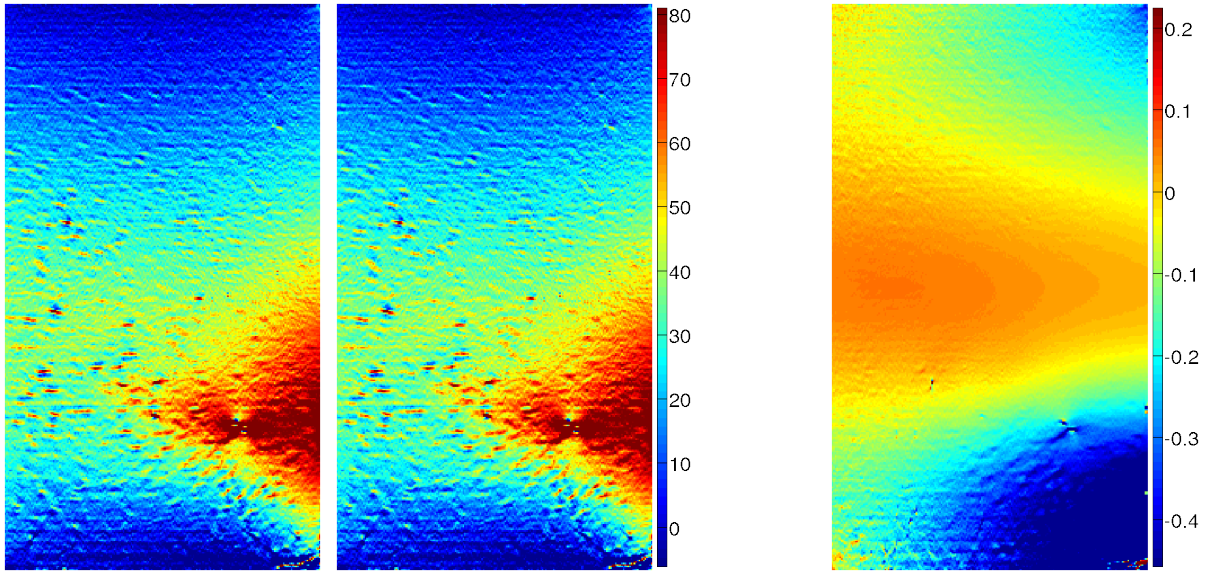

(a) With correction (b) Without correction (c) Difference

Figure 4.5: Effect of simplifications in (2.19) compared to (2.16) on measured ε_y strain fields (in µm/m).

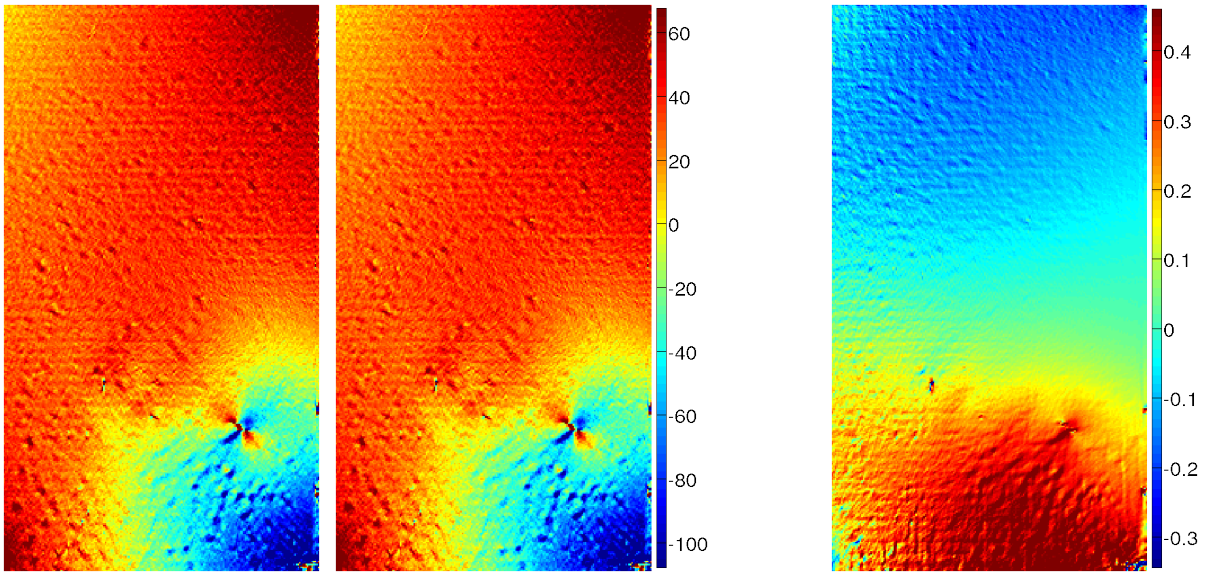

(a) With correction (b) Without correction (c) Difference

Figure 4.6: Effect of simplifications in (2.19) compared to (2.16) on measured ε_s strain fields (in µm/m).

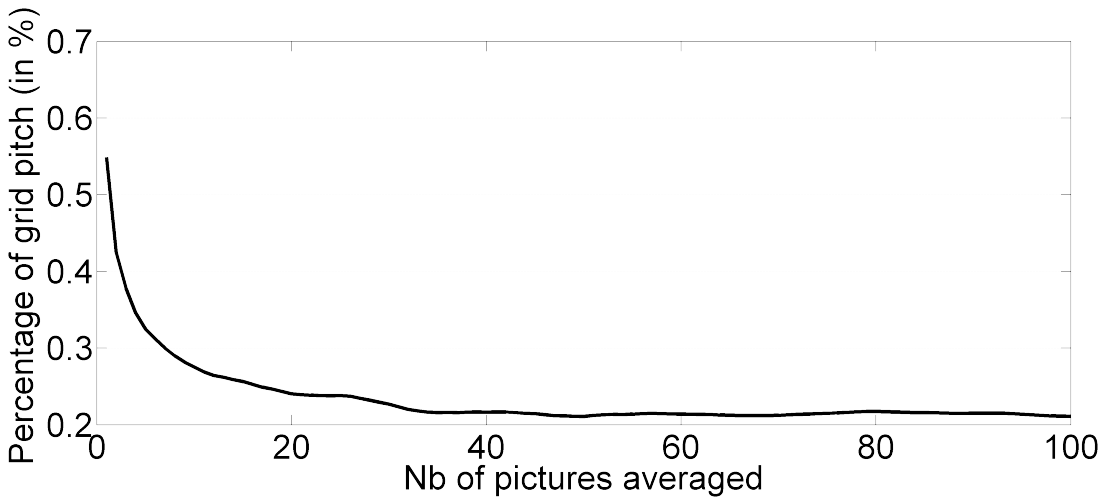

Figure 4.7: Influence of the number of averaged pictures on the noise level in phase.

The maximum difference between the two expressions linking phases to slopes compared to the resolution is small (0.5 µm/m compared to 2.2 µm/m). However, the effect of an out-of-plane displacement on the strain fields is close to the resolution (2.5 µm/m compared to 2.2 µm/m). The global error in strains is evaluated to 5.2 µm/m for these experiments. This means that the plate is small enough compared to the grid-to-sample distance not to introduce non-linearities in the link between phases and slopes. Therefore the simpler expression from (2.19) can be used.

Time of flight c-scans were obtained for all impacted samples using an automated machine equipped with a 25 MHz transducer in the pulse-echo mode. The horizontal speed is 400 mm/s and the vertical step 0.5 mm. The obtained maps are represented in Figs. 4.47a, 4.54a, 4.61a, and 4.68a. The delaminations clearly appear in different colors varying with the depth.

4.3 Finite element models

Plate models have been built-up using the approach developed in the previous chapter. The element dimensions are 0.5 mm long, 0.5 mm wide and 0.125 mm thick (1 element per ply). Because CT-scans were not available for the samples, an assumption was made for one of them. Because sample S1 has the same boundary conditions during impact as the impacted beams R50-25, it is assumed that the damage pattern inside the plate is similar to that in the beams. This model follows the twin peanuts approach for delamination modelling. It is illustrated in Fig. 4.8.

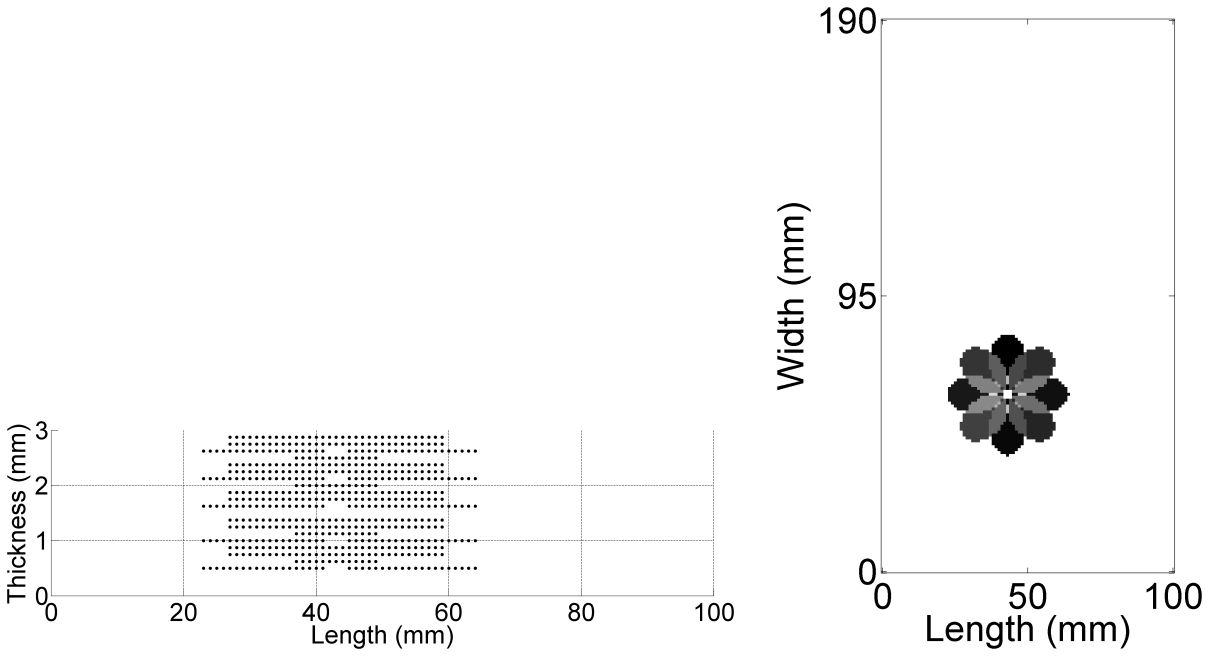

(a) Side view

(b) Top view

Figure 4.8: Side view (a) and top view (b) of the FE-model for the sample called S1.

4.4 Application of the virtual fields method to damage detection

The virtual fields method, first developed in [207], is based on the principle of virtual work. A book detailing the method and its applications is available in [208]. This technique can be used to solve the inverse problem using a set of linear equations where the unknowns are the material properties [148,149,153,209,210]. Here, a new application is developed to reveal discrepancies in equilibrium using a sliding window. The window is the zone over which the virtual work is computed. The following subsections present the theoretical developments for the equilibrium gap (EG) indicator. It must be noted that this indicator is based on the same general principle as the method presented by Claire et al. [137] as it is based on discrepancies of the mechanical equilibrium from zero to identify a damage. An error indicator for finite element computations already exists based on a similar formulation [211].

4.4.1 General equation

The principle of virtual work describes the system's global equilibrium. Its expression for static loading in absence of volume forces is written in its weak form as:

$$\int_V \sigma_{ij}\varepsilon^*_{ij}dV = \int_{\partial V} T_i u^*_i dS \qquad (i,j) = (x,y,z)^2 \tag{4.1}$$

where index repetition indicates summation and:
– V : volume of the solid
– ∂V : external surface of the solid
– σ : stress field
– ε^* : virtual strain field
– T : surface traction applied on ∂V
– u^* : virtual displacement field associated with ε^*
(4.1) highlights the equilibrium between the internal virtual work (left hand side of the equation) and the virtual work done by the external forces (right hand side of the equation). u^*, the virtual displacement field, is a mathematical function of class C^0 over V. Because some of the external forces and moments are not precisely defined, the virtual displacement and slope fields can be chosen to zero out their work. This condition is also known as kinematically admissible virtual fields. The constitutive equation for linear elasticity is written as:

$$\sigma_{ij} = C_{ijkl}\varepsilon_{kl} \qquad (i,j,k,l) = (x,y,z)^4 \tag{4.2}$$

Combining (4.2) and (4.1), one obtains:

$$\int_V C_{ijkl}\varepsilon_{kl}\varepsilon^*_{ij}dV = \int_{\partial V} T_i u^*_i dS \qquad (i,j,k,l) = (x,y,z)^4 \tag{4.3}$$

ε_{kl} and T_i are experimental data, C_{ijkl} the material properties, and u^*_i and ε^*_{ij} the virtual fields. It must be noted that the virtual fields do not necessarily represent a physical quantity. This equation highlights the independence of this method from the stress distribution and the geometry of the specimen.

4.4.2 Application to thin plates in bending

Because in this case, experimental data are only available on the surface of the specimen, through-thickness kinematic assumptions must be used. As the sample is a thin plate, the Love-Kirchhoff plate theory has been chosen. In the case of a thicker plate, plate theories that account for through-thickness shear stresses/strains should be preferred. A review of several plate models is available in [212]. The displacement and strain field for the Love-Kirchhoff theory were given in (2.36) and (2.37), respectively.

Combining (2.42) and (2.40), one can express the stress tensor as a function of forces and moments:

$$\{\sigma\} = \frac{1}{h}\{N\} + \frac{12z}{h^3}\{M\} \tag{4.4}$$

In the case of a plate under pure bending ($N = 0$), the internal virtual work from (4.1) combined with (4.4) can be written as:

$$\int_V \sigma_{ij}\varepsilon^*_{ij}dV = \frac{12}{h^3}\int_V M_i\varepsilon^*_i z dV \qquad (i,j) = (x,y,z) \tag{4.5}$$

Because real kinematic fields are odd functions for their through-thickness variations, choosing a function with an even through-thickness evolution for the virtual fields zeroes out the integrals. Therefore, an odd function should be used:

$$\{\varepsilon^*\} = z\{\kappa^*\} \tag{4.6}$$

with $\{\kappa^*\}$ being the virtual surface curvature fields.

Because moments and curvatures are independent of the through-thickness position, (4.5) combined with (4.6), can be simplified as:

$$\int_V \sigma_{ij}\varepsilon^*_{ij}dV = \int_S M_i\kappa^*_i dS \qquad (i,j) = (x,y,z) \tag{4.7}$$

where S is the studied surface where experimental data are available.

The external forces applied to the sliding window are the single out-of-plane point load and the reaction forces and moments of the rest of the plate on the studied zone. By choosing the virtual displacement field to zero the work of the reaction forces, the external virtual work from (4.1) can be written as:

$$\int_{\partial V} T_i u^*_i dS = Fw^*(x_f, y_f) \qquad i = (x,y,z) \tag{4.8}$$

where F is the force of the point load, x_f and y_f the coordinates of the point where the load is applied and w^* the out-of-plane virtual displacement calculated at the position of the point load. It must be noted that if the point load is outside the sliding window, its virtual work is zero.

As the material is considered homogeneous, the $[B]$ matrix is zero in (2.45). As $\{N\}$ is zero (no in-plane forces), this leads to $\{\varepsilon_0\} = 0$. (2.45) can be simplified to:

$$\{M\} = [D]\{\kappa\} \tag{4.9}$$

Combining (4.7), (4.8), and (4.9), gives the following expression in the orthotropy basis considering a plane stress state:

$$\begin{aligned}\int_S D_{xx}\kappa_x\kappa^*_x dS + \int_S D_{yy}\kappa_y\kappa^*_y dS + \int_S D_{ss}\kappa_s\kappa^*_s dS + \int_S D_{xy}\left(\kappa_x\kappa^*_y + \kappa_y\kappa^*_x\right) dS \\ + \int_S D_{xs}\left(\kappa_x\kappa^*_s + \kappa_s\kappa^*_x\right) dS + \int_S D_{ys}\left(\kappa_y\kappa^*_s + \kappa_s\kappa^*_y\right) dS = Fw^*(x_f, y_f)\end{aligned} \tag{4.10}$$

If the stiffness components D_{uv} $(u, v = x, y, s)$ are constant over the studied area S, they can be moved outside of the integration sign:

$$D_{xx}I_{xx} + D_{yy}I_{yy} + D_{ss}I_{ss} + D_{xy}I_{xy} + D_{xs}I_{xs} + D_{ys}I_{ys} = Fw^*(x_f, y_f) \tag{4.11}$$

with $D_{uv}(u, v = x, y, s)$ the homogeneized bending stiffness components supposed to be constant over the whole plate, w^* the out-of-plane displacement and:

$$\kappa^*_x(x,y) = -\frac{\partial^2 w^*(x,y)}{\partial x^2} \qquad \kappa^*_y(x,y) = -\frac{\partial^2 w^*(x,y)}{\partial y^2} \qquad \kappa^*_s(x,y) = -2\frac{\partial^2 w^*(x,y)}{\partial x \partial y} \tag{4.12}$$

$$
\begin{aligned}
I_{xx} &= \int_S \kappa_x \kappa_x^* dS & I_{yy} &= \int_S \kappa_y \kappa_y^* dS & I_{ss} &= \int_S \kappa_s \kappa_s^* dS \\
I_{xy} &= \int_S \left(\kappa_x \kappa_y^* + \kappa_y \kappa_x^*\right) dS & I_{xs} &= \int_S \left(\kappa_x \kappa_s^* + \kappa_s \kappa_x^*\right) dS & I_{ys} &= \int_S \left(\kappa_y \kappa_s^* + \kappa_s \kappa_y^*\right) dS
\end{aligned}
\tag{4.13}
$$

(4.11) is the application of the principle of virtual work to thin symmetric plates in pure bending. By selecting six different virtual fields, a linear system where the unknowns are the stiffnesses can be built-up and solved for identification as done in [149].

4.4.3 Application to discrete data

As the experimental data are discrete, the integrals need to be approximated by discrete sums where experimental data points are available. p and q are the number of data points along the x and y directions, respectively, and S the area under study. (4.13) can therefore be written as:

$$
\begin{cases}
I_{xx} = \dfrac{S}{pq} \displaystyle\sum_{i=1}^{p} \sum_{j=1}^{q} \kappa_x(x_i, y_j) \kappa_x^*(x_i, y_j) \\
I_{yy} = \dfrac{S}{pq} \displaystyle\sum_{i=1}^{p} \sum_{j=1}^{q} \kappa_y(x_i, y_j) \kappa_y^*(x_i, y_j) \\
I_{ss} = \dfrac{S}{pq} \displaystyle\sum_{i=1}^{p} \sum_{j=1}^{q} \kappa_s(x_i, y_j) \kappa_s^*(x_i, y_j) \\
I_{xy} = \dfrac{S}{pq} \displaystyle\sum_{i=1}^{p} \sum_{j=1}^{q} \left[\kappa_x(x_i, y_j) \kappa_y^*(x_i, y_j) + \kappa_y(x_i, y_j) \kappa_x^*(x_i, y_j)\right] \\
I_{xs} = \dfrac{S}{pq} \displaystyle\sum_{i=1}^{p} \sum_{j=1}^{q} \left[\kappa_x(x_i, y_j) \kappa_s^*(x_i, y_j) + \kappa_s(x_i, y_j) \kappa_x^*(x_i, y_j)\right] \\
I_{ys} = \dfrac{S}{pq} \displaystyle\sum_{i=1}^{p} \sum_{j=1}^{q} \left[\kappa_y(x_i, y_j) \kappa_s^*(x_i, y_j) + \kappa_s(x_i, y_j) \kappa_y^*(x_i, y_j)\right]
\end{cases}
\tag{4.14}
$$

4.4.4 Formulation of the virtual fields

The virtual fields can be expanded using different kinds of continuous (cosine, square root, polynomials, ...) or piecewise (finite elements as in [148, 149, 213, 214]) basis functions. The piecewise approach was chosen here because it is more stable and flexible than polynomials [215]. The virtual deflection field can therefore be written as:

$$
w^*(x, y) =< N(x, y) \mid\mid q^* > \tag{4.15}
$$

where $< N(x,y) \mid$ contains the shape functions of an element in a row vector and $\mid q^* >$ the nodal virtual degrees of freedom in a column vector. They can be written as:

$$\begin{cases} < N(x,y) \mid = \begin{pmatrix} \cdots & N_{i1}(x,y) & N_{i2}(x,y) & N_{i3}(x,y) & N_{i4}(x,y) & \cdots \end{pmatrix} \\ < q^* \mid = \begin{pmatrix} \cdots & q^*_{i1} & q^*_{i2} & q^*_{i3} & q^*_{i4} & \cdots \end{pmatrix} \end{cases} \tag{4.16}$$

with N^*_{ij} the shape function associated with the j^{th} degree of freedom (q^*_{ij}) of node i. The horizontal lengths of $< N(x,y) \mid$ and $< q^* \mid$ are $k \times n$ with k the number of degrees of freedom and n the number of nodes.

The associated virtual curvature field is:

$$\begin{cases} \kappa^*_x(x,y) = - < \dfrac{\partial^2 N(x,y)}{\partial x^2} \mid\mid q^* > & =< N_x(x,y) \mid\mid q^* > \\ \kappa^*_y(x,y) = - < \dfrac{\partial^2 N(x,y)}{\partial y^2} \mid\mid q^* > & =< N_y(x,y) \mid\mid q^* > \\ \kappa^*_s(x,y) = -2 < \dfrac{\partial^2 N(x,y)}{\partial x \partial y} \mid\mid q^* > & =< N_s(x,y) \mid\mid q^* > \end{cases} \tag{4.17}$$

(4.14) can be written in vector form:

$$\begin{cases} I_{xx} =< I_{xx} \mid\mid q^* > & I_{yy} =< I_{yy} \mid\mid q^* > & I_{ss} =< I_{ss} \mid\mid q^* > \\ I_{xy} =< I_{xy} \mid\mid q^* > & I_{xs} =< I_{xs} \mid\mid q^* > & I_{ys} =< I_{ys} \mid\mid q^* > \end{cases} \tag{4.18}$$

with:

$$\begin{cases} < I_{xx} \mid \simeq \dfrac{S}{pq} \displaystyle\sum_{i=1}^{p} \sum_{j=1}^{q} \kappa_x(x_i,y_j) < N_x(x_i,y_j) \mid \\ < I_{yy} \mid \simeq \dfrac{S}{pq} \displaystyle\sum_{i=1}^{p} \sum_{j=1}^{q} \kappa_y(x_i,y_j) < N_y(x_i,y_j) \mid \\ < I_{ss} \mid \simeq \dfrac{S}{pq} \displaystyle\sum_{i=1}^{p} \sum_{j=1}^{q} \kappa_s(x_i,y_j) < N_s(x_i,y_j) \mid \\ < I_{xy} \mid \simeq \dfrac{S}{pq} \displaystyle\sum_{i=1}^{p} \sum_{j=1}^{q} \left[\kappa_x(x_i,y_j) < N_y(x_i,y_j) \mid + \kappa_y(x_i,y_j) < N_x(x_i,y_j) \mid\right] \\ < I_{xs} \mid \simeq \dfrac{S}{pq} \displaystyle\sum_{i=1}^{p} \sum_{j=1}^{q} \left[\kappa_x(x_i,y_j) < N_s(x_i,y_j) \mid + \kappa_s(x_i,y_j) < N_x(x_i,y_j) \mid\right] \\ < I_{ys} \mid \simeq \dfrac{S}{pq} \displaystyle\sum_{i=1}^{p} \sum_{j=1}^{q} \left[\kappa_y(x_i,y_j) < N_s(x_i,y_j) \mid + \kappa_s(x_i,y_j) < N_y(x_i,y_j) \mid\right] \end{cases} \tag{4.19}$$

Because of the particular choice of 'bending virtual fields' here, it is clear from (4.12) that w^* must be of class C^1 and not just C^0. This is explained in more details in [208]. Therefore,

the choice of the virtual element shape functions must be performed carefully to enforce this condition. Most standard plate bending elements do not exhibit this property as it is not essential for FE calculations where kinematic fields are approximated by shape functions. Here, if this condition is not enforced strictly, the resulting equations will just be incorrect. Therefore, the 4-noded Hermitian element has been chosen. It has four degrees of freedom per node and the fourth degree of freedom ensures the continuity of the slope field. The four (virtual here) degrees of freedom for node i are:

$$q_{i1}^* = w^* \qquad q_{i2}^* = \frac{\partial w^*}{\partial x} \qquad q_{i3}^* = \frac{\partial w^*}{\partial y} \qquad q_{i4}^* = \frac{\partial^2 w^*}{\partial x \partial y} \tag{4.20}$$

4.4.5 Equilibrium gap (EG) indicator

(4.11) can also be written in this form:

$$-\left(D_{xx}I_{xx} + D_{yy}I_{yy} + D_{ss}I_{ss} + D_{xy}I_{xy} + D_{xs}I_{xs} + D_{ys}I_{ys}\right) + Fw^*(x_f, y_f) = 0 \tag{4.21}$$

This equation transcribes that the particular part of the specimen over which it is written is in equilibrium if all underlying assumptions are respected (thin plate model, constant stiffnesses over the area etc.). The piecewise approach was used here with four elements as illustrated in Fig. 4.9. It must be noted that the four elements do not cover the whole sample. This allows to obtain a map of gap in equilibrium by moving this window over the specimen. Two parameters can be modified to optimize the obtained maps: the window size and the sliding pitch. The window size controls the number of data points used to compute the equilibrium and acts as a regularization parameter to control the influence of the noise. The sliding pitch corresponds to the number of pixels by which the sliding window must be moved before computing the next equilibrium. It will affect the computational time and the smoothness of the EG maps.

All virtual degrees of freedom of the nodes on the perimeter of the sliding window (node numbers 1 to 4 and 6 to 9) are set to zero. This zeroes out the work of the external forces and moments on the boundaries of the sliding window (bending stresses). There are now only the four virtual degrees of freedom of the central node (number 5) which are still to be defined. Here, they have all been set arbitrarily to zero except for the virtual deflection that was fixed to 1. The virtual deflection and curvature fields are illustrated in Fig. 4.10. Other choices are possible but have not been explored here.

As the gap to equilibrium is proportional to the level of stress, the results have been normalized

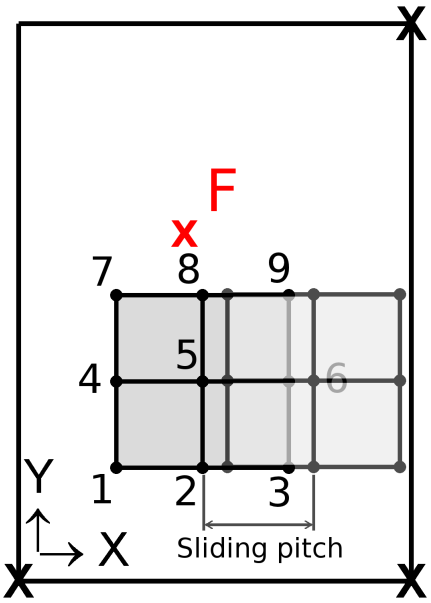

Figure 4.9: Illustration of the four virtual elements with the relevant node numbers for the equilibrium gap indicator.

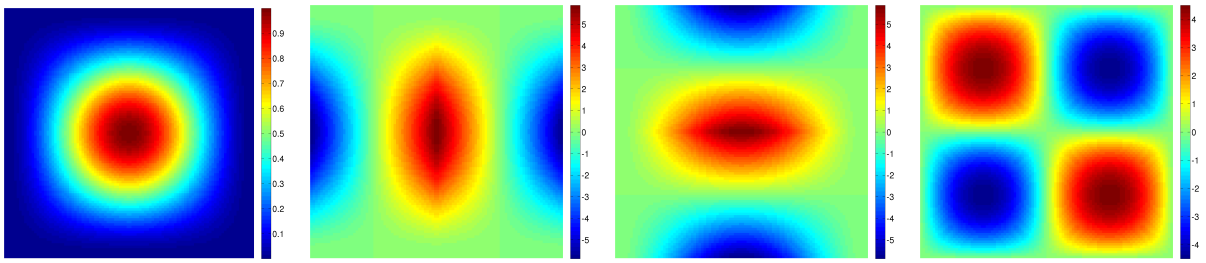

(a) w_x^* (b) κ_x^* (c) κ_y^* (d) κ_s^*

Figure 4.10: Virtual (a) deflection and (b) to (d) curvature fields.

by the following coefficient:

$$\frac{1}{\sqrt{[D_{xx}\max(\kappa_{xx})]^2+[D_{yy}\max(\kappa_{yy})]^2+[D_{ss}\max(\kappa_{ss})]^2}} \tag{4.22}$$

This was done in order to avoid the equilibrium gap maps being too influenced by areas of large stresses instead of areas where damage is present.

If the applied point load (red cross) is outside the zone covered by the four elements, the virtual work of external forces is zero. Otherwise, it is not zero. Fig. 4.11b presents the EG maps of the undamaged sample loaded at point 1 with a sliding pitch of 3 pixels and 40×40 pixels^2 per sliding window using simulated data. Two discrepancies are visible: on the edges and around the point load. Both of them can be explained by the fact that the numerical model is a full 3D implementation of the laminate. They both come from the free edge effect causing a violation of the thin plate assumptions (plane strain/stress). Because both discrepancies are known *a-priori*, they can be corrected to not appear in the final results. The discrepancy coming from the free edge effect will not be visible in the final maps because the data on the edges cannot be retrieved experimentally. To correct the discrepancy coming from the point load, the EG value is forced to 0 if the load point is covered by the sliding window as illustrated in Fig. 4.11c. It must be noted that the EG maps have been padded with *NaN* values at the edges in order to present the same aspect ratio than the original equivalent strain maps (loss of half of sliding window).

4.4.5.1 Effect of window size

Fig. 4.12 presents the effect of the size of the sliding window on the computed EG maps for the experimental results from sample S1 loaded at point 5. Three different sizes were considered: 10×10, 24×24, 40×40 and 60×60 pixels^2. The large orange zone in the centre of Fig. 4.12e corresponds to EG values of 0 because the sliding window was covering the load point. Reducing the window size helps to define more precisely the location of the damage but increases the effect of noise. A window size of 40×40 pixels^2 is a good compromise here and will therefore be used in the following results.

4.4.5.2 Effect of sliding pitch

Fig. 4.13 presents the effect of the sliding pitch on the computed EG maps for the numerical results from sample S1 loaded at point 5. Four different sliding pitches were considered: 1, 3,

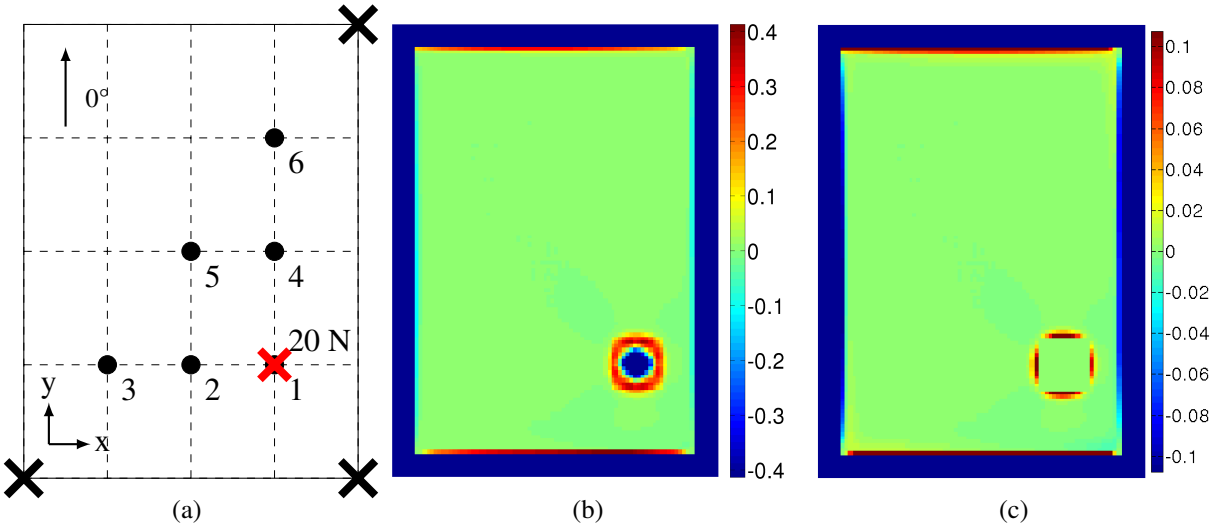

(a) (b) (c)

Figure 4.11: EG map for the undamaged sample loaded at point 1 with a sliding pitch of 3 pixels and 40×40 pixels^2 sliding window. (b) the virtual work of external forces is considered in the equilibrium and (c) the virtual fields are set to 0 when the sliding window contains the load point.

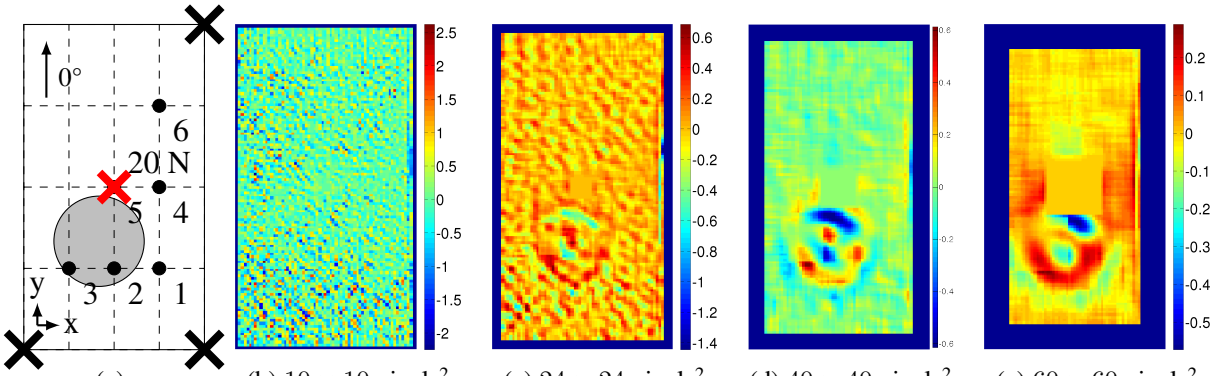

(a) (b) 10×10 pixels^2 (c) 24×24 pixels^2 (d) 40×40 pixels^2 (e) 60×60 pixels^2

S1: impacted at 15 J while clamped between two plates

Figure 4.12: EG map for the experimental results from sample S1 loaded at point 5 with a sliding pitch of 3 pixels and different sizes of sliding window.

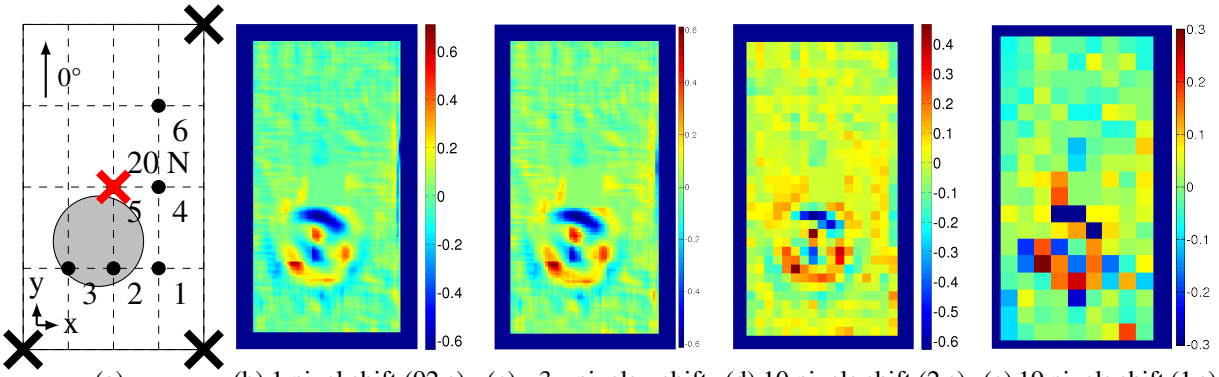

(a) (b) 1 pixel shift (92 s) (c) 3 pixels shift (11 s) (d) 10 pixels shift (2 s) (e) 19 pixels shift (1 s)

S1: impacted at 15 J while clamped between two plates

Figure 4.13: EG map for the experimental results from sample S1 loaded at point 5 with different sliding pitches and 40×40 pixels^2 sliding window. Times were measured on a laptop equipped with an Intel Core2 Duo CPU T8100 (2×2.10 GHz) and 3 Gb RAM.

10 and 19 pixels. Reducing the sliding pitch helps to define more precisely the location of the damage but increases the computational time. A sliding pitch of 3 is a good compromise here and will therefore be used in the following results.

4.5 Results

In the following representations of the equivalent strain maps, the bottom left, bottom right, and top right corners are simply supported and the load is applied at different points. Fig. 4.3 presents the loaded points and simple support conditions. Also, it must be noted that in these results the studied side is in tension whereas in the previous chapter it was the compressive side. All the figures of this section are available in Section 4.8 from page 121.

4.5.1 Undamaged specimen

Fig. 4.14 presents a schematic of the specimen with the loading points, the simple support conditions, the 0° fibre orientation, and the coordinate system.

Figs. 4.20 to 4.30 pp. 122–132 present the numerical results for the undamaged sample loaded at 20 N at points 1 to 6, respectively. The effect of the point load (local bulge) is very distinct in all three equivalent strain maps for the different loading configurations. In Fig. 4.20a, one can

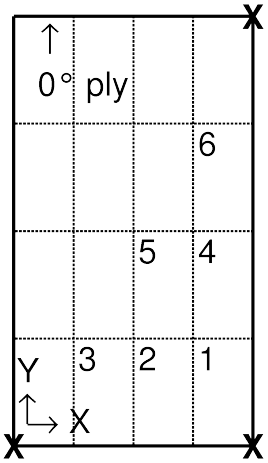

Figure 4.14: Schematic of the undamaged specimen with the simple support conditions, the 0° fibre orientation, and the coordinate system.

visualize the moment around the y-direction by looking at the red zone in the ε_x map and it is also true for the moment around x in the ε_y map Fig. 4.20b. Also, the strain level is higher in the ε_y than ε_x maps because the moment is higher in the y direction than in the x direction. In Fig. 4.20c, the inversion of sign between bottom left and right corners of shear equivalent strain is a mechanically consistent result because of the structural warping of the plate. When moving the location of the load point, the moments are varying accordingly.

Fig. 4.32 p. 134 present the EG maps for the undamaged sample loaded at different points using numerical and experimental results, respectively. Because this sample is undamaged, the map should be zero everywhere but there are some discrepancies. The first one concerns the edges all around the sample and the second one the point load. Both of them are caused by the type of finite-element model used here, a full 3D model representing all layers. Around the load point and on the edges, the plane strain assumption is violated because of a non zero through-thickness shear strain and a through-thickness compressive strain, respectively. This leads to a non zero value in the considered equilibrium. Fig. 4.15 presents the EG map for the undamaged sample loaded at point P1 using numerical data with a 1-pixel sliding pitch and a 2×2 pixels^2 sliding window. The zone over which the equilibrium is disturbed by the transverse shearing has an approximate diameter of 5 times the thickness. This is comparable to the design requirements of the short beam shear test where the span to thickness ratio should be smaller than 5. As explained previously, to compensate for *a-priori* known gaps in equilibrium, the EG values have been forced to zero when the sliding window covers the load point. If the sliding window is close to the load point but does not cover it, the computed equilibrium will also be affected because of the extent of the effect of the point load but this was ignored here as it is a minor effect for large sliding windows.

Figure 4.15: EG map for the numerical results from the undamaged sample with 1 pixels sliding pitch and 2×2 pixels^2 sliding window. The dashed circle has a diameter of 5 times the thickness.

4.5.2 S1: clamped between 2 plates during impact

Fig. 4.16 presents a schematic of the specimen with the loading points, the simple support conditions, the approximate damage location (blue area), the 0° fibre orientation, and the coordinate system.

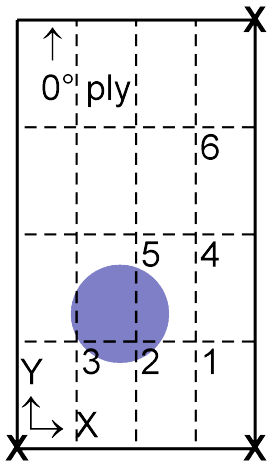

Figure 4.16: Schematic of the S1 specimen with the simple support conditions, the approximate damage location (blue area), the 0° fibre orientation, and the coordinate system.

Figs. 4.34 to 4.45 pp. 136–147 present the numerical and experimental results for sample S1 (circular cut-out impact, 15 J). Anywhere away from the damage zone, there is a very good correlation between numerical and experimental results. This means that the numerical and ex-

perimental boundary conditions (simply supported and point load) are very close and also that the material stiffness parameters are correct. Around the impacted area, the correlation is not as good as expected and the patterns vary with the loading points. Generally, it appears that the effect of experimental damage is less marked than for the numerical model, as was also evidenced on beams. This shows that the FE models need to be refined using fine CT-scans. Nevertheless, the effect of the damage on the strain fields is captured by the measurement technique even though its visual detection is not easy depending on the loading point. Also, it is visible that the boundary conditions during the impact constrained the propagation of delaminations to a 40 mm diameter area, as expected. The visible dots in Fig. 4.43 are slight loss of focus caused by the generally higher level of out-of-plane displacements.

Fig. 4.46 p. 148 and Fig. 4.47 p. 150 present the EG maps for sample S1 loaded at different points using numerical and experimental results, respectively. Regardless of the load point, the contour of the damaged zone is clearly highlighted in the maps using numerical or experimental results and the results are consistent with the c-scan Fig. 4.47a. The circular shape resulting of the boundary conditions during impact is correctly identified. The alternation of negative and positive values are partially explained by the inversion of sign in the virtual curvature fields as illustrated in Figs. 4.10b and 4.10c. Even though the correlation between numerical and experimental results is not as good as expected, both results present similar results: the orientations of the blue-red-blue-red alternations are consistent between numerical and experimental results. To improve the correlation more work should be done on the FE models. The edge effect is not visible in the maps of EG using experimental data because the experimental data have been slightly trimmed at the edges (blurred edges from the experiments).

4.5.3 Simply supported during impact

This section presents the results for the plates impacted at different energies following the ASTM-D7136 standard illustrated in Fig. 4.1.

4.5.3.1 S2: 15 J impact

Fig. 4.17 presents a schematic of the specimen with the loading points, the simple support conditions, the approximate damage location (blue area), the 0° fibre orientation, and the coordinate system.

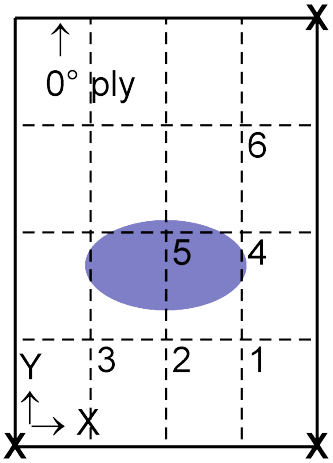

Figure 4.17: Schematic of the S2 specimen with the simple support conditions, the approximate damage location (blue area), the 0° fibre orientation, and the coordinate system.

Figs. 4.48 to 4.53 pp. 151–156 present the experimental results for sample S2 loaded at 20 N. Even though the same level of energy was used for the impact of this sample and the previous one (S1), the induced damage is less severe in this case. During the impact, more energy was stored in elastic bending deformation with the large rectangular cut-out than with the small circular one. Also the shape of the damage is not the same. Fig. 4.53b shows that the damage pattern is ellipsoidal and the main axis of this ellipse is horizontal. This is explained by the fact that the delaminations can freely propagate in any direction (no physical constraint) and that the interlaminar shear stress σ_{xz} is more important than σ_{yz} (shorter span). Therefore the delaminations propagate further along the x-direction than in the y-direction. It is easier to locate the damage in the ε_x and ε_y maps because the moments around the x and y-direction are mostly activated in these maps. The ε_s maps reveal the damage for only some load cases (P4 and P5).

Fig. 4.54 p. 158 presents the EG maps for sample S2 loaded at different points. The damage is clearly located along with its extent. The damage is clearly located along with its extent as visible in the c-scan Fig. 4.54a. The ellipsoidal shape of the contours is correctly identified regardless of the position of the load point. It is difficult to interpret the maps quantitatively because of the fact that it is sensitive to stiffness variations but also to violations of the thin plate assumptions. However, such maps could be used quantitatively to validate refined FE models of the impacted plates.

4.5.3.2 S3: 25 J impact

Fig. 4.18 presents a schematic of the specimen with the loading points, the simple support conditions, the approximate damage location (blue area), the 0° fibre orientation, and the coordinate system.

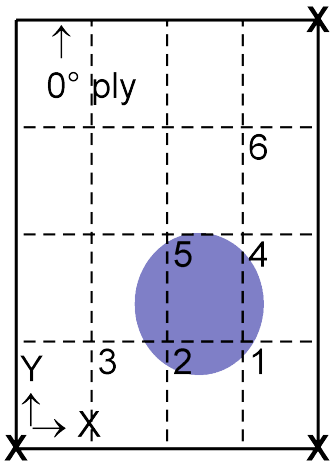

Figure 4.18: Schematic of the S3 specimen with the simple support conditions (crosses at corners), the 0° fibre orientation, the approximate damage location (blue area), and the coordinate system.

Figs. 4.55 to 4.60 pp. 159–164 present the experimental results for sample S3 loaded at 20 N at points 1 to 6, respectively. The visible mark near the centre of the right edge comes from stains on the reflective coating. The visible effect of the impact is larger because the impact energy is higher than for sample S2. The shape of the damaged region is more circular now. Also, one can notice that in the x-direction the size of the delamination is approximatively half the width which corresponds to the size of the underneath opening during the impact. This means that delaminations were prevented from propagating in this direction, explaining also why the main axis of the damage is along the vertical direction.

Fig. 4.61 p. 166 presents the EG maps for sample S3 loaded at different points. For this sample, the contour detection of the damage depends on the loading point. The c-scans are available in Fig. 4.61a to compare. For instance, loadings P2 and P6 reveal nearly all the edges of the damage whereas the others highlight only part of it. This is clearly visible in Fig. 4.61 for point P2: at the centre top of the damaged area, the equilibrium gap is nearly zero whereas the contours of the damage are highlighted.

4.5.3.3 S4: 20 J impact

Fig. 4.19 presents a schematic of the specimen with the loading points, the simple support conditions, the approximate damage location (blue area), the 0° fibre orientation, and the coordinate system. It must be emphasized that this specimen has the 0° fibre orientation parallel to the x axis (instead of the y axis for the other specimens). This means that the fibres of the surface plies are parallel to the horizontal direction. To have the same levels of strain for this sample than for the others, the load was increased to 40 N.

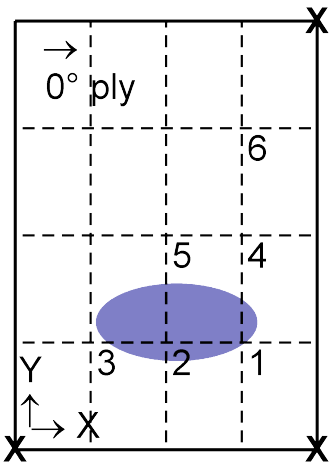

Figure 4.19: Schematic of the S4 specimen with the simple support conditions, the approximate damage location (blue area), the 0° fibre orientation, and the coordinate system.

Figs. 4.62 to 4.67 pp. 167–172 present the experimental results for sample S4 loaded at 40 N at points 1 to 6, respectively. The visible mark at the middle of the upper quarter comes from defects on the reflective coating. From the experimental maps, the damage induced by the impact seems very small and for some loading configurations the damage is only barely visible, P6 for instance Fig. 4.67. In Fig. 4.65a, the visible waves are numerical artefacts from the phase extraction algorithm. It is created by a too large distortion of the reflection of the grid. The relatively small size of the damage compared to the previous samples can be explained by the lower impact energy and the higher stiffness of the plate now along the x-axis.

Fig. 4.68 p. 174 presents the EG maps for sample S4 loaded at different points. Here the effect of the damage on the equilibrium gap is very small but still visible. Its c-scan is available in Fig. 4.68a.

4.6 Discussion

As opposed to the case of beams, visually looking at the strain maps does not necessary provide direct evidence that there is a damage. Indeed, in cantilever beams, the strain maps of undamaged specimens have very low spatial frequency contents (smooth fields) and the main strain component varies linearly with the beam length. Therefore, a local impact damage presents a very clearly visible disruption of this smooth strain field. In the case of plates with more complex loading conditions, the strain maps for undamaged plates have much richer spatial frequency contents, as illustrated in Fig. 4.21. Therefore, when a damage is present, it is much more difficult to locate and evaluate by visual inspection, as in Fig. 4.62, for instance. The idea of using the spatial frequency contents of the maps to detect the presence of damage has recently been proposed by Patki et al. [216]. Using different orthogonal polynomial decomposition, they were able to show the difference in spatial frequency contents between damaged and undamaged panels. However, the main drawbacks of this approach are that an exact undamaged reference case must be obtained. When the damaged structure is tested, the method will struggle to discriminate between spatial frequency contents differences arising from a change in boundary conditions, for instance, and from material damage. The rationale behind the damage indicator developed in the next section is to overcome these limitations by developing a more mechanical damage indicator, in the same spirit as what was proposed by Claire et al. [217]. In this case however, the strain levels involved are much smaller and the procedure is extremely challenging.

This damage indicator is very sensitive because it is based on a mechanical equilibrium. It is capable of revealing a damage (Fig. 4.68b) that is not visible in the strain maps Fig. 4.62a. This is made possible because the deflectometry technique is capable of measuring very small strains with very high resolution and spatial resolution. It would not be possible to obtain such results using stereo-correlation. Considering a resolution of $\sigma_u = 0.01\ pix$ in deflection, a pixel size of 0.1 mm and a 30-by-30 pixels subset, the resolution in displacement can be expressed in millimetres $\sigma_u = 1\ \mu m/m$ the resolution in slopes is expressed as:

$$\sigma_\theta = \frac{\partial \sigma_u}{\partial x} \tag{4.23}$$

Because discrete data are used, the resolution in curvatures can be expressed as:

$$\sigma_\theta = \sqrt{2}\frac{\sigma_u}{dx} \tag{4.24}$$

where dx is the distance between two measurement point and $dx = 30 \times 0.1 = 3\ mm$.

For the same reason, the resolution in curvatures can be expressed as:

$$\sigma_\kappa = \frac{\partial \sigma_\theta}{\partial x} = \sqrt{2}\frac{\sigma_\theta}{dx} \tag{4.25}$$

Using the Love-Kirchhoff thin plate theory, the resolution in strain can be expressed as:

$$\sigma_\varepsilon = \frac{t}{2}\sigma_\kappa \tag{4.26}$$

with t the plate thickness.

Using the experimental parameters from Tab. 4.3, one obtains:

$$\sigma_\varepsilon = 328\ \mu m/m \tag{4.27}$$

This value is much higher than the measured level of strains. This means that using stereo-correlation, the signal will be lost in noise.

The strength of this approach compared to techniques based on spatial frequency contents such as Zernike polynomials [216] for instance is the fact that it is based on a local mechanical equilibrium and does not require an undamaged reference. It is therefore insensitive to slight changes in boundary conditions. Nevertheless, this approach is currently limited to thin plates because integrals must be computed using measurement available only on the surface. It is less general than the one in [216]. Finally, to apply the present approach to real components it is necessary to extend the deflectometry to curved surfaces as it is currently limited to flat panels. However this should be possible as a similar system already exists to perform shape measurements [151, 218].

4.7 Conclusion

The experimental technique developed previously has been successfully applied to plate samples and revealed the location and extent of low energy impact damage (15 J) in composite specimens using high quality surface slope measurements provided by deflectometry. It was shown that the various stiffness components are activated in different proportions when the point of the applied load changes. Comparing numerical and experimental results showed a correlation not as good as expected. Some work should therefore be done on the finite element analysis to improve the correlation by modelling more accurately the structure and behaviour

of the impacted zone using fine CT-scans of these samples. It could also be interesting to study the effect of friction and/or fibre-bridging for various delamination sizes.

A damage indicator based on the virtual fields method was presented and applied to numerical and experimental data. It revealed the location and extent of the damage even when the damage was barely visible in the strain maps. This indicator is sensitive to violation of the thin plate theory and to stiffness variations. It reveals the impact by highlighting the contours of the damaged regions. Two parameters can be adjusted to optimize the computational time and the robustness to noise. Combined with the work reported in [149], this indicator could be used to parameterize the damage and the standard VFM could be applied with this *a-priori* knowledge to identify the stiffnesses in the damaged and undamaged areas, for instance. Some work can be done on the formulation of the virtual fields: optimizing the choice of the virtual degrees of freedom and/or varying the number of elements. In order to apply the current methodology on real components, some work is required to extend the experimental technique to curved surfaces starting with a technique to obtain mirror-like finish on curved surfaces. Also, it could be interesting to apply this technique to thick plates. For that, some work is required on the formulation of the damage indicator.

4.8 Figures

4.8.1 undamaged - P1 - Numerical strain maps

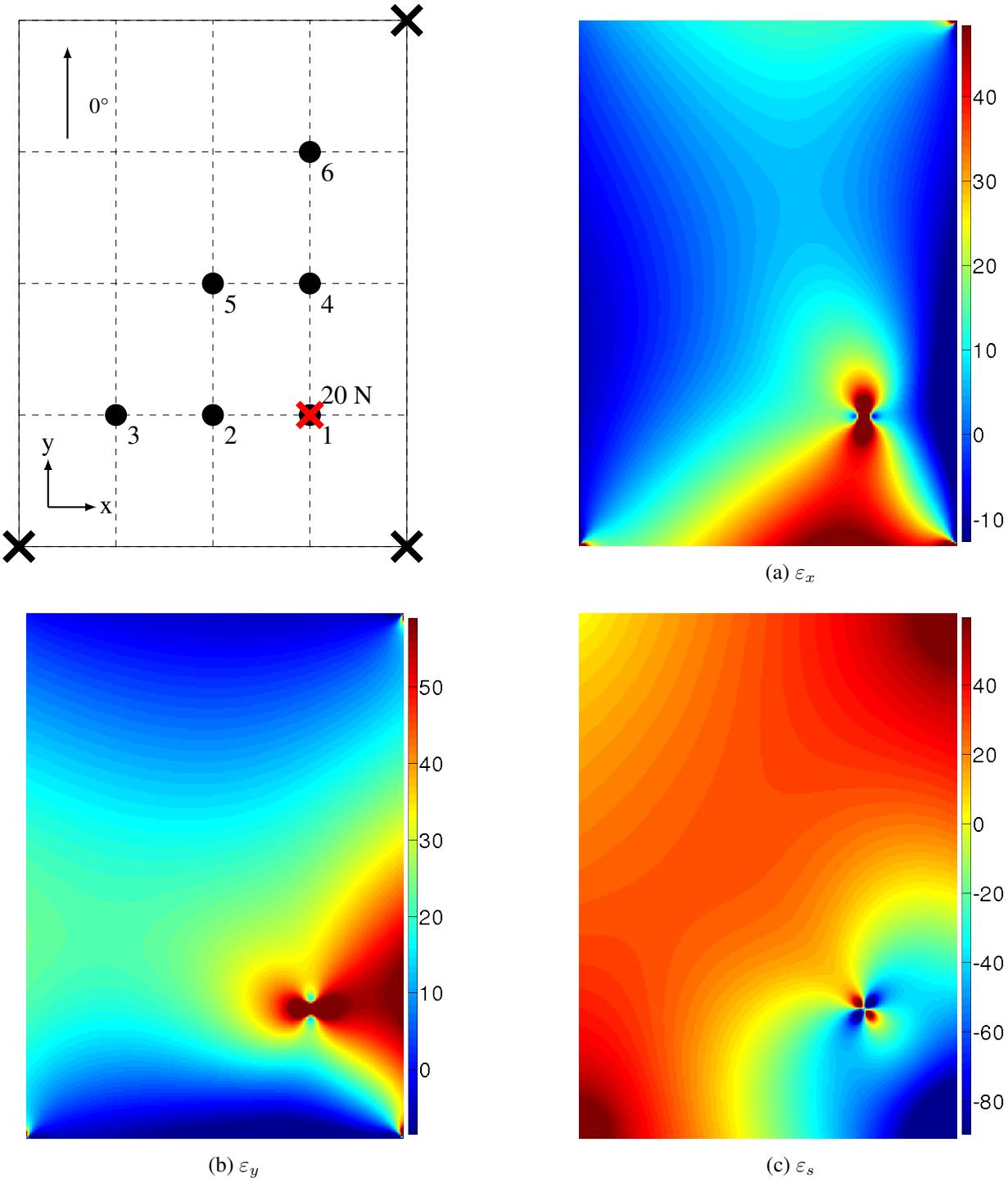

(a) ε_x

(b) ε_y

(c) ε_s

Figure 4.20: Numerical equivalent strain maps for the undamaged case loaded at point 1 with 20 N (in µm/m).

4.8.2 undamaged - P1 - Experimental strain maps

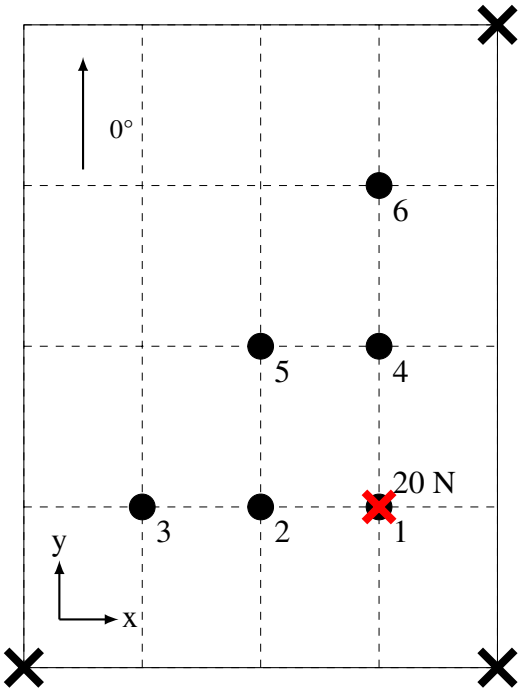

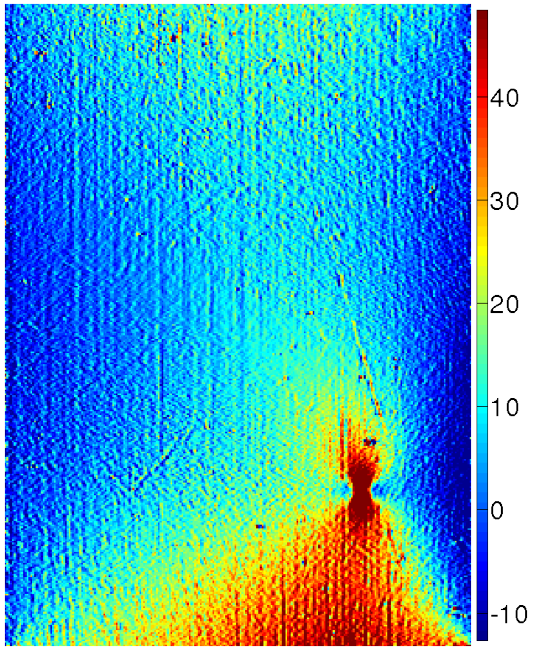

(a) ε_x

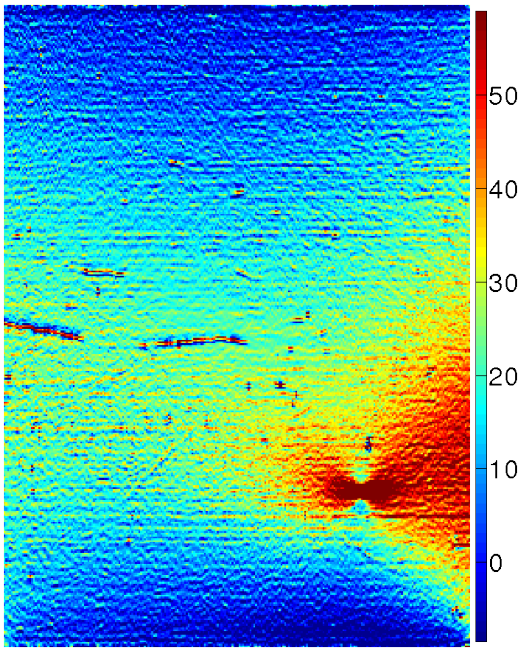

(b) ε_y

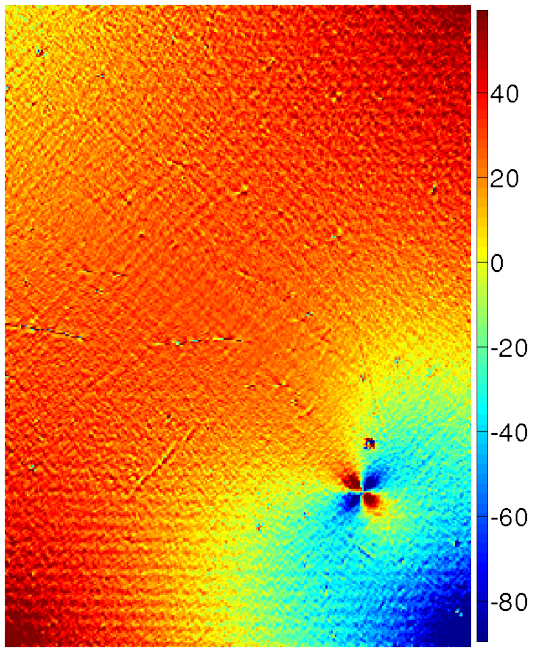

(c) ε_s

Figure 4.21: Experimental equivalent strain maps for the undamaged case loaded at point 1 with 20 N (in µm/m).

4.8.3 undamaged - P2 - Numerical strain maps

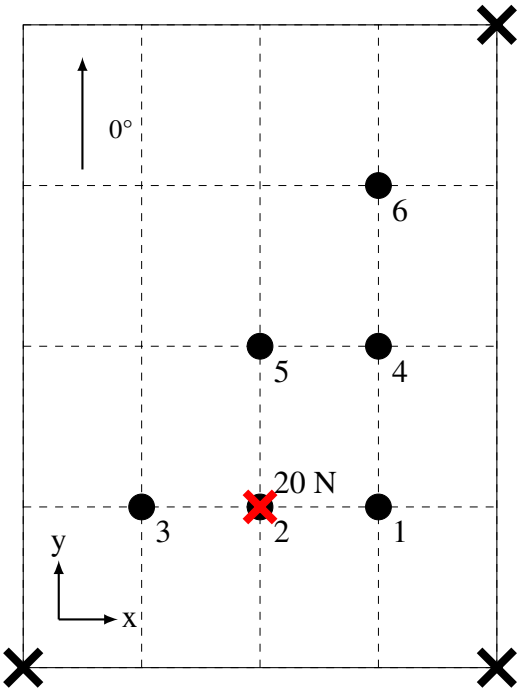

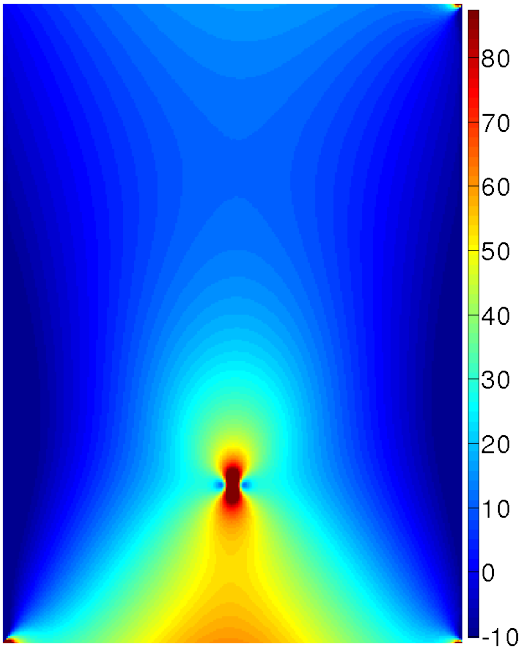

(a) ε_x

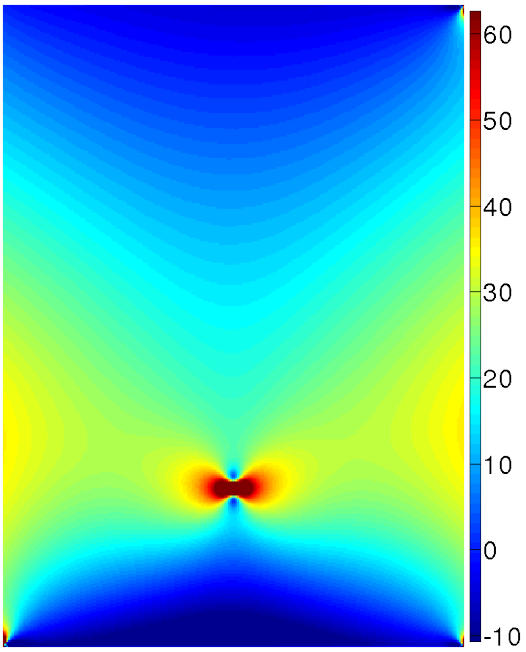

(b) ε_y

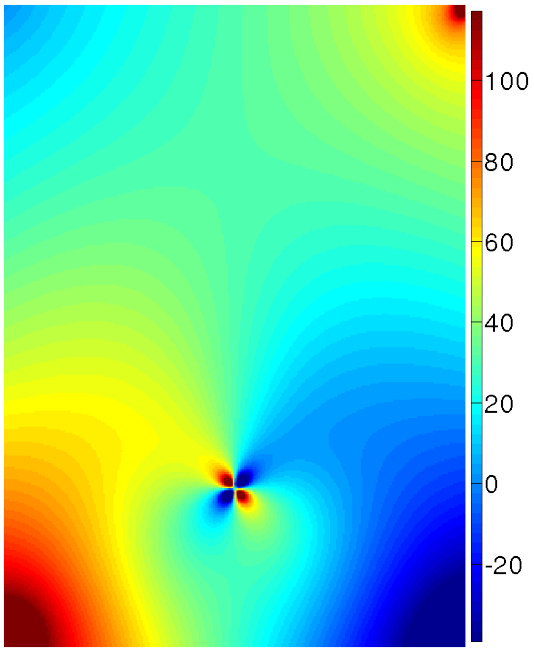

(c) ε_s

Figure 4.22: Numerical equivalent strain maps for the undamaged case loaded at point 2 with 20 N (in µm/m).

4.8.4 undamaged - P2 - Experimental strain maps

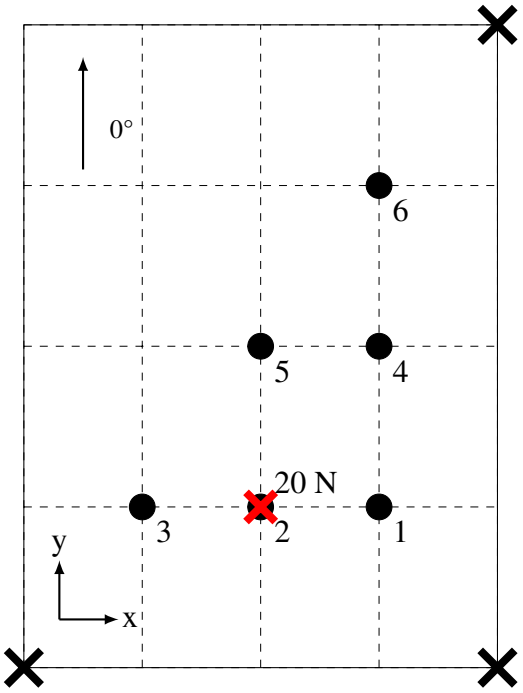

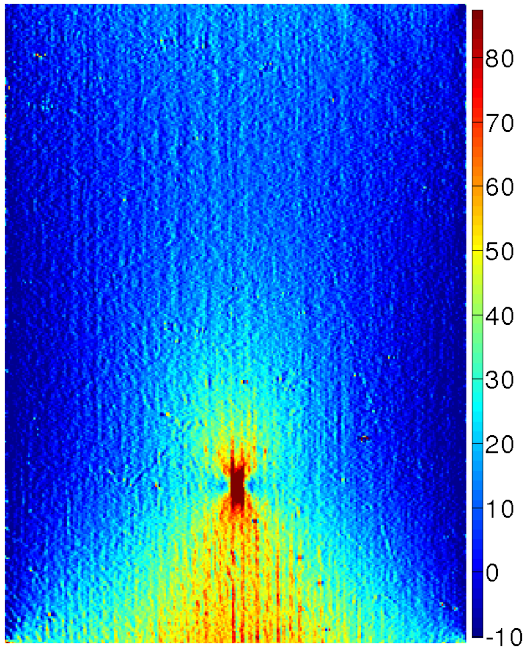

(a) ε_x

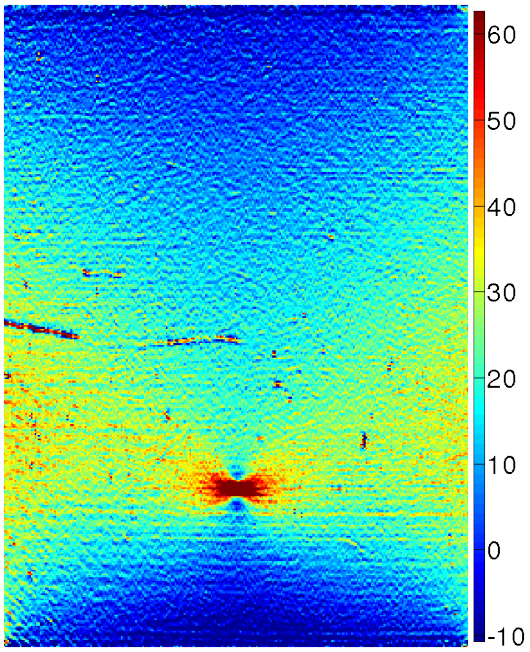

(b) ε_y

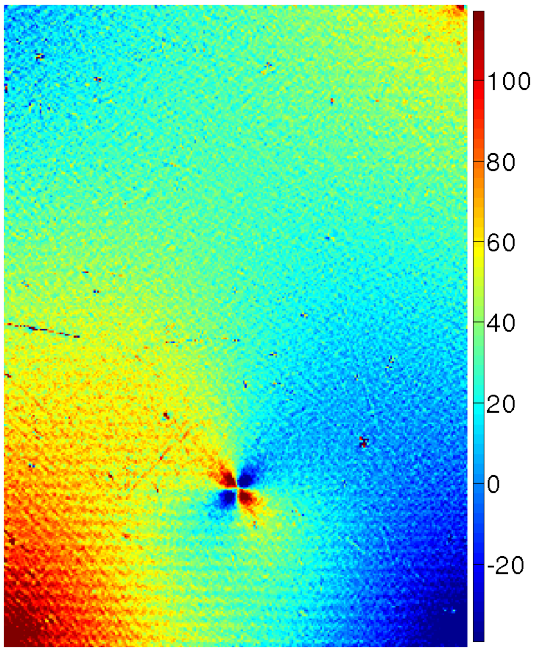

(c) ε_s

Figure 4.23: Experimental equivalent strain maps for the undamaged case loaded at point 2 with 20 N (in µm/m).

4.8.5 undamaged - P3 - Numerical strain maps

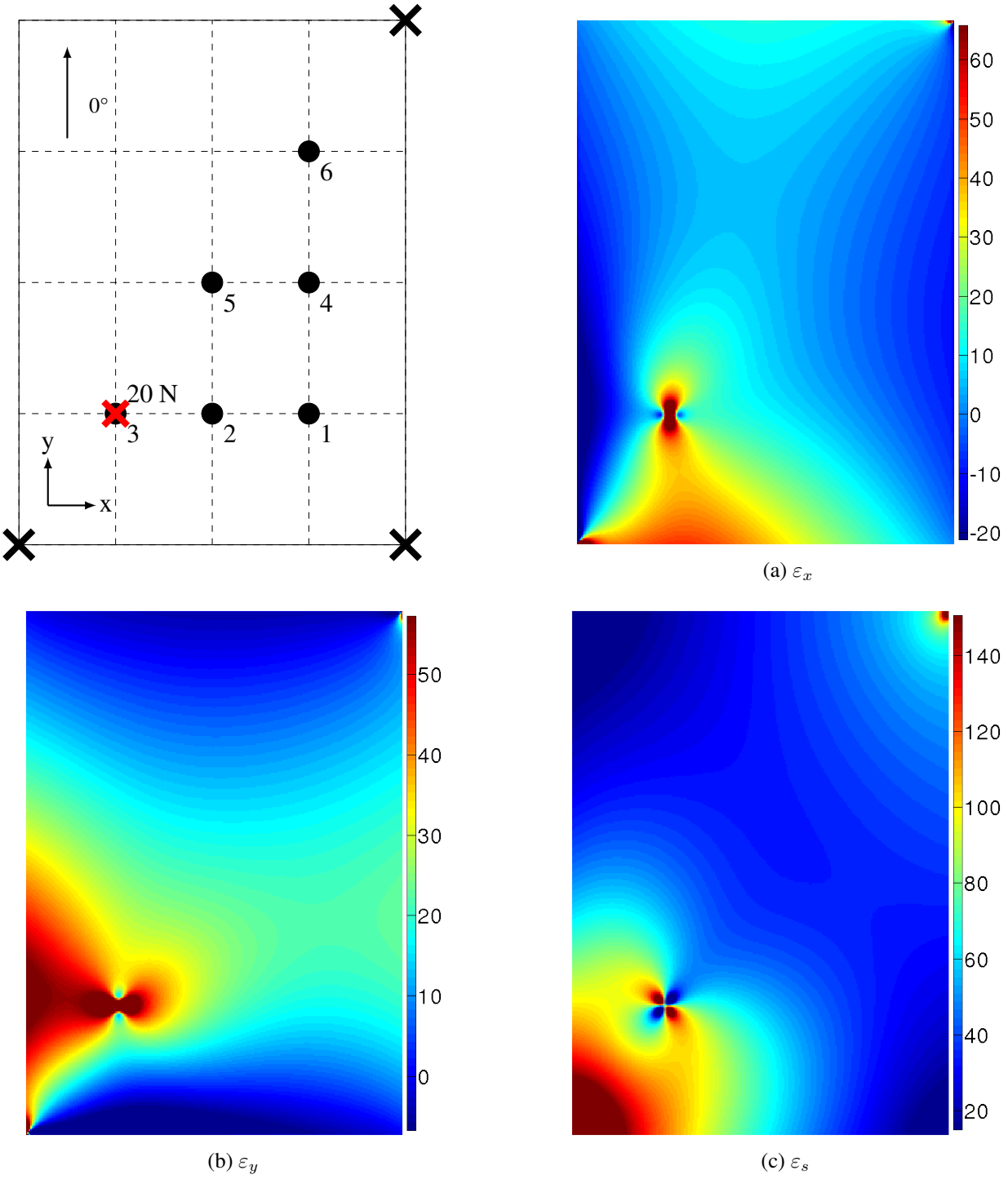

(a) ε_x

(b) ε_y

(c) ε_s

Figure 4.24: Numerical equivalent strain maps for the undamaged case loaded at point 3 with 20 N (in µm/m).

4.8.6 undamaged - P3 - Experimental strain maps

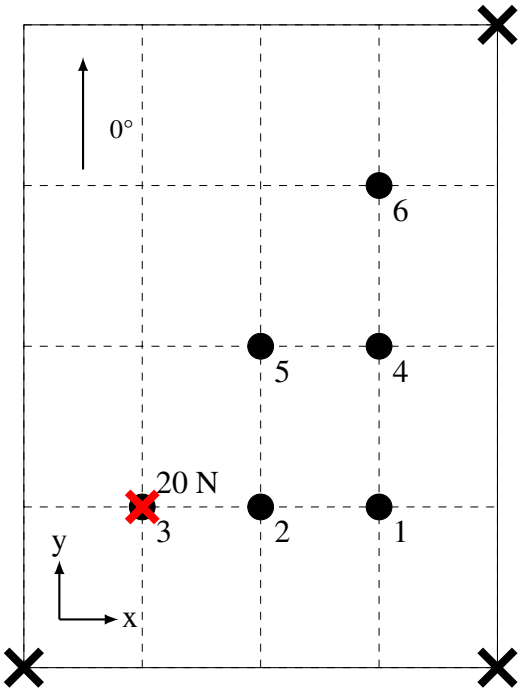

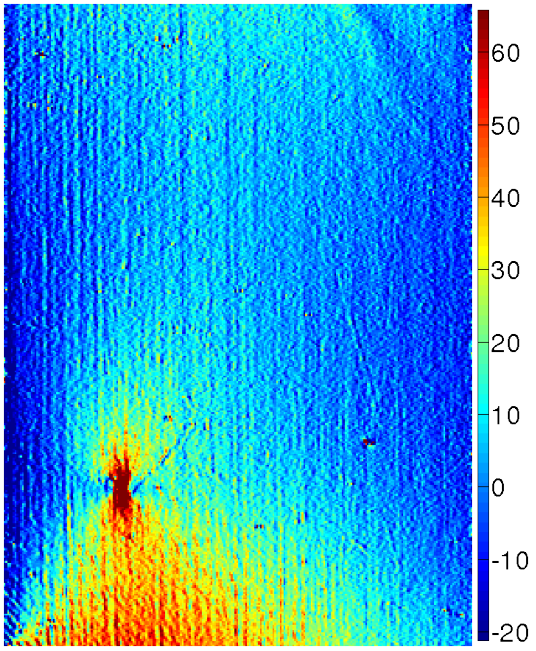

(a) ε_x

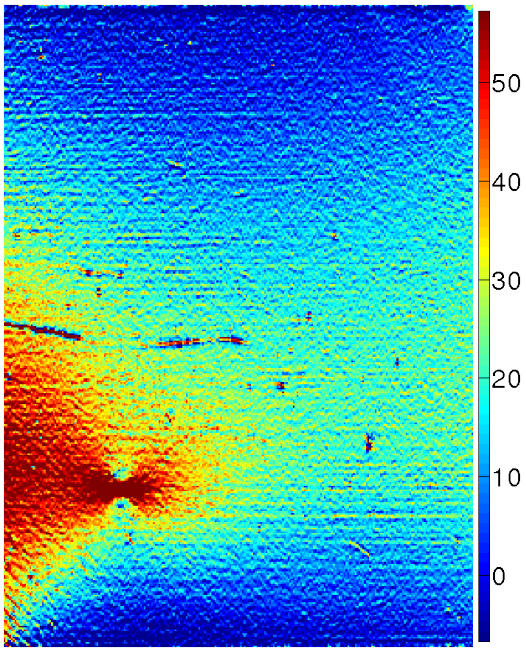

(b) ε_y

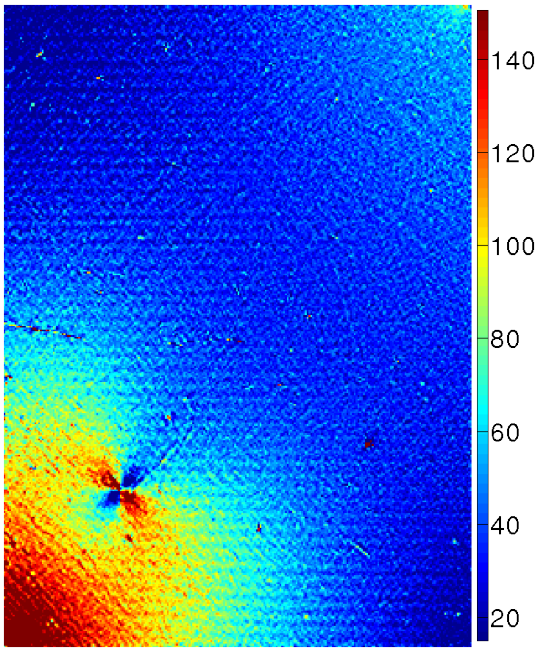

(c) ε_s

Figure 4.25: Experimental equivalent strain maps for the undamaged case loaded at point 3 with 20 N (in µm/m).

4.8.7 undamaged - P4 - Numerical strain maps

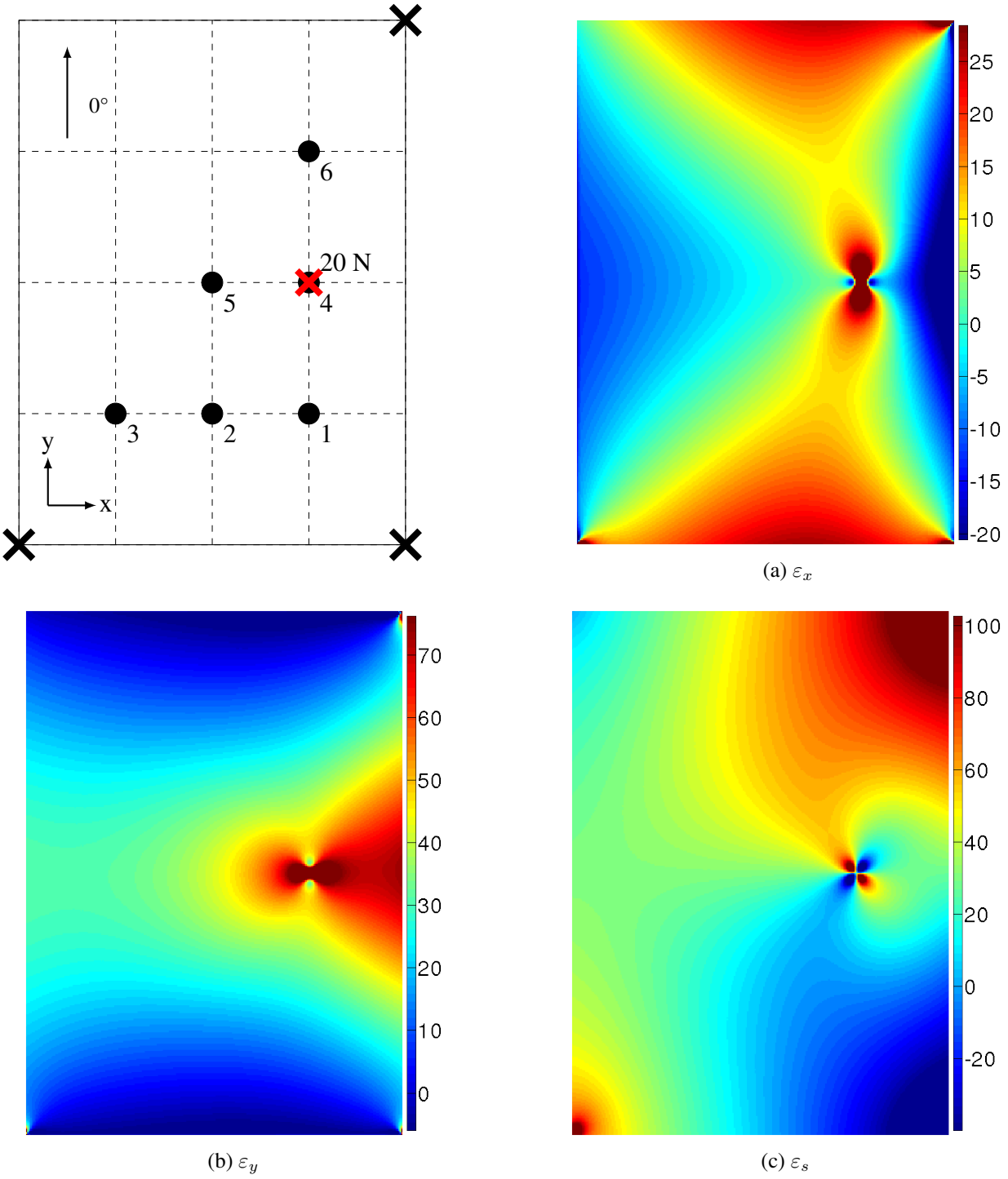

(a) ε_x

(b) ε_y

(c) ε_s

Figure 4.26: Numerical equivalent strain maps for the undamaged case loaded at point 4 with 20 N (in µm/m).

4.8.8 undamaged - P4 - Experimental strain maps

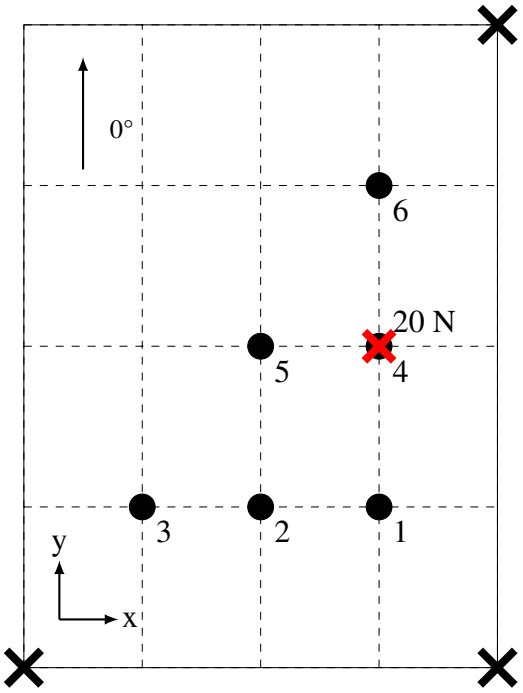

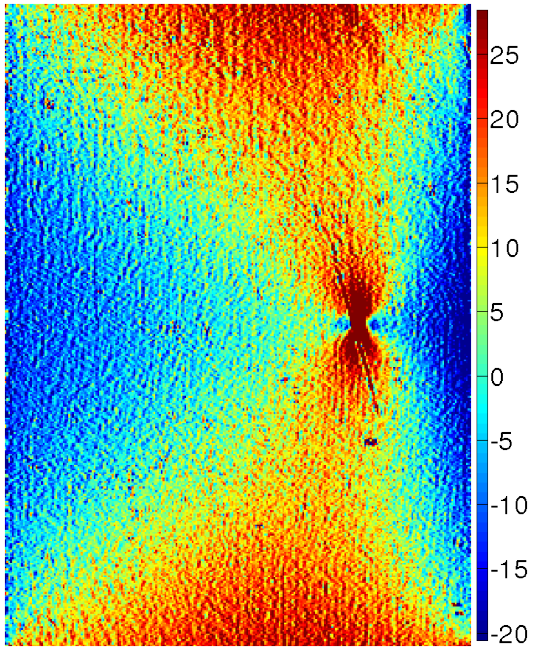

(a) ε_x

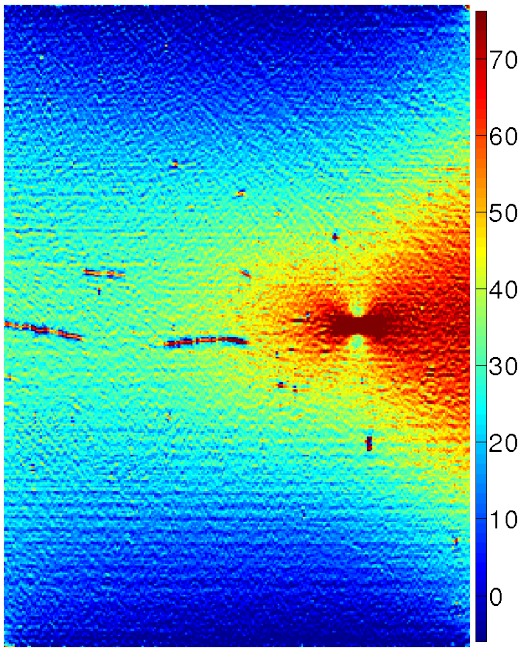

(b) ε_y

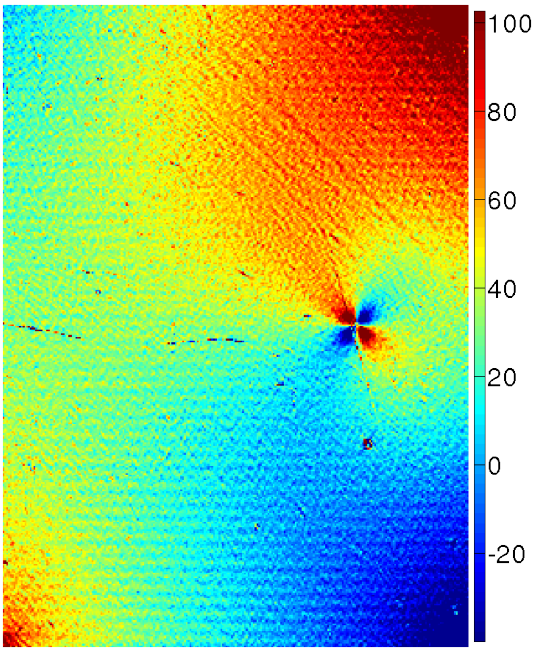

(c) ε_s

Figure 4.27: Experimental equivalent strain maps for the undamaged case loaded at point 4 with 20 N (in µm/m).

4.8.9 undamaged - P5 - Numerical strain maps

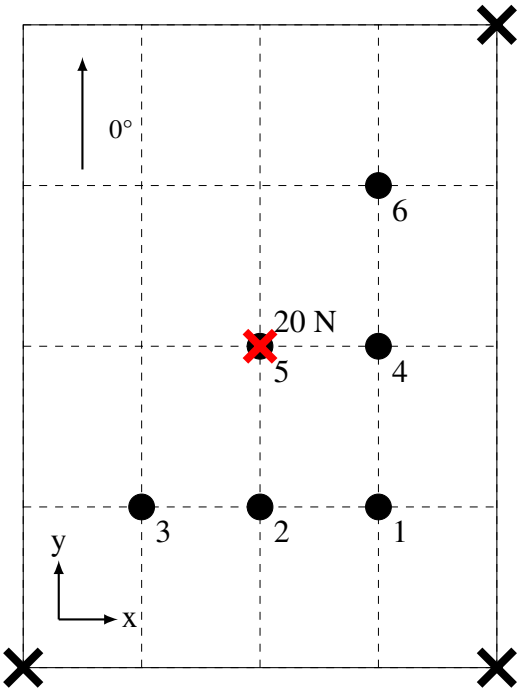

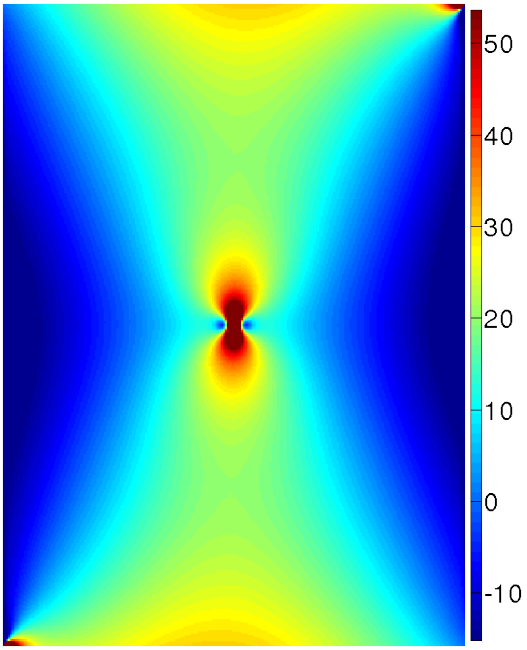

(a) ε_x

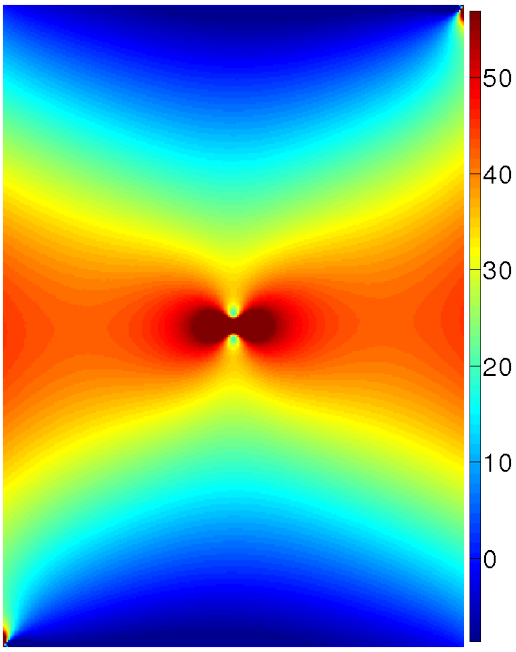

(b) ε_y

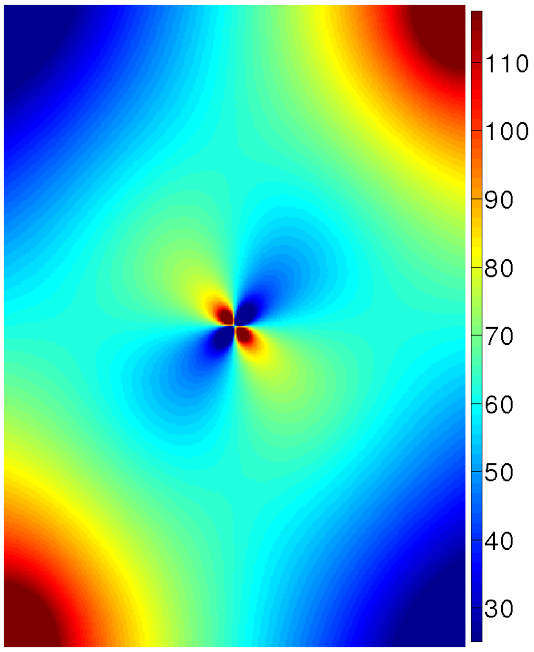

(c) ε_s

Figure 4.28: Numerical equivalent strain maps for the undamaged case loaded at point 5 with 20 N (in µm/m).

4.8.10 undamaged - P5 - Experimental strain maps

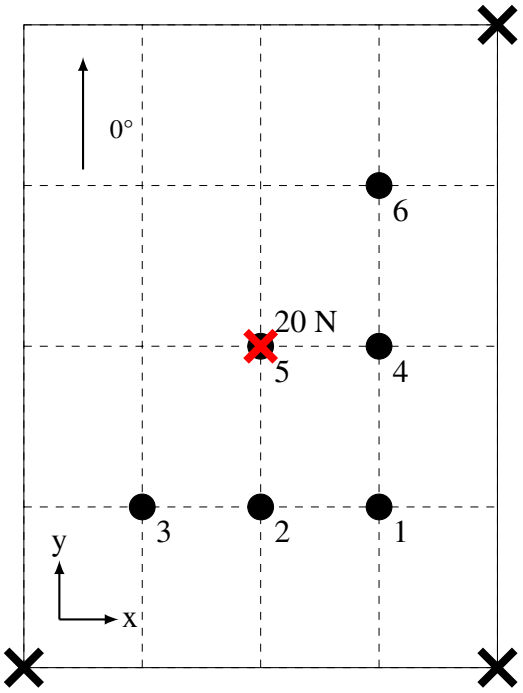

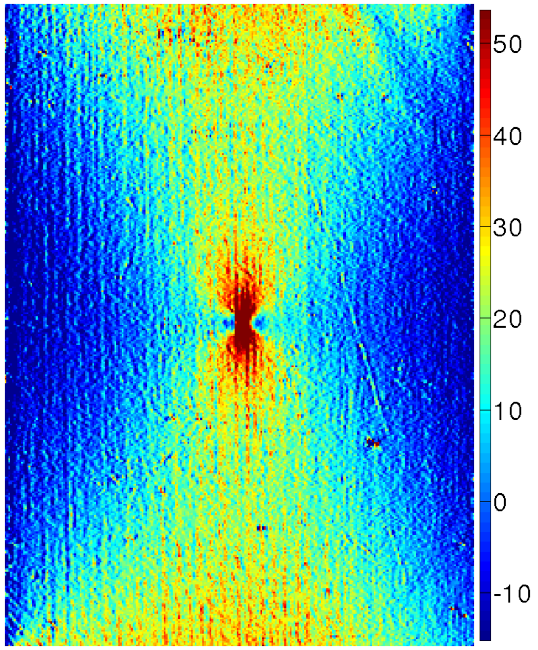

(a) ε_x

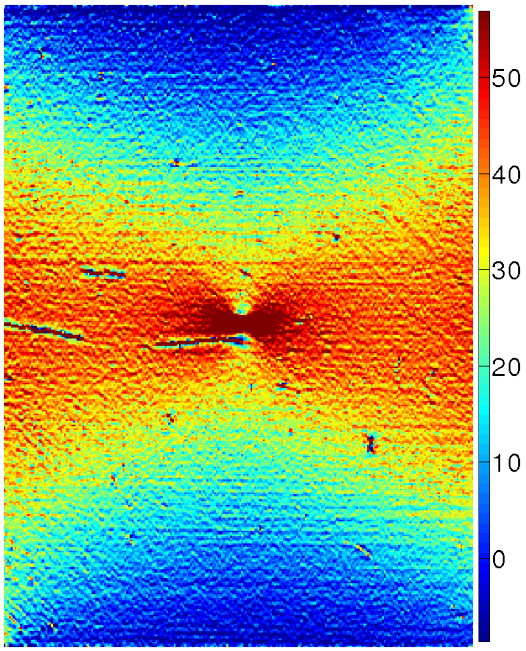

(b) ε_y

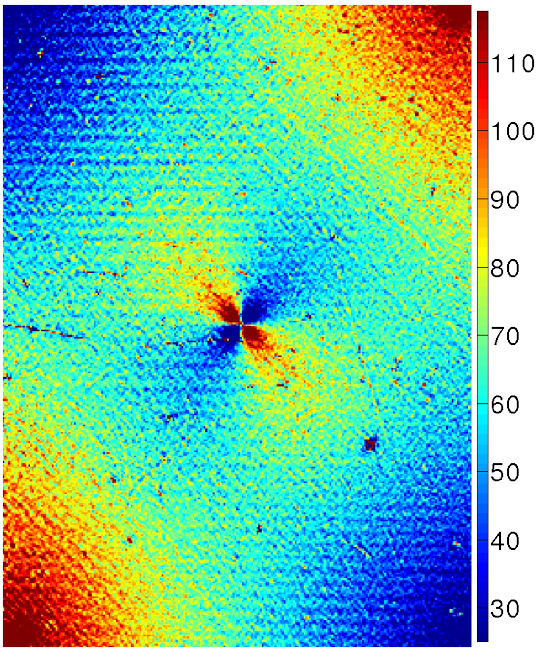

(c) ε_s

Figure 4.29: Experimental equivalent strain maps for the undamaged case loaded at point 5 with 20 N (in µm/m).

4.8.11 undamaged - P6 - Numerical strain maps

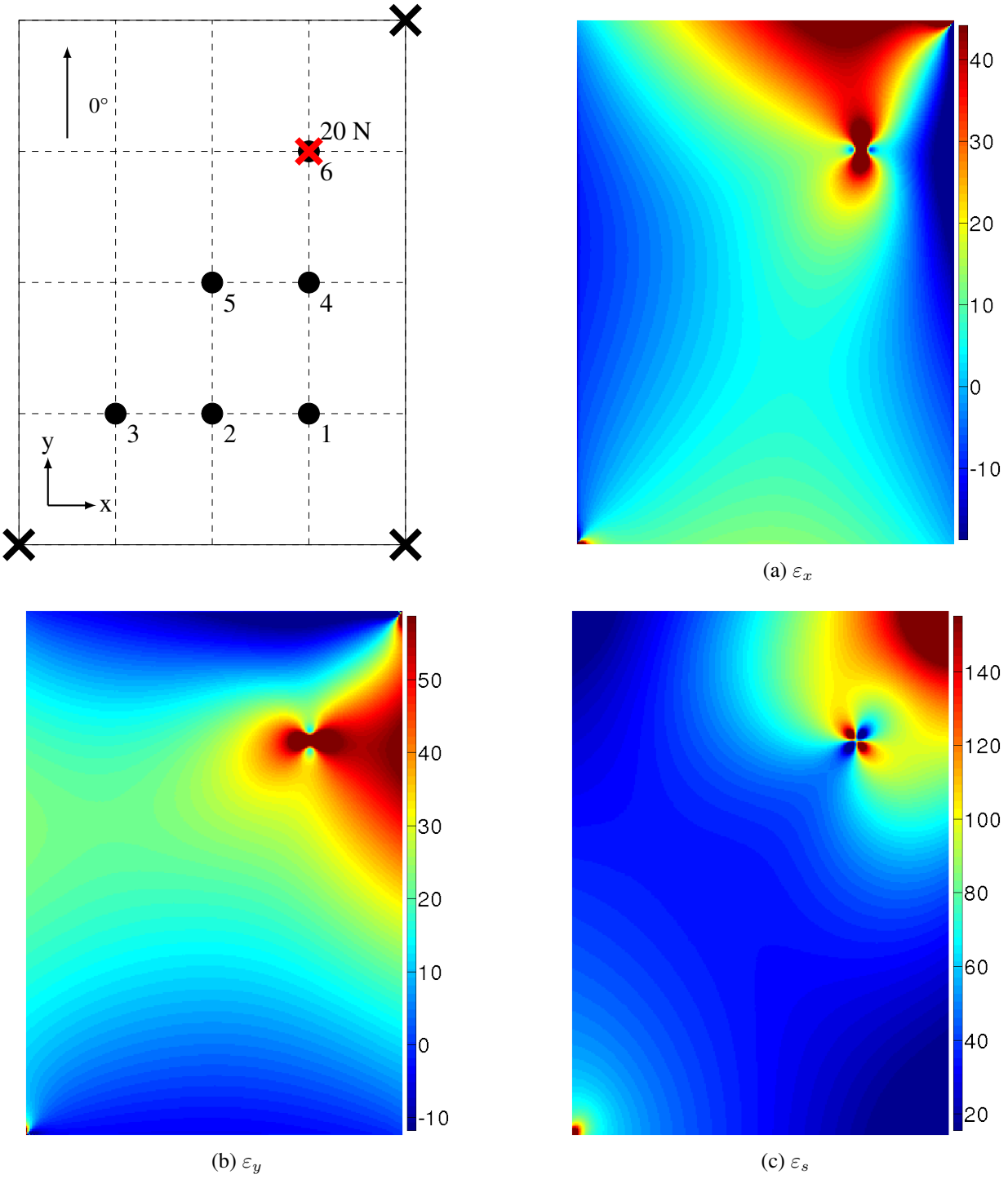

(a) ε_x

(b) ε_y

(c) ε_s

Figure 4.30: Numerical equivalent strain maps for the undamaged case loaded at point 6 with 20 N (in µm/m).

4.8.12 undamaged - P6 - Experimental strain maps

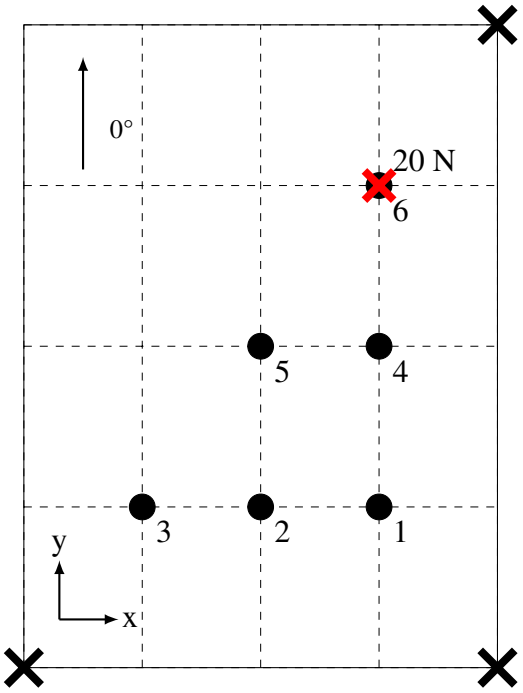

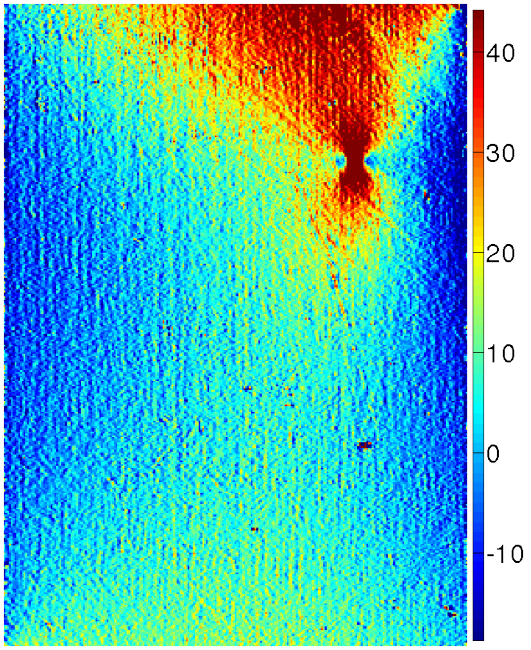

(a) ε_x

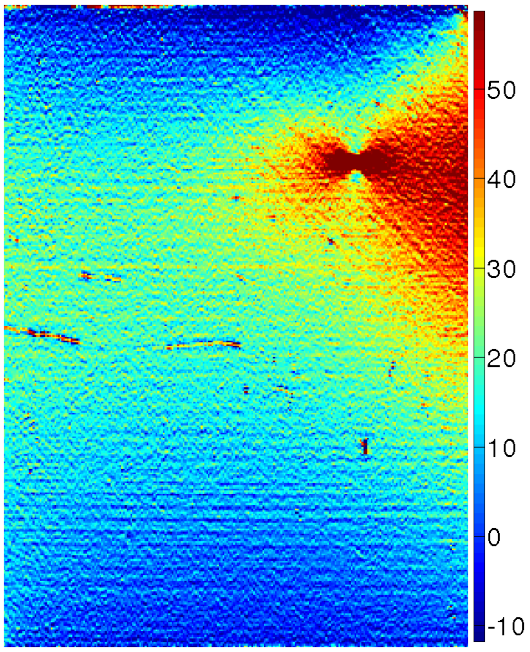

(b) ε_y

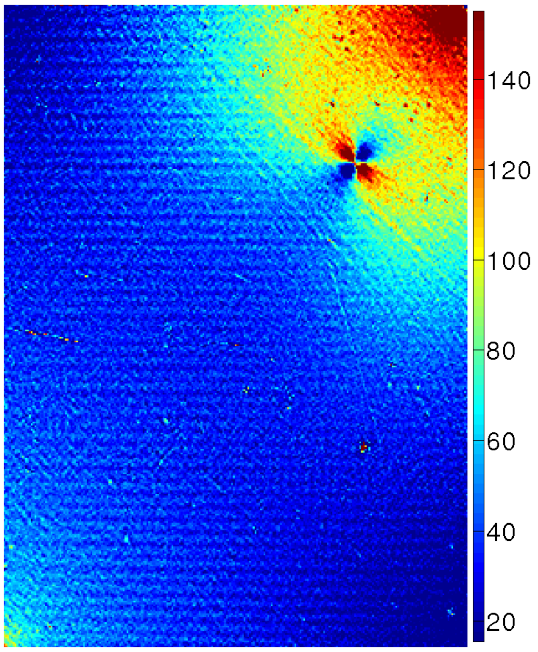

(c) ε_s

Figure 4.31: Experimental equivalent strain maps for the undamaged case loaded at point 6 with 20 N (in µm/m).

4.8.13 undamaged - Numerical EG maps

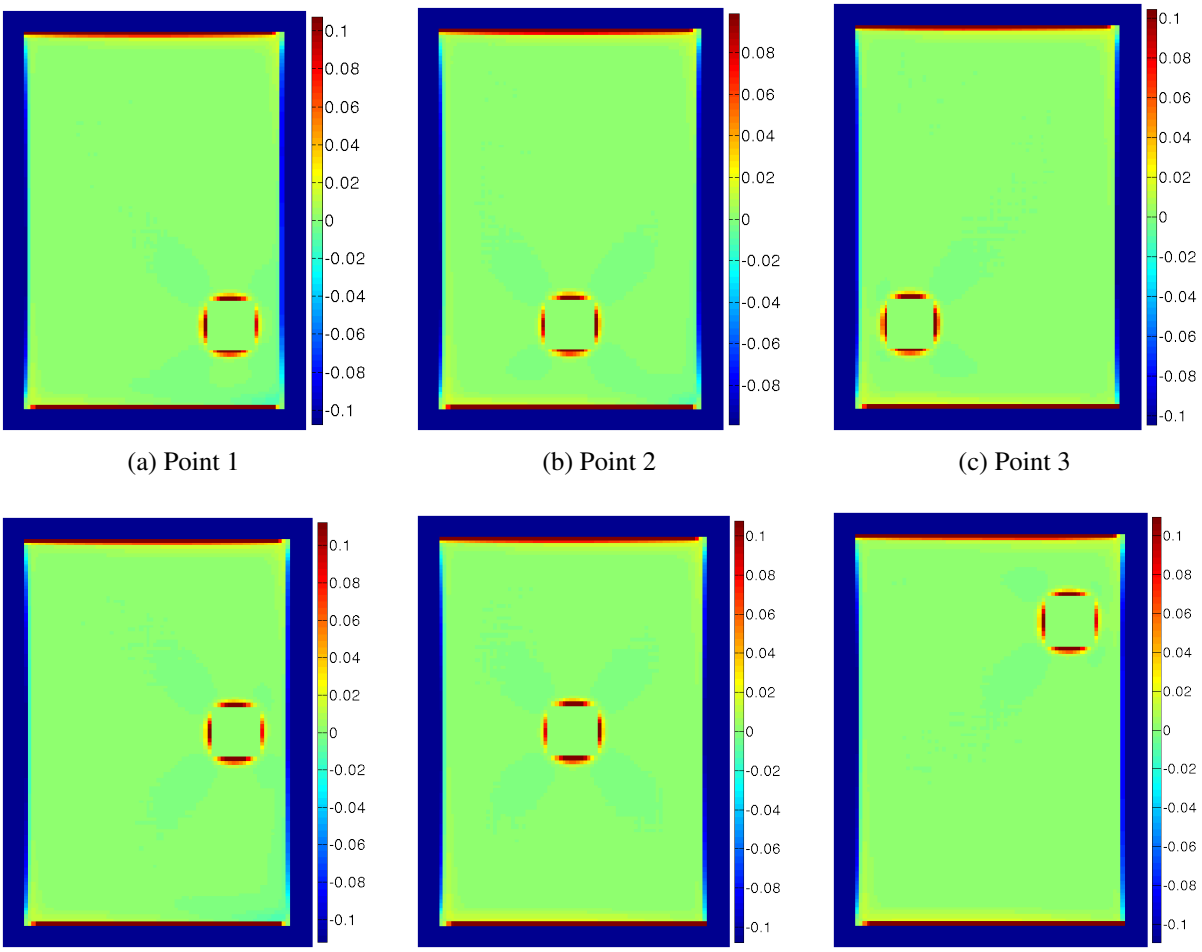

(a) Point 1 (b) Point 2 (c) Point 3

(d) Point 4 (e) Point 5 (f) Point 6

Figure 4.32: EG map for the numerical results from the undamaged sample with 3 pixels sliding pitch and 40×40 pixels^2 sliding window.

4.8.14 undamaged - Experimental EG maps

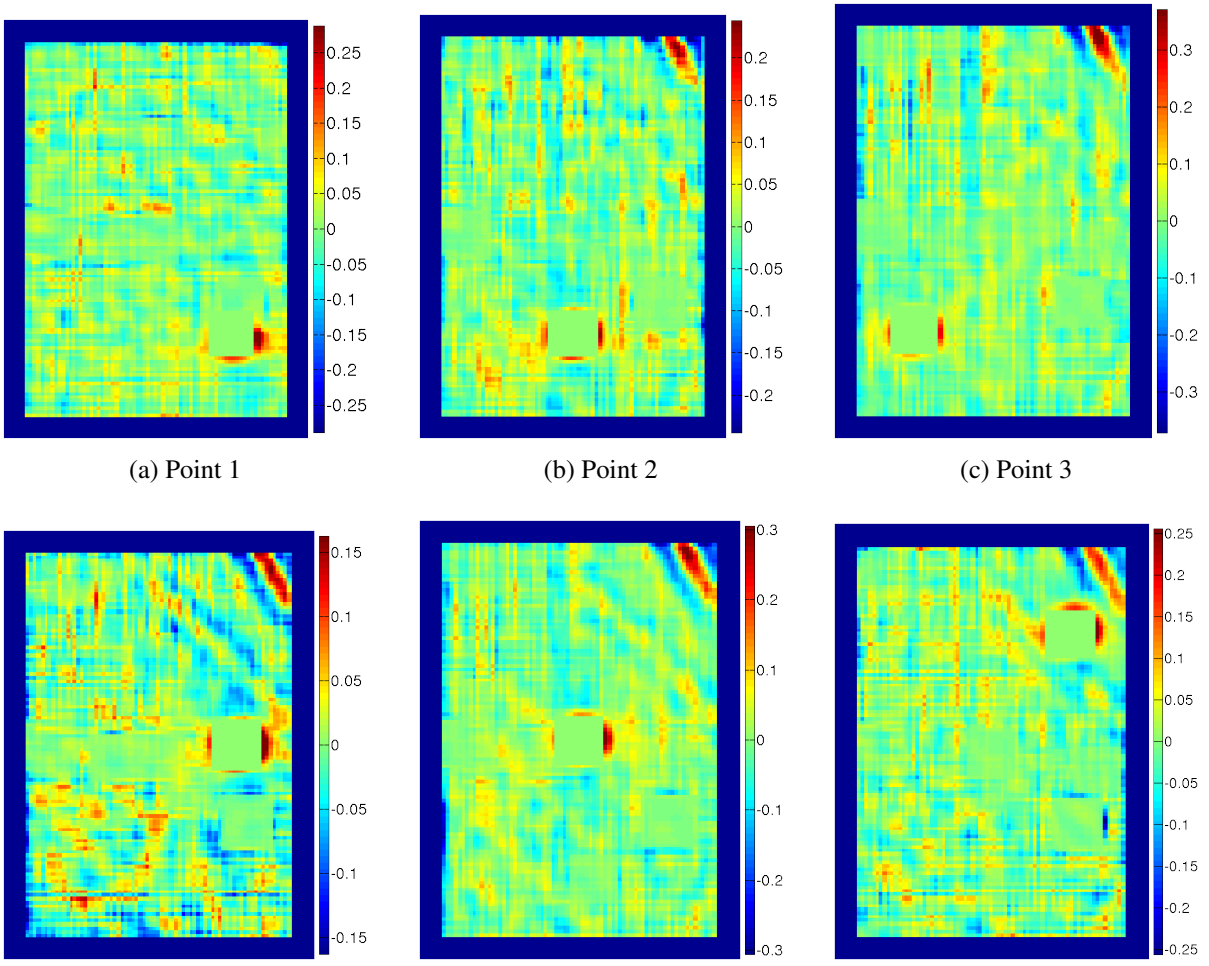

(a) Point 1 (b) Point 2 (c) Point 3

(d) Point 4 (e) Point 5 (f) Point 6

Figure 4.33: EG map for the experimental results from the undamaged sample with 3 pixels sliding pitch and 40×40 pixels^2 sliding window.

4.8.15 S1 - P1 - Numerical strain maps

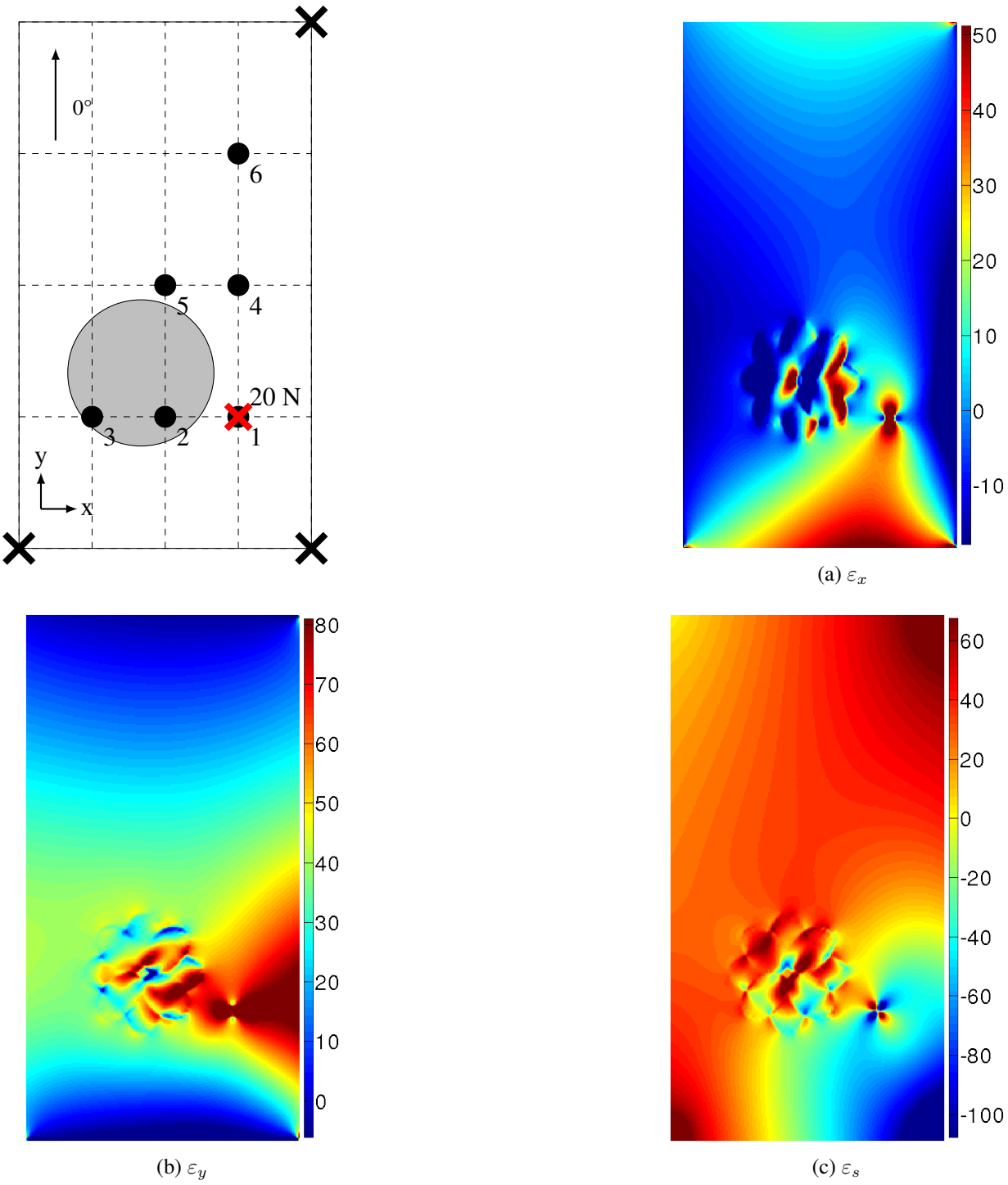

(a) ε_x

(b) ε_y

(c) ε_s

S1: impacted at 15 J while clamped between two plates

Figure 4.34: Numerical equivalent strain maps for the S1 case loaded at point 1 with 20 N (in µm/m).

4.8.16 S1 - P1 - Experimental strain maps

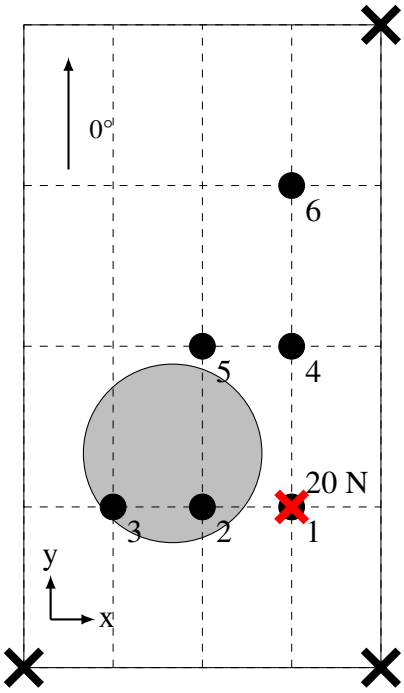

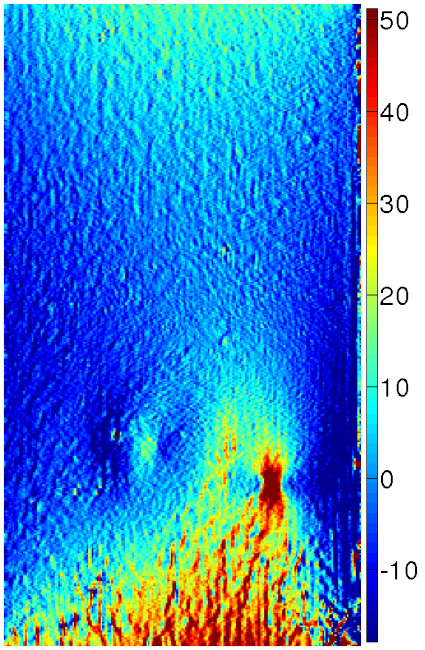

(a) ε_x

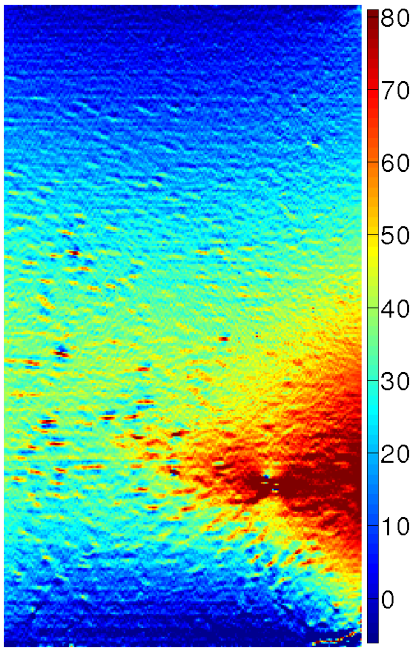

(b) ε_y

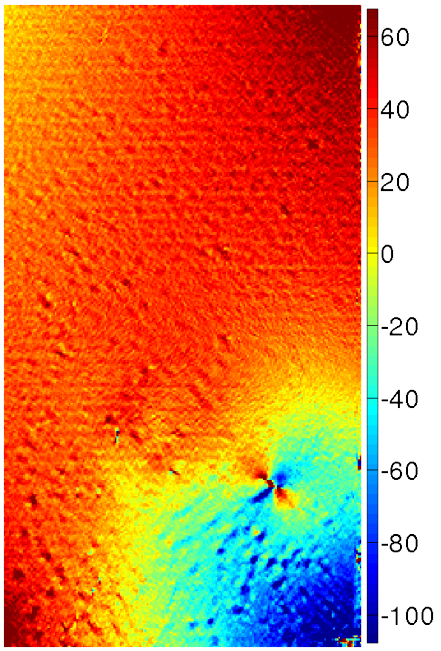

(c) ε_s

S1: impacted at 15 J while clamped between two plates

Figure 4.35: Experimental equivalent strain maps for the S1 case loaded at point 1 with 20 N (in µm/m).

4.8.17 S1 - P2 - Numerical strain maps

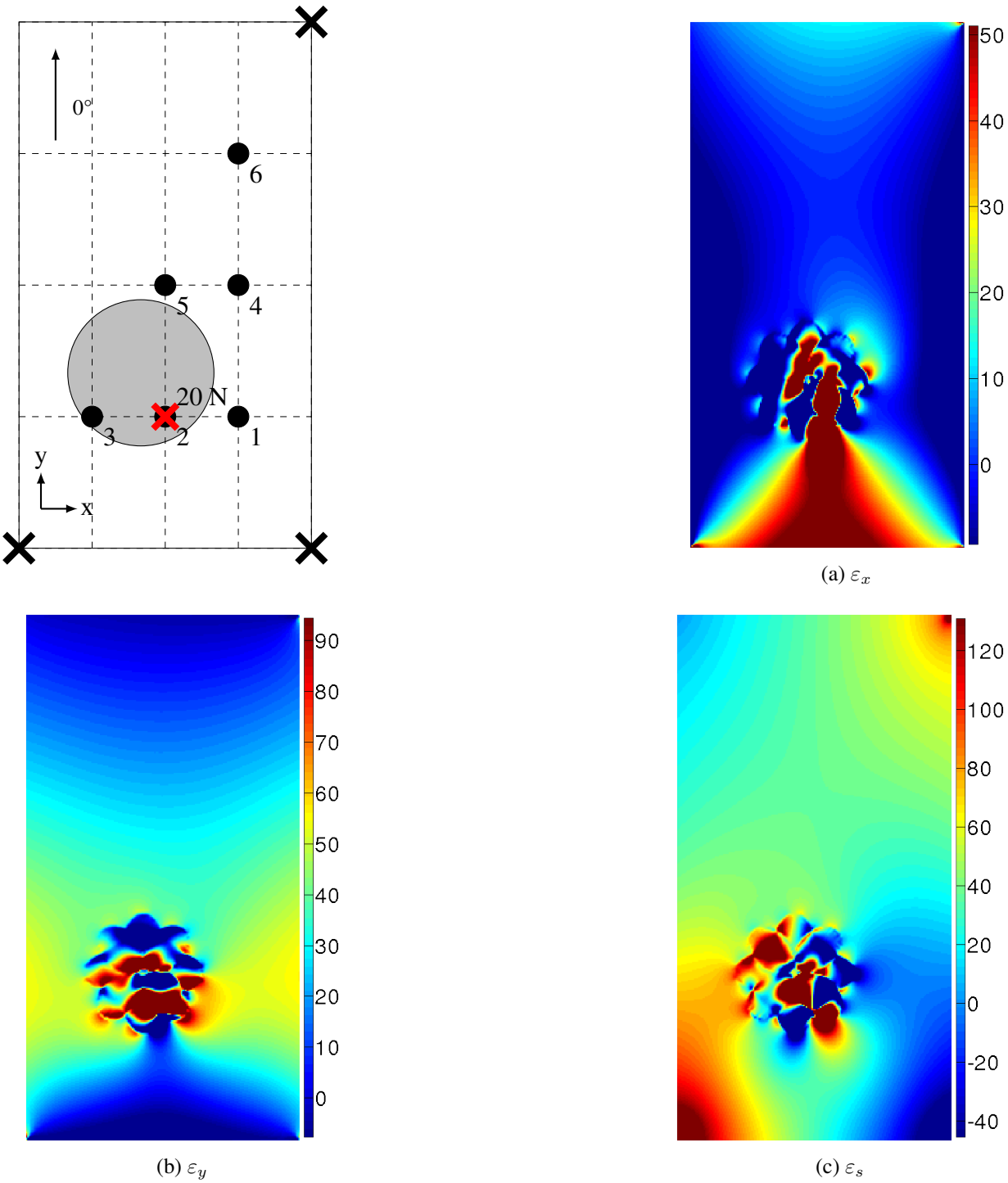

(a) ε_x

(b) ε_y

(c) ε_s

S1: impacted at 15 J while clamped between two plates

Figure 4.36: Numerical equivalent strain maps for the S1 case loaded at point 2 with 20 N (in µm/m).

4.8.18 S1 - P2 - Experimental strain maps

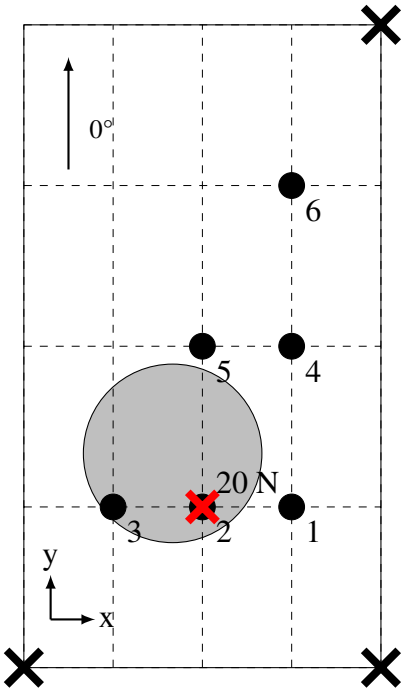

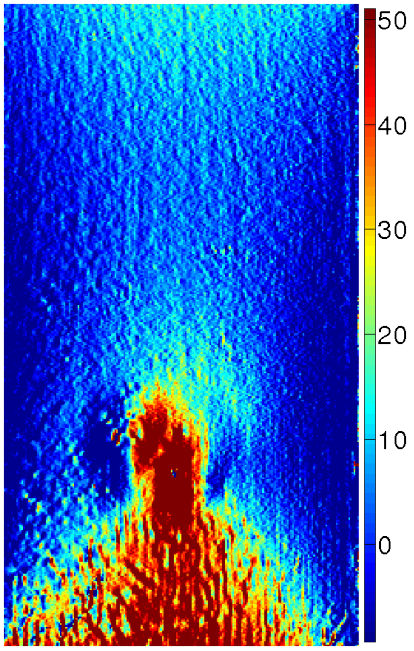

(a) ε_x

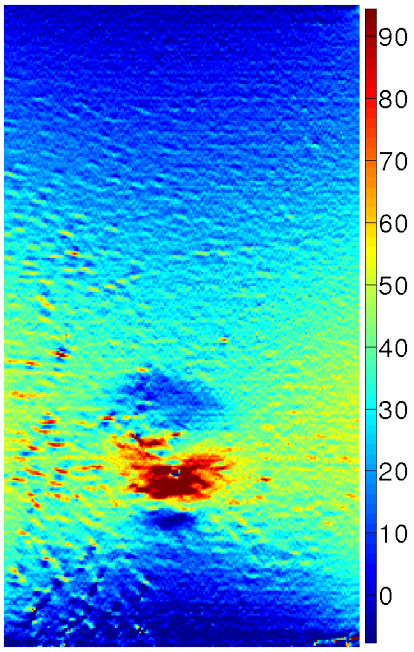

(b) ε_y

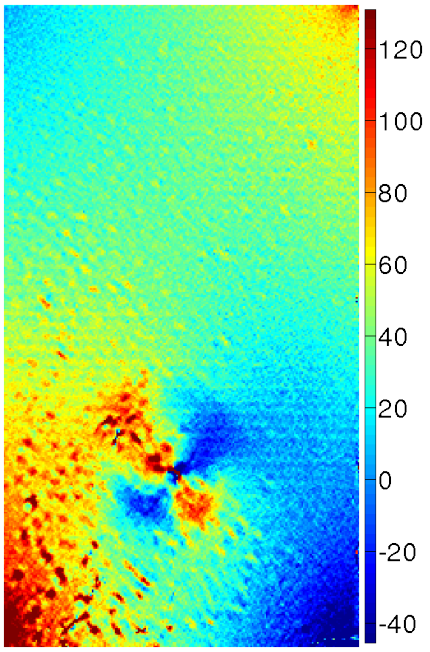

(c) ε_s

S1: impacted at 15 J while clamped between two plates

Figure 4.37: Experimental equivalent strain maps for the S1 case loaded at point 2 with 20 N (in µm/m).

4.8.19 S1 - P3 - Numerical strain maps

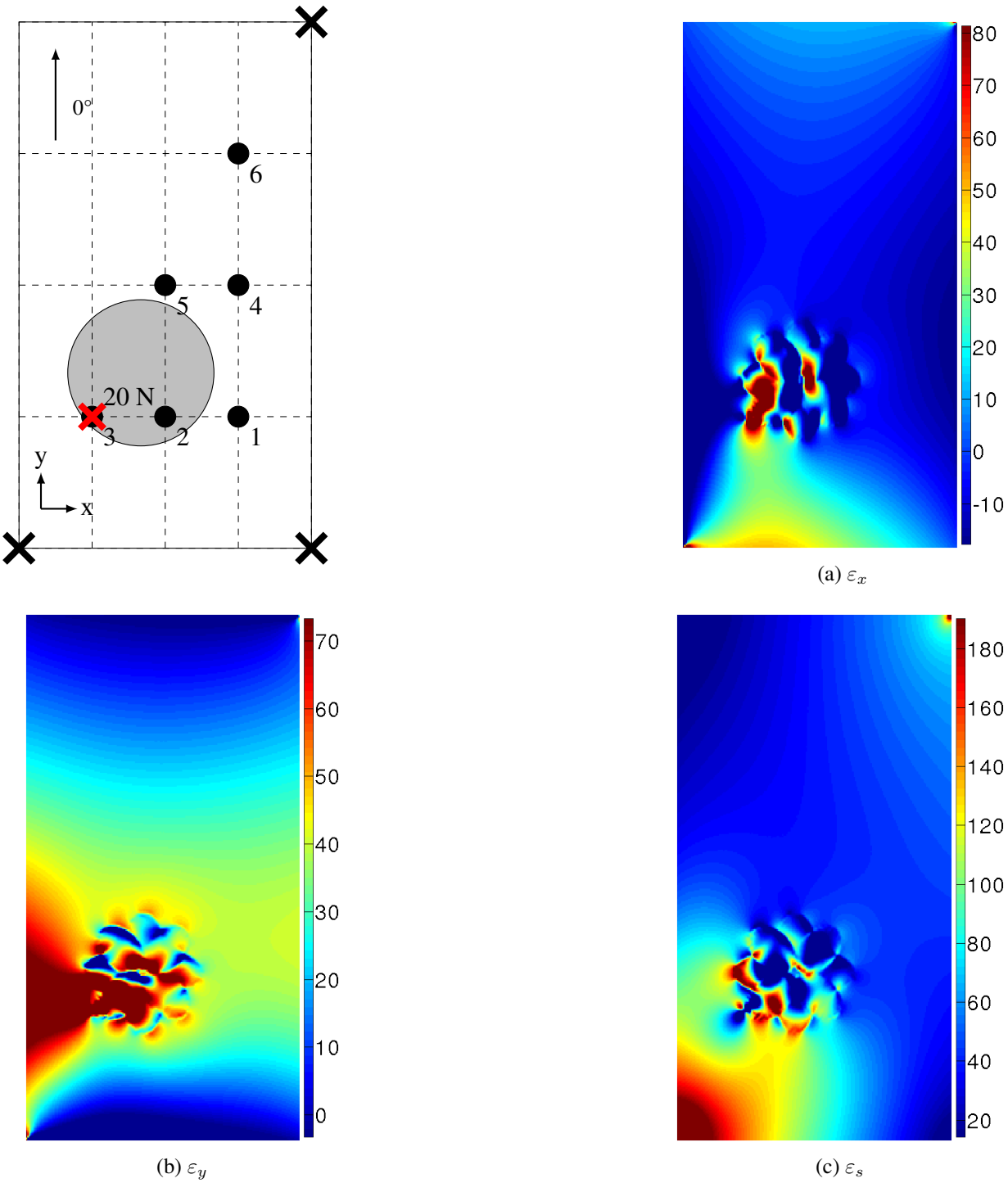

(a) ε_x

(b) ε_y

(c) ε_s

S1: impacted at 15 J while clamped between two plates

Figure 4.38: Numerical equivalent strain maps for the S1 case loaded at point 3 with 20 N (in µm/m).

4.8.20 S1 - P3 - Experimental strain maps

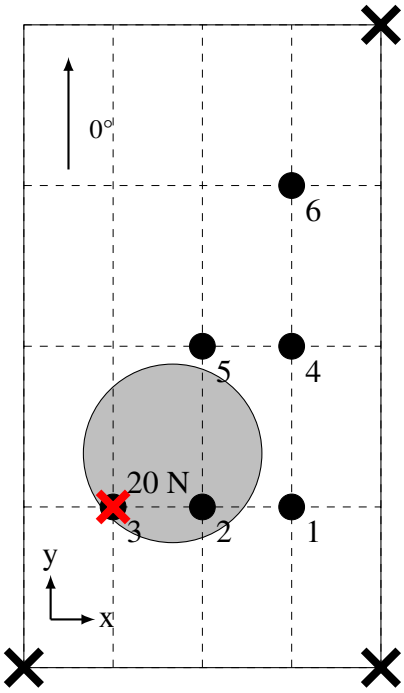

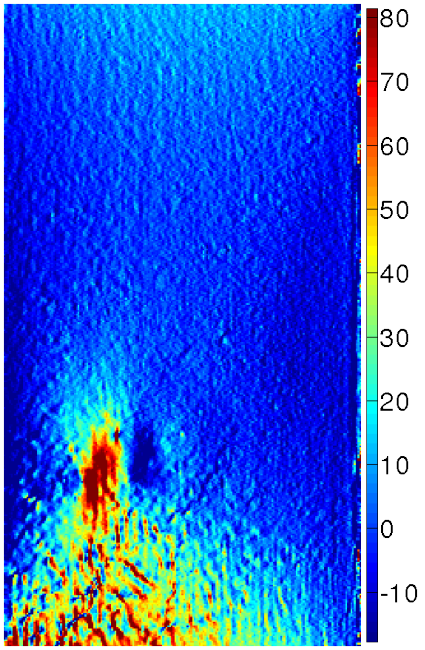

(a) ε_x

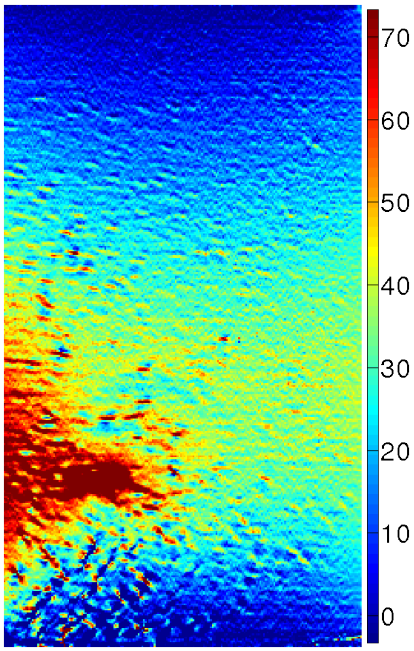

(b) ε_y

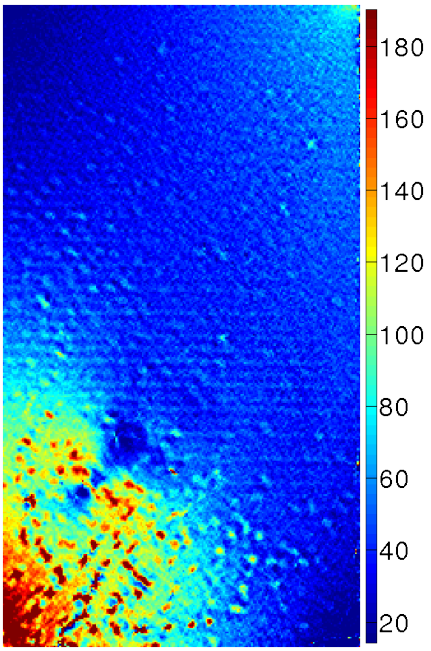

(c) ε_s

S1: impacted at 15 J while clamped between two plates

Figure 4.39: Experimental equivalent strain maps for the S1 case loaded at point 3 with 20 N (in µm/m).

4.8.21 S1 - P4 - Numerical strain maps

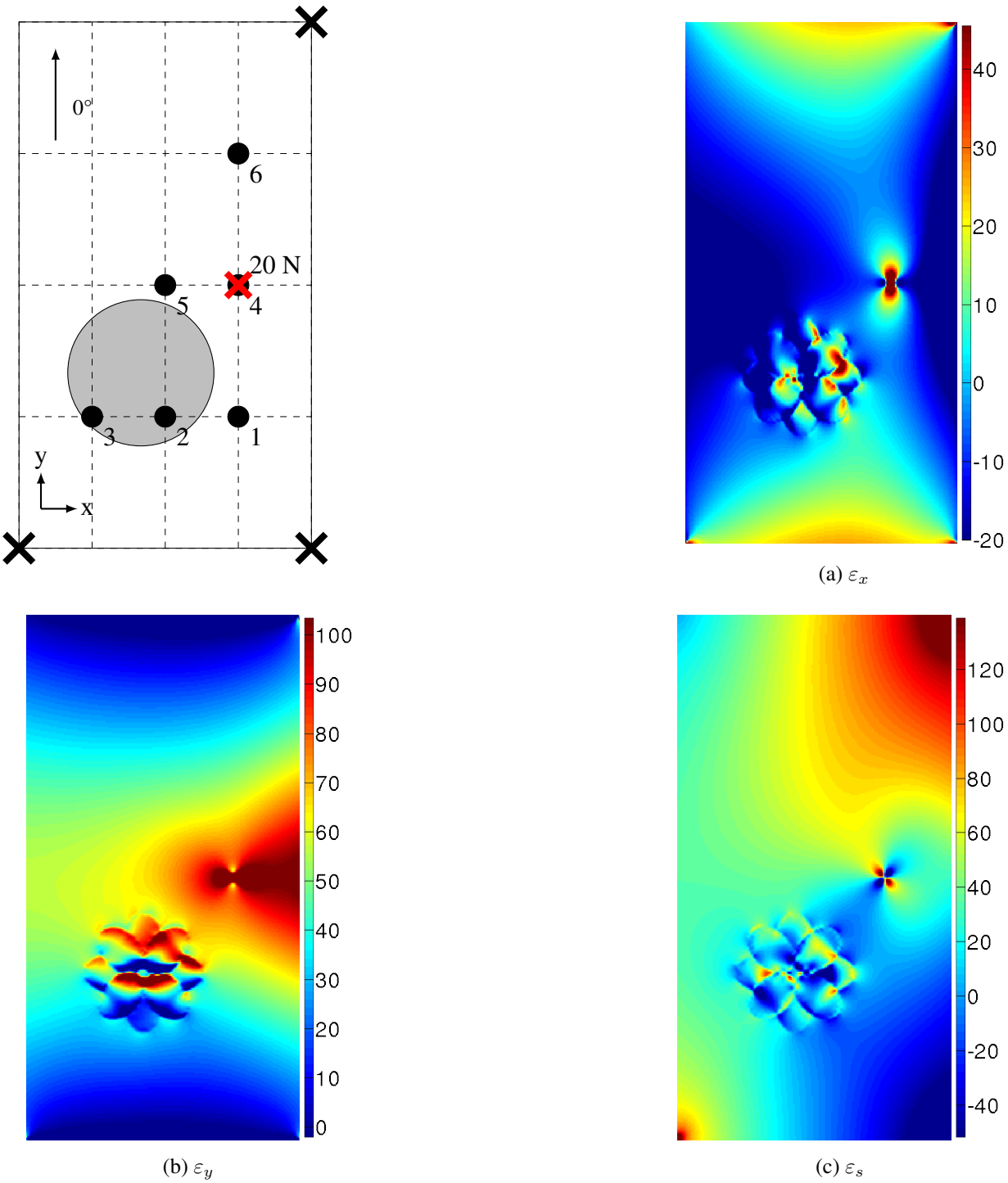

(a) ε_x

(b) ε_y

(c) ε_s

S1: impacted at 15 J while clamped between two plates

Figure 4.40: Numerical equivalent strain maps for the S1 case loaded at point 4 with 20 N (in µm/m).

4.8.22 S1 - P4 - Experimental strain maps

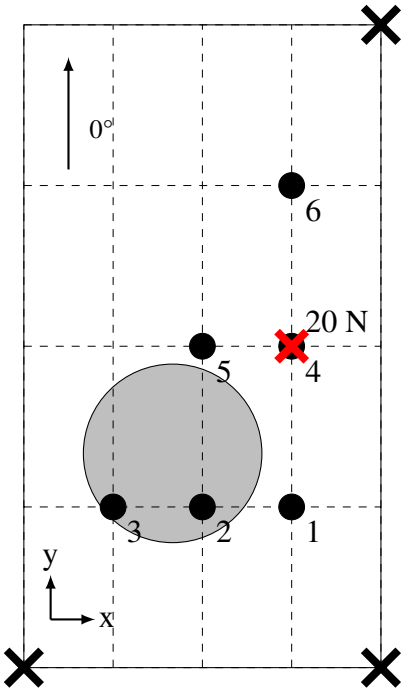

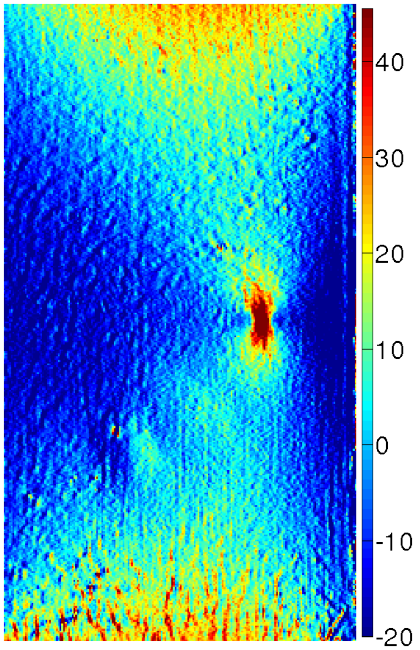

(a) ε_x

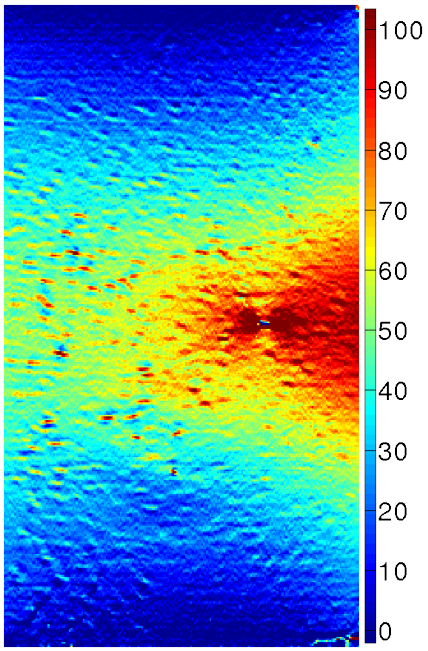

(b) ε_y

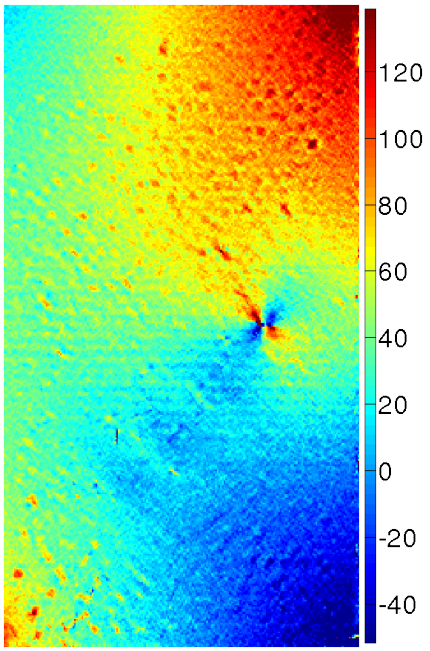

(c) ε_s

S1: impacted at 15 J while clamped between two plates

Figure 4.41: Experimental equivalent strain maps for the S1 case loaded at point 4 with 20 N (in µm/m).

4.8.23 S1 - P5 - Numerical strain maps

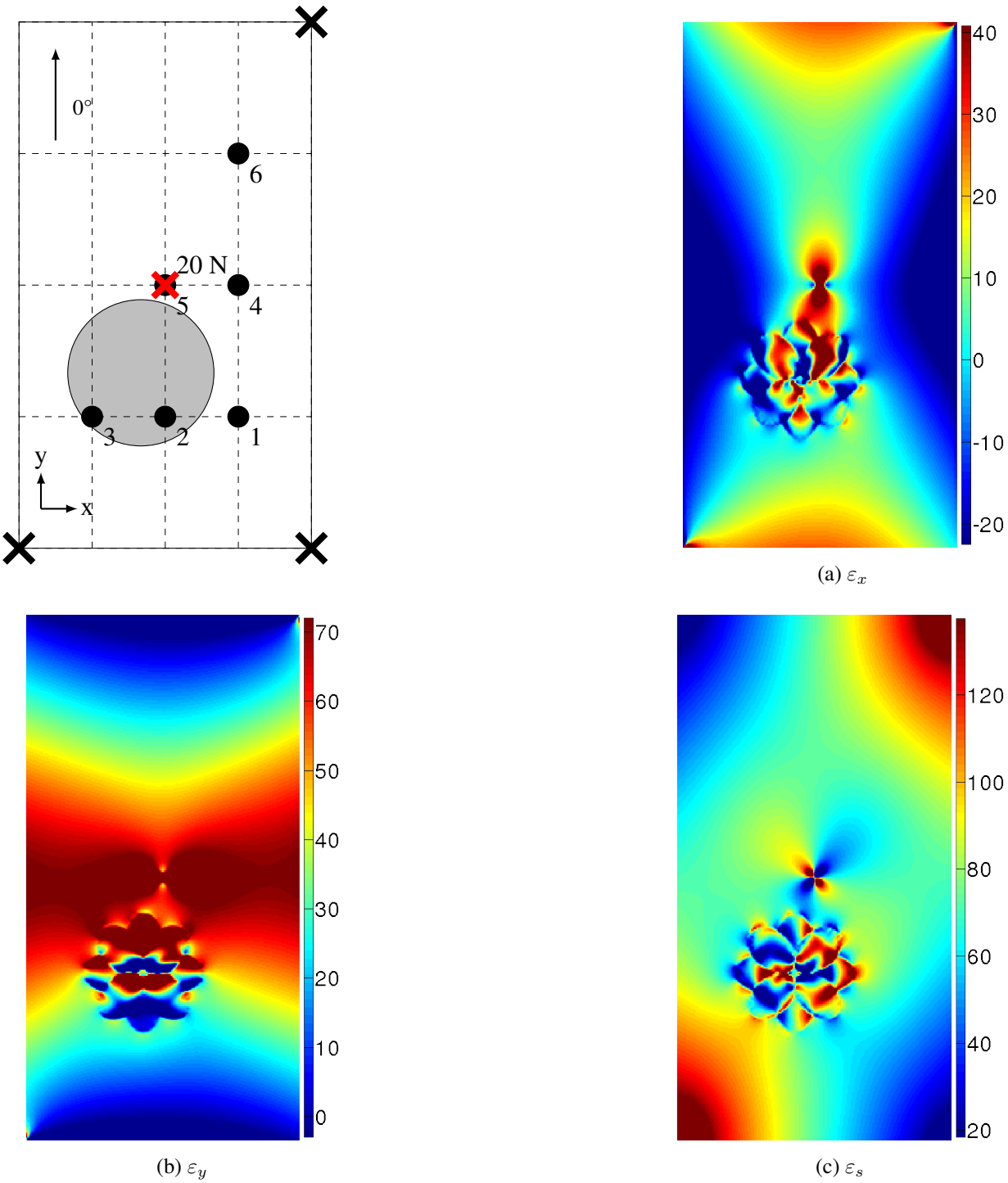

(a) ε_x

(b) ε_y

(c) ε_s

S1: impacted at 15 J while clamped between two plates

Figure 4.42: Numerical equivalent strain maps for the S1 case loaded at point 5 with 20 N (in µm/m).

4.8.24 S1 - P5 - Experimental strain maps

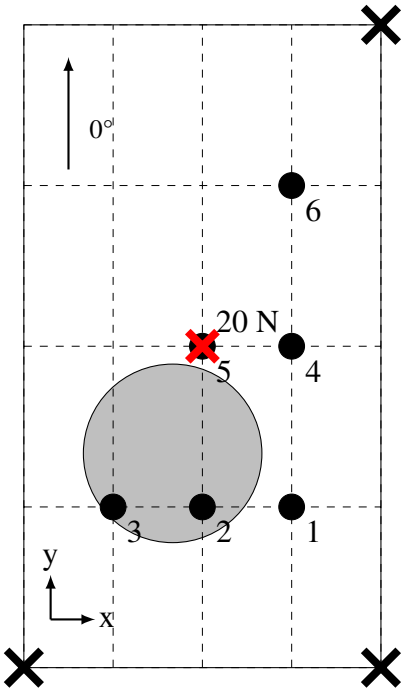

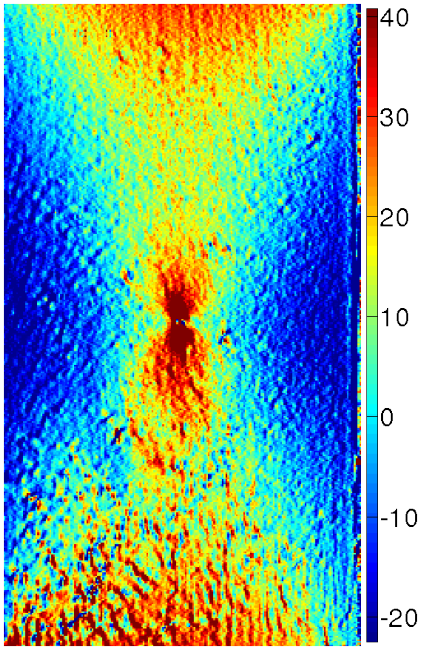

(a) ε_x

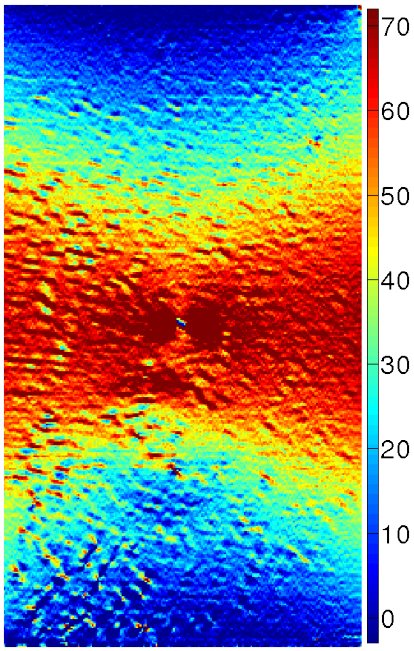

(b) ε_y

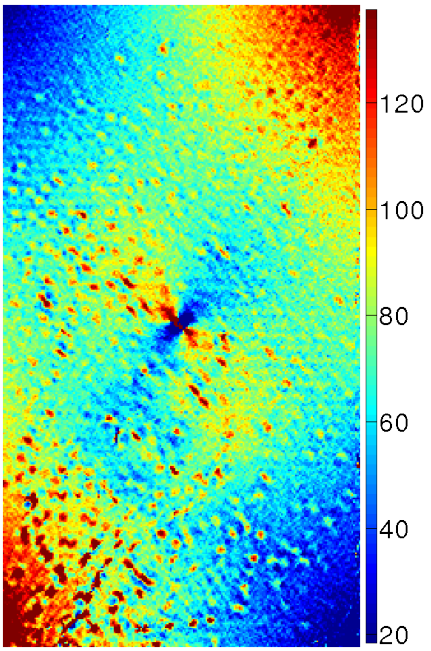

(c) ε_s

S1: impacted at 15 J while clamped between two plates

Figure 4.43: Experimental equivalent strain maps for the S1 case loaded at point 5 with 20 N (in µm/m).

4.8.25 S1 - P6 - Numerical strain maps

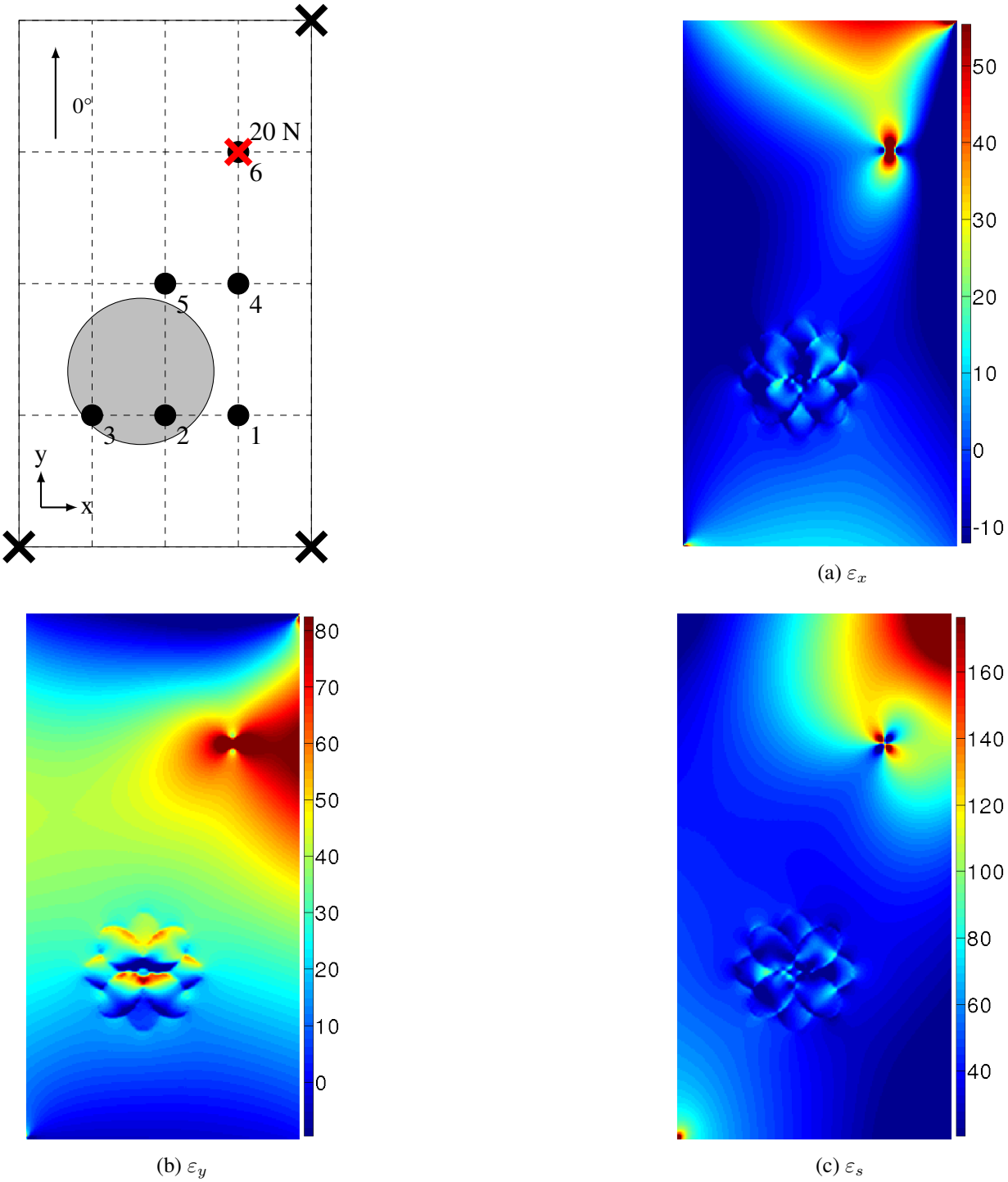

(a) ε_x

(b) ε_y

(c) ε_s

S1: impacted at 15 J while clamped between two plates

Figure 4.44: Numerical equivalent strain maps for the S1 case loaded at point 6 with 20 N (in µm/m).

4.8.26 S1 - P6 - Experimental strain maps

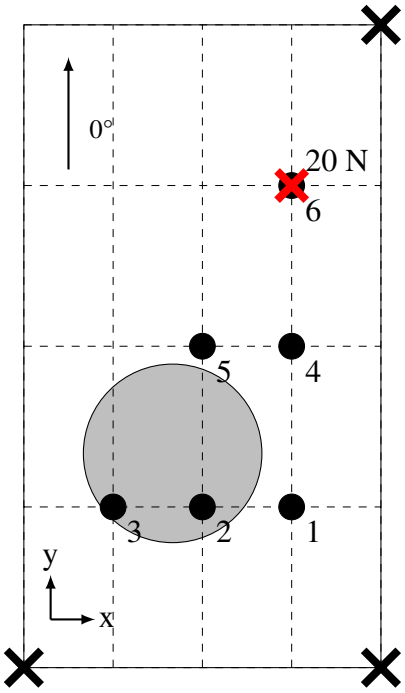

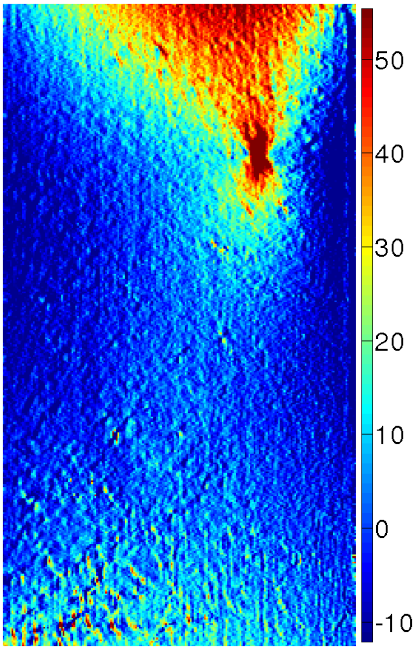

(a) ε_x

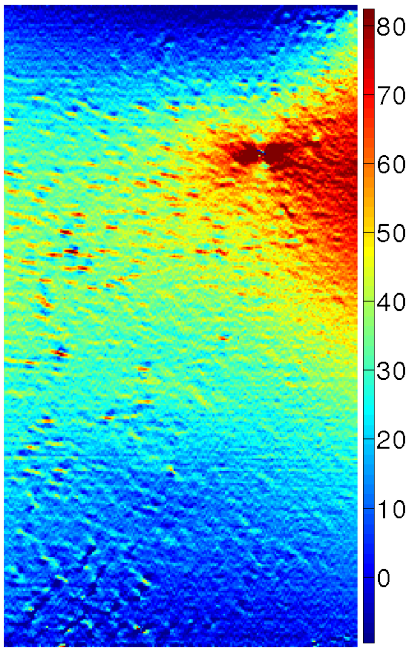

(b) ε_y

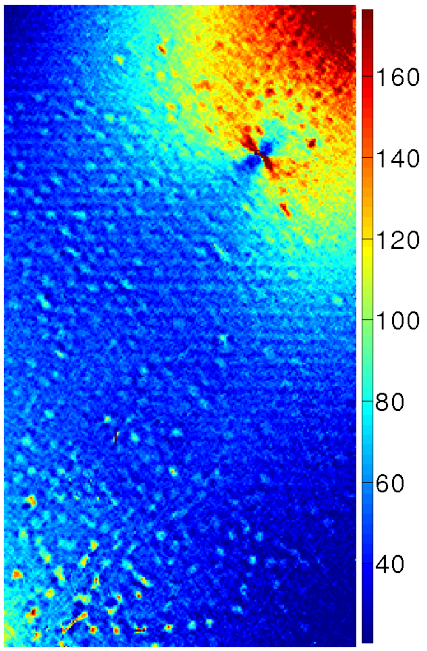

(c) ε_s

S1: impacted at 15 J while clamped between two plates

Figure 4.45: Experimental equivalent strain maps for the S1 case loaded at point 6 with 20 N (in µm/m).

4.8.27 S1 - Numerical EG maps

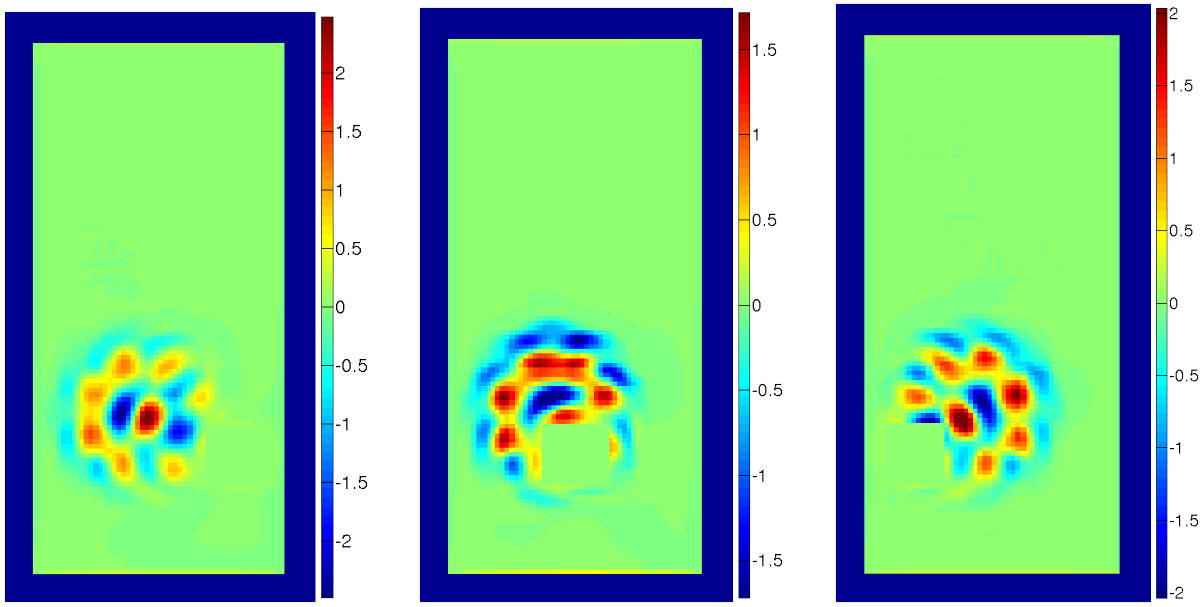

(a) Point 1 (b) Point 2 (c) Point 3

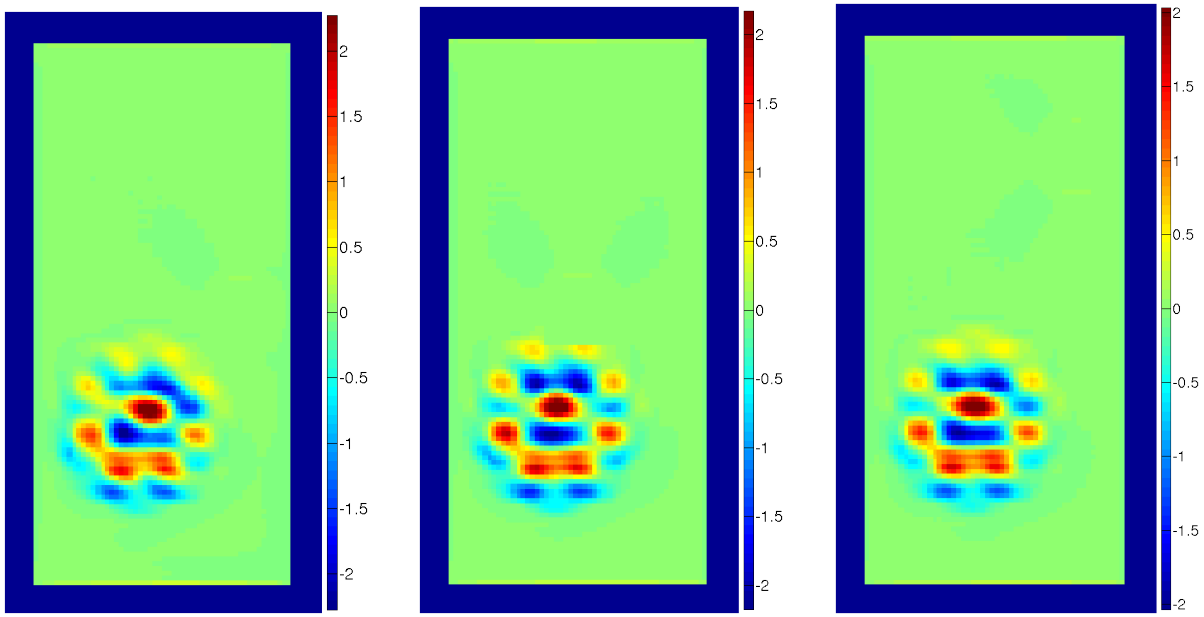

(d) Point 4 (e) Point 5 (f) Point 6

S1: impacted at 15 J while clamped between two plates

Figure 4.46: EG map for the numerical results from the S1 sample with 3 pixels sliding pitch and 40×40 pixels^2 sliding window.

4.8.28 S1 - Experimental EG maps

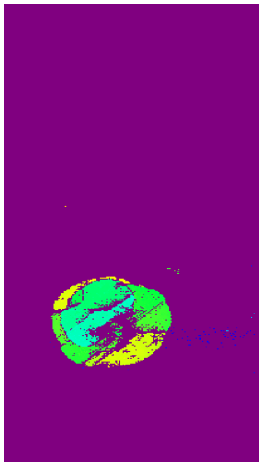

(a) C-scan

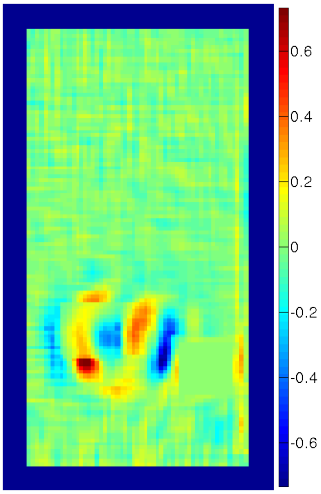

(b) Point 1

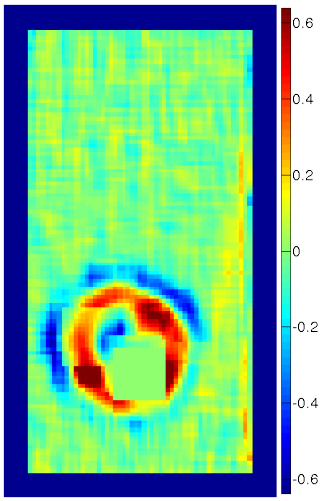

(c) Point 2

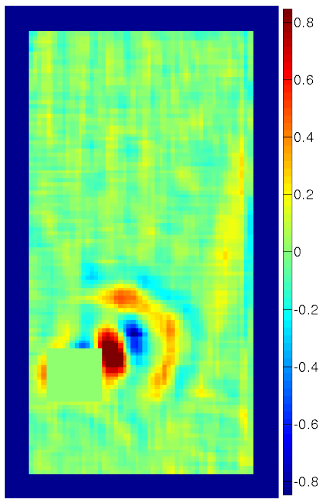

(d) Point 3

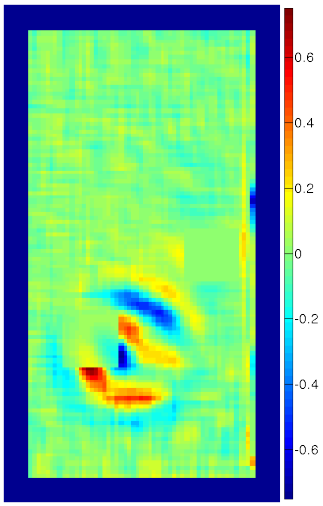

(e) Point 4

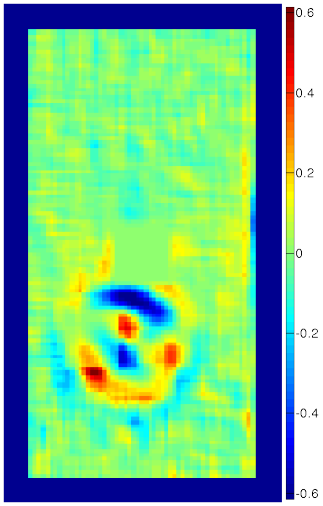

(f) Point 5

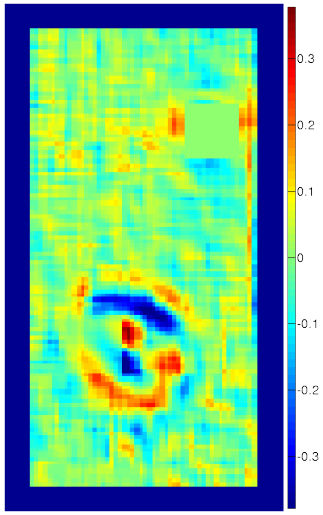

(g) Point 6

S1: impacted at 15 J while clamped between two plates

Figure 4.47: EG map for the experimental results from the S1 sample with 3 pixels sliding pitch and 40×40 pixels^2 sliding window.

4.8.29 S2 - P1 - Experimental strain maps

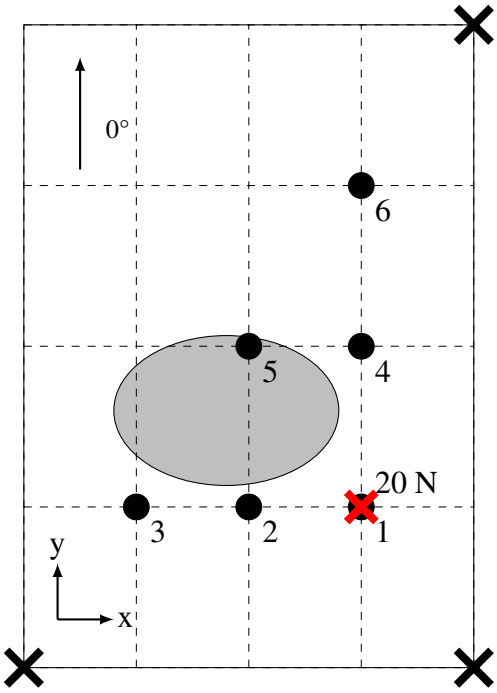

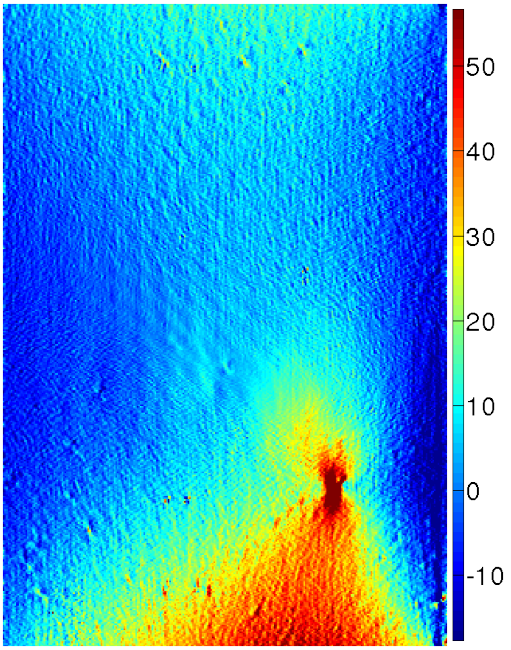

(a) ε_x

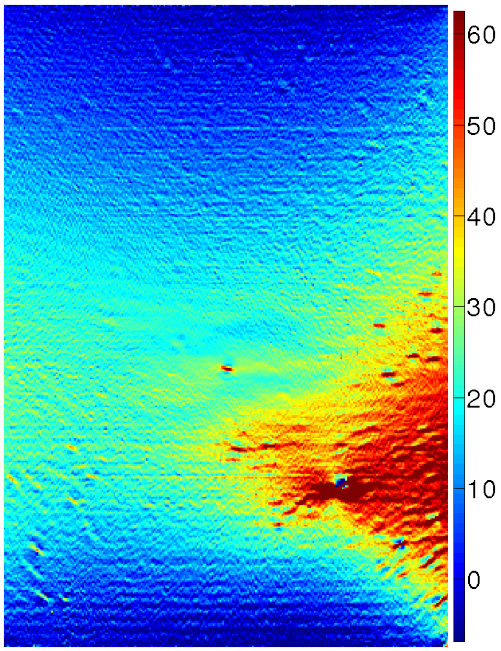

(b) ε_y

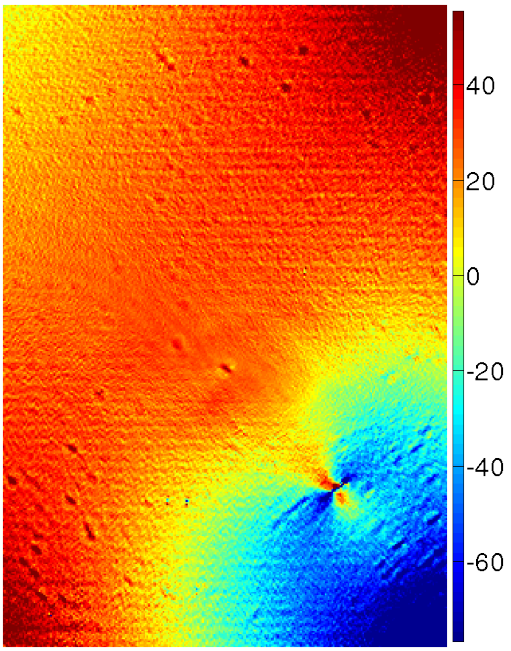

(c) ε_s

S2: impacted at 15 J while simply supported

Figure 4.48: Experimental equivalent strain maps for the S2 case loaded at point 1 with 20 N (in µm/m).

4.8.30 S2 - P2 - Experimental strain maps

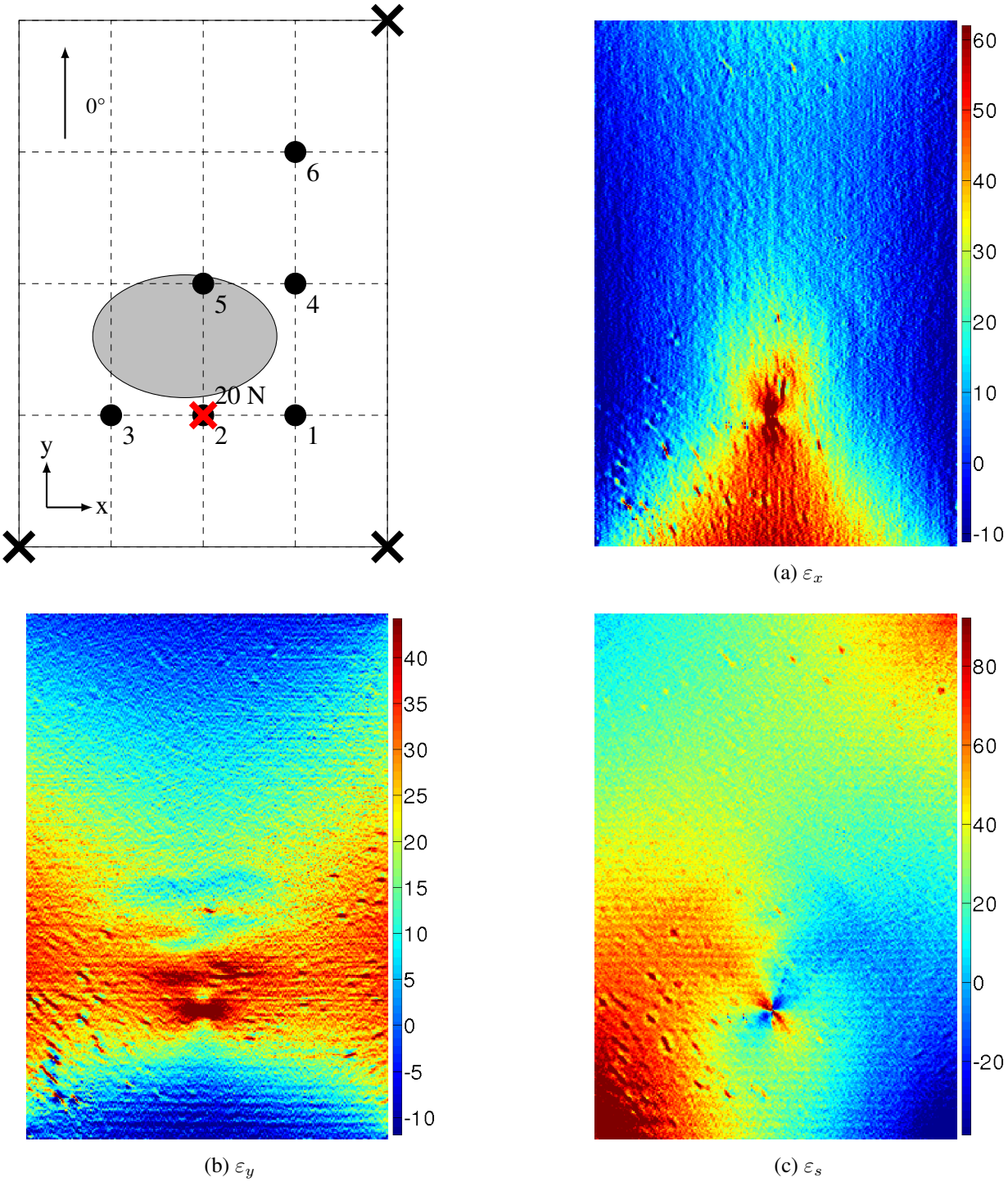

(a) ε_x

(b) ε_y

(c) ε_s

S2: impacted at 15 J while simply supported

Figure 4.49: Experimental equivalent strain maps for the S2 case loaded at point 2 with 20 N (in µm/m).

4.8.31 S2 - P3 - Experimental strain maps

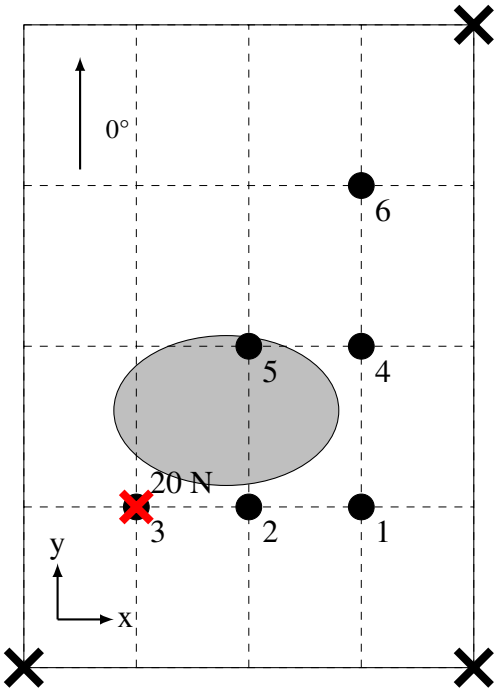

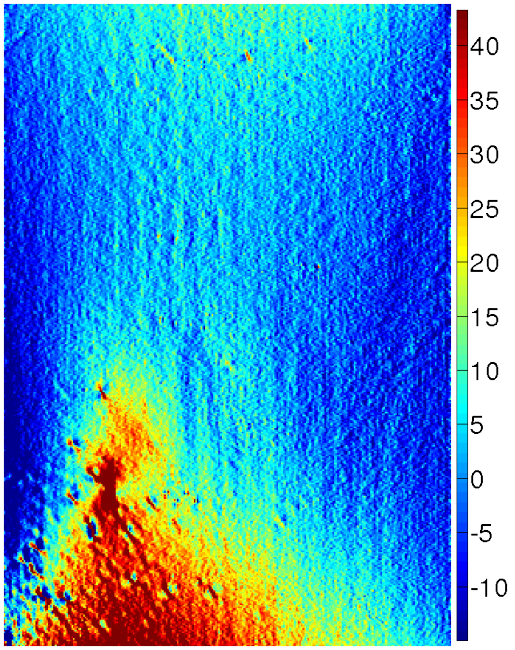

(a) ε_x

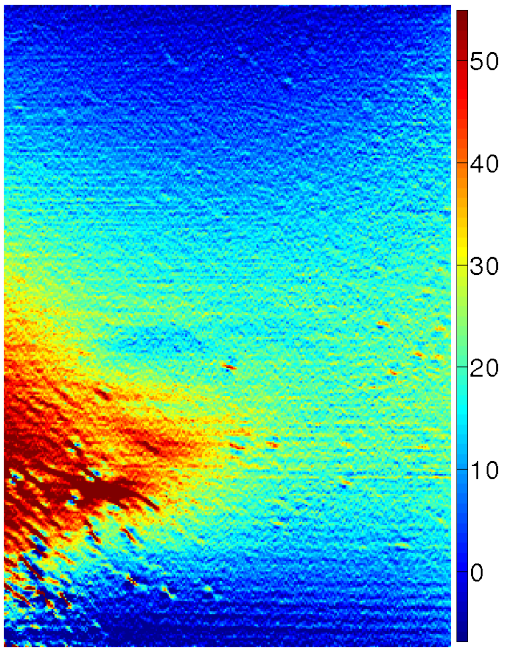

(b) ε_y

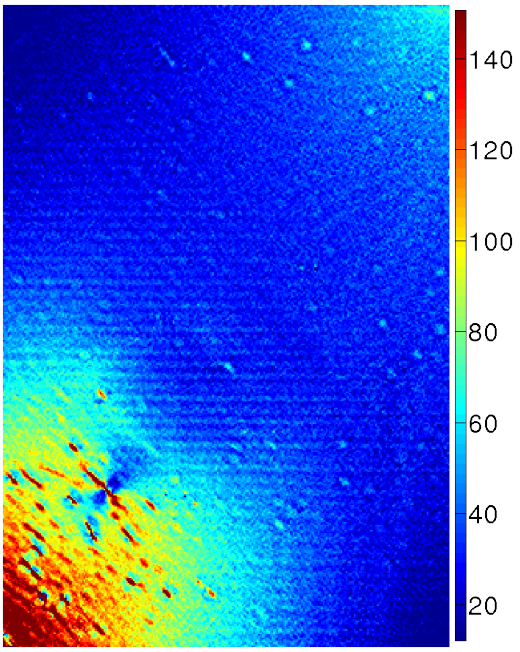

(c) ε_s

S2: impacted at 15 J while simply supported

Figure 4.50: Experimental equivalent strain maps for the S2 case loaded at point 3 with 20 N (in µm/m).

4.8.32 S2 - P4 - Experimental strain maps

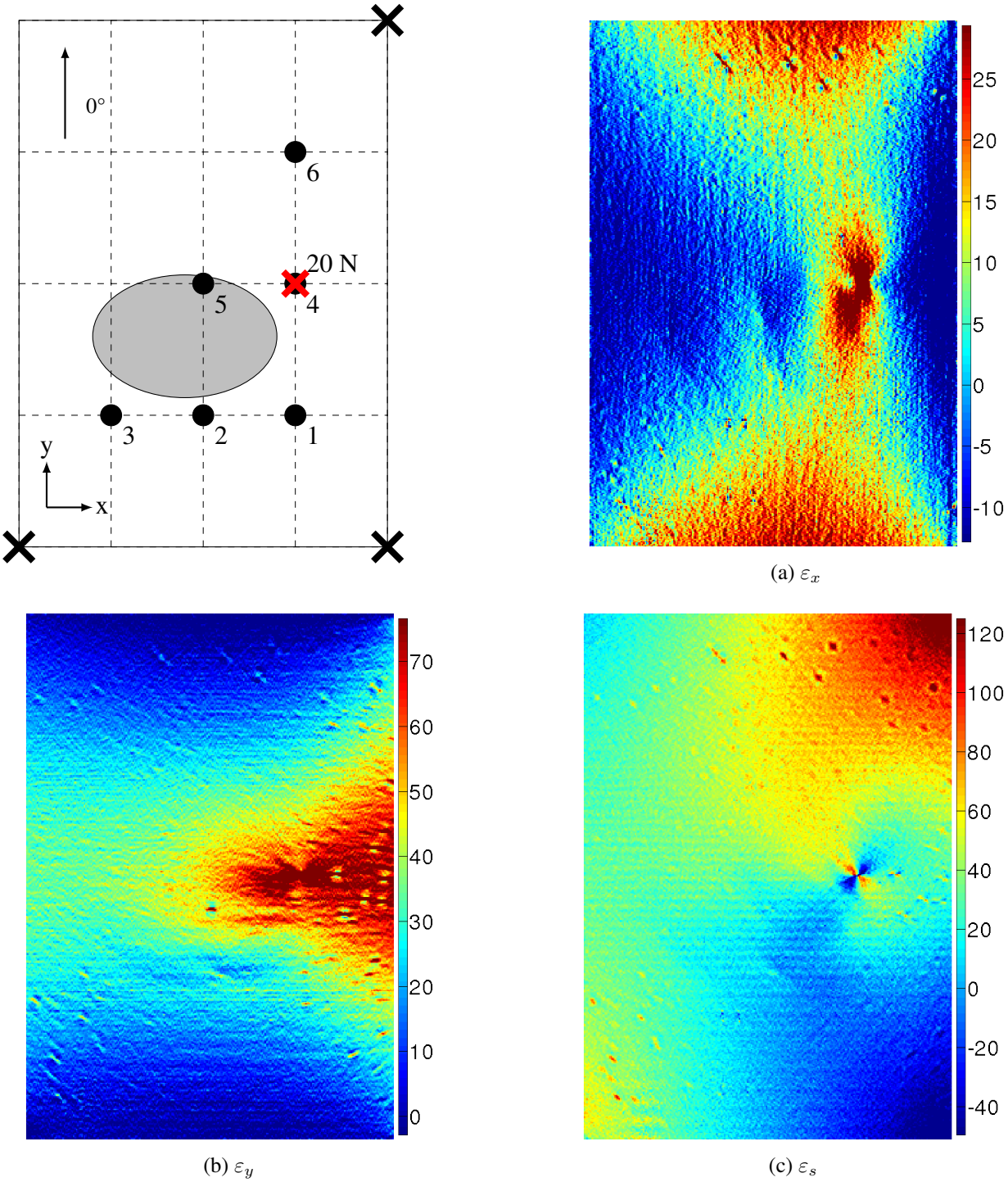

(a) ε_x

(b) ε_y

(c) ε_s

S2: impacted at 15 J while simply supported

Figure 4.51: Experimental equivalent strain maps for the S2 case loaded at point 4 with 20 N (in µm/m).

4.8.33 S2 - P5 - Experimental strain maps

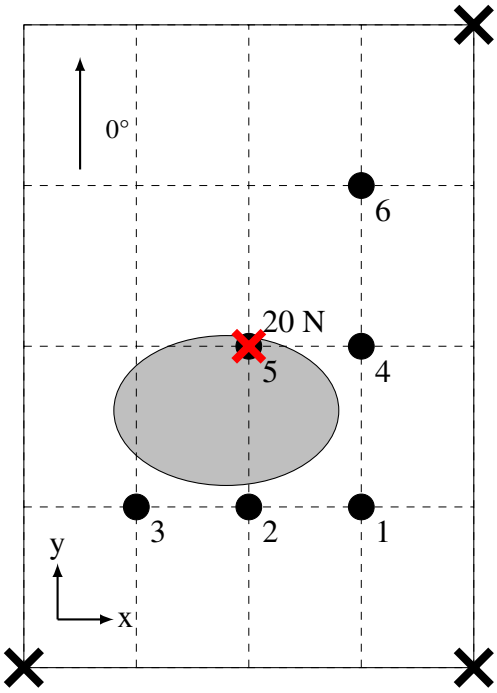

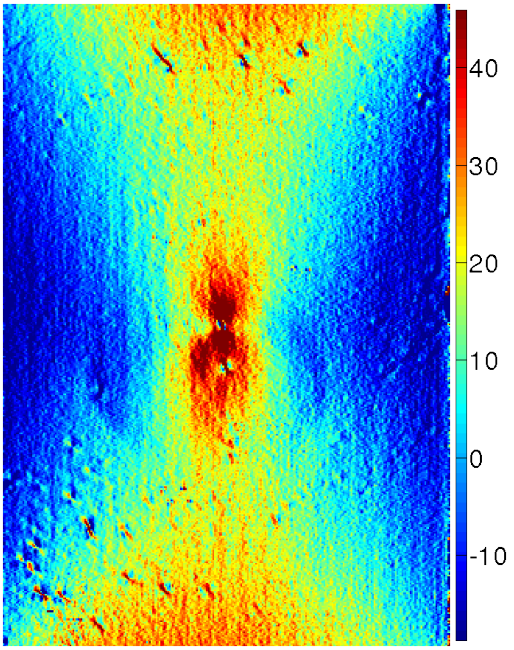

(a) ε_x

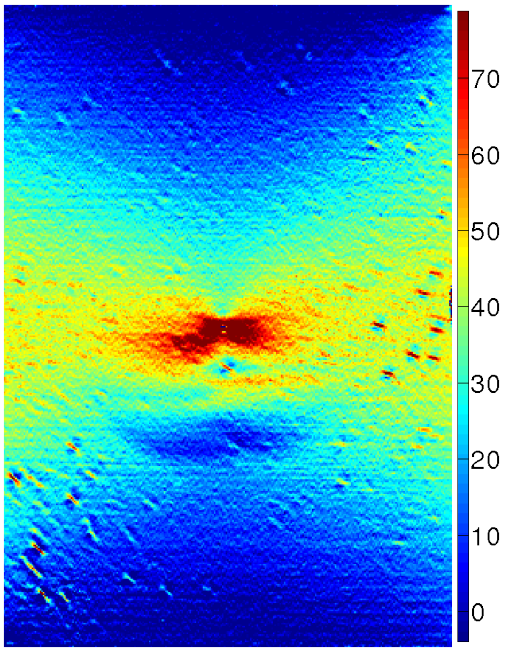

(b) ε_y

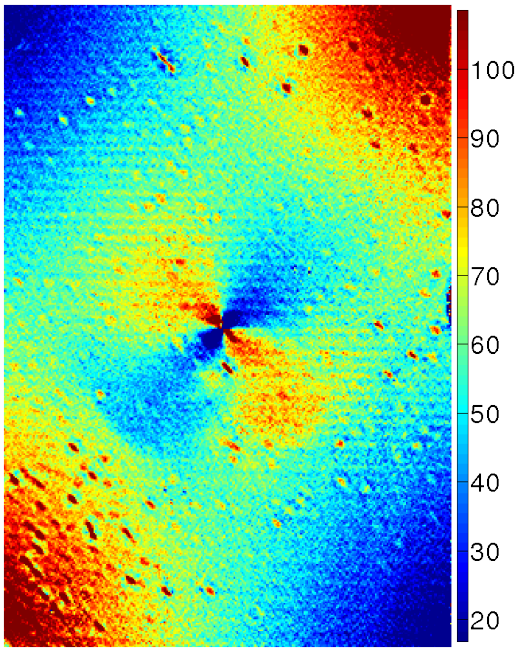

(c) ε_s

S2: impacted at 15 J while simply supported

Figure 4.52: Experimental equivalent strain maps for the S2 case loaded at point 5 with 20 N (in µm/m).

4.8.34 S2 - P6 - Experimental strain maps

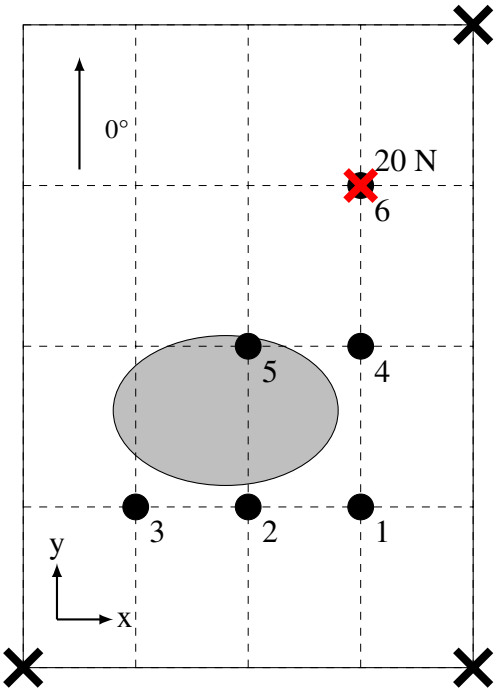

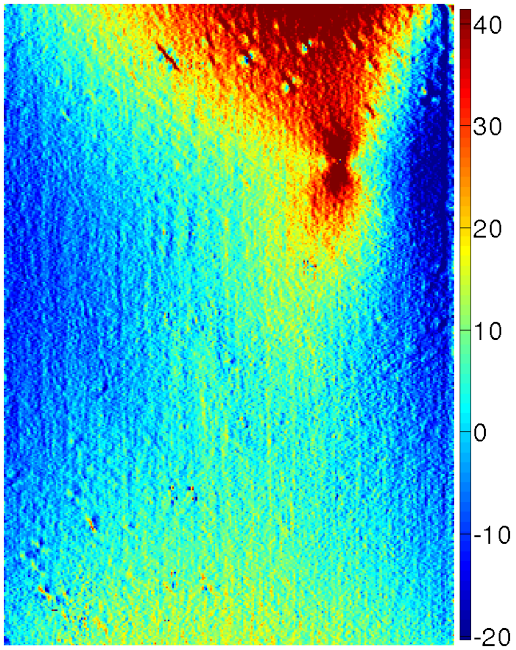

(a) ε_x

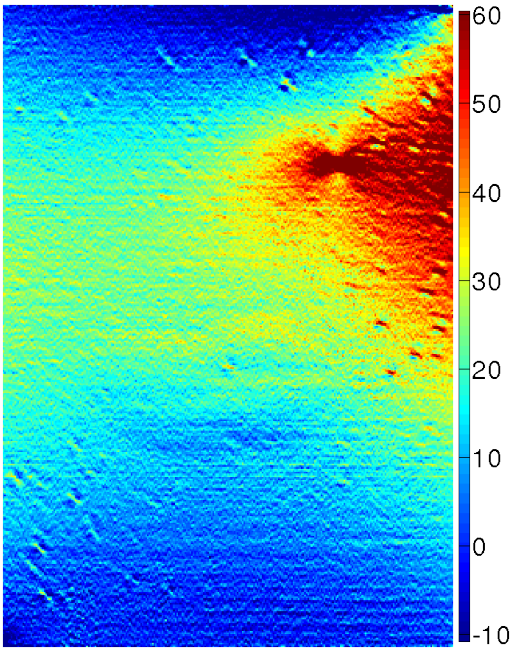

(b) ε_y

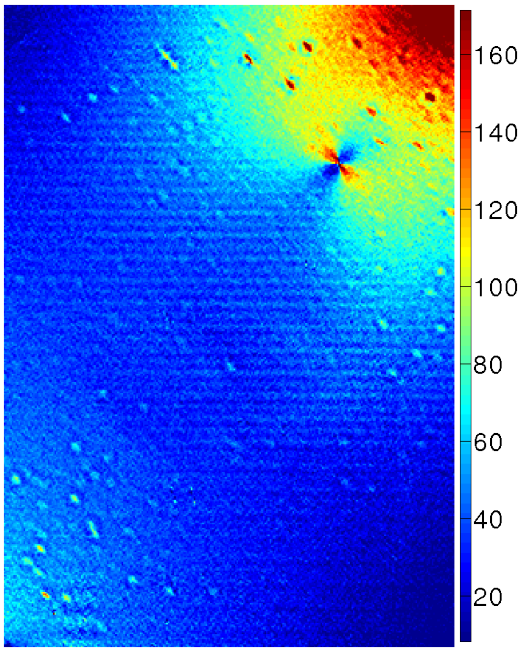

(c) ε_s

S2: impacted at 15 J while simply supported

Figure 4.53: Experimental equivalent strain maps for the S2 case loaded at point 6 with 20 N (in µm/m).

4.8.35 S2 - Experimental EG maps

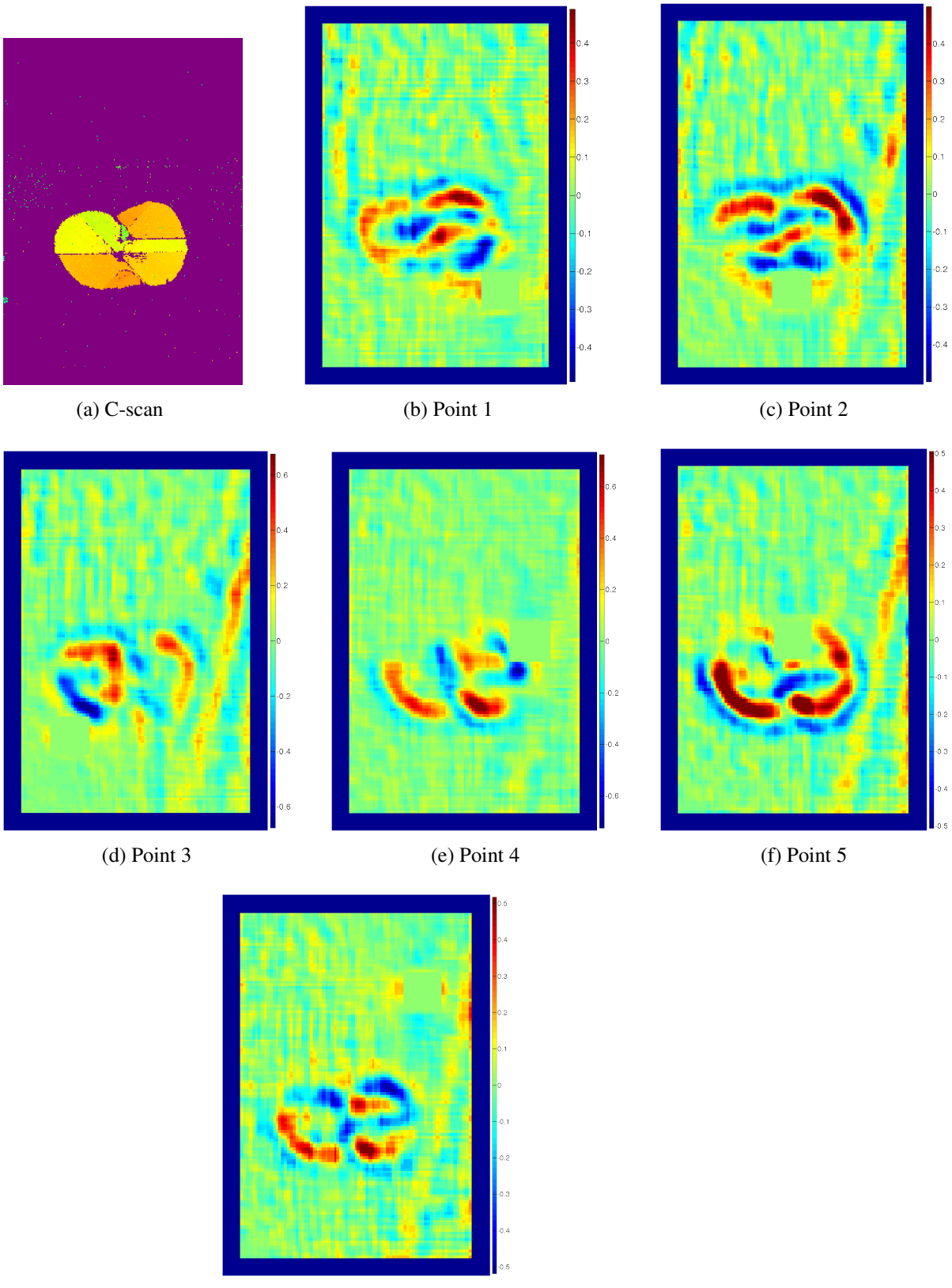

(a) C-scan (b) Point 1 (c) Point 2

(d) Point 3 (e) Point 4 (f) Point 5

(g) Point 6

S2: impacted at 15 J while simply supported

Figure 4.54: EG map for the experimental results from the S2 sample with 3 pixels sliding pitch and 40×40 pixels^2 sliding window.

4.8.36 S3 - P1 - Experimental strain maps

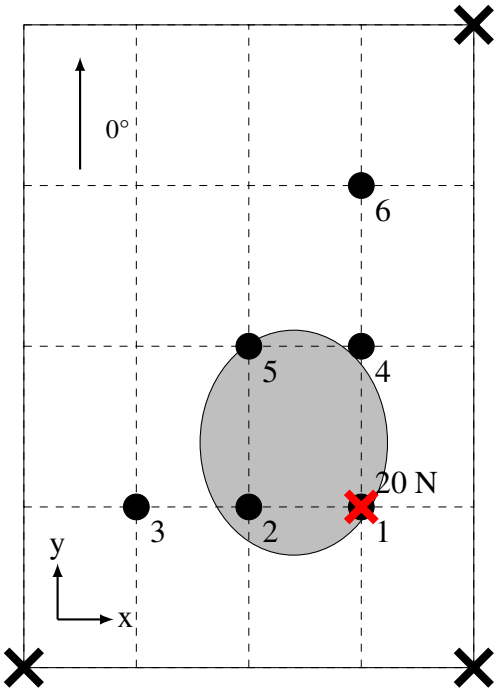

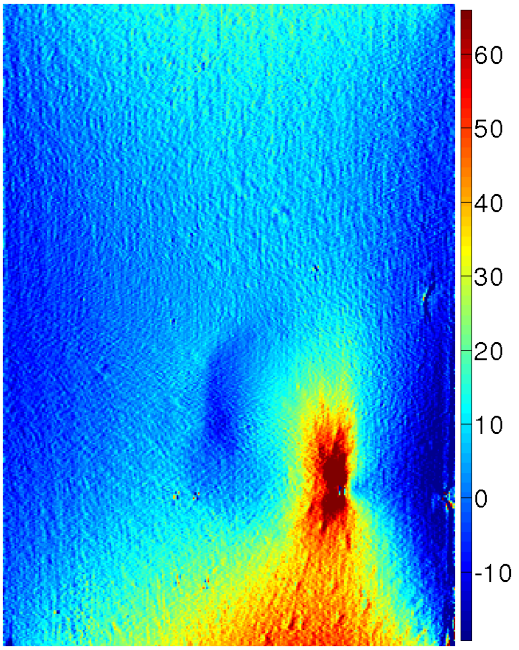

(a) ε_x

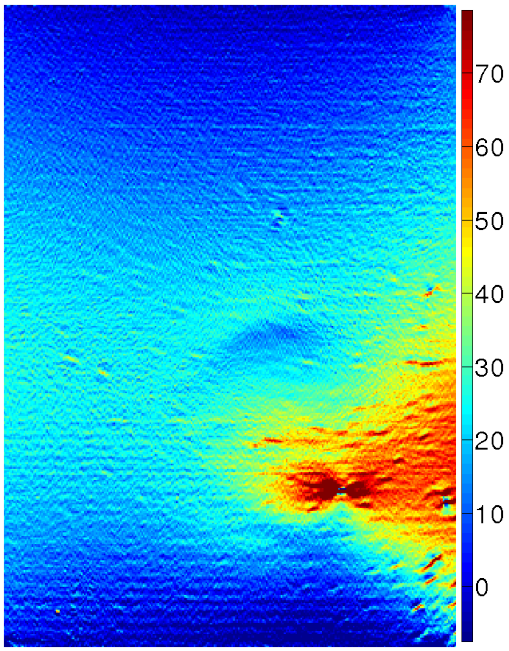

(b) ε_y

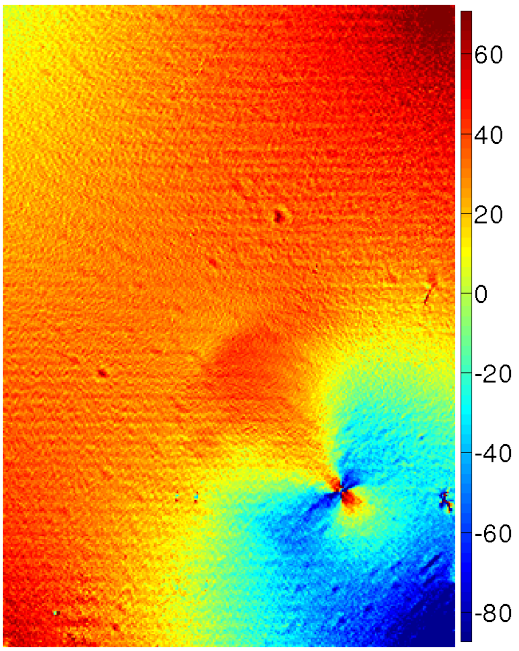

(c) ε_s

S3: impacted at 25 J while simply supported

Figure 4.55: Experimental equivalent strain maps for the S3 case loaded at point 1 with 20 N (in µm/m).

4.8.37 S3 - P2 - Experimental strain maps

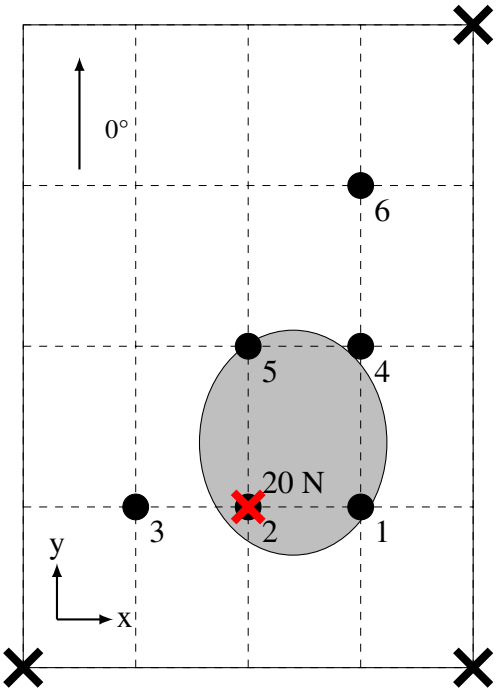

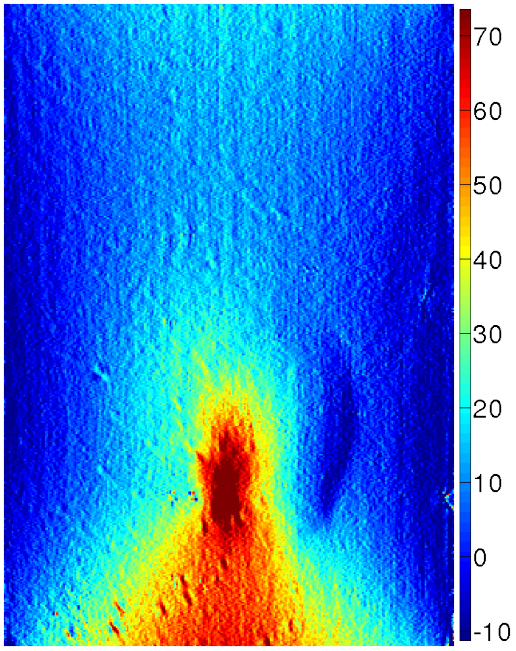

(a) ε_x

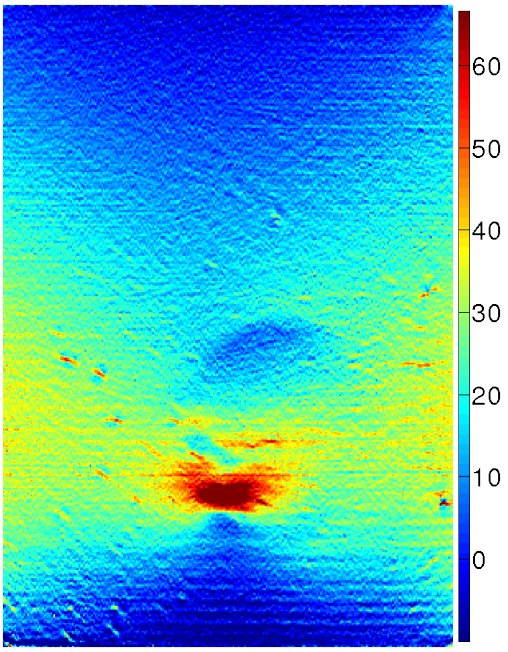

(b) ε_y

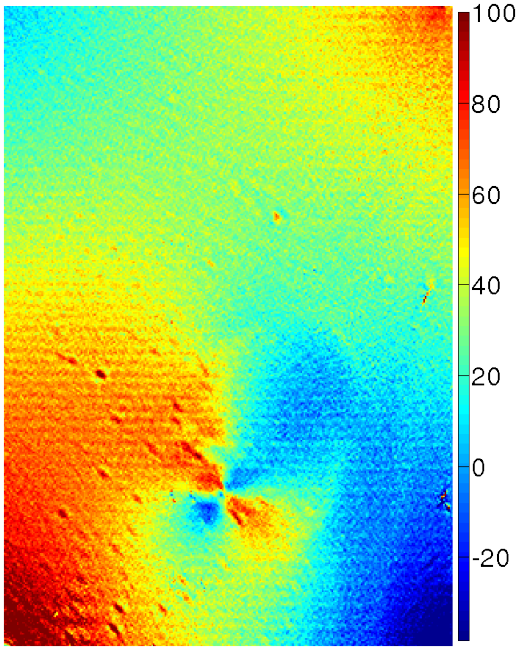

(c) ε_s

S3: impacted at 25 J while simply supported

Figure 4.56: Experimental equivalent strain maps for the S3 case loaded at point 2 with 20 N (in µm/m).

4.8.38 S3 - P3 - Experimental strain maps

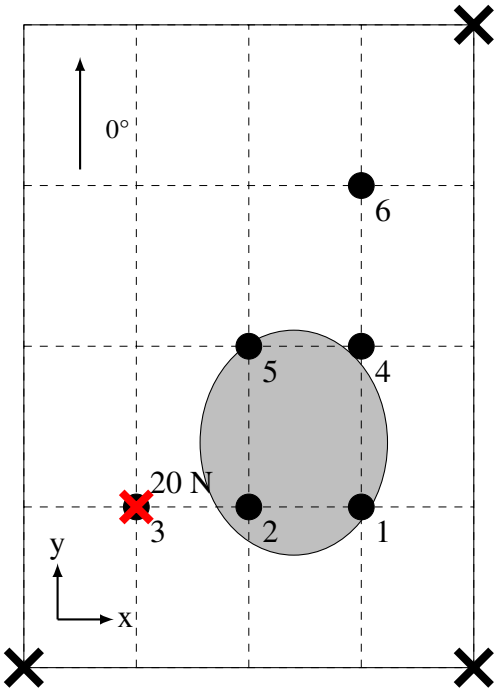

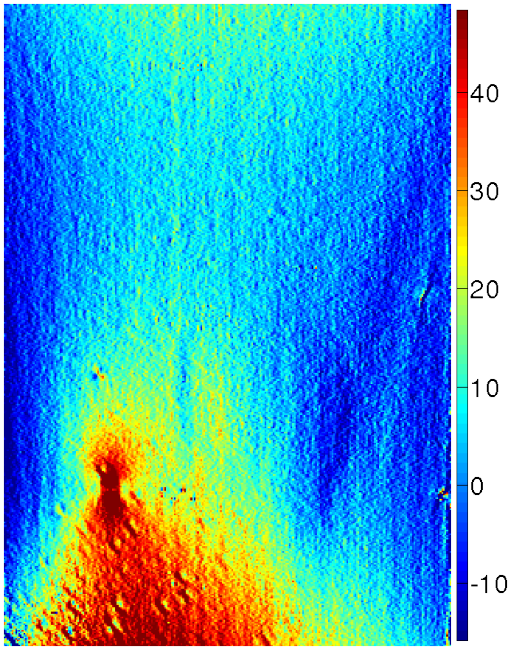

(a) ε_x

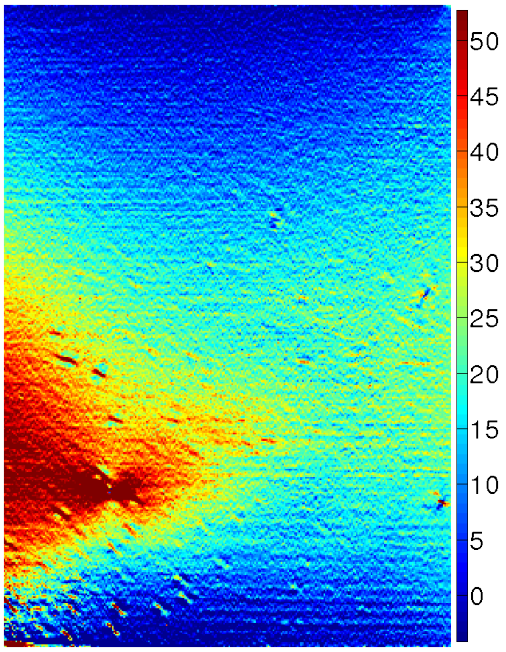

(b) ε_y

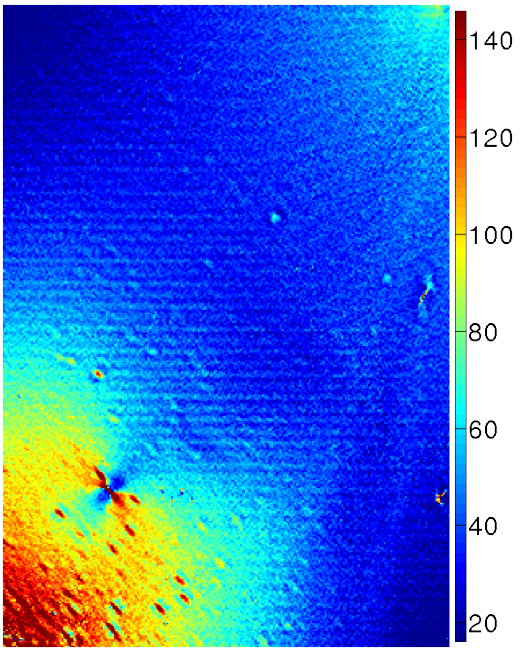

(c) ε_s

S3: impacted at 25 J while simply supported

Figure 4.57: Experimental equivalent strain maps for the S3 case loaded at point 3 with 20 N (in µm/m).

4.8.39 S3 - P4 - Experimental strain maps

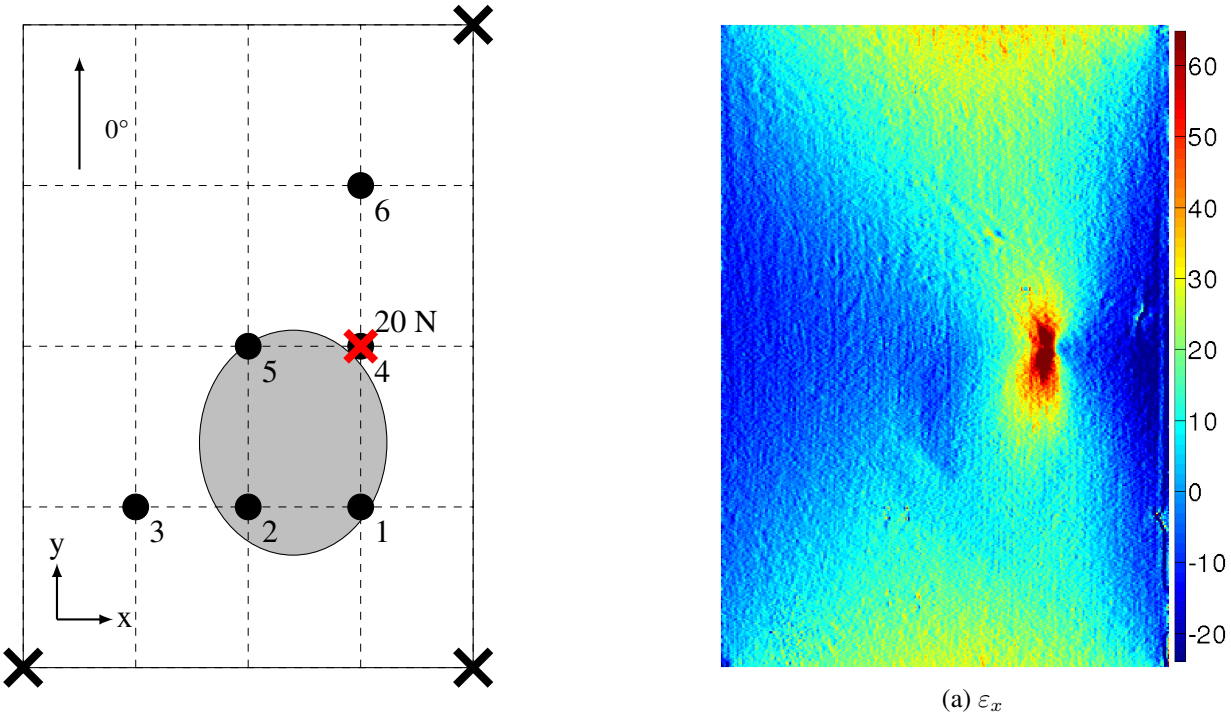

(a) ε_x

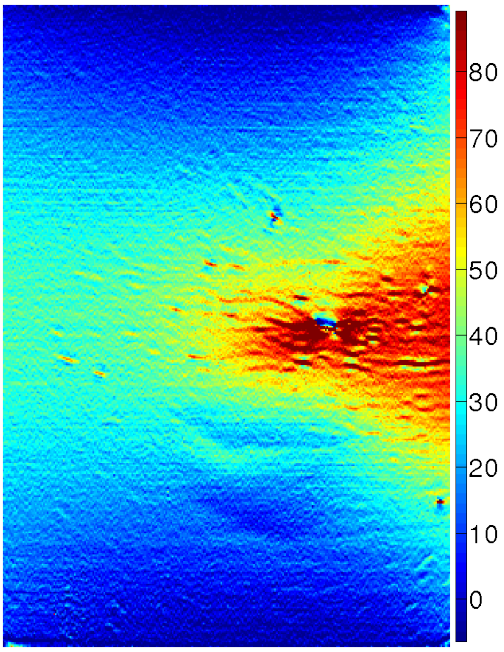

(b) ε_y

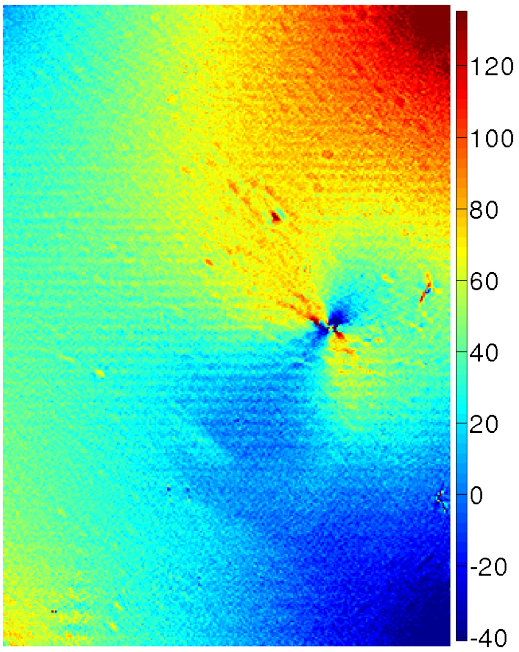

(c) ε_s

S3: impacted at 25 J while simply supported

Figure 4.58: Experimental equivalent strain maps for the S3 case loaded at point 4 with 20 N (in µm/m).

4.8.40 S3 - P5 - Experimental strain maps

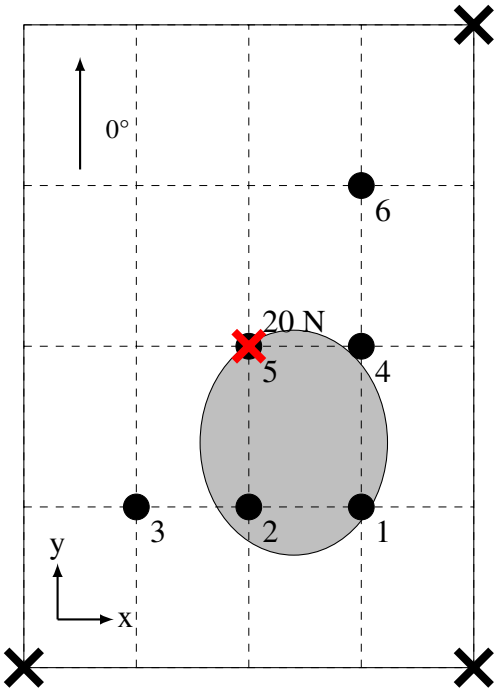

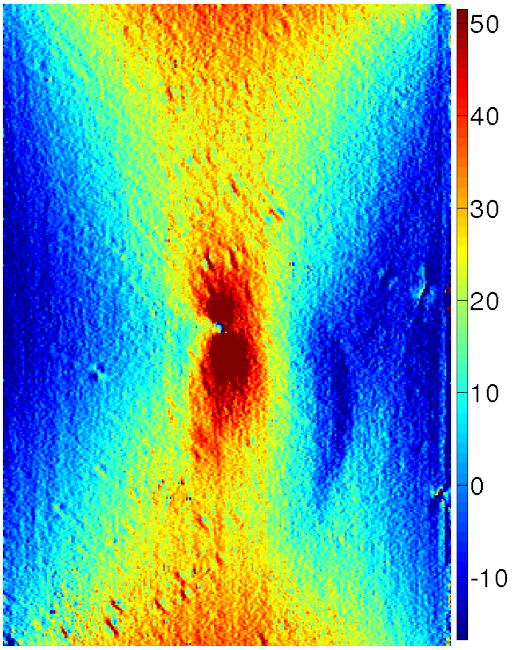

(a) ε_x

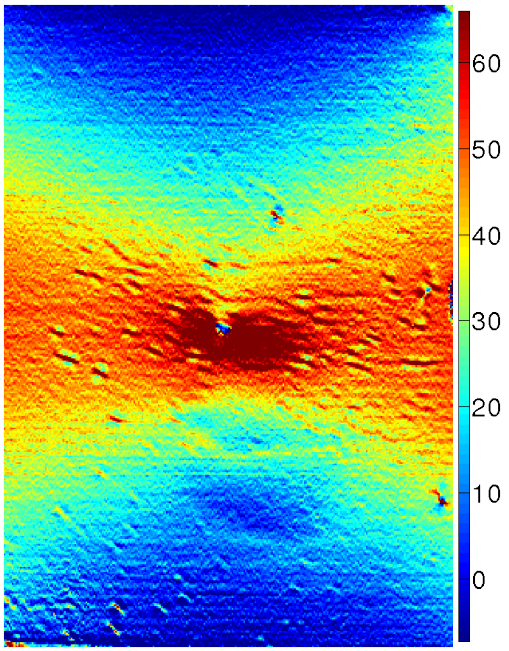

(b) ε_y

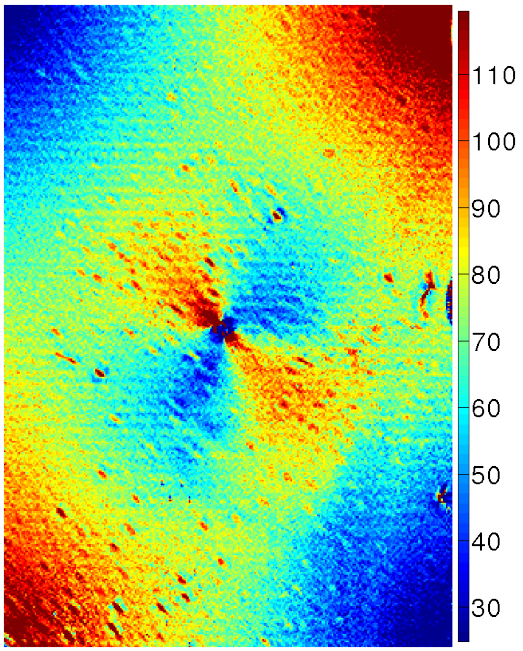

(c) ε_s

S3: impacted at 25 J while simply supported

Figure 4.59: Experimental equivalent strain maps for the S3 case loaded at point 5 with 20 N (in µm/m).

4.8.41 S3 - P6 - Experimental strain maps

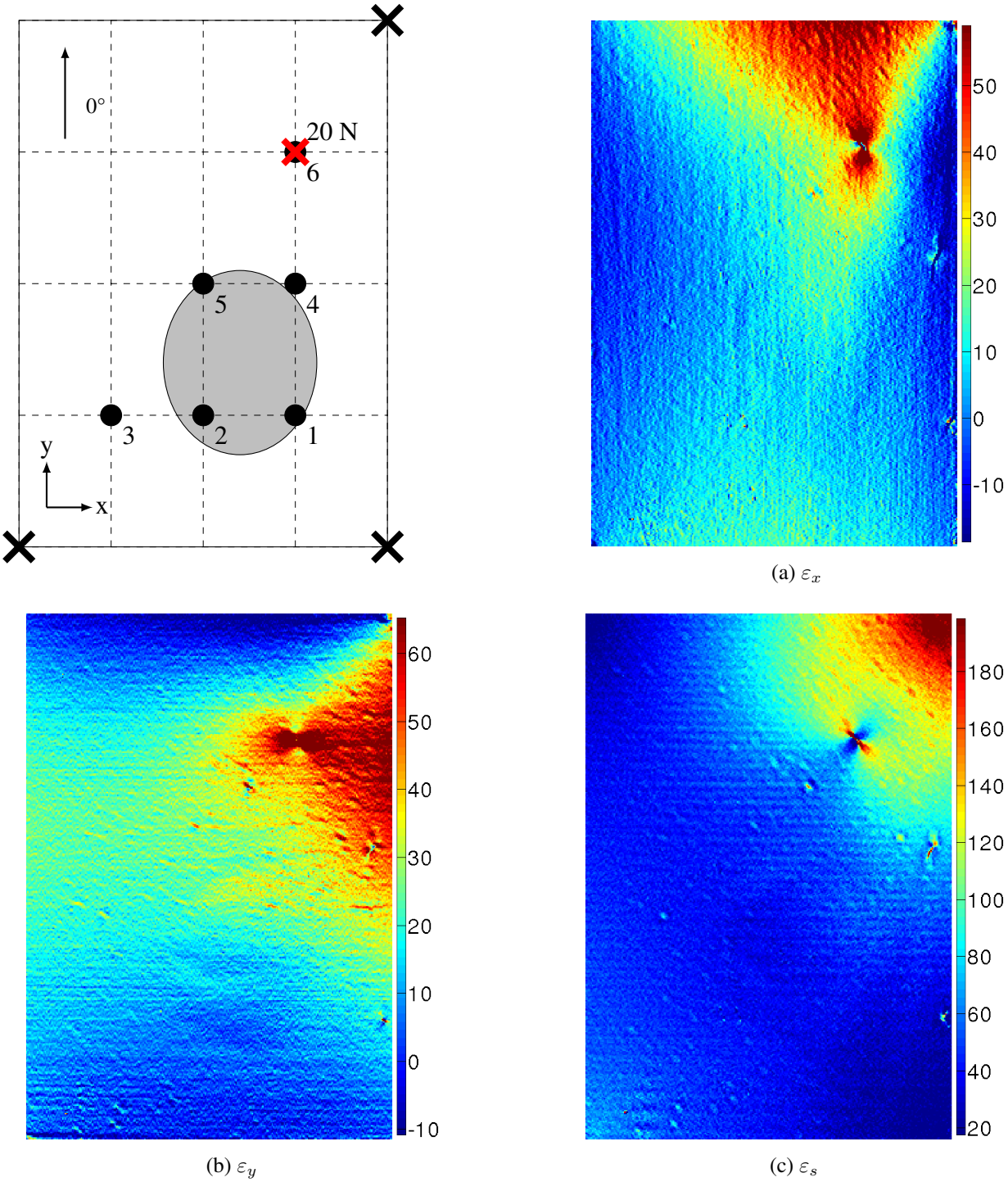

(a) ε_x

(b) ε_y

(c) ε_s

S3: impacted at 25 J while simply supported

Figure 4.60: Experimental equivalent strain maps for the S3 case loaded at point 6 with 20 N (in µm/m).

4.8.42 S3 - Experimental EG maps

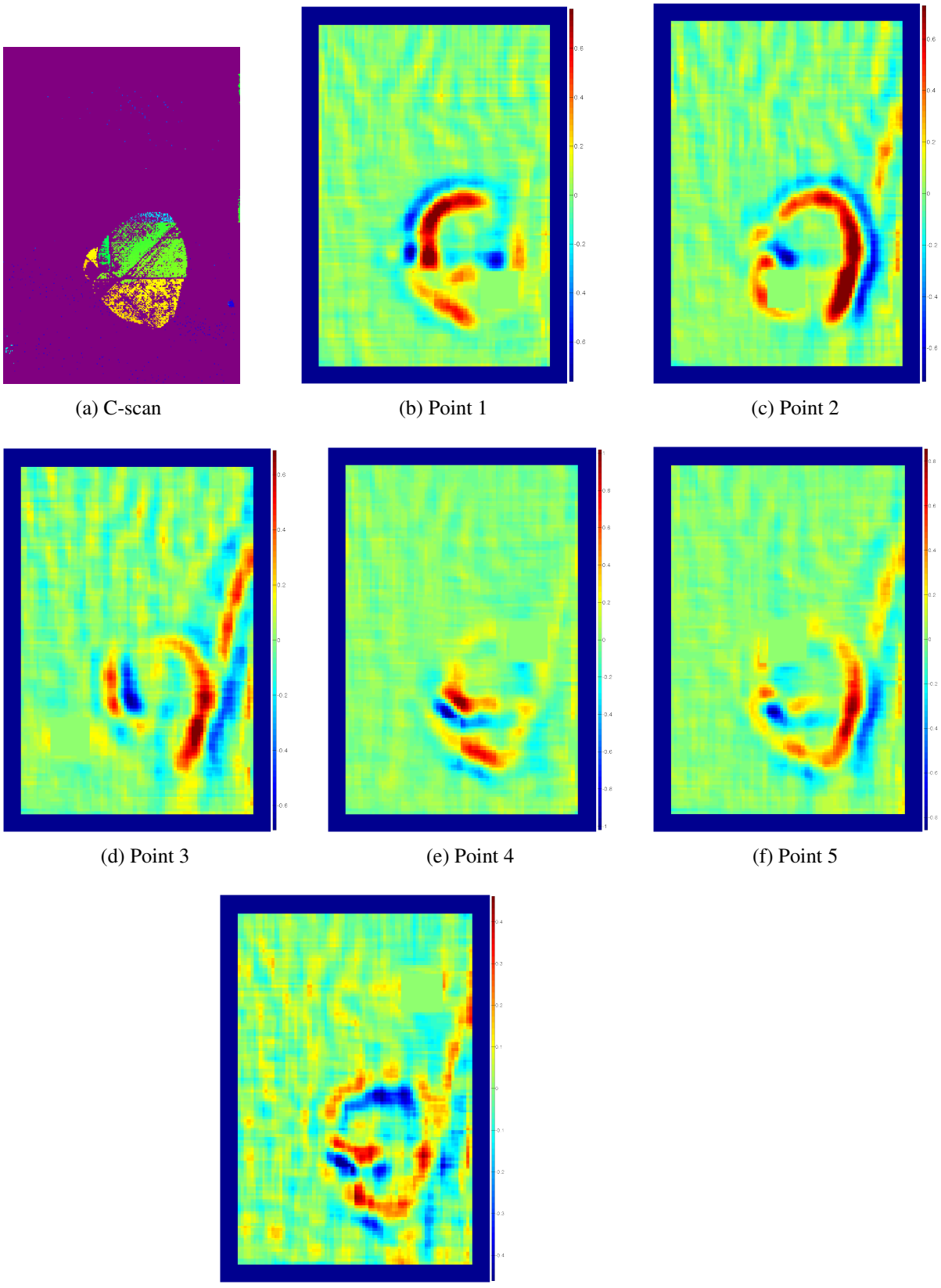

(a) C-scan (b) Point 1 (c) Point 2

(d) Point 3 (e) Point 4 (f) Point 5

(g) Point 6

S3: impacted at 25 J while simply supported

Figure 4.61: EG map for the experimental results from the S3 sample with 3 pixels sliding pitch and 40×40 pixels^2 sliding window.

4.8.43 S4 - P1 - Experimental strain maps

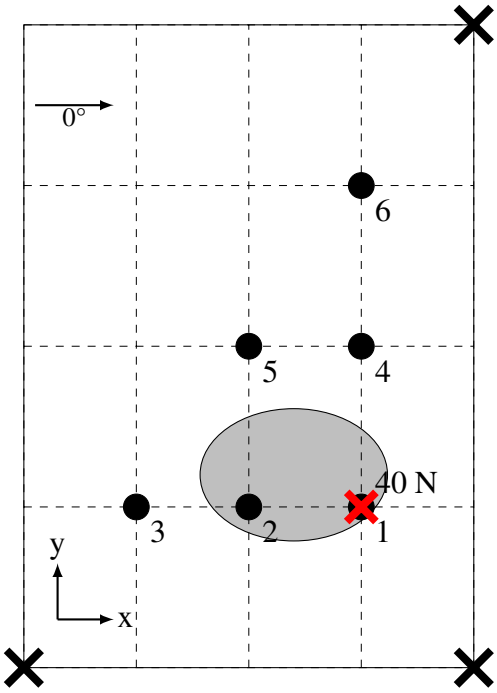

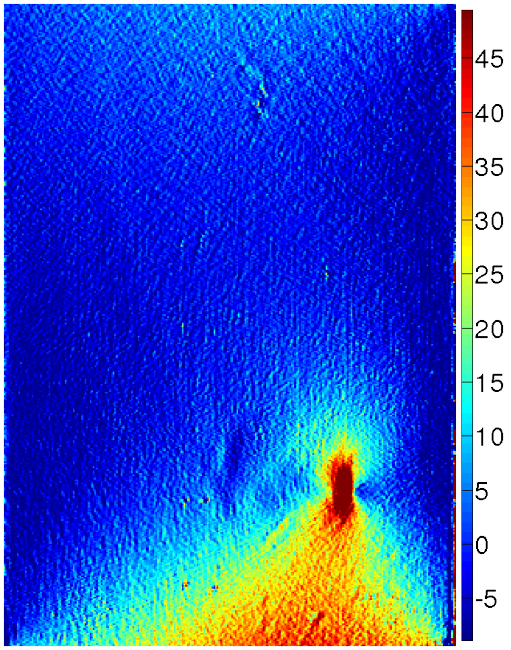

(a) ε_x

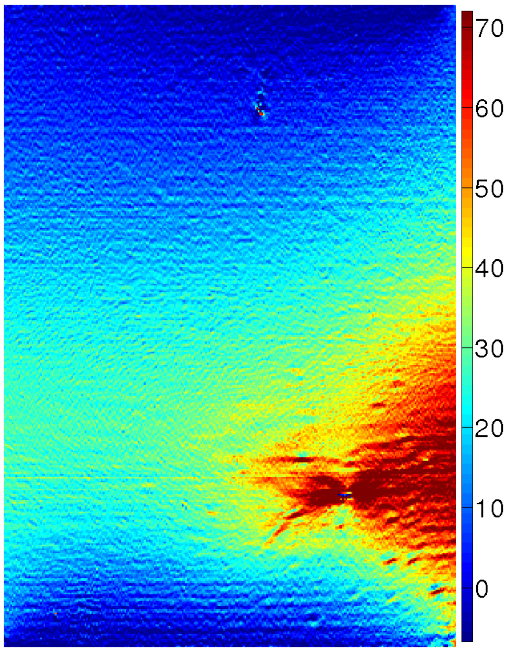

(b) ε_y

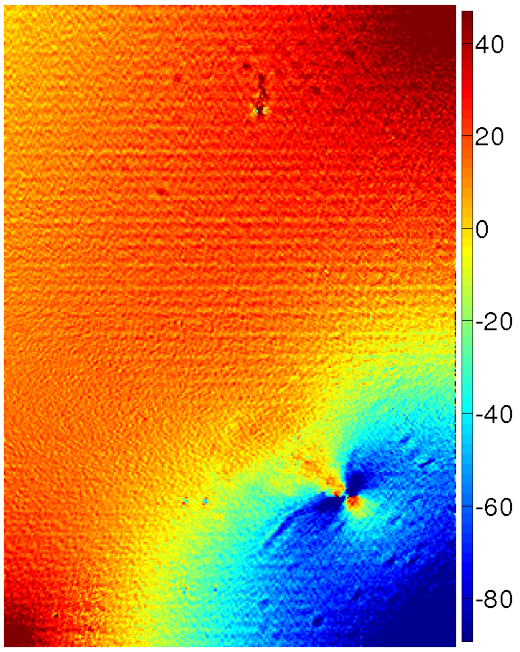

(c) ε_s

S4: impacted at 20 J while simply supported

Figure 4.62: Experimental equivalent strain maps for the S4 case loaded at point 1 with 40 N (in µm/m).

4.8.44 S4 - P2 - Experimental strain maps

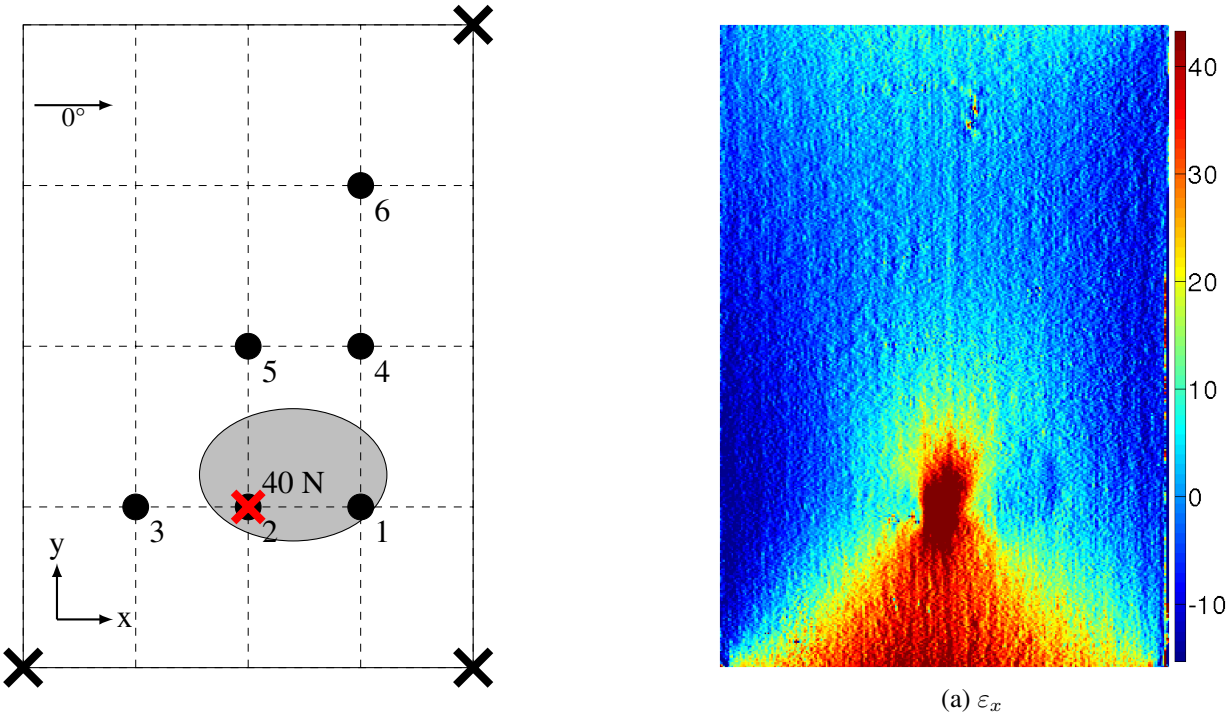

(a) ε_x

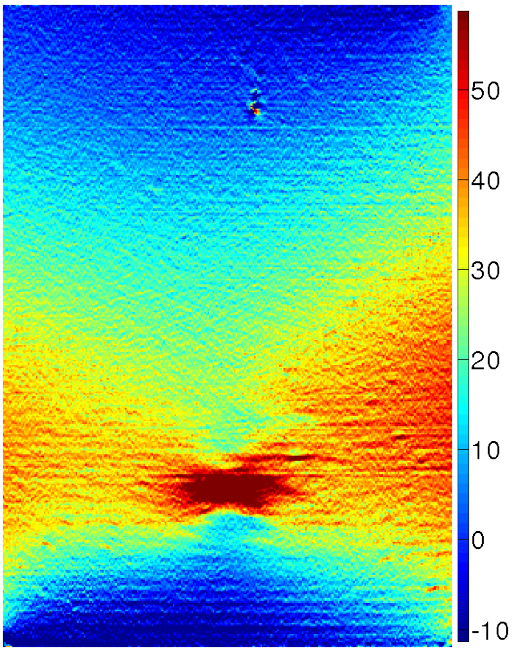

(b) ε_y

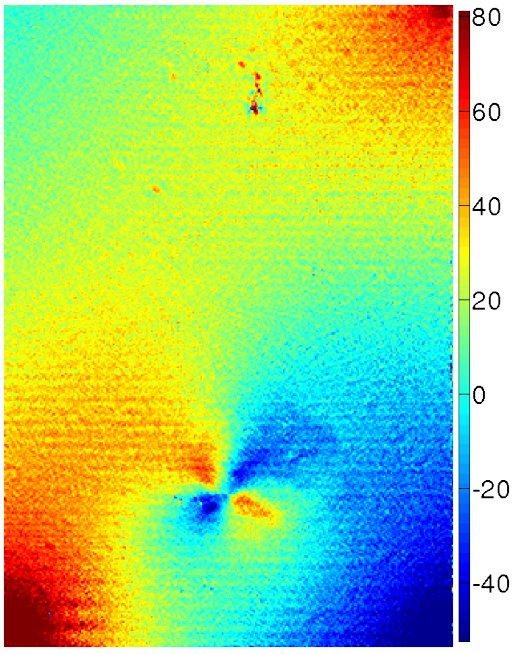

(c) ε_s

S4: impacted at 20 J while simply supported

Figure 4.63: Experimental equivalent strain maps for the S4 case loaded at point 2 with 40 N (in µm/m).

4.8.45 S4 - P3 - Experimental strain maps

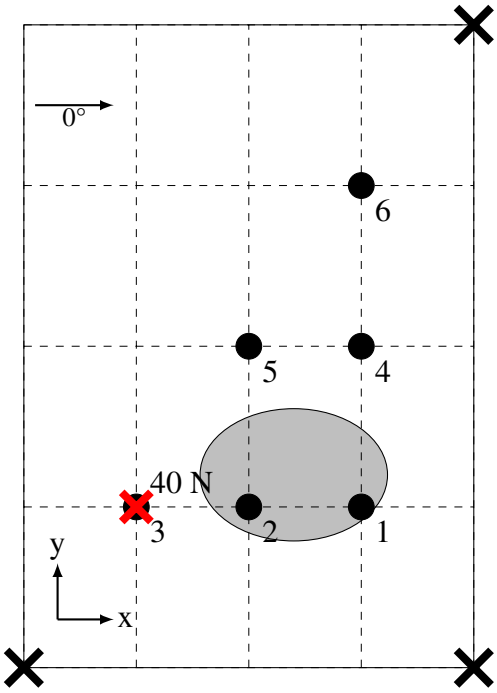

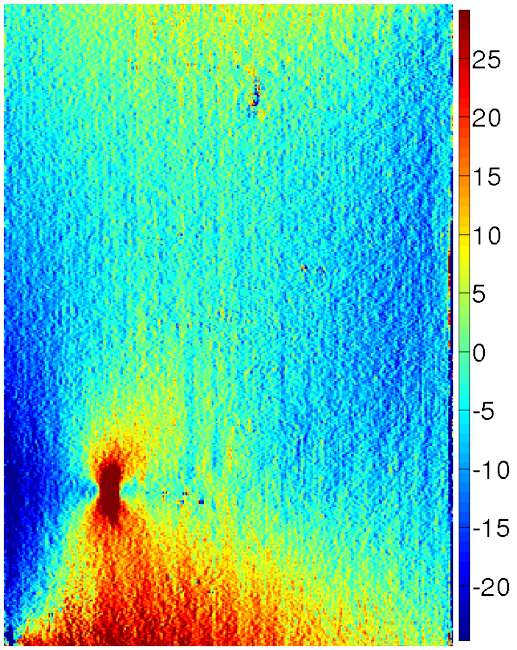

(a) ε_x

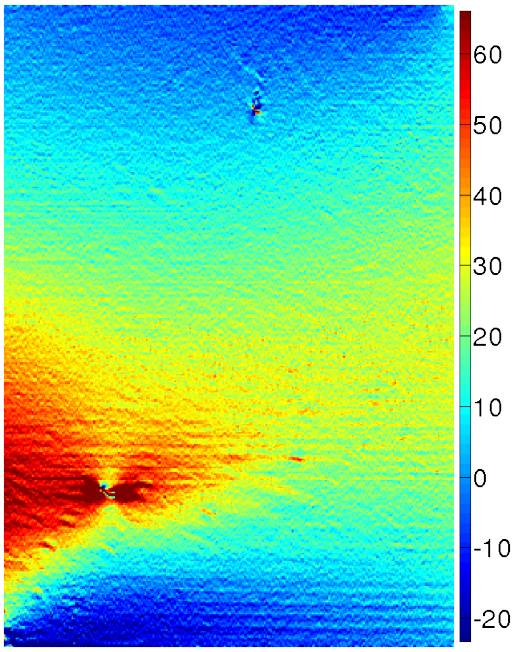

(b) ε_y

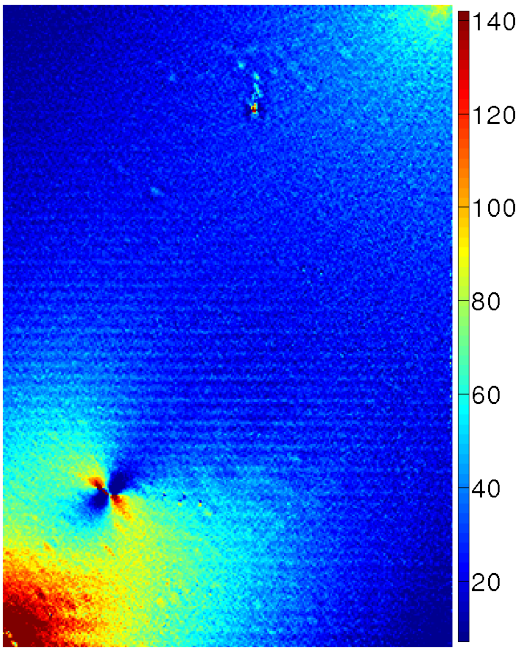

(c) ε_s

S4: impacted at 20 J while simply supported

Figure 4.64: Experimental equivalent strain maps for the S4 case loaded at point 3 with 40 N (in µm/m).

4.8.46 S4 - P4 - Experimental strain maps

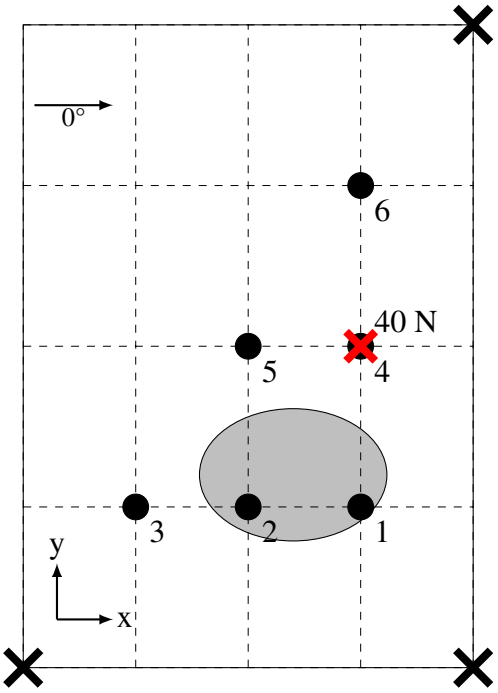

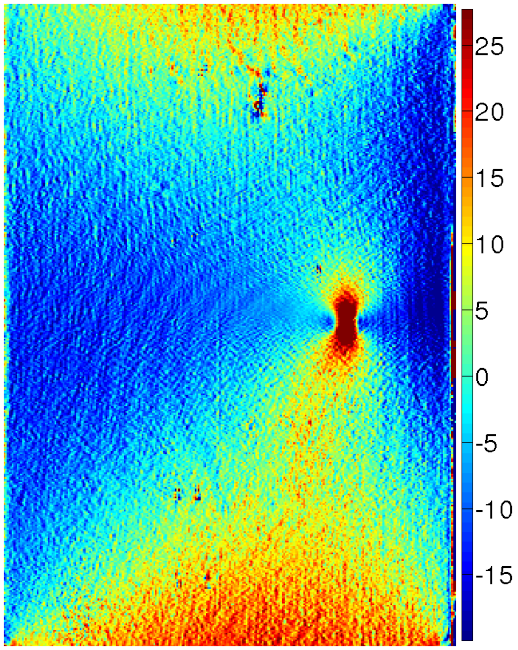

(a) ε_x

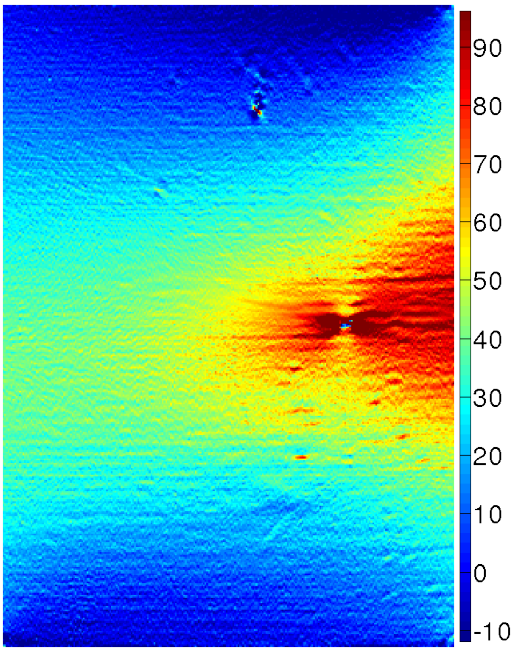

(b) ε_y

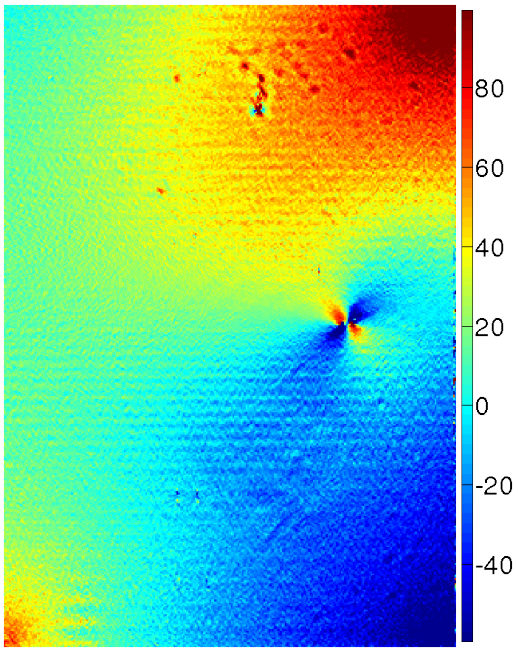

(c) ε_s

S4: impacted at 20 J while simply supported

Figure 4.65: Experimental equivalent strain maps for the S4 case loaded at point 4 with 40 N (in µm/m).

4.8.47 S4 - P5 - Experimental strain maps

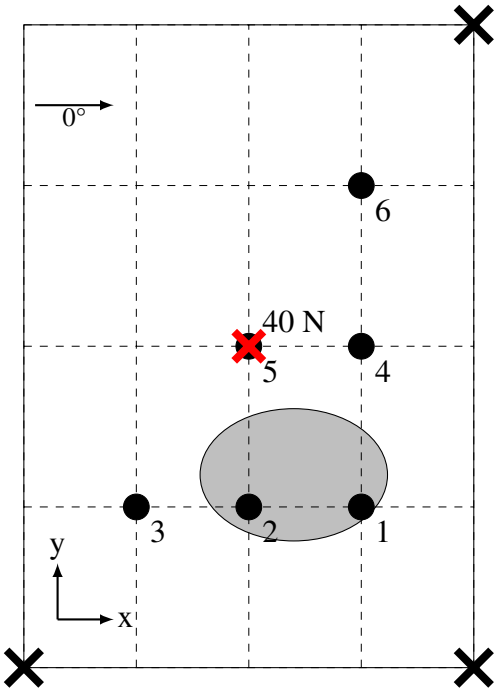

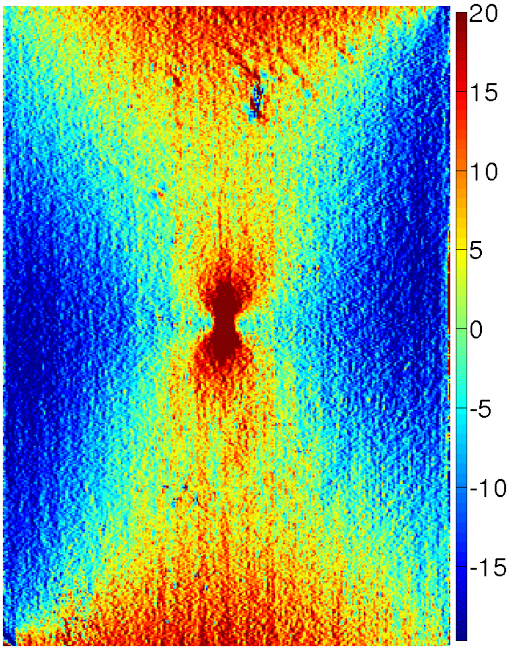

(a) ε_x

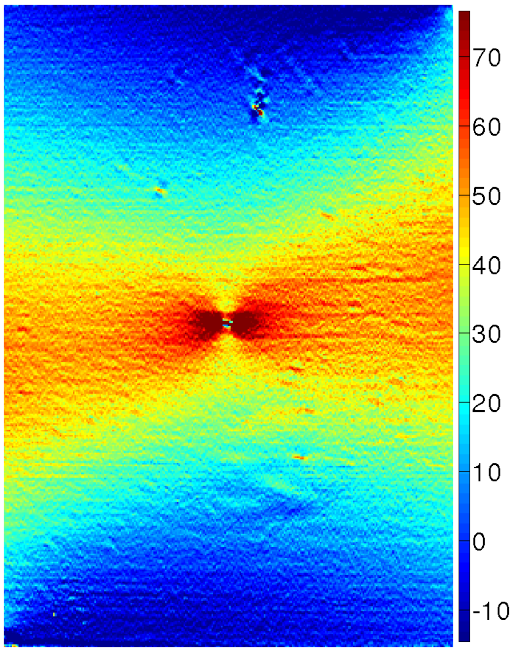

(b) ε_y

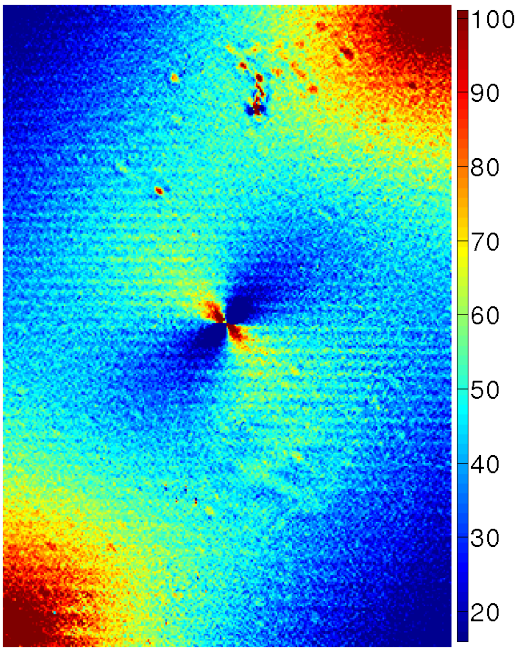

(c) ε_s

S4: impacted at 20 J while simply supported

Figure 4.66: Experimental equivalent strain maps for the S4 case loaded at point 5 with 40 N (in µm/m).

4.8.48 S4 - P6 - Experimental strain maps

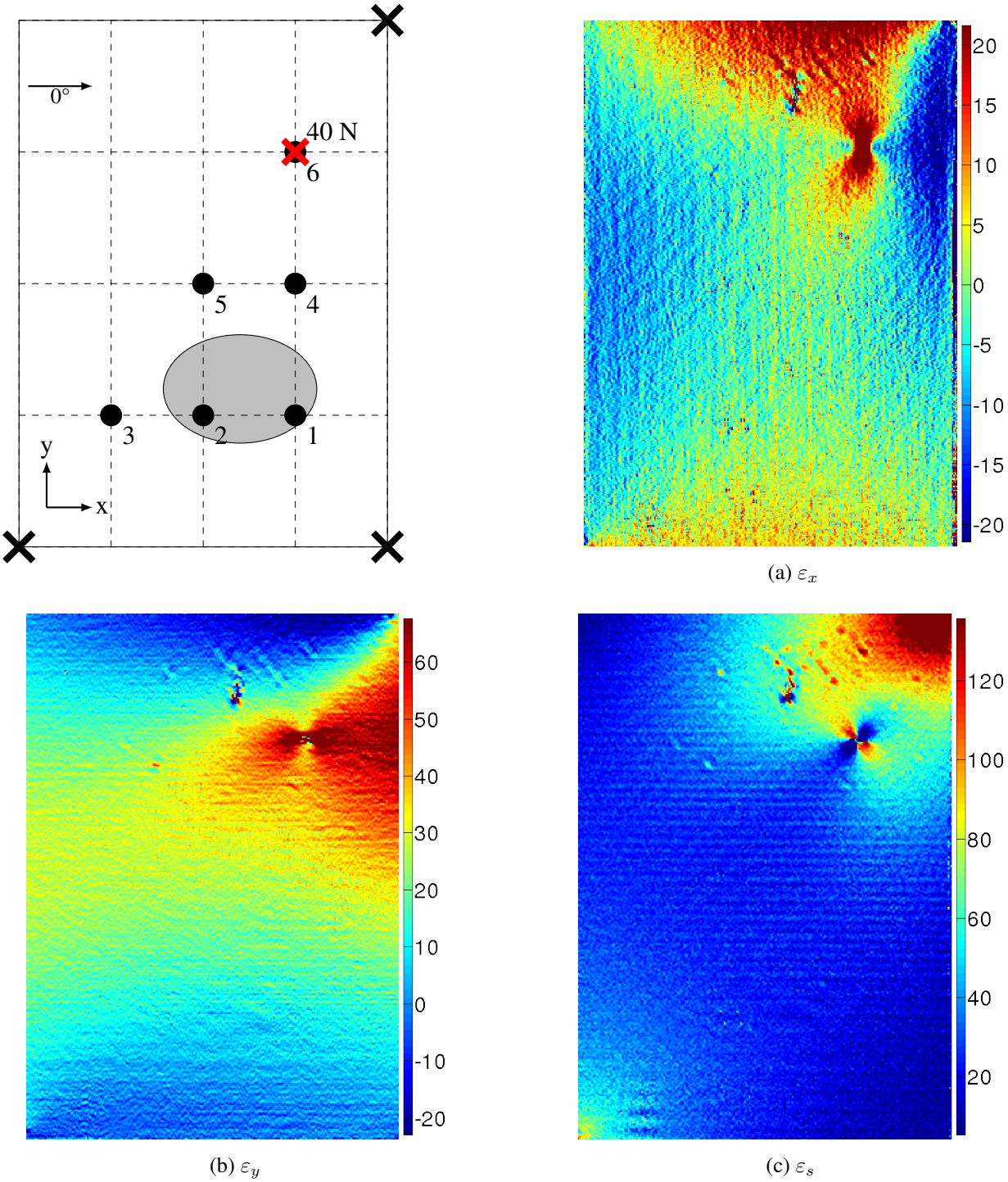

(a) ε_x

(b) ε_y

(c) ε_s

S4: impacted at 20 J while simply supported

Figure 4.67: Experimental equivalent strain maps for the S4 case loaded at point 6 with 40 N (in µm/m).

4.8.49 S4 - Experimental EG maps

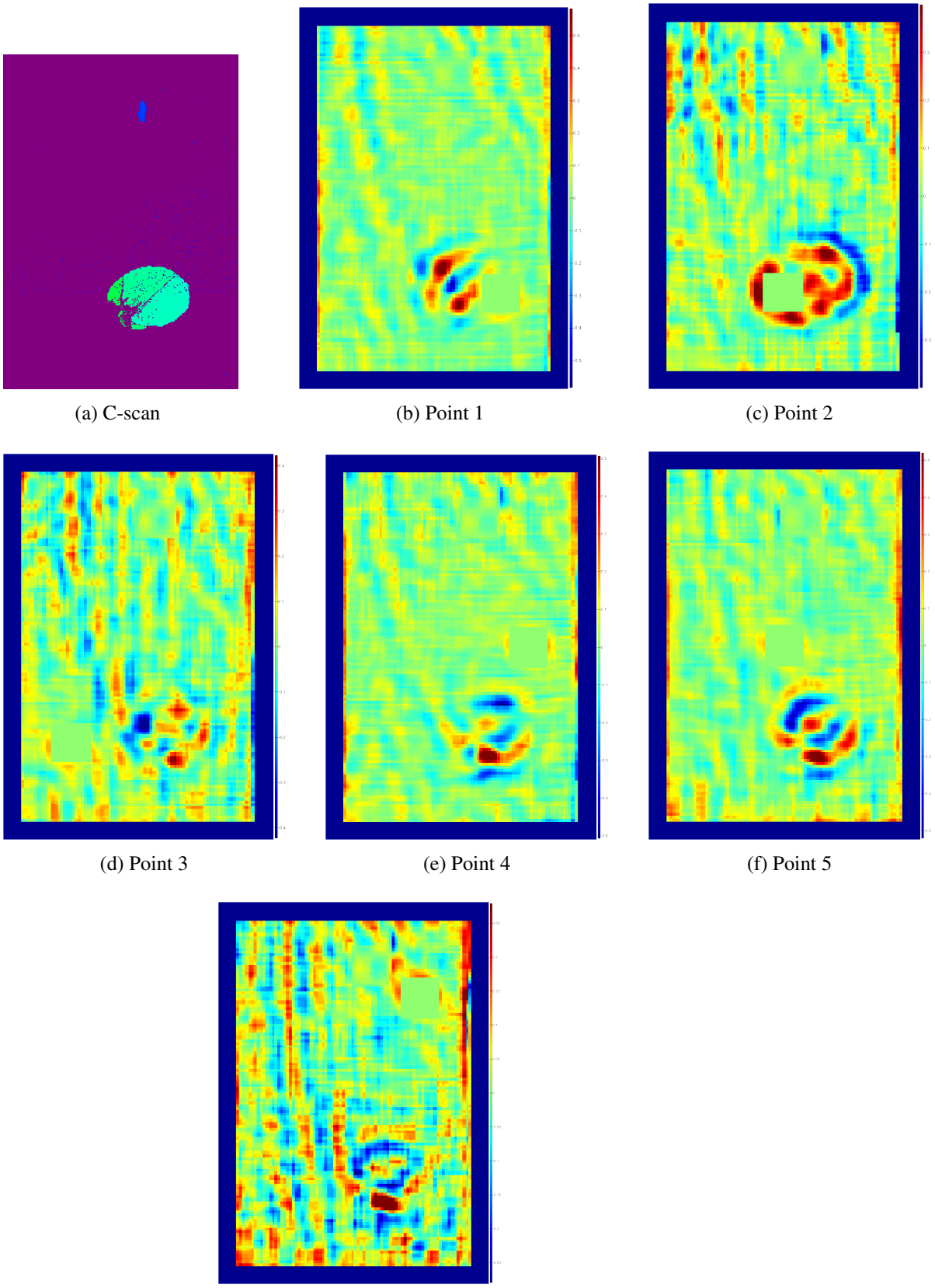

(a) C-scan (b) Point 1 (c) Point 2

(d) Point 3 (e) Point 4 (f) Point 5

(g) Point 6

S4: impacted at 20 J while simply supported

Figure 4.68: EG map for the experimental results from the S4 sample with 3 pixels sliding pitch and 40×40 pixels^2 sliding window.

GENERAL CONCLUSIONS AND PERSPECTIVES

In this work, a new methodology has been proposed to experimentally validate numerical models simulating the behaviour at low load of impacted layered composite structures. The validation is based on experimental results obtained by means of an optical full-field kinematic measurement technique: deflectometry.

General conclusions

– A new formula was derived to link-up the spatial grid shifts to the local slope changes. It takes into account the geometrical non-linearity of this two dimensional problem. For a large distance between the sample and the grid compared to the dimensions of the sample, this non-linearity can be ignored and the simple linear formula proposed in previous studies can be used. A formula was also derived to study the effect of a rigid-body out-of-plane displacement on the strain fields and the effect was found to be negligible compared to the strain levels present in the experimental maps for the configurations used in this work.

– An improvement was brought to the specimen preparation in order to reduce the effect of diffusive reflections from the specimen surface on the measured strain fields. The gel coat has been opacified using an inert graphite powder filler. Also the effect of the coating on the structural stiffnesses has been quantified using a theoretical approach and evaluated to be smaller than 2%.

– Deflectometry was applied to beam samples with artificial delaminations or real impacts. The measurement technique was sensitive enough to capture the effect of small scale damage such as a 30 mm artificial delamination or a 10 J impact thanks to its high strain and spatial resolutions.

– Based on the observations of CT-scans of the impacted samples, finite element models were built-up to simulate the post-impact behaviour. Different forms of delamination were implemented in the models and compared to the experimental results. Similar patterns were observed but the correlation was not perfect.

– Artificial delaminations were manufactured by inserting PTFE films between plies but the experimental results did not reveal any form of delamination. In order to debond the PTFE film from the plies so as to obtain a more realistic delamination, two mechanical straining methods were used: shim insertion and short beam shear test. The deflectometry results after short beam shear tests presented a better correlation with the numerical results. The short beam shear test is therefore recommended to trigger debonding of inserted PTFE films when trying to create an artificial delamination.

– Impacted plates with different boundary conditions during impact were tested with the deflectometry technique. The location and extent of damage were revealed for most loading configurations by observation of the strain maps. However, some loading conditions revealed the effect of the damage only faintly, if at all. This illustrates the need for a loading configuration which activates the different stiffnesses in the damaged region. However, this detection of damage is only based on visual appraisal. The maps are very useful to help develop and validate refined and accurate finite element simulations of impact damage. However, detecting damage is not so easy by visual examination of these maps as they are already spatially complex and the effect of damage is just an additional feature.

– A new damage indicator based on the virtual fields method has been developed and applied to the results obtained with the plates in order to try to extract the damage location without relying on any subjective visual appraisal. It identified the edges of the damaged area for most loading configurations when enough spatial information was available. Combining load cases helped the detection by providing more spatial information coming from the different load cases. One of the advantages of this indicator is its capacity to take advantage of the available complex spatial information in the three curvature maps to produce a single map representing the information in a nearly binary format.

Perspectives

– In the expression of the link between the spatial grid shift and the local slope changes, the out-of-plane displacement was studied separately from the deformation of the sample. It could be interesting to derive the equations considering both effects at the same time. Because of the link between the out-of-plane displacement and the slopes, a set of non-linear differential equations should be obtained. This equation could be used to numerically simulate the deflectometry experiments. It is not envisaged however that this will change the conclusions from this work.

– Because the spatial resolution of the CT-scans was too small, the shape of the delaminations was arbitrarily chosen and cracks were not modelled. More refined CT-scans could help to build-up more representative FE models. These models could be experimentally validated using the deflectometry technique for post-impact behaviour at low load as performed here. Especially, the effect of friction or fibre-bridging could be explored more in depth. Refined numerical models are of primary importance to accurately predict compression after impact for instance. It is believed that pursuing the present work might lead to an invaluable tool to help design engineers.

– Work could be undertaken to find a film material creating a better delamination without the need for mechanical straining. If it is not possible to bypass the straining, the material should at least minimize the resin/film adhesion so that a short beam shear test could be performed at low load levels reducing the risk of fibre failure at the loaded point.

– The results obtained using the equilibrium gap indicator may be improved by increasing the spatial resolution of the experimental results. The main limitation is the noise level corrupting the equilibrium, therefore a minimum number of data points are required to compute the equilibria. If more data points were available, more equilibrium gap values could be extracted and the damaged zone would be more precisely defined.

– Currently, deflectometry is limited to flat surfaces. It would be extremely interesting to extend its use to curved surfaces. If this could be done, the method could be applied to fan blades and help understanding how they are affected by impact damage. Another current limitation is the surface preparation to obtain specular reflection. Extending this surface preparation procedure to curved surfaces will be of primary importance to extend the usage of deflectometry to that case. This is probably not going to be an easy and straightforward problem to solve.

BIBLIOGRAPHY

[1] S. Hong and D. Liu, "On the relationship between impact energy and delamination area," *Experimental Mechanics*, vol. 29, no. 2, pp. 115–120, 1989. 1

[2] J.-K. Kim, D. B. MacKay, and Y.-W. Mai, "Drop-weight impact damage tolerance of CFRP with rubber-modified epoxy matrix," *Composites*, vol. 24, no. 6, pp. 485–494, 1993. 1, 12, 13

[3] D. Liu and L. E. Malvern, "Matrix cracking in impacted glass/epoxy plates," *Journal of Composite Materials*, vol. 21, no. 7, pp. 594–609, 1987. 1, 7

[4] D. Liu, "Impact-induced delamination: a view of bending stiffness mismatching," *Journal of Composite Materials*, vol. 22, no. 7, pp. 674–692, 1988. 1, 5

[5] W. J. Cantwell and J. Morton, "The impact resistance of composite materials - a review," *Composites*, vol. 22, no. 5, pp. 347–362, 1991. 1, 11

[6] M. J. Pavier and M. P. Clarke, "Experimental techniques for the investigation of the effects of impact damage on carbon-fibre composites," *Composites Science and Technology*, vol. 55, no. 2, pp. 157–169, 1995. 1, 16, 60, 67

[7] K. Dransfield, C. Baillie, and Y.-W. Mai, "Improving the delamination resistance of CFRP by stitching - a review," *Composites Science and Technology*, vol. 50, no. 3, pp. 305–317, 1994. 4

[8] S. Abrate, *Impact on composite structures*. Cambridge University Press, 1998. 4, 7, 8, 9, 12, 67, 88

[9] P. P. Camanho, C. G. Davila, and M. F. de Moura, "Numerical simulation of mixed-mode progressive delamination in composite materials," *Journal of Composite Materials*, vol. 37, no. 16, pp. 1415–1438, 2003. 4, 5

[10] V. V. Bolotin, "Delaminations in composite structures: its origin, buckling, growth and stability," *Composites Part B: Engineering*, vol. 27, no. 2, pp. 129–145, 1996. 4, 5, 7

[11] C. Mittelstedt and W. Becker, "Free-edge effects in composite laminates," *Applied Mechanics Reviews*, vol. 60, no. 5, pp. 217–245, 2007. 5

[12] Z. Petrossian and M. R. Wisnom, "Parametric study of delamination in composites with discontinuous plies using an analytical solution based on fracture mechanics," *Composites Part A: Applied Science and Manufacturing*, vol. 29, no. 4, pp. 403–414, 1998. 5

[13] R. Y. Kim and S. R. Soni, "Experimental and analytical studies on the onset of delamination in laminated composites," *Journal of Composite Materials*, vol. 18, no. 1, pp. 70–80, 1984. 5

[14] J. M. Whitney and R. J. Nuismer, "Stress fracture criteria for laminated composites containing stress concentrations," *Journal of Composite Materials*, vol. 8, pp. 253–265, 1974. 5

[15] P. P. Camanho and F. L. Matthews, "Delamination onset prediction in mechanically fastened joints in composite laminates," *Journal of Composite Materials*, vol. 33, no. 10, pp. 906–927, 1999. 5

[16] C. G. Davila and E. R. Johnson, "Analysis of delamination initiation in postbuckled dropped-ply laminates," *AIAA journal*, vol. 31, no. 4, pp. 721–727, 1993. 5

[17] C. Fan, P.-Y. B. Jar, and J. J. R. Cheng, "Energy-based analyses of delamination development in fibre-reinforced polymers under 3-point bending," *Composites Science and Technology*, vol. 66, no. 13, pp. 2143–2155, 2006. 5

[18] G. A. Kardomateas and A. A. Pelegri, "The stability of delamination growth in compressively loaded composite plates," *International Journal of Fracture*, vol. 65, pp. 261–276, 1994. 5

[19] E. J. Barbero and J. N. Reddy, "Modeling of delamination in composite laminates using a layer-wise plate theory," *International Journal of Solids and Structures*, vol. 28, no. 3, pp. 373–388, 1991. 5

[20] K. T. O'Brien, "Interlaminar fracture toughness: the long and winding road to standardization," *Composites Part B: Engineering*, vol. 29, no. 1, pp. 57–62, 1998. 6, 60

[21] P. Davies, B. R. K. Blackman, and A. J. Brunner, "Standard test methods for delamination resistance of composite materials: Current status," *Applied Composite Materials*, vol. 5, pp. 345–364, 1998. 6, 60, 93

[22] W. Cui, M. R. Wisnom, and M. Jones, "New model to predict static strength of tapered laminates," *Composites*, vol. 26, no. 2, pp. 141–146, 1995. 6

[23] G. Caprino, J. C. Halpin, and L. Nicolais, "Fracture mechanics in composite materials," *Composites*, vol. 10, no. 4, pp. 223–227, 1979. 7

[24] J. Renard and F. Roudolff, "Analytical and numerical calculation of strain energy release rate during delamination growth in a carbon epoxy laminate," *Composites Science and Technology*, vol. 42, no. 4, pp. 305–316, 1991. 7

[25] A. Diaz Diaz, J.-F. Caron, and A. Ehrlacher, "Analytical determination of the modes i, ii and iii energy release rates in a delaminated laminate and validation of a delamination criterion," *Composite Structures*, vol. 78, no. 3, pp. 424–432, 2007. 7

[26] G. P. Cherepanov, "Crack propagation in continuous media," *Journal of Applied Mathematics and Mechanics*, vol. 31, no. 3, pp. 503–512, 1967. 7

[27] J. R. Rice, "A path independent integral and the approximate analysis of strain concentration by notches and cracks," *Journal of Applied Mechanics*, vol. 35, no. 2, pp. 379–386, 1968. 7

[28] T. K. Hellen, "On the method of virtual crack extensions," *International Journal for Numerical Methods in Engineering*, vol. 9, no. 1, pp. 187–207, 1975. 7

[29] G. C. Sih, "Fracture mechanics of composite materials," in *1st USA-USSR Symposium on Fracture of Composite Materials*, 1978. 7

[30] E. F. Rybicki and M. F. Kanninen, "A finite element calculation of stress intensity factors by a modified crack closure integral," *Engineering Fracture Mechanics*, vol. 9, no. 4, pp. 931–938, 1977. 7

[31] T. K. O'Brien, "Characterization of delamination onset and growth in a composite laminate," *Damage in Composite Materials*, vol. ASTM STP-775, p. 140, 1982. 7

[32] R. Krueger, "Virtual crack closure technique: history, approach, and applications," *Applied Mechanics Reviews*, vol. 57, no. 2, pp. 109–143, 2004. 7

[33] S. Abrate, "Impact on laminated composite materials," *Applied Mechanics Reviews*, vol. 44, no. 4, pp. 155–190, 1991. 7, 11, 76

[34] W. J. Cantwell and J. Morton, "Comparison of the low and high velocity impact response of CFRP," *Composites*, vol. 20, no. 6, pp. 545–551, 1989. 7

[35] G. A. O. Davies and P. Robinson, "Predicting failure by debonding/delamination," in *AGARD: 74th Structures and Materials Meeting*, vol. 74, pp. 60–87, 1992. 7

[36] S. P. Joshi and C. T. Sun, "Impact induced fracture in a laminated composite," *Journal of Composite Materials*, vol. 19, no. 1, pp. 51–66, 1985. 7

[37] P. Robinson and G. A. O. Davies, "Impactor mass and specimen geometry effects in low velocity impact of laminated composites," *International Journal of Impact Engineering*, vol. 12, no. 2, pp. 189–207, 1992. 7

[38] K. N. Shivakumar, W. Elber, and W. Illg, "Prediction of low-velocity impact damage in thin circular laminates," *AIAA Journal*, vol. 23, no. 3, pp. 442–449, 1985. 7

[39] P. O. Sjoblom, T. J. Hartness, and T. M. Cordell, "On low-velocity impact testing of composite materials," *Journal of Composite Materials*, vol. 22, no. 1, pp. 30–52, 1988. 7

[40] M. O. W. Richardson and M. J. Wisheart, "Review of low-velocity impact properties of composite materials," *Composites Part A: Applied Science and Manufacturing*, vol. 27, no. 12, pp. 1123–1131, 1996. 7, 10, 12

[41] D. S. Bartus, "A review: impact damage of composite materials," *Journal of advanced materials*, vol. 39, no. 3, pp. 3–21, 2007. 7

[42] G. A. Bibo and P. J. Hogg, "The role of reinforcement architecture on impact damage mechanisms and post-impact compression behaviour," *Journal of Materials Science*, vol. 31, no. 5, pp. 1115–1137, 1996. 8, 9, 10

[43] B. P. Jang, W. Kowbel, and B. Z. Jang, "Impact behavior and impact-fatigue testing of polymer composites," *Composites Science and Technology*, vol. 44, no. 2, pp. 107–118, 1992. 8, 12

[44] K. L. Reifsnider and A. Highsmith, "The relationship of stiffness changes in composite laminates to fracture-related damage mechanisms," in *Fracture of composite materials*, vol. 2, pp. 279–290, 1981. 9

[45] K.-H. Im, J.-K. Sim, and I.-Y. Yang, "Impact damages and residual bending strength of CFRP composite laminates subjected to impact loading," *Journal of Mechanical Science and Technology*, vol. 10, pp. 423–434, 1996. 9

[46] K. S. Mazdiyasni, *Fiber reinforced ceramic composites: materials, processing, and technology*. Noyes Publications, 1990. 10

[47] J. Morton and E. W. Godwin, "Impact response of tough carbon fibre composites," *Composite Structures*, vol. 13, no. 1, pp. 1–19, 1989. 10

[48] J. E. L. da Silva Junior, S. Paciornik, and J. R. M. d'Almeida, "Evaluation of the effect of the ballistic damaged area on the residual impact strength and tensile stiffness of glass-fabric composite materials," *Composite Structures*, vol. 64, no. 1, pp. 123–127, 2004. 10

[49] H.-P. Cui, W.-D. Wen, and H.-T. Cui, "An integrated method for predicting damage and residual tensile strength of composite laminates under low velocity impact," *Computers & Structures*, vol. 87, no. 7-8, pp. 456–466, 2009. 10

[50] A. Sjogren, A. Krasnikovs, and J. Varna, "Experimental determination of elastic properties of impact damage in carbon fibre/epoxy laminates," *Composites Part A: Applied Science and Manufacturing*, vol. 32, no. 9, pp. 1237–1242, 2001. 10, 11, 12

[51] G. Caprino, "Residual strength prediction of impacted CFRP laminates.," *Journal of Composite Materials*, vol. 18, no. 6, pp. 508–518, 1984. 11

[52] S. K. Chaturvedi and R. L. Sierakowskis, "Effects of impactor size on impact damage-growth and residual properties in an SMC-R50 composite.," *Journal of Composite Materials*, vol. 19, no. 2, pp. 100–113, 1985. 11

[53] D. A. Wyrick and D. F. Adams, "Residual strength of a carbon/epoxy composite material subjected to repeated impact," *Journal of Composite Materials*, vol. 22, no. 8, pp. 749–765, 1988. 11

[54] M. S. El-Zein and K. L. Reifsnider, "On the prediction of tensile strength after impact of composite laminates," *Journal of Composites Technology and Research*, vol. 12, no. 3, pp. 147–154, 1990. 11

[55] O. Ishai and A. Shragai, "Effect of impact loading on damage and residual compressive strength of CFRP laminated beams," *Composite Structures*, vol. 14, no. 4, pp. 319–337, 1990. 11

[56] F. J. Guild, P. J. Hogg, and J. C. Prichard, "A model for the reduction in compression strength of continuous fibre composites after impact damage," *Composites*, vol. 24, no. 4, pp. 333–339, 1993. 11

[57] J. Y. Huang, "Prediction of the residual strength of laminated composites subjected to impact loading," *Journal of Materials Processing Tech.*, vol. 54, no. 1-4, pp. 205–210, 1995. 11

[58] A. Kinsey, D. E. J. Saunders, and C. Soutis, "Post-impact compressive behaviour of low temperature curing woven CFRP laminates," *Composites*, vol. 26, no. 9, pp. 661–667, 1995. 11

[59] G. A. Bibo and P. J. Hogg, "Influence of reinforcement architecture on damage mechanisms and residual strength of glass-fibre/epoxy composite systems," *Composites Science and Technology*, vol. 58, no. 6, pp. 803–813, 1998. 11

[60] X. Zhang, G. A. O. Davies, and D. Hitchings, "Impact damage with compressive preload and post-impact compression of carbon composite plates," *International Journal of Impact Engineering*, vol. 22, no. 5, pp. 485–509, 1999. 11

[61] J. Wei, J. H. Zhao, and Y. M. Liang, "Experimental research on residual mechanical properties laminates subjected to low energy impact," *Journal of Astronautics*, vol. 20, no. 1, pp. 92–98, 1999. 11

[62] D. D. R. Cartié and P. E. Irving, "Effect of resin and fibre properties on impact and compression after impact performance of CFRP," *Composites - Part A: Applied Science and Manufacturing*, vol. 33, no. 4, pp. 483–493, 2002. 11

[63] G. J. Short, F. J. Guild, and M. J. Pavier, "Post-impact compressive strength of curved GFRP laminates," *Composites Part A: Applied Science and Manufacturing*, vol. 33, no. 11, pp. 1487–1495, 2002. 11

[64] N. K. Naik, M. N. Joglekar, H. Arya, S. V. Borade, and K. N. Ramakrishna, "Impact and compression after impact characteristics of plain weave fabric composites: effect of plate thickness," *Advanced Composite Materials: The Official Journal of the Japan Society of Composite Materials*, vol. 12, no. 4, pp. 261–280, 2004. 11

[65] O. A. Khondker, I. Herszberg, and H. Hamada, "Measurements and prediction of the compression-after-impact strength of glass knitted textile composites," *Composites Part A: Applied Science and Manufacturing*, vol. 35, no. 2, pp. 145–157, 2004. 11

[66] S. Sanchez-Saez, E. Barbero, R. Zaera, and C. Navarro, "Compression after impact of thin composite laminates," *Composites Science and Technology*, vol. 65, no. 13, pp. 1911–1919, 2005. 11

[67] V. P. W. Shim and L. M. Yang, "Characterization of the residual mechanical properties of woven fabric reinforced composites after low-velocity impact," *International Journal of Mechanical Sciences*, vol. 47, no. 4-5, pp. 647–665, 2005. 11, 12

[68] X. Zhang, L. Hounslow, and M. Grassi, "Improvement of low-velocity impact and compression-after-impact performance by z-fibre pinning," *Composites Science and Technology*, vol. 66, no. 15, pp. 2785–2794, 2006. 11

[69] P. M. Schubel, J.-J. Luo, and I. M. Daniel, "Impact and post impact behavior of composite sandwich panels," *Composites Part A: Applied Science and Manufacturing*, vol. 38, no. 3, pp. 1051–1057, 2007. 11

[70] S. Sihn, R. Y. Kim, K. Kawabe, and S. W. Tsai, "Experimental studies of thin-ply laminated composites," *Composites Science and Technology*, vol. 67, no. 6, pp. 996–1008, 2007. 11

[71] S. Sanchez-Saez, E. Barbero, and C. Navarro, "Compressive residual strength at low temperatures of composite laminates subjected to low-velocity impacts," *Composite Structures*, vol. 85, no. 3, pp. 226–232, 2008. 11

[72] P. J. Hogg and G. A. Bibo, *Mechanical Testing of Advanced Fibre Composites*, ch. Impact and damage tolerance, pp. 211–247. Woodhead Publishing Ltd, 2000. 11

[73] G. Zhou, "Compressive behaviour of large undamaged and damaged thick laminated panels," *Composite Structures*, vol. 38, no. 1-4, pp. 589–597, 1997. 11

[74] J. H. Starnes, "Failure characteristics of graphite-epoxy structural components loaded in compression," tech. rep., NASA, 1982. 11

[75] N. Sela and O. Ishai, "Interlaminar fracture toughness and toughening of laminated composite materials: a review," *Composites*, vol. 20, no. 5, pp. 423–435, 1989. 11

[76] A. T. Nettles and A. J. Hodge, "Compression-after-impact testing of thin composite materials," in *International SAMPE Technical Conference, 23rd*, pp. 177–183, 1991. 11

[77] D30.05, "ASTM D7137 / D7137M - 07: Standard test method for compressive residual strength properties of damaged polymer matrix composite plates," 2007. 11, 24

[78] E. F. Dost, S. R. Finn, J. J. Stevens, K. Y. Lin, and C. E. Fitch, "Experimental investigations into composite fuselage impact damage resistance and post-impact compression behavior," in *Society for the Advancement of Material and Process Engineering (USA)*, pp. 1199–1212, 1992. 11

[79] L. E. Asp, S. Nilsson, and S. Singh, "An experimental investigation of the influence of delamination growth on the residual strength of impacted laminates," in *11th International Conference on Composite Materials*, 1998. 11

[80] E. Greenhalgh, S. Singh, and D. Roberts, "Impact damage growth and failure of carbon-fibre reinforced plastics," in *11th International Conference on Composite Materials*, vol. 2-6, pp. 573–582, 1997. 11

[81] S. Nilsson, "Static compressive strength of impacted composite panels," in *58th conference of The Aeronautical Research Institute of Sweden (FFA TN 1996-58)*, 1997. 11

[82] K. Mizukawa, T. Fujii, K. Itami, and K. Osaka, "Impact strength of thin-walled composite structures under combined bending and torsion," *Composite Structures*, vol. 4, no. 2, pp. 179–192, 1985. 11

[83] G. Minak, S. Abrate, D. Ghelli, R. Panciroli, and A. Zucchelli, "Residual torsional strength after impact of CFRP tubes," *Composites Part B: Engineering*, vol. 41, no. 8, pp. 637–645, 2010. 11

[84] K. R. Hirschbuehler, "Comparison of several mechanical tests used to evaluate the toughness of composites," in *ASTM Special Technical Publication*, pp. 61–73, 1987. 12

[85] A. P. Mouritz, J. Gallagher, and A. A. Goodwin, "Flexural strength and interlaminar shear strength of stitched GRP laminates following repeated impacts," *Composites Science and Technology*, vol. 57, no. 5, pp. 509–522, 1997. 12

[86] X. Cheng, C. Kou, and Z. Li, "Behavior of bending after low velocity impact and quasi-static transverse indentation of composite honeycomb core sandwich panels," *Acta Materiae Compositae Sinica*, vol. 17, no. 2, pp. 114–118, 2000. 12

[87] A. M. Amaro, P. N. B. Reis, and M. F. S. F. de Moura, "Residual strength after low velocity impact in carbon-epoxy laminates," *Materials Science Forum*, vol. 514-516, pp. 624–628, 2006. 12

[88] Z. Y. Zhang and M. O. W. Richardson, "Low velocity impact induced damage evaluation and its effect on the residual flexural properties of pultruded GRP composites," *Composite Structures*, vol. 81, no. 2, pp. 195–201, 2007. 12

[89] H. Chenghong, L. Yubin, Z. Zuoguang, and S. Zhijie, "Impact damage modes and residual flexural properties of composites beam," *Journal of Reinforced Plastics and Composites*, vol. 27, no. 11, pp. 1163–1175, 2008. 12, 13

[90] C. Santiuste, S. Sanchez-Saez, and E. Barbero, "Residual flexural strength after low-velocity impact in glass/polyester composite beams," *Composite Structures*, vol. 92, no. 1, pp. 25–30, 2010. 12

[91] D. Hull and T. W. Clyne, *An introduction to composite materials*. Cambridge University Press, 1981. 12

[92] P. K. Mallick, *Fiber-reinforced composites: materials, manufacturing, and design*. Mechanical engineering, M. Dekker, 1993. 12

[93] G. Caprino, V. Lopresto, C. Scarponi, and G. Briotti, "Influence of material thickness on the response of carbon-fabric/epoxy panels to low velocity impact," *Composites Science and Technology*, vol. 59, no. 15, pp. 2279–2286, 1999. 14

[94] H. Kaczmarek and S. Maison, "Comparative ultrasonic analysis of damage in CFRP under static indentation and low-velocity impact," *Composites Science and Technology*, vol. 51, no. 1, pp. 11–26, 1994. 14

[95] O. S. Salawu, "Detection of structural damage through changes in frequency: a review," *Engineering Structures*, vol. 19, no. 9, pp. 718–723, 1997. 14

[96] H. G. Chen, Y. J. Yan., W. H. Chen, J. S. Jiang, L. Yu, and Z. Y. Wu, "Early damage detection in composite wingbox structures using Hilbert-Huang transform and genetic algorithm," *Structural Health Monitoring*, vol. 6, no. 4, pp. 281–297, 2007. 14

[97] S. W. Doebling, C. R. Farrar, and M. B. Prime, "A summary review of vibration-based damage identification methods," *Identification Methods,The Shock and Vibration Digest*, vol. 30, pp. 91–105, 1998. 14, 15

[98] W. Ke, M. Castaings, and C. Bacon, "3D finite element simulations of an air-coupled ultrasonic NDT system," *NDT & E International*, vol. 42, no. 6, pp. 524–533, 2009. 14

[99] T. Hajzargerbashi, T. Kundu, and S. Bland, "An improved algorithm for detecting point of impact in anisotropic inhomogeneous plates," *Ultrasonics*, vol. 51, no. 3, pp. 317–324, 2011. 14

[100] J. P. Komorowski, R. W. Gould, and D. L. Simpson, "Synergy between advanced composites and new NDI methods," *Advanced Performance Materials*, vol. 5, pp. 137–151, 1998. 15

[101] L. Iannucci and M. L. Willows, "An energy based damage mechanics approach to modelling impact onto woven composite materials: part II. experimental and numerical results," *Composites Part A: Applied Science and Manufacturing*, vol. 38, no. 2, pp. 540–554, 2007. 16

[102] C. Garnier, M.-L. Pastor, F. Eyma, and B. Lorrain, "The detection of aeronautical defects in situ on composite structures using non destructive testing," *Composite Structures*, vol. 93, no. 5, pp. 1328–1336, 2011. 16, 18, 19, 20

[103] R. Ambu, F. Aymerich, F. Ginesu, and P. Priolo, "Assessment of NDT interferometric techniques for impact damage detection in composite laminates," *Composites Science and Technology*, vol. 66, no. 2, pp. 199–205, 2006. 16, 19

[104] C. Bouvet, B. Castanié, M. Bizeul, and J.-J. Barrau, "Low velocity impact modelling in laminate composite panels with discrete interface elements," *International Journal of Solids and Structures*, vol. 46, no. 14-15, pp. 2809–2821, 2009. 16, 67

[105] H. Niemann, J. Morlier, A. Shahdin, and Y. Gourinat, "Damage localization using experimental modal parameters and topology optimization," *Mechanical Systems and Signal Processing*, vol. 24, no. 3, pp. 636–652, 2010. 16

[106] J. V. Araujo dos Santos, H. M. R. Lopes, M. Vaz, C. M. Mota Soares, C. A. Mota Soares, and M. J. M. de Freitas, "Damage localization in laminated composite plates using mode shapes measured by pulsed TV holography," *Composite Structures*, vol. 76, no. 3, pp. 272–281, 2006. 16, 19

[107] R. Olsson, "Analytical model for delamination growth during small mass impact on plates," *International Journal of Solids and Structures*, vol. 47, no. 21, pp. 2884–2892, 2010. 16, 67

[108] T. E. Preuss and G. Clark, "Use of time-of-flight c-scanning for assessment of impact damage in composites," *Composites*, vol. 19, no. 2, pp. 145–148, 1988. 16

[109] L. W. Kessler, "Review of progress and applications in acoustic microscopy," *The Journal of the Acoustical Society of America*, vol. 55, no. 5, pp. 909–918, 1974. 16

[110] A. Todoroki, H. Kobayashi, and J. G. Lee, "Image analysis of delamination cracks in carbon-fibre composites by scanning acoustic microscopy," *Composites Science and Technology*, vol. 52, no. 4, pp. 551–559, 1994. 16

[111] W. J. Cantwell and J. Morton, "Detection of impact damage in CFRP laminates," *Composite Structures*, vol. 3, no. 3-4, pp. 241–257, 1985. 16, 17

[112] M. T. Kortschot and C. J. Zhang, "Characterization of composite mesostructures and damage by de-ply radiography," *Composites Science and Technology*, vol. 53, no. 2, pp. 175–181, 1995. 17

[113] K. T. Tan, N. Watanabe, and Y. Iwahori, "X-ray radiography and micro-computed tomography examination of damage characteristics in stitched composites subjected to impact loading," *Composites Part B: Engineering*, vol. 42, no. 4, pp. 874–884, 2011. 17

[114] C. Devivier, F. Pierron, and M. R. Wisnom, "Damage detection in composite materials using deflectometry, a full-field slope measurement technique," *Composites Part A: Applied Science and Manufacturing*, vol. 43, no. 10, pp. 1650–1666, 2012. 17

[115] A. J. Moffat, P. Wright, J.-Y. Buffière, I. Sinclair, and S. M. Spearing, "Micromechanisms of damage in 0°splits in a [90/0]s composite material using synchrotron radiation computed tomography," *Scripta Materialia*, vol. 59, no. 10, pp. 1043–1046, 2008. 17, 21

[116] A. J. Moffat, P. Wright, L. Helfen, T. Baumbach, G. Johnson, S. M. Spearing, and I. Sinclair, "In situ synchrotron computed laminography of damage in carbon fibre-epoxy [90/0]s laminates," *Scripta Materialia*, vol. 62, no. 2, pp. 97–100, 2010. 17, 21

[117] A. E. Scott, M. Mavrogordato, P. Wright, I. Sinclair, and S. M. Spearing, "In situ fibre fracture measurement in carbon-epoxy laminates using high resolution computed tomography," *Composites Science and Technology*, vol. 71, no. 12, pp. 1471–1477, 2011. 17

[118] P. Wright, X. Fu, I. Sinclair, and S. M. Spearing, "Ultra high resolution computed tomography of damage in notched carbon fiber-epoxy composites," *Journal of Composite Materials*, vol. 42, no. 19, pp. 1993–2002, 2008. 17, 21

[119] P. Wright, A. J. Moffat, A. Renault, I. Sinclair, and S. M. Spearing, "High resolution computed tomography for modelling laminate damage," in *17th International Conference on Composite Materials*, 2009. 17, 21

[120] P. Wright, A. Moffat, I. Sinclair, and S. M. Spearing, "High resolution tomographic imaging and modelling of notch tip damage in a laminated composite," *Composites Science and Technology*, vol. 70, no. 10, pp. 1444–1452, 2010. 17, 21

[121] R. F. Anastasi, J. N. Zalameda, and E. I. Madaras, "Damage detection in rotorcraft composite structures using thermography and laser-based ultrasound," in *SEM X International Congress and Exposition on Experimental and Applied Mechanics*, 2004. 18

[122] J. N. Zalameda, W. P. Winfree, J. P. Seebo, and P. H. Johnston, "Thermography inspection for detection and tracking of composite cylinder damage during load testing," *AIP Conference Proceedings*, vol. 1335, no. 1, pp. 450–457, 2011. 18

[123] J. Gryzagoridis and D. Findeis, "Impact damage detection on composites using optical NDT techniques," *Insight - Non-Destructive Testing and Condition Monitoring*, vol. 52, no. 5, pp. 248–251, 2010. 18, 19

[124] J. Gryzagoridis, D. Findeis, and W. Bopape, "Impact damage detection on composites using electronic speckle pattern inferferometry," in *Condition Monitoring and Diagnostic Engineering Management, Cambridge*, 2005. 19

[125] W. C. Wang, C. W. Su, and P. W. Liu, "Full-field non-destructive analysis of composite plates," *Composites Part A: Applied Science and Manufacturing*, vol. 39, no. 8, pp. 1302–1310, 2008. 19

[126] N. Akhter, H. C. Jung, H. S. Chang, and K. S. Kim, "Location of delamination in laminated composite plates by pulsed laser holography," *Optics and Lasers in Engineering*, vol. 47, no. 5, pp. 584–588, 2009. 19

[127] A. Maranon, P. D. Ruiz, A. D. Nurse, J. M. Huntley, L. Rivera, and G. Zhou, "Identification of subsurface delaminations in composite laminates," *Composites Science and Technology*, vol. 67, no. 13, pp. 2817–2826, 2007. 19

[128] E. Moser, "Detection capabilities of state-of-the-art shearography systems," *Insight - Non-Destructive Testing and Condition Monitoring*, vol. 52, no. 5, pp. 22–29, 2010. 19

[129] Y. Y. Hung, "Shearography for non-destructive evaluation of composite structures," *Optics and Lasers in Engineering*, vol. 24, no. 2-3, pp. 161–182, 1996. 19

[130] Y. Y. Hung, "Applications of digital shearography for testing of composite structures," *Composites Part B: Engineering*, vol. 30, no. 7, pp. 765–773, 1999. 19

[131] G. D. Angelis, M. Meo, D. P. Almond, S. G. Pickering, and S. L. Angioni, "A new technique to detect defect size and depth in composite structures using digital shearography and unconstrained optimization," *NDT & E International*, vol. 45, no. 1, pp. 91–96, 2012. 19

[132] C. Meola, G. M. Carlomagno, A. Squillace, and A. Vitiello, "Non-destructive evaluation of aerospace materials with lock-in thermography," *Engineering Failure Analysis*, vol. 13, no. 3, pp. 380–388, 2006. 20

[133] C. Meola and G. M. Carlomagno, "Impact damage in GFRP: New insights with infrared thermography," *Composites Part A: Applied Science and Manufacturing*, vol. 41, no. 12, pp. 1839–1847, 2010. 20

[134] T. R. Emery and J. M. Dulieu-Barton, "Thermoelastic stress analysis of damage mechanisms in composite materials," *Composites Part A: Applied Science and Manufacturing*, vol. 41, no. 12, pp. 1729–1742, 2010. 20, 21

[135] S. Quinn, R. K. Fruehmann, and J. M. Dulieu-Barton, "Development of thermoelastic stress analysis as a non-destructive evaluation tool," in *17th International Conference on Composite Materials*, p. 9, 2009. 20

[136] M. A. Sutton, J. J. Orteu, and H. W. Schreier, *Image correlation for shape, motion and deformation measurements: basic concepts, theory and applications*. Springer, 2009. 21

[137] D. Claire, F. Hild, and S. Roux, "Identification of damage fields using kinematic measurements," *Comptes Rendus Mecanique*, vol. 330, no. 11, pp. 729–734, 2002. 21, 103

[138] J. N. Périé, H. Leclerc, S. Roux, and F. Hild, "Digital image correlation and biaxial test on composite material for anisotropic damage law identification," *International Journal of Solids and Structures*, vol. 46, no. 11-12, pp. 2388–2396, 2009. 21

[139] P. Sztefek and R. Olsson, "Tensile stiffness distribution in impacted composite laminates determined by an inverse method," *Composites Part A: Applied Science and Manufacturing*, vol. 39, no. 8, pp. 1282–1293, 2008. 21

[140] P. Sztefek and R. Olsson, "Nonlinear compressive stiffness in impacted composite laminates determined by an inverse method," *Composites Part A: Applied Science and Manufacturing*, vol. 40, no. 3, pp. 260–272, 2009. 21

[141] M. C. de Verdiere, A. K. Pickett, A. A. Skordos, and V. Witzel, "Evaluation of the mechanical and damage behaviour of tufted non crimped fabric composites using full field measurements," *Composites Science and Technology*, vol. 69, no. 2, pp. 131–138, 2009. 21

[142] Z. Y. Zhang and M. O. W. Richardson, "Visualisation of barely visible impact damage in polymer matrix composites using an optical deformation and strain measurement system (ODSMS)," *Composites Part A: Applied Science and Manufacturing*, vol. 36, no. 8, pp. 1073–1078, 2005. 21, 22

[143] B. Bay, T. Smith, D. Fyhrie, and M. Saad, "Digital volume correlation: three-dimensional strain mapping using X-ray tomography," *Experimental Mechanics*, vol. 39, pp. 217–226, 1999. 21

[144] H. Leclerc, J.-N. Périé, A. Fanget, E. Maire, F. Hild, and S. Roux, "Microstructure-aided digital volume correlation," in *14th International Conference on Experimental Mechanics*, vol. 6, 2010. 21

[145] S. Fhaikhao, "Detecting and monitoring surface damage on composites by grid method," Master's thesis, University of Bristol, 2007. 22, 23

[146] F. Pierron, B. Green, and M. R. Wisnom, "Full-field assessment of the damage process of laminated composite open-hole tensile specimens. Part I: methodology," *Composites Part A: Applied Science and Manufacturing*, vol. 38, no. 11, pp. 2307–2320, 2007. 22

[147] F. Pierron, B. Green, M. R. Wisnom, and S. R. Hallett, "Full-field assessment of the damage process of laminated composite open-hole tensile specimens. Part II: experimental results," *Composites Part A: Applied Science and Manufacturing*, vol. 38, no. 11, pp. 2321–2332, 2007. 22

[148] J.-H. Kim, F. Pierron, M. R. Wisnom, and K. Syed-Muhamad, "Identification of the local stiffness reduction of a damaged composite plate using the virtual fields method," *Composites Part A: Applied Science and Manufacturing*, vol. 38, no. 9, pp. 2065–2075, 2007. 22, 103, 106

[149] J.-H. Kim, F. Pierron, M. R. Wisnom, and S. Avril, "Local stiffness reduction in impacted composite plates from full-field measurements," *Composites Part A: Applied Science and Manufacturing*, vol. 40, no. 12, pp. 1961–1974, 2009. 22, 23, 31, 44, 103, 106, 121

[150] T. Ishikawa, S. Sugimoto, M. Matsushima, and Y. Hayashi, "Some experimental findings in compression-after-impact (CAI) tests of CF/PEEK (APC-2) and conventional CF/epoxy flat plates," *Composites Science and Technology*, vol. 55, no. 4, pp. 349–363, 1995. 24

[151] Y. Surrel, N. Fournier, M. Grédiac, and P.-A. Paris, "Phase-stepped deflectometry applied to shape measurement of bent plates," *Experimental Mechanics*, vol. 39, no. 1, pp. 66–70, 1999. 25, 120

[152] Y. Surrel, "Deflectometry: a simple and efficient noninterferometric method for slope measurement," in *Xth International Congress on Experimental & Applied Mechanics*, Society for experimental mechanics, 2004. 25, 31

[153] J.-H. Kim, *Identification of the local stiffness reduction of damaged composite plates using the virtual fields method.* PhD thesis, Ecole Nationale Supérieure d'Arts et Métiers (ENSAM), 2008. 25, 26, 103

[154] A. Davila, P. D. Ruiz, G. H. Kaufmann, and J. M. Huntley, "Measurement of sub-surface delaminations in carbon fibre composites using high-speed phase-shifted speckle interferometry and temporal phase unwrapping," *Optics and Lasers in Engineering*, vol. 40, no. 5-6, pp. 447–458, 2003. 36

[155] Y. Surrel, "Fringe analysis," in *Photomechanics* (P. Rastogi, ed.), vol. 77 of *Topics in Applied Physics*, pp. 55–102, Springer Berlin / Heidelberg, 2000. 36, 38, 39

[156] Y. Y. Hung and H. P. Ho, "Shearography: An optical measurement technique and applications," *Materials Science and Engineering: R: Reports*, vol. 49, no. 3, pp. 61–87, 2005. 38, 39

[157] Y. Surrel, "Phase stepping: a new self-calibrating algorithm," *Applied Optics*, vol. 32, no. 19, pp. 3598–3600, 1993. 39

[158] Y. Surrel, "Design of algorithms for phase measurements by the use of phase stepping," *Applied Optics*, vol. 35, no. 1, pp. 51–60, 1996. 39

[159] Y. Surrel, "Design of phase-detection algorithms insensitive to bias modulation," *Applied Optics*, vol. 36, no. 4, pp. 805–807, 1997. 39

[160] C. Badulescu, M. Grédiac, and J. D. Mathias, "Investigation of the grid method for accurate in-plane strain measurement," *Measurement Science and Technology*, vol. 20, no. 9, p. 17, 2009. 39, 40, 53, 88

[161] K. Itoh, "Analysis of the phase unwrapping algorithm," *Applied Optics*, vol. 21, no. 14, pp. 2470–2470, 1982. 43

[162] D. C. Ghiglia and M. D. Pritt, *Two-dimensional phase unwrapping: theory, algorithms, and software*. Wiley-Interscience publication, Wiley, 1998. 43

[163] A. Baldi, F. Bertolino, and F. Ginesu, "On the performance of some unwrapping algorithms," *Optics and Lasers in Engineering*, vol. 37, no. 4, pp. 313–330, 2002. 43

[164] L. Ying, *Wiley Encyclopedia of Biomedical Engineering*, ch. Phase Unwrapping, pp. 1–10. John Wiley & Sons, Inc., 2006. 43

[165] H. Abdul-Rahman, *Three-Dimensional Fourier Fringe Analysis and Phase Unwrapping*. PhD thesis, Liverpool John Moores University, 2007. 43

[166] E. Zappa and G. Busca, "Comparison of eight unwrapping algorithms applied to fourier-transform profilometry," *Optics and Lasers in Engineering*, vol. 46, no. 2, pp. 106–116, 2008. 43

[167] J. M. Bioucas-Dìas and G. V. ao, "Phase unwrapping via graph cuts," *IEEE Transactions on Image Processing*, vol. 16, no. 3, pp. 698–709, 2007. 43

[168] M. A. Herráez, D. R. Burton, M. J. Lalor, and M. A. Gdeisat, "Fast two-dimensional phase-unwrapping algorithm based on sorting by reliability following a noncontinuous path," *Applied Optics*, vol. 41, no. 35, pp. 7437–7444, 2002. 43

[169] S. Avril, P. Feissel, F. Pierron, and P. Villon, "Estimation of the strain field from full-field displacement noisy data: comparing finite elements global least squares and polynomial diffuse approximation," *European Journal of Computational Mechanics*, vol. 17, no. 5-7, pp. 857–868, 2008. 44

[170] B. Nayroles, G. Touzot, and P. Villon, "Generalizing the finite element method: diffuse approximation and diffuse elements," *Computational Mechanics*, vol. 10, pp. 307–318, 1992. 44

[171] A. Savitzky and M. J. E. Golay, "Smoothing and differentiation of data by simplified least squares procedures," *Analytical Chemistry*, vol. 36, no. 8, pp. 1627–1639, 1964. 44

[172] J. Steinier, Y. Termonia, and J. Deltour, "Smoothing and differentiation of data by simplified least square procedure," *Analytical Chemistry*, vol. 44, no. 11, pp. 1906–1909, 1972. 44

[173] P. A. Gorry, "General least-squares smoothing and differentiation by the convolution (Savitzky-Golay) method," *Analytical Chemistry*, vol. 62, no. 6, pp. 570–573, 1990. 44

[174] J. Luo, K. Ying, and J. Bai, "Savitzky-Golay smoothing and differentiation filter for even number data," *Signal Processing*, vol. 85, no. 7, pp. 1429–1434, 2005. 44

[175] J.-H. Kim, F. Pierron, M. Grédiac, and M. R. Wisnom, "A procedure for producing reflective coatings on plates to be used for full-field slope measurements by a deflectometry technique," *Strain*, vol. 43, no. 2, pp. 138–144, 2007. 44, 51

[176] J. M. Berthelot, *Composite materials: mechanical behavior and structural analysis*. Mechanical engineering series, Springer, 1999. 47

[177] I. Elishakoff, Y. Li, and J. H. Starnes, *Non-classical problems in the theory of elastic stability*. Cambridge University Press, 2001. 50

[178] T. K. O'Brien and R. Krueger, "Analysis of ninety degree flexure tests for characterization of composite transverse tensile strength and fatigue life," NASATM-2001-211227 ARL-TR-2568, NASA, 2001. 50, 57, 95

[179] M. E. Tuttle, "Demonstrating moiré fringes using gratings produced with a laser printer," *Experimental Techniques*, vol. 21, no. 5, pp. 19–22, 1997. 53

[180] J.-L. Piro and M. Grédiac, "Producing and transferring low-spatial-frequency grids for measuring displacement fields with moiré and grid methods," *Experimental Techniques*, vol. 28, no. 4, pp. 23–26, 2004. 53

[181] E08.03, "ASTM E2208 - 02(2010)e1: Standard guide for evaluating non-contacting optical strain measurement," 2010. 53

[182] T. J. Fellers and M. W. Davidson, "CCD Noise sources and signal-to-noise ratio." http://learn.hamamatsu.com/articles/ccdsnr.html. 53

[183] R. Berge-Gras and J. Molimard, "Optimisation de la dérivation en fonction de la résolution et de la résolution spatiale sur les déformations," in *19ème Congrès Français de Mécanique*, 2009. In French. 53

[184] P. J. Sevenhuijsen, J. S. Sirkis, and F. Bremand, "Current trends in obtaining deformation data from grids," *Experimental Techniques*, vol. 17, no. 3, pp. 22–26, 1993. 55

[185] P. J. Sevenhuijsen, "The photonical, pure grid method," *Optics and Lasers in Engineering*, vol. 18, no. 3, pp. 173–194, 1993. 55

[186] P. Davies, W. Cantwell, and H. H. Kausch, "Measurement of initiation values of GIC in IM6/PEEK composites," *Composites Science and Technology*, vol. 35, no. 3, pp. 301–313, 1989. 60

[187] P. Davies, C. Moulin, H. H. Kausch, and M. Fischer, "Measurement of GIc and GIIc in carbon/epoxy composites," *Composites Science and Technology*, vol. 39, no. 3, pp. 193–205, 1990. 60

[188] M. P. Clarke and M. J. Pavier, "Artificial damage techniques for low velocity impact in carbon fibre composites," *Composite Structures*, vol. 25, no. 1-4, pp. 113–120, 1993. 60

[189] M. Hojo, K. Kageyama, and K. Tanaka, "Prestandardization study on mode I interlaminar fracture toughness test for CFRP in japan," *Composites*, vol. 26, no. 4, pp. 243–255, 1995. 60

[190] K. Tanaka, K. Kageyama, and M. Hojo, "Prestandardization study on mode II interlaminar fracture toughness test for CFRP in japan," *Composites*, vol. 26, no. 4, pp. 257–267, 1995. 60

[191] K. D. Potter, F. J. Guild, H. J. Harvey, M. R. Wisnom, and R. D. Adams, "Understanding and control of adhesive crack propagation in bonded joints between carbon fibre composite adherends I. experimental," *International Journal of Adhesion and Adhesives*, vol. 21, no. 6, pp. 435–443, 2001. 60

[192] Hexcel, "Hexply 8552, product data." 63

[193] D20.10, "ASTM D5628 - 10: Standard test method for impact resistance of flat, rigid plastic specimens by means of a falling dart (tup or falling mass)," 2007. 66, 96

[194] F. Aymerich, F. Dore, and P. Priolo, "Prediction of impact-induced delamination in cross-ply composite laminates using cohesive interface elements," *Composites Science and Technology*, vol. 68, no. 12, pp. 2383–2390, 2008. 67

[195] C. Scarponi and G. Briotti, "Ultrasonic technique for the evaluation of delaminations on CFRP, GFRP, KFRP composite materials," *Composites Part B: Engineering*, vol. 31, no. 3, pp. 237–243, 2000. 67

[196] T. Lendze, R. Wojtyra, L. Guillaumat, C. Biateau, and K. Imielinska, "Low velocity impact damage in glass/polyester composite sandwich panels," *Advances in Materials Science*, vol. 6, no. 1, pp. 26–34, 2006. 67

[197] P. Kumar and B. Rai, "Delaminations of barely visible impact damage in CFRP laminates," *Composite Structures*, vol. 23, no. 4, pp. 313–318, 1993. 67

[198] M.-K. Yeh, L.-B. Fang, and M.-H. Kao, "Bending behavior of delaminated composite plates with contact effects," *Composite Structures*, vol. 39, no. 3-4, pp. 347–356, 1997. 73

[199] B. D. Davidson, "On modelling the residual strength of impact damaged compression loaded laminates," in *21st international SAMPE Technical Conference*, pp. 109–119, 1989. 76, 77

[200] D. S. Cairns, *Impact and post-impact response of graphite/epoxy and Kevlar/epoxy structures*. PhD thesis, Massachusetts Institute of Technology, 1987. 76

[201] D. Hull and Y. B. Shi, "Damage mechanism characterization in composite damage tolerance investigations," *Composite Structures*, vol. 23, no. 2, pp. 99–120, 1993. 76

[202] H. Suemasu, W. Sasaki, Y. Aoki, and T. Ishikawa, "Compressive behavior of impact damaged composite laminates," in *16th International Conference on Composite Materials*, 2007. 76, 77, 78

[203] R. Craven, P. Sztefek, and R. Olsson, "Investigation of impact damage in multidirectional tape laminates and its effect on local tensile stiffness," *Composites Science and Technology*, vol. 68, no. 12, pp. 2518–2525, 2008. 76

[204] M. R. Wisnom, "Measurement friction in mode II delamination with of through thickness compression," in *7th European Conference on Composite Materials: Realising Their Commercial Potential*, 1996. 77

[205] D30.05, "ASTM D7136 / D7136M - 07: Standard test method for measuring the damage resistance of a fiber-reinforced polymer matrix composite to a drop-weight impact event," 2007. 96

[206] E. V. Gonzalez, P. Maimi, P. P. Camanho, C. S. Lopes, and N. Blanco, "Effects of ply clustering in laminated composite plates under low-velocity impact loading," *Composites Science and Technology*, vol. 71, no. 6, pp. 805–817, 2011. 96

[207] M. Grédiac, "Principe des travaux virtuels et identification / Principle of virtual work and identification," *Comptes rendus de l'Académie des sciences. Série II*, vol. 309, no. 1, pp. 1–5, 1989. In French with abridged English version. 103

[208] F. Pierron and M. Grédiac, *The Virtual Fields Method: Extracting Constitutive Mechanical Parameters from Full-Field Deformation Measurements*. Springer, New-York, 2012. 103, 107

[209] S. Avril, M. Grédiac, F. Pierron, and E. Toussaint, "Deflectometry and virtual fields for identification of static plate bending stiffnesses," in *Conference: 2004 SEM X International Congress & Exposition on Experimental & Applied Mechanics*, 2004. 103

[210] M. Grédiac, "On the direct determination of invariant parameters governing anisotropic plate bending problems," *International Journal of Solids and Structures*, vol. 33, no. 27, pp. 3969–3982, 1996. 103

[211] P. Ladeveze and D. Leguillon, "Error estimate procedure in the finite element method and applications," *Journal on Numerical Analysis*, vol. 20, no. 3, pp. 485–509, 1983. 103

[212] J. N. Reddy and C. M. Wang, "An overview of the relationships between solutions of the classical and shear deformation plate theories," *Composites Science and Technology*, vol. 60, no. 12-13, pp. 2327–2335, 2000. 104

[213] K. Syed-Muhammad, E. Toussaint, M. Grédiac, S. Avril, and J.-H. Kim, "Characterization of composite plates using the virtual fields method with optimized loading conditions," *Composite Structures*, vol. 85, no. 1, pp. 70–82, 2008. 106

[214] E. Toussaint, M. Grédiac, and F. Pierron, "The virtual fields method with piecewise virtual fields," *International Journal of Mechanical Sciences*, vol. 48, no. 3, pp. 256–264, 2006. 106

[215] A. Giraudeau, F. Pierron, and B. Guo, "An alternative to modal analysis for material stiffness and damping identification from vibrating plates," *Journal of Sound and Vibration*, vol. 329, no. 10, pp. 1653–1672, 2010. 106

[216] A. S. Patki and E. A. Patterson, "Damage assessment of fibre reinforced composites using shape descriptors," *Journal of Strain Analysis*, vol. 47, no. 4, pp. 244–253, 2012. 119, 120

[217] D. Claire, F. Hild, and S. Roux, "Identification of a damage law by using full-field displacement measurements," *International Journal of Damage Mechanics*, vol. 16, no. 2, pp. 179–197, 2007. 119

[218] P. Rose, Y. Surrel, and J. M. Becker, "Specific design requirements for a reliable slope and curvature measurement standard," *Measurement Science And Technology*, vol. 20, p. 10, 2009. 120

IDENTIFICATION D'ENDOMMAGEMENTS AU SEIN DE PLAQUES COMPOSITES STRATIFIÉES À L'AIDE DE MESURES DE CHAMPS CINÉMATIQUES

Résumé : Ce travail porte sur le développement d'une technique expérimentale qui peut aider à définir les paramètres clefs du comportement après impact de panneaux composites stratifiés. Pour cela, des modèles éléments finis ont été construits pour inclure des délaminages à partir d'observations de CT-scans d'échantillons impactés. Les résultats de ces modèles ont été comparés à des mesures expérimentales obtenues par une technique de mesure de champs de pentes: la déflectométrie. Ce travail aussi présente un nouvel indicateur d'endommagements basé sur l'application de la méthode des champs virtuels à l'évaluation d'écarts locaux à l'équilibre. Cette procédure d'abord détaillée est ensuite appliquée à des échantillons de types poutres et plaques. Les résultats expérimentaux illustrent la remarquable sensibilité de cette technique de mesure : elle permet de capturer les effets de très faibles endommagements. Aussi, cette technique montre que les simples modèles numériques présentés dans ce travail nécessitent des améliorations pour se rapprocher des données expérimentales. L'indicateur d'écart à l'équilibre a détecté correctement le contour des zones endommagées quand suffisamment d'information spatiale était disponible. Poursuivre ce travail permettrait de créer un outil précieux aidant la conception de pièces en composites.

Mots clés : Composites à fibres de carbone; Mesures optiques; Impact; Contrôle non destructif; Simulation par ordinateur

---

DAMAGE IDENTIFICATION IN LAYERED COMPOSITE PLATES USING KINEMATIC FULL-FIELD MEASUREMENTS

Abstract: This work focuses on the development of an experimental technique which can help to define the key parameters for post-impact behaviour of laminated composite panels. To address this issue, finite element models were built to represent delaminations based on the observations of CT-scans of impacted samples. The results of these models have been correlated to experimental data obtained using a slope full-field measurement technique: deflectometry. This work also develops a new damage indicator based on the application of the virtual fields method to compute a local equilibrium gap. The procedure is first presened and then applied to beam and plate samples. The experimental results illustrate the remarkable sensitivity of this measurement method as it captures the effect of very small amount of damage and shows that the simple numerical models need to be refined to present a better correlation to experimental results. The damage indicator successfully detects contours of damaged areas when sufficient spatial information is available. It is believed that pursuing the present work could lead to an invaluable tool to help design engineers.

Keywords: Carbon composites; Optical measurements; Impact; Non-destructive testing; Computer simulation